Electronic structure and morphology of organic semiconductors and the impact of molecular modifications

Dissertation
zur Erlangung des Grades
des Doktors der Naturwissenschaften
der Naturwissenschaftlich-Technischen Fakultät
der Universität des Saarlandes

von
Clemens Matt

Saarbrücken
2021

Tag des Kolloquiums: 6. August 2021

Dekan: Prof. Dr. Jörn Erik Walter

Berichterstatter: Priv.-Doz. Dr. Till Biskup

Prof. Dr.-Ing. Markus Gallei

Vorsitz: Prof. Dr. Claus Jacob

Akad. Mitarbeiter: Dr. Dan Durneata

Contents

List of Figures

Abbreviations

General expressions

ETM	electron-transporting material
HTM	hole-transporting material
OSC	Organic solar cell
OLED	Organic light-emitting diode
OFET	Organic field-effect transistor
HOMO	Highest occupied molecular orbital
LUMO	Lowest unoccupied molecular orbital
UV-VIS	Ultraviolet-visible
EPR	electron paramagnetic resonance
cwEPR	continuous-wave electron paramagnetic resonance
TREPR	time-resolved electron paramagnetic resonance
EZ	electron Zeeman
ZF	zero field
ZFS	zero-field splitting
SOC	spin-orbit coupling
QN	quantum number
MW	microwave
A	acceptor
D	donor
ISC	intersystem crossing
CT	charge transfer
RP	radical pair
DFT	density functional theory
HF	Hartree–Fock
BO	Born–Oppenheimer
KS	Kohn–Sham

TDDFT	time-dependent density functional theory
LDA	local density approach
GGA	generalised gradient approach
TDA	Tamm–Dancoff approximation

Molecules

T	Thiophene
BT	Benzothiadiazole
Cbz	Carbazole
NDI	Naphthalenediimide
T-NDI-T	*N*,*N’*-bis(2-octyldodecyl)-naphthalene-1,4,5,8-bis(dicarboximide)-5,5’-(2-thiophene)
NDI-T2	*N*,*N’*-bis(2-octyldodecyl)-naphthalene-1,4,5,8-bis(dicarboximide)-5-(2,2’-bithiophene)
T2-NDI-T2	*N*,*N’*-bis(2-octyldodecyl)-naphthalene-1,4,5,8-bis(dicarboximide)-5,5’-(2,2’-bithiophene)
TBT	4,7-di-(5-thienyl)-2,1,3-benzothiadiazole
hexTBT	4,7-di-(4-hexyl-2-thienyl)-2,1,3-benzothiadiazol
PCDTBT	Poly[*N*-9’-hepta-decanyl-2,7-carbazole-*alt*-5,5-(4’,7’-di-2-thienyl-2’,1’,3’-benzothiadiazole)]
hexPCDTBT	Poly[*N*-9’-hepta-decanyl-2,7-carbazole-*alt*-5,5-(4’,7’-(di-4-hexyl-2-thienyl)-2’,1’,3’-benzothiadiazole)]
PNDIT2	Poly[*N*,*N’*-bis(2-octyldodecyl)-naphthalene-1,4,5,8-bis(dicarboximide)-2,6-diyl]-*alt*-5,5’-(2,2’-bithiophene)
PNDITBT	Poly[*N*,*N’*-bis(2-octyldodecyl)-naphthalene-1,4,5,8-bis(dicarboximide)-2,6-diyl]-*alt*-5,5’-(4’,7’-di-2-thienyl-2’,1’,3’-benzothiadiazole)

Kurzzusammenfassung

Konjugierte Copolymere aus alternierenden Donator- und Akzeptor-Einheiten spielen eine herausragende Rolle in der organischen Elektronik, da sich ihre Eigenschaften durch chemische Modifikationen und Austausch von Donatoren oder Akzeptoren flexibel an das jeweilige Anwendungsgebiet anpassen lassen. Voraussetzung zum Verständnis ihrer Funktionsweise ist eine tiefe Kenntnis ihrer Struktur-Funktions-Beziehungen. Dazu werden Methoden mit einer molekularen Auflösung benötigt. Insbesondere die TREPR-Spektroskopie eignet sich zur Untersuchung der elektronischen Struktur und Morphologie dieser Materialien. In dieser Arbeit wurden ergänzend dazu DFT-Rechnungen durchgeführt und notwendige Auswertungsroutinen erarbeitet.

Eingangs wurde die elektronische Struktur und die Morphologie des Polymers PCDTBT und von Fragmenten verschiedener Länge untersucht. Basierend auf diesen Ergebnissen wurde der Einfluss zusätzlicher Hexyl-Seitenketten detailliert ergründet. Für die dominierende Einheit TBT konnten Triplett-Entstehungswege, insbesondere die direkte Anregung aus dem Singulett-Grundzustand in den Triplett-Zustand, aufgeklärt werden. Durch das Verknüpfen von TBT mit dem bereits bekannten Akzeptor NDI wurde darüber hinaus der Einfluss zweier konkurrierender Akzeptoren auf die elektronische Struktur erfasst. Abschließend wurden für das Polymer PNDIT2 zwei potentielle Wiederholeinheiten, NDI-T2 und T-NDI-T, untersucht und NDI-T2 als der im Polymer dominierende Chromophor identifiziert.

Abstract

Conjugated copolymers consisting of alternating donor and acceptor units play a prominent role in organic electronics, as their properties can be flexibly adapted to the respective field of application by chemical modifications and exchange of donors or acceptors. A prerequisite for understanding how these materials function is a deep knowledge of their structure-function relationships. This requires methods with a molecular resolution. TREPR spectroscopy in particular is suitable for investigating the electronic structure and morphology of these materials. In this work, DFT calculations were carried out in addition and necessary evaluation routines were developed.

First, the electronic structure and morphology of the polymer PCDTBT and fragments of different lengths were investigated. Based on these results, the influence of additional hexyl side chains was investigated in detail. For the dominant unit TBT, triplet formation pathways could be elucidated, in particular the direct excitation from the singlet ground state into the triplet state. Furthermore, by linking TBT with the already known acceptor NDI, the influence of two competing acceptors on the electronic structure was detected. Finally, two potential repeat units, NDI-T2 and T-NDI-T, were investigated for the polymer PNDIT2 and NDI-T2 was unequivocally identified as the dominant chromophore in the polymer.

Part I.

Introduction

1. Organic electronics

1.1. Introduction

Semiconducting properties of organic molecules were first found for a perylene-bromine complex in the year 1954 [1]. Shortly afterwards, in 1958, the photovoltaic effect was encountered for the first time in an organic material, in this case a thin film of magnesium phthalocyanine combined with tetramethyl p-phenylenediamine [2]. In 1963 electroluminescence was first observed in an anthracene crystal [3]. Scientists then turned their attention towards larger conjugated systems, leading to the first organic field-effect transistor (OFET) [4] and more efficient organic solar cells (OSCs) [5], organic light emitting diodes (OLEDs) [6], sensors [7, 8] and molecular wires [9]. These successful developments culminated in the Nobel Prize being awarded to Alan J. Heeger [10], Alan G.MacDiarmid [11] and Hideki Shirakawa [12] “ for the discovery and development of conductive polymers ” [13].

The materials investigated in this work fall into the same category. They are conjugated copolymers built from alternating donor and acceptor moieties. The terms donor and acceptor refer to molecules or parts of a polymer donating or accepting electrons. The polymers themselves can also be divided in two similar categories, donor and acceptor polymers. Figure 1.1 (c) presents a scheme of a ppositively charged hole and a negatively charged electron on a donor and acceptor polymer. In the context of poylmers, the terms donor and acceptor refers, more precisely, to hole or electron transporting materials (HTMs/ETMs). To avoid misunderstandings the terms donor and acceptor will be used for the building blocks of the copolymers, and hole transporting material (HTM) and electron transporting material (ETM) for the entire polymers. In order to build devices, both types of materials play an inportant role, explained in section 1.2. The two polymers investigated in this work poly[*N*,*N’*-bis(2-octyldodecyl)-naphthalene-1,4,5,8-bis(dicarboximide)-2,6-diyl]-*alt*-5,5’-(2,2’-bithiophene) (PNDIT2) and poly[*N*-9’-hepta-decanyl-2,7-carbazole-*alt*-5,5-(4’,7’-di-2-thienyl-2’,1’,3’-benzothiadiazole)] (PCDTBT) [14, 15] fall into these two categories. PNDIT2 built from alternating bithiophene (T2) as donor and naphthalenediimide (NDI) as acceptor units. It became popular for its high charge carrier mobility and oxygen resistance, and was used as a component for transistors [16]. It also serves as electron transporting material; a field of application previously dominated by fullerenes [17, 18]. PNDIT2 is one of the first polymers used as ETM, leading to high efficiencies in OSCs [19, 20]. The other copolymer PCDTBT consists of two donors, thiophene (T) and carbazole (Cbz), and one acceptor, the benzothiadiazole (BT). It was used as HTM and in combination with [6,6]-phenyl C_{70}-butyric acid methyl ester $PC_{71}BM$ as ETM in OSCs. This way an internal quantum efficiency close to 100% and a 6% total efficiency could be achieved [21]. The hexylated form of the polymer, with hexyl side chains attached to the thiophenes, shows a high fluorescence efficiency and is therefore an interesting material for OLEDs [22].

From the beginning, organic electronics have had to compete with their inorganic counterparts based on silicon. Promising advantages are their flexibility [23–25], transparency [26], low production costs [27] and the possibility to print them [28]. Also, recent developments are leading towards sustainable materials [29]. Unlike silicon, polymers can easily be manipulated via organic synthesis, which makes it possible to tailor them according to the needs in their field of application. Despite all the promising advantages and applications of organic electronics, some challenges remain that must be overcome in order to reach their full potential. These are, in comparison to the inorganic materials: sensitivity to environmental conditions and in particular to oxygen, short lifespan, lower efficiency and conductivity. To tackle those issues it is important to analyse the structure-function relationship. The idea behind this is to understand how molecular modifications influence the aforementioned properties of interest, resulting in design rules for new materials.

Investigating the structure-function relationship requires knowledge of the molecular processes involved in organic electronics, in order so see how structural changes of the polymer affect them. Therefore it is important to understand the basic concepts behind the working principle of organic electronics and how they apply to the devices.

1.2. Concepts and working principle

Organic semiconductors are characterised by three major material properties: they are made of organic molecules, their conductivity must be high enough and they need to possess a band gap in the visible spectral range [30]. Even though the last two properties are mostly shared with their inorganic counterparts, differences remain. In the following band gap and conductivity will be discussed and the mentioned differences will be addressed.

The band gap depends highly on the energy gap between the highest occupied molecular orbital (HOMO) and the lowest unoccupied molecular orbital (LUMO). It is an important property indicating the amount of energy that needs to be invested to generate an exciton. It consists of the negatively charged electrons and their positively charged counterparts, the holes. Those opposite charges attract each other via a Coulomb interaction. In inorganic materials those electron–hole pairs are delocalised over several atoms, with a distance of $\approx$ 10 nm [31]. The excitons in organic materials are more localised because of the poorer charge stabilisation originating from a lower dielectric constant [32]. Distances of $\approx$ 0.1 nm between the particles are typically observed [31]. Common ways to separate charges are via an electric potential, or light excitation. Only the latter is relevant in the context of this work. In Figure 1.1 the generation of a light-induced exciton is shown. First, a photon which sufficient energy to surpass the HOMO–LUMO gap needs to be absorbed. This way, singlet excitons with a total electronic spin of 0 are created. Those singlet excitons can transition into triplet excitons via an intersystem crossing (ISC) mechanism. Triplet excitons have a total electronic spin of 1, are usually lower in energy and more localised than singlets, due to the additional exchange energy, as discussed in more detail in chapter 3. They have also longer life times because relaxation into the ground state involves a forbidden spin flip. A more detailed description is presented in section 2.2.1.

A key aspect contributing to the conductivity is the ability of charge carriers to move though the material. The way exciton transport takes place in organic and inorganic semiconductors

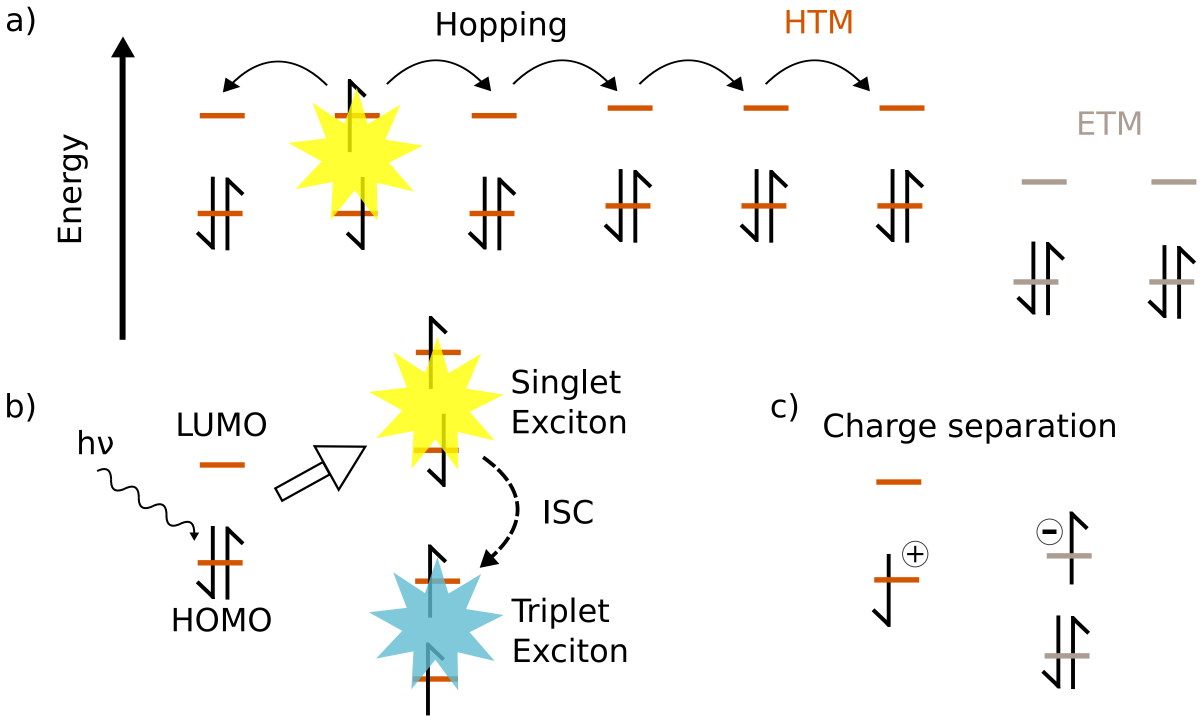

Figure 1.1.: Exciton migration (a), creation (b) and charge separation (c). The orange and grey bars represent the HOMO and LUMO of the HTM and the ETM respectively, the half arrows the electrons. The creation of singlet and triplet excitons is shown at the example of light absorption followed by ISC. Via a hopping mechanism those excitons can move through different molecules. If they reach the interface between HTM and ETM a charge separation can take place leading to negative and positive charged polarons.

is different. For inorganic crystalline materials it takes place via the conduction band, which is formed by contributions from all the atoms in the solid. In organic materials both the single molecule and the morphology play an important role in how excitons move. In an ordered crystalline region such as formed by anthracene, the charge carrier transport proceeds via a band model. At the interface between crystalline domains, the mode of transport is then changed to intermolecular hopping [33] depicted in Figure 1.1. Such a mechanism can be explained by Förster resonance energy transfer (FRET) or Dexter energy transfer [32]. At low temperatures (< 150 K) a downhill migration is observed were the exciton moves towards the energetically most favourable state. This process usually takes place in the time scale of 100–500 ps for singlet excitons [32, 34]. Observed diffusion lengths are 5–20 nm for singlet and 10–250 nm for triplet excitons [31].

The generation of photocurrent relies on the separation of the electron–hole pair forming the exciton. For efficient charge separation in organic materials, usually two types of molecules are used acting as HTM and ETM, respectively. The role of the HTM is to generate an exciton and to transfer the excited electron onto the ETM. To energetically favour this separation process, the ETM needs a lower lying LUMO than the HTM. At this stage, the two charge carriers are still Coulomb bound and therefore usually referred to as a charge-transfer (CT) exciton. In the last step, this Coulomb interaction needs to be overcome to obtain separated holes and electrons referred to as polarons, which can then be used to create a current.

Since the mentioned processes all take place on a molecular scale, methods with the appropriate resolution are required. With time-resolved electron paramagnetic resonance (TREPR), the paramagnetic triplet excitons can be detected after light excitation [35]. Previous studies have shown that it is possible to investigate the morphology [36], the pathways to triplet excitons [37], and the electronic structure of polymers in solution [38] and as thin film on a substrate [39].

1.3. Outline of this work

The focus of the investigations was on the impact of systematic molecular variations onto the electronic structure and the morphology of both polymers PCDTBT and PNDIT2. To examine the electronic structure, TREPR spectroscopy was used to probe the triplet excitons. From these experiments information about the delocalisation and the environment of the exciton could be gained. UV-VIS spectroscopy delivered details about the singlet exciton, most importantly the HOMO–LUMO gap and its delocalisation length. UV-VIS and TREPR measurements were performed on solutions, frozen ones in the case of TREPR, unless described otherwise. Insights into the morphology were gained by performing UV-VIS measurement series at different temperatures revealing possible aggregation. Additionally, thin films of the polymer PCDTBT cast on a substrate were analysed with angular-dependent TREPR spectroscopy, to detect a possible ordered structure.

The largest addition compared to previous works are the added density functional theory (DFT) calculations of TREPR and UV-VIS properties. This enabled us to locate the triplet excitons on a molecular level via its spin density distribution. Additionally the spatial allocation of the dipolar coupling between both unpaired electrons could be invested. Also the singlet exciton could be located through calculating the orbitals involved in the UV-VIS transition. Through optimisations of the molecular geometries the impact of modifications could directly be revealed. This way observed differences in the exciton behaviour could be linked to the molecular structure. At this point it shall be mentioned that DFT calculation have limited significance if not backed up by experimental data.

From the building block to the polymer (Publications 1 and 2)

One way to better understand the electronic structure of a polymer is by analysing its building blocks, starting with the monomers up to fragments of the polymer with different lengths [38, 40]. Using this approach the donor-acceptor alternating copolymers PCDTBT and its hexylated counterpart are analysed. The chosen units are TBT, Cbz-TBT, Cbz-TBT-Cbz, TBT-Cbz-TBT and the polymer for both forms, hexylated and nonhexylated. With the combined effort of DFT calculations, UVVIS and TREPR spectroscopy, it could be shown that a single TBT unit dominates the electronic structure of the entire polymer in both cases. By comparing singlet and triplet exciton delocalisations with growing chain lengths, a similar behaviour could be observed. These findings showed that knowledge about the singlets could be gained out of analysis from the triplets. Both studies show how extensive investigations have to be, in order to obtain detailed information about the electronic structure.

Side-chain impact (Publications 1, 2 and 3)

The hexylation of the thiophenes of the PCDTBT system was introduced to increase the solubility of the polymer in organic solvents. The additional effects of this modification onto the electronic and the molecular structure, as well as the morphology was looked at. To get the impact of the hexylation onto the molecular structure extensive additional DFT calculation to the previous one [22] were performed. The obtained torsions between the Cbz and TBT moieties for the hexPCDTBT were closer analysed and could be associated with a poorer conjugation. This impact onto the electronic structure could also be found in the smaller delocalisations of the triplet and singlet excitons in hexPCDTBT compared to PCDTBT. By comparing TREPR data from PCDTBT with different degrees of hexylation, a systematic decrement of the exciton delocalisations could be detected. Confirming the impact of the hexylation on the conjugation. Additionally to the geometries and the spin-density distributions, the dipolar coupling between the two unpaired electrons forming the triplet exciton was calculated. It allowed for more advanced assignment of the TREPR data and thus to a deeper understanding of the impact of the hexylation onto the polymers curvature.

Thin Films of PCDTBT on a substrate, with the same different degrees of hexylation as mentioned earlier, were used to probe the morphology. It could be shown that the films show a larger delocalisation than the solutions, what could be correlated with a more planar backbone of the polymer when deposed on substrate. Different measured orientation of the films revealed an underlying order of the polymer. Taking into account that TBT dominates the electronic structure and knowing the spatial orientation of the dipolar coupling between the unpaired electrons, advanced TREPR experiments (magnetophotoselection) allowed to determine a face on orientation of PCDTBT on the substrate, even though PCDTBT being amorphous.

Pathways towards triplet states (Publication 4)

Previously the pathways towards the triplet state via light excitation was investigated for repeat unit of PCDTBT the Cbz-TBT [37]. Knowing that TBT entirely dominates the electronic structure, the same TREPR experiments were performed on the smaller unit. Like Cbz-TBT, TBT showed a triplet signal when excited with lower energies than its HOMO–LUMO gap. In this case excitation goes via a direct singlet–triplet excitation out of the ground state. Also the path via ISC lead to the same triplet, whereas different triplet states are populated via the direct singlet–triplet excitation. A faster decomposition of the sample provides hints that Cbz is important for the photo stability of the polymer.

Different donor-acceptor constellations (publications 5 and 6)

Changes in the donor–acceptor constellations of the PNDIT2 and their impact onto the electronic structure were analysed. In a first step the donor unit T2 was extended with the acceptor bezothiadiazol into a TBT unit. Through these modifications the polymer PNDITBT was obtained. To capture the impact of both acceptors NDI and BT onto the electronic structure, profound knowledge about the single acceptors was needed. It could be obtained from the studies of PNDIT2 [41] and PCDTBT. By comparing TREPR spectra and DFT calculations of the two polymers with PNDITBT, it could be shown that the acceptor BT is a stronger acceptor than NDI. In a second step, the two potential repeat units of PNDIT2, T-NDI-T and NDI-T2 equivalent to D-A-D and A-D-D systems, were analysed. As demonstrated with the former studies of this work, knowledge about the unit dominating the electronic structure has proven to be key for further analysis of related systems. From TREPR and DFT data NDI-T2 could be determined as the true repeat unit in terms of the electronic structure.

Part II.

Theory

2. EPR spectroscopy

In a variety of important processes that take place on a molecular level, paramagnetic species are found. Some examples are cofactors like iron-sulfur complexes [42] or flavines [43] found in proteins, doped organic or inorganic materials [44, 45], defects in crystal structures [46], transition metal complexes [47, 48], intermediate radical products in chemical reactions [49–51], or photoexcited states [35, 52, 53]. The method of choice to investigate these species is electron paramagnetic resonance (EPR) spectroscopy. It is only sensitive to paramagnetic species and can give information about the quantity [54, 55], the spin multiplicity [56, 57] and the molecular environment of the paramagentic species. Application of EPR spectroscopy outside of the academic world are in the food industry [58–60] and for alanine dosimetry [61].

The first EPR experiment was reported in 1945 by Zavoisky [62]. To detect a signal the sample needs to be paramagnetic, *i.e.* contain unpaired electrons. Electrons possess a property called the electronic spin, which can quantum-mechanically be expressed as an angular momentum [63], resulting in a reversely oriented magnetic moment. If positioned into an external magnetic field the magnetic moment can orient itself antiparallel or parallel to the magnetic flux. A parallel orientation leads to a lowering and antiparallel to an increase in energy. This splitting of the spin levels, named after its discoverer Pieter Zeeman [64], builds the foundation for EPR spectroscopy. Radiation matching the energy of the splitting can induce transition between both states. More precisely, the magnetic component of the matching photon is absorbed, what then can be detected as a EPR signal.

In this work, a special variant of EPR spectroscopy, time-resolved EPR spectroscopy has been used to investigate the excited triplet states of organic electronics materials. The first part of this chapter deals with the theory needed to understand the basics of TREPR spectroscopy. In the second part, details of the experimental setups used and resulting spectra are shown.

2.1. Spin Hamiltonian

In quantum mechanics the Hamilton operator contains all terms describing physical interactions. Applied onto the corresponding wavefunction the energies correlated with those interactions can be calculated. For EPR spectroscopy, the relevant interactions are summed up in the so-called spin Hamiltonian [65, 66]. The different contributions relevant for this work will be presented in this section.

2.1.1. Zeeman splitting

The resulting magnetic moment $\hat{\boldsymbol{\mu}}_\mathrm{e}$ of the spin of a single electron in vacuum is described by

$$\hat{\boldsymbol{\mu}}_\mathrm{e} = -g_\mathrm{e}\frac{\mu_\mathrm{B}}{\hbar} \cdot \hat{\boldsymbol{S}}, \tag{2.1}$$

where g_e is the Landé factor, μ_B (Bohr magneton) and $\hbar$ (reduced Planck constant) are two constants, and $\hat{\boldsymbol{S}}$ is the spin vector operator [67]. The latter can be expressed as:

$$\hat{\boldsymbol{S}} = \frac{\hbar}{2}\begin{pmatrix} -\hat{\sigma}_\mathrm{x} \\ \hat{\sigma}_\mathrm{y} \\ \hat{\sigma}_\mathrm{z} \end{pmatrix}, \tag{2.2}$$

with the Pauli spin matrices [68]

$$\hat{\sigma}_\mathrm{x} = \begin{pmatrix} 0 & 1 \\ 1 & 0 \end{pmatrix}, \quad \hat{\sigma}_\mathrm{y} = \begin{pmatrix} 0 & -i \\ i & 0 \end{pmatrix} \quad \text{and} \quad \hat{\sigma}_\mathrm{z} = \begin{pmatrix} 1 & 0 \\ 0 & -1 \end{pmatrix}. \tag{2.3}$$

Eigenvectors of the z component of the spin vector operator are the two spin vectors $|\alpha\rangle = \binom{1}{0}$ and $|\beta\rangle = \binom{0}{1}$, denoting spin up and spin down. Applying $\hat{S}_z$ on those spin vectors gives in the bra ket notation

$$\hat{S}_z|\alpha\rangle = \frac{\hbar}{2}\begin{pmatrix} 1 \\ 0 \end{pmatrix} \tag{2.4}$$

and

$$\hat{S}_z|\beta\rangle = -\frac{\hbar}{2}\begin{pmatrix} 0 \\ 1 \end{pmatrix}. \tag{2.5}$$

Their expectation values are

$$\langle\alpha|\hat{S}_z|\alpha\rangle = \frac{\hbar}{2} \tag{2.6}$$

and

$$\langle\beta|\hat{S}_z|\beta\rangle = -\frac{\hbar}{2}. \tag{2.7}$$

Those equations lead to the more general expression of the expectation value $\langle\hat{S}_z\rangle = M_\mathrm{S}\hbar$. A single electron possesses a spin quantum number (QN) of $S = \frac{1}{2}$ and the corresponding magnetic-spin QNs are $M_\mathrm{S} = \pm\frac{1}{2}$. If an external magnetic field $\boldsymbol{B}$ is applied onto a magnetic moment, their interaction can be described by the following Hamilton operator [67]

$$\hat{H} = -\hat{\boldsymbol{\mu}} \cdot \boldsymbol{B}. \tag{2.8}$$

If $\boldsymbol{B}$ is only applied in the z direction and by taking equation (2.1) into account, the Hamiltonian is reduced to

$$\hat{H}_\mathrm{EZ} = g_\mathrm{e}\frac{\mu_\mathrm{B}}{\hbar}\hat{S}_z B_z \tag{2.9}$$

and is often referred to as the electron Zeeman (EZ) Hamiltonian named after Pieter Zeeman [64] who first discovered the splitting of the different magnetic angular moments in a homogenous magnetic field. The expectation values of energies of α and β electrons can be calculated similarly to equation (2.6) and (2.7) by replacing the spin operator with $\hat{H}_\mathrm{EZ}$. Energies of

$$E_\alpha = \langle\alpha|\hat{H}_\mathrm{EZ}|\alpha\rangle = \frac{1}{2}g_\mathrm{e}\mu_\mathrm{B}B_z \tag{2.10}$$

and

$$E_\beta = \langle\beta|\hat{H}_\mathrm{EZ}|\beta\rangle = -\frac{1}{2}g_\mathrm{e}\mu_\mathrm{B}B_z \tag{2.11}$$

are obtained. The energy difference ΔE between the two spin states, the so-called Zeeman splitting, can easily be calculated by subtraction. As illustrated in Figure 2.1, it increases with the strength of the external magnetic field. Electromagnetic radiation can induce transitions between those states. The energy of the applied photons must match the energy difference

$$\Delta E = h\nu = g_\mathrm{e}\mu_\mathrm{B}B_z\,. \tag{2.12}$$

In case of exact resonance, the photons angular frequency $\omega = 2\pi\nu$ matches the Larmor frequency ω_L, describing the rotation of the electron spin around B_0.

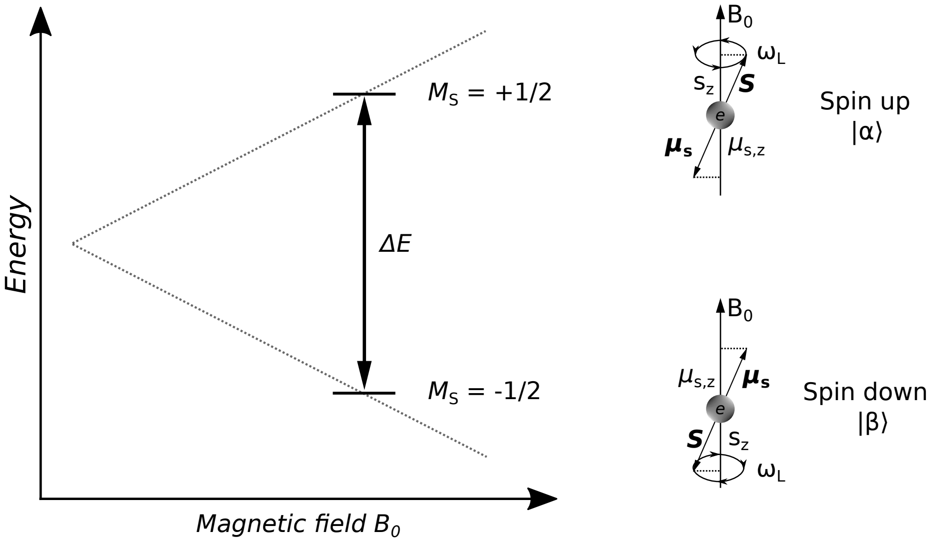

Figure 2.1.: Zeeman splitting of the electron spin states $|\alpha\rangle$ and $|\beta\rangle$ as function of the magnetic field B_0. The magnetic moment is antiparallel to the spin and is aligned with B_0 for the spin state $|\beta\rangle$, resulting in reduction of the energy. For $|\alpha\rangle$ an increase in energy is observed due to the antiparallel orientation of the magnetic moment with respect to B_0. In both states the spin rotates with the Larmor frequency ω_L but in different directions.

As indicated in Figure 2.1, transitions can be induced from α to β and *vice versa.* Because of the energy difference between both spin states, they are not equally populated. According to the Boltzmann distribution, state β is more populated than α. So statistically more transitions of β to α are induced than *vice versa.*

2.1.2. Interaction with the environment

The previous equations were derived for a single electron in vacuum. For real systems, environmental influences are affecting the electron and need to be taken into account. Especially effects causing anisotropy can not be described by a single term like in equation (2.9). Replacing the Landé factor by the **g** tensor, a 3×3 matrix [67], solves this problem. Equation (2.9) can be rewritten as

$$\hat{H}_\mathrm{EZ} = \frac{\mu_\mathrm{B}}{\hbar}\hat{\boldsymbol{S}} \cdot \mathbf{g} \cdot \boldsymbol{B}\,. \tag{2.13}$$

Two effects included in the **g** tensor are the interactions of the magnetic field $\boldsymbol{B}$ with the angular momentum $\hat{\boldsymbol{L}}$ of the electron and that of $\hat{\boldsymbol{L}}$ with $\hat{\boldsymbol{S}}$. For the coupling of $\boldsymbol{B}$ and $\hat{\boldsymbol{L}}$ a similar expression to equation (2.9) can be derived, by replacing $\hat{\boldsymbol{S}}$ with $\hat{\boldsymbol{L}}$ and g_e with the corresponding

Landé Factor of the angular momentum $g_\mathrm{l} = 1$. The second mentioned interaction is known as the spin–orbit coupling (SOC). It is expressed by the product of the vector operators, multiplied by the coupling constant λ. By adding up all contributions to the **g** tensor, equation (2.13) becomes [67, 69]:

$$\hat{H}_\mathrm{EZ} = \frac{\mu_\mathrm{B}}{\hbar} g_\mathrm{e} \hat{\boldsymbol{S}} \cdot \boldsymbol{B} + \frac{\mu_\mathrm{B}}{\hbar} g_\mathrm{l} \hat{\boldsymbol{L}} \cdot \boldsymbol{B} + \frac{\lambda}{\hbar^2} \hat{\boldsymbol{L}} \cdot \hat{\boldsymbol{S}} \,. \tag{2.14}$$

When compared with the total Hamiltonian of the system including Coulomb and kinetic energies, $\hat{H}_\mathrm{EZ}$ represents only a small contribution. Therefore, it is possible to treat it via Rayleigh–Schrödinger perturbation theory [70, 71]. Including terms of second order, the Hamiltonian describing this perturbation can be written as [67]:

$$\hat{H}_\mathrm{Perturbation} = \sum_{a,b=x,y,z} \mu_\mathrm{B}^2 \Lambda_{ab} B_a B_b + \frac{\mu_\mathrm{B}}{\hbar} B_a (g_\mathrm{e} \delta_{ab} + 2\lambda \Lambda_{ab}) \hat{S}_b + \frac{\lambda^2}{\hbar^2} \Lambda_{ab} \hat{S}_a \hat{S}_b \,, \tag{2.15}$$

with

$$\Lambda_{ab} = \hbar^{-2} \sum_{K \neq 0} \frac{\langle 0 | \hat{L}_a | K \rangle \langle K | \hat{L}_b | 0 \rangle}{E_0 - E_K} \,. \tag{2.16}$$

The term 0 denotes the unperturbed state and K all other (unperturbed) states. A more detailed background to perturbation theory and the derivation of the equation can be found in [72], [73] and [74]. The first term in equation (2.15) gives rise to the same shift in energy to all states. EPR spectroscopy is only sensitive to the energy difference between states, therefore the first term can be dropped. From the second term, the matrix elements of the **g** tensor from equation (2.14) can be calculated. The last term contains contributions from two electronic spins and is only important for systems with $S > \frac{1}{2}$.

2.1.3. Interaction between two electron spins

For systems with more than one unpaired electron spin, additional interactions occur. For triplet states with two unpaired electron spins, they are described by the spin–spin interaction Hamiltonian. It can be written as the sum of the Heisenberg exchange ($\hat{H}_\mathrm{EX}$) and the zero-field splitting ($\hat{H}_\mathrm{ZFS}$) Hamiltonians [75]:

$$\hat{H}_\mathrm{SS} = \hat{H}_\mathrm{EX} + \hat{H}_\mathrm{ZFS} \,. \tag{2.17}$$

Two-electron-spin wavefunctions

The spins QNs of the two spins S_1 and S_2 can be summed up to a total spin QN $S = S_1 + S_2$ of 1 if both spins point in the same, or to 0 if the spins point in opposite directions, respectively. In the case of $S = 1$ three different spin wavefunctions $|T_+\rangle$,$|T_0\rangle$ and $|T_-\rangle$ corresponding to $M_\mathrm{S} = \{-1, 0, 1\}$ can be constructed from the single spin functions $|\alpha\rangle$ and $|\beta\rangle$. They are antisymmetric with respect to the exchange of the electrons and are associated with the triplet state. For $S = 0$ and $M_\mathrm{S} = 0$, there is only one spin wavefunction $|S_0\rangle$, which is symmetric to the exchange of the electrons, associated with the singlet state. All four wavefunctions expressed with the single spin vectors $|\alpha\rangle$ and $|\beta\rangle$ are:

$$\begin{aligned}
&|T_{+}\rangle = |\alpha(1)\alpha(2)\rangle\,, \\
&|T_{0}\rangle = \frac{1}{\sqrt{2}}[|\alpha(1)\beta(2)\rangle + |\beta(1)\alpha(2)\rangle]\,, \\
&|T_{-}\rangle = |\beta(1)\beta(2)\rangle \\
&\text{and} \\
&|S_{0}\rangle = \frac{1}{\sqrt{2}}[|\alpha(1)\beta(2)\rangle - |\beta(1)\alpha(2)\rangle]\,.
\end{aligned} \tag{2.18}$$

To differentiate the wavefunctions their corresponding electronic states, the states will be addressed as T_{+}, T_{0}, T_{-} and S_{0} using upright letters, whereas the wavefunctions will be written in in the bra ket notation like in equation (2.18) and using italic letters.

Heisenberg exchange

The Heisenberg exchange operator consists of an isotropic and an anisotropic part. For organic molecules that are considered in this work, the isotropic part dominates the interaction [69] and can be described by the Hamiltonian

$$\hat{H}_{\mathrm{EX,iso}} = J\hat{\boldsymbol{S}}_{1}^{\mathrm{T}} \cdot \hat{\boldsymbol{S}}_{2}\,, \tag{2.19}$$

with the two single spin operators $\hat{\boldsymbol{S}}_{1}$ and $\hat{\boldsymbol{S}}_{2}$. The term J is given by:

$$J = -2\langle\phi_{a}(1)\phi_{b}(2)|\frac{e^{2}}{4\pi\varepsilon_{0}r}|\phi_{a}(2)\phi_{b}(1)\rangle\,, \tag{2.20}$$

where e is the electric charge of an electron, ε_{0} is the vacuum permittivity, r is the distance between the electrons, and $\phi_{a,b}$ are the spatial molecular orbitals occupied by the two electrons. The overlap of those orbitals show a dependency of $\exp(-r)$, and therefore J in equation (2.20) becomes very small for large distances between the electrons [75]. J represents the energy difference between the singlet and triplet states as shown in Figure 2.2. The sign of J defines whether the triplet state lies above (positive J) or below (negative J) the singlet state.

Zero-field splitting

States with a total spin QN equal to or larger than $S = 1$ show a splitting of their sublevels even in the absence of an external magnetic field. This effect is known as the zero-field splitting (ZFS) and its interaction is denoted by the Hamiltonian

$$\hat{H}_{\mathrm{ZFS}} = \hat{H}_{\mathrm{DD}} + \hat{H}_{\mathrm{SOC}}\,. \tag{2.21}$$

It consists of two parts: the already known second-order SOC term from equation (2.15) and a dipole–dipole coupling originating from the interaction of the two magnetic moments of the spins of the unpaired electrons. For organic molecules built of light atoms and with no transition metals involved, the dipole–dipole interaction dominates and the SOC is often neglected [67].

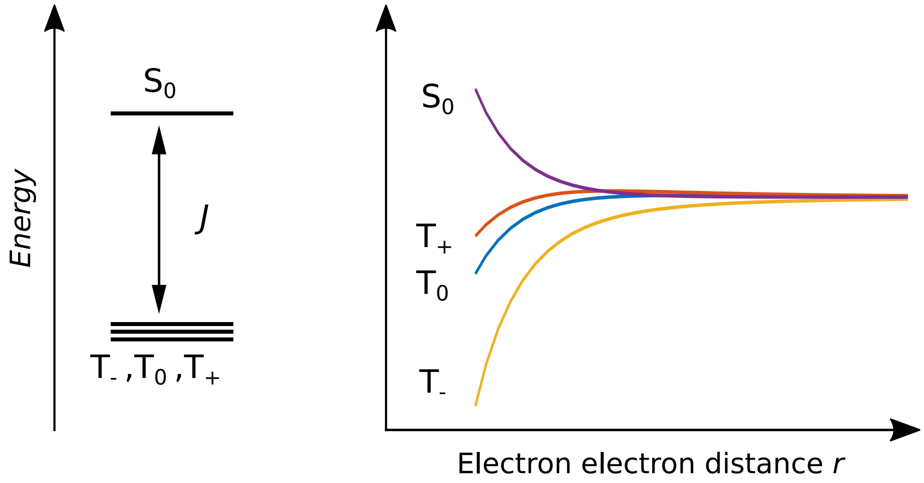

Figure 2.2.: Energy splitting of the singlet and triplet states (left) and dependence of the splitting on the electron electron distance (right). The triplet sublevels are split according to equation (2.28).

The strength of the SOC is proportional to the atomic number ($\propto Z^4$ [76]) and becomes only important for heavier atoms or transition metals. In analogy to a classical dipole–dipole interaction, the Hamiltonian can be written as [69, 75]

$$\hat{H}_{\mathrm{DD}} = \frac{1}{|\boldsymbol{r}|^3}\frac{\mu_0}{4\pi\hbar}g_e^2\mu_{\mathrm{B}}^2\left\{\hat{\boldsymbol{S}}_1\hat{\boldsymbol{S}}_2 - \frac{3}{|\boldsymbol{r}|^2}(\hat{\boldsymbol{S}}_1\boldsymbol{r})(\hat{\boldsymbol{S}}_2\boldsymbol{r})\right\}\,, \tag{2.22}$$

where μ_0 is the vacuum permeability and r the distance between both unpaired electron spins. With the total spin operator $\hat{\boldsymbol{S}} = \hat{\boldsymbol{S}}_1 + \hat{\boldsymbol{S}}_2$, the dipole–dipole Hamiltonian can be written in a simple tensorial form

$$\hat{H}_{\mathrm{DD}} = \hat{\boldsymbol{S}}^{\mathrm{T}}\mathbf{D}\hat{\boldsymbol{S}}\,, \tag{2.23}$$

with the diagonal ZFS tensor

$$\mathbf{D} = \begin{pmatrix} -\frac{1}{3}D + E & 0 & 0 \\ 0 & -\frac{1}{3}D - E & 0 \\ 0 & 0 & \frac{2}{3}D \end{pmatrix}. \tag{2.24}$$

This tensor is traceless, therefore it can be fully described by the two ZFS parameters

$$D = \frac{3D_z}{2} = \frac{3}{4}\left(\frac{\mu_0}{4\pi}\right)(g_e\mu_{\mathrm{B}})^2\left\langle\frac{|\boldsymbol{r}|^2 - 3z^2}{|\boldsymbol{r}|^5}\right\rangle \tag{2.25}$$

and

$$E = \frac{D_x - D_y}{2} = \frac{3}{4}\left(\frac{\mu_0}{4\pi}\right)(g_e\mu_{\mathrm{B}})^2\left\langle\frac{x^2 - y^2}{|\boldsymbol{r}|^5}\right\rangle\,. \tag{2.26}$$

The D parameter represents the overall strength of the dipole–dipole coupling and depends on r^{-3}. The E parameter describes the difference between the x and the y component of the $\mathbf{D}$

tensor. The eigenfunctions of the triplet state, in the absence of a magnetic field, are

$$\begin{aligned}
|T_x\rangle &= \frac{1}{\sqrt{2}}[|\alpha(1)\alpha(2)\rangle - |\beta(1)\beta(2)\rangle]\,,\\
|T_y\rangle &= \frac{1}{\sqrt{2}}[|\alpha(1)\alpha(2)\rangle + |\beta(1)\beta(2)\rangle]\\
&\text{and}\\
|T_z\rangle &= \frac{1}{\sqrt{2}}[|\alpha(1)\beta(2)\rangle + |\beta(1)\alpha(2)\rangle]\,.
\end{aligned} \tag{2.27}$$

The first two are constructed by the linear combinations of $|T_{+1}\rangle \pm |T_{-1}\rangle$ from equation (2.18) and the last one is identical to $|T_0\rangle$. Applying those wavefunctions to $\hat{H}_{\mathrm{DD}}$ gives the triplet sublevel energies

$$\begin{aligned}
U_x &= \frac{1}{3}D - E\,,\\
U_y &= \frac{1}{3}D + E\\
&\text{and}\\
U_z &= -\frac{2}{3}D\,.
\end{aligned} \tag{2.28}$$

The splitting between the triplet sublevels is shown in Figure 2.3. The convention for the orientation of the axis and ZFS parameters used in this work is the one from EasySpin documentation [77]. It demands that $|U_z| > |U_y| > |U_x|$ and that the ZFS parameter E always has the same sign as D. However, opposite signs for D and E are also commonly found in the literature. If the energy of U_y gets bigger than that of U_z, the y and z axis are switched. For the ZFS parameters this means $\frac{1}{3}D \geq E$. If the sign is positive, the spin-density of the triplet state is localised mainly in the x, y plane like a disc, whereas for a negative sign the spin density would be localised along the z axis like a cigar. More elaborated representations can be found in [78]. For symmetric aromatic compounds or conjugated polymers, mostly positive signs for the ZFS parameters are found [79]. Representations of such spin-density distributions are shown in Figure 2.3 for different values of the ZFS parameters.

If D and E are equal to zero, all states have the same energy and the ZFS would vanish. This shows the anisotropic character of the interaction. If $D > 0$ and $E = 0$, the energies of the states $|T_x\rangle$ and $|T_y\rangle$ are identical and one would speak of an axial system. As E becomes larger and gets close to $\frac{1}{3}D$, the two energy differences get very close and one speaks of a rhombic system.

Total spin Hamiltonian for TREPR experiments

In this work the triplet state of organic semiconductors has been explored. For such systems the Hamiltonian consists of the two terms $\hat{H}_{\mathrm{EZ}}$ and $\hat{H}_{\mathrm{SS}}$. Fortunately, not all parts need to be taken into account. In triplet states the distance between the electrons is very small ($\approx$ 100 pm for triplet excitons in organic solids [31]). Therefore, J is large and the triplet and singlet states are energetically separated, no mixing of them can take place. Since only the triplet sublevels are of interest, the Heisenberg exchange term can be neglected. As mentioned earlier, SOC ($\propto Z^4$) can be neglected for light atoms. By substituting hydrogens with halogens in the fluorescein

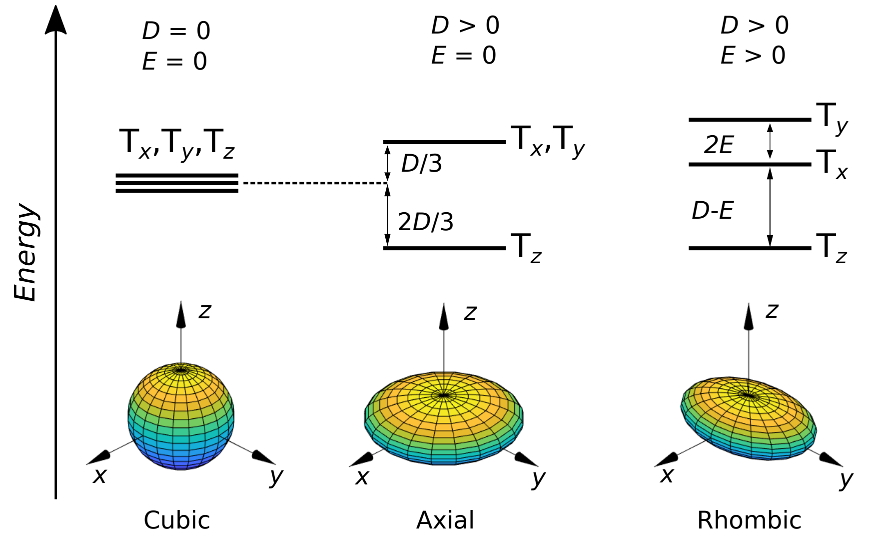

Figure 2.3.: Energy splitting of the triplet sublevels $|T_x\rangle$,$|T_y\rangle$ and $|T_z\rangle$ for a cubic, axial and rhombic system. The energies of the states are given by equation (2.28). Below each of the three cases, the spin-density distribution is outlined. The arrows in the spheres were made with an additional package [80].

molecule, hints have been found that significant SOC effects only occur if iodine is involved [79]. For bromine and chlorine no major changes of D were detected. The heaviest atom in the molecules considered in this work is sulphur, so the SOC term of the ZFS is negligible. The total spin operator for an organic molecule in its triplet state can be written as

$$\hat{H}_\mathrm{S} = \hat{H}_\mathrm{EZ} + \hat{H}_\mathrm{DD}\,. \tag{2.29}$$

Without magnetic field, the Hamiltonian is reduced to $\hat{H}_\mathrm{DD}$ with the already known zero-field eigenfunctions $|T_x\rangle$, $|T_y\rangle$ and $|T_z\rangle$. By applying a strong external magnetic field, the electron-Zeeman interaction becomes the dominant part of of the total spin Hamiltonian. The eigenfunctions are then changed to the high-field eigenfunctions $|T_+\rangle$, $|T_0\rangle$ and $|T_-\rangle$. The high-field eigenfunctions are superpositions of the zero-field eigenfunctions and depend on the respective orientation to B_0.

2.2. Time-resolved EPR spectroscopy

Most organic semiconductor materials possess a diamagnetic singlet ground state which can't be detected directly by EPR spectroscopy. One way to create paramagnetic species in these materials is through light excitation, resulting typically in short-lived (spin-polarised) triplet states for conjugated organic molecules. This initial spin polarisation leads to an enhancement of the recorded signal, so immediate detection after the excitation will provide the best results. Time-resolved EPR (TREPR) spectroscopy is a pump–probe experiment, a pulsed laser is used as pump to generate paramagnetic species and continuous-wave EPR spectroscopy (cwEPR) is used to probe them. In a first step, the concepts behind cwEPR and TREPR experiments will be briefly described. In a second step, characteristics of TREPR spectra and important simulation parameters will then be discussed. Extended information about the experiment and the composition of the resulting spectra are available in a number of reviews [35, 81, 82]; for more details about the triplet state in general [83] is recommended.

2.2.1. Experimental setup

Continuous-wave (cw) EPR spectroscopy In this mode of operation, microwaves (MWs) of an adjustable frequency are constantly emitted from the source, in general a Gunn diode or klystron. The MWs are led towards the circulator, a component which redirects the MWs. From the source they are sent into the resonator where the sample is located. The resonator is a cavity which only allows MWs of a specific frequency to build up a standing wave, depending on the geometry of the resonator. Only those MWs are later able to interact with the sample and induce electron spin flips as indicated in equation (2.12). MWs not matching this frequency are reflected, pass a second time through the circulator and are directed to the detector. To perform measurements only MWs matching the resonator frequency are emitted by the source, so none of them are reaching the detector. The resonator is then called critically coupled. Further details about the critical coupling can be found in [54] and [75]. The resonator is placed in a homogeneous and adjustable magnetic field. When the field hits the point where the resonance condition of magnetic resonance according to equation (2.9) is satisfied, the sample absorbs the incoming MWs. Because of this absorption the critical coupling is cancelled, some of the MWs are reflected from the resonator towards the circulator and are then reaching the detector giving rise to a signal. In the so called X-Band, MW frequencies between $9-10$ GHz are used, together with magnetic fields centered around 340 mT for organic molecules. To obtain a better signal-to-noise ratio, a lock-in amplification of the signal is commonly used. In this case, additional magnet coils apply a small magnetic field which oscillates with a fixed frequency between $10-100$ kHz. In this case detection is phase-sensitive with respect to the oscillating field. The advantages of modulating the magnetic field are that noise which oscillates with other frequencies is filtered out and that the more intense derivative of the signal is detected. With this technique small signals due to a small population differences between the spin states and/or a small amount of paramagnetic species ($5 \cdot 10^{11}$ spins/mT [55]) can be detected. In the context of detection limit, the unit spins/mT seems more appropriate than an overall number of spins. If all spins absorb at the same magnetic field a smaller total number of spins could give an decent signal, whereas the same total number of spins might not be detectable if their signal is spread over a large magnetic field range.

Time-resolved EPR (TREPR) spectroscopy In Figure 2.4 the experimental setup of a TREPR spectrometer is presented. As mentioned earlier, many molecules are diamagnetic in their ground state and are therefore EPR-inactive. Some molecules show paramagnetic states after laser excitation, in general triplets, detectable by EPR spectroscopy. The main differences between the experimental setups of cwEPR and TREPR spectroscopy are the additional laser, trigger and recorder of the latter. The modulation coils needed for the lock-in amplification are missing.

The principle of measurement is similar in many regards to that of cwEPR. MWs are constantly emitted into the critically coupled resonator. An optical window in the resonator allows a pulsed

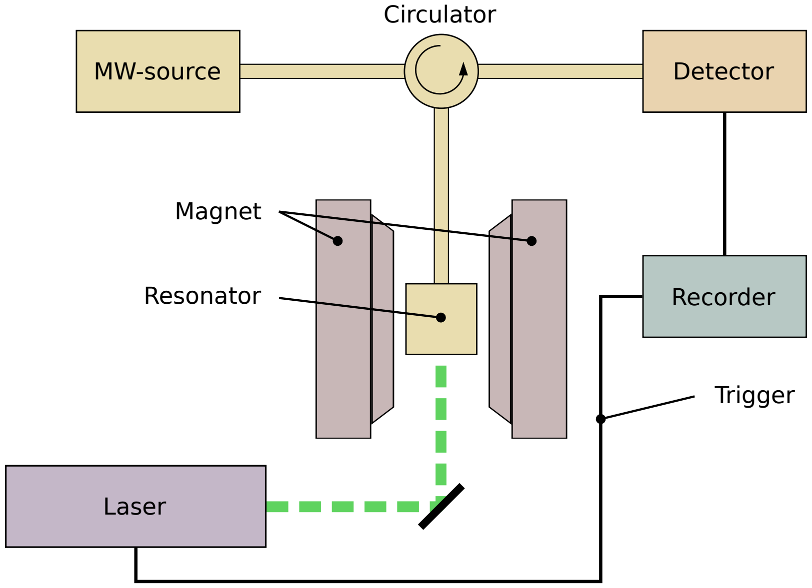

Figure 2.4.: Simplified scheme of a TREPR spectrometer. The setup consists of a MW source, in general a klystron or Gunn diode, a circulator which hinders the MW to go directly into the detector before passing through the resonator where the sample is located. The magnet coils around the resonator provide the homogeneous magnetic field B_0. The laser aims at a small window in the resonator to excite the sample. Each laser shot triggers the recorder and a time trace of the signal is detected. Image taken and modified from [35].

laser to hit the sample and to generate the paramagnetic species. Those species can absorb the MWs, cancelling the critical coupling and leading to a signal on the detector. In many cases the decay of triplet states is faster than miliseconds [84]. So no modulation of the field can be used, as the excited state would be gone without the modulation coils being able to perform one field oscillation. As mentioned earlier the signal is enhanced due to spin polarisation (a overpopulation of one sublevel) so no lock-in amplification is needed for the TREPR experiment. Therefore the lock-in detection scheme is replaced by a direct detecting one. In terms of time a detection limit lying above 10 ns [81] can be achieved with TREPR spectroscopy.

The common way to generate triplet states is via intersystem crossing (ISC) from an excited state S_n into a triplet state T_m, with $n, m > 0$. This transition is spin-forbidden and depends on many different factors like the symmetries of the orbitals involved, the energy difference between singlet and triplet states [85] and involved SOC [86]. This path into a triplet state is illustrated in Figure 2.5 on the left side. The ISC rates into the triplet sublevels are different leading to different populations. The faster a rate, the more populated is the corresponding sublevel resulting in a non-Boltzmann distribution. Such a distribution is depicted on the right side of Figure 2.5, one would speak of spin-polarised system. Because of this polarisation the detected signal is enhanced and no field modulation is required. In absence of an external magnetic field, one speaks of the zero-field populations p_x, p_y and p_z. These are important parameters that need to be considered for the simulation of spectra. If different moieties like linked donors and acceptors are involved, not only the classical spin–orbit intersystem crossing (SO-ISC) described above but also spin–orbit charge–transfer (SOCT-ISC) [87] and the radical-pair (RP-ISC) mechanisms are possible [88]. RP-ISC mechanism can be verified by TREPR spectroscopy because of the specific polarisation patterns of the TREPR spectrum [87, 89]. Also, a triplet CT complex can be detected by TREPR spectroscopy thus providing hints for a possible SOCT-ISC.

One less common way into triplet state T_1 is via a direct $S_0 \rightarrow T_1$ excitation. For smaller molecules this pathway has first been observed by Kasha [90, 91] and was recently observed on a carbazole derivative [92].

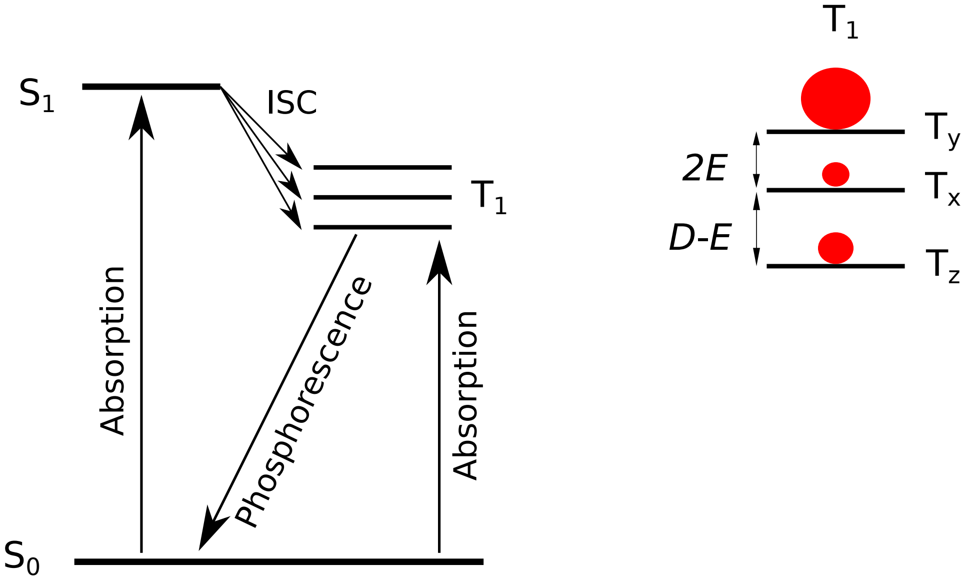

Figure 2.5.: Simplified Jabłonsky therm scheme and the non-Boltzmann populations of the triplet sublevels. On the left side the path from the singlet ground state (S_0) into the triplet state (T_1) via absorption and ISC is represented. The triplet sublevels show the same splitting as in Figure 2.3. Because of the ISC mechanism, the populations of the triplet, depicted as red spheres, show a non-Boltzmann distribution, which is needed for the detection of a TREPR signal. An additional uncommon way into the triplet state T_1 is via the spin forbidden direct $S_0 \rightarrow T_1$ transition.

The TREPR experiment results in a two-dimensional dataset with time and magnetic field as variable parameters. Recorded spectra consist of many time traces recorded at different magnetic fields and are represented in three-dimensional plots with axes along time, magnetic field and signal intensity. In order to reduce those to a more handable two-dimensional representation, the signal intensity is often plotted against the magnetic field at a fixed time, usually where the signal intensity is at a maximum.

2.2.2. TREPR spectra and their simulation parameters

For the TREPR spectra of triplet states such as those observed in organic semiconducting materials, the electron Zeeman and the dipole–dipole interaction mentioned in section 2.1.3 are relevant. The dipole–dipole interaction gives rise to field-independent energy contributions and determines the splitting of the triplet sublevel manifold. Strength and shape of the splitting depend on the distance, and, with an external magnetic field involved, on the angle between this field and the axis connecting both electrons [93]. The dipole–dipole interaction has no isotropic part [93], therefore no splitting in liquid and gaseous samples can be observed because of the fast movement of the molecules. Thus only solid or highly viscous samples, where molecular movement is much slower, *i.e.* above the detection timescale of TREPR spectroscopy, can be investigated. To correctly describe the spectra of such samples, the whole powder average of the orientation from the ZFS tensor to the external magnetic field needs to be taken into account. In Figure 2.6 the Zeeman splitting of the triplet sublevels for the three orientations, where the magnetic field is parallel to one of the axis of the ZFS tensor, is shown.

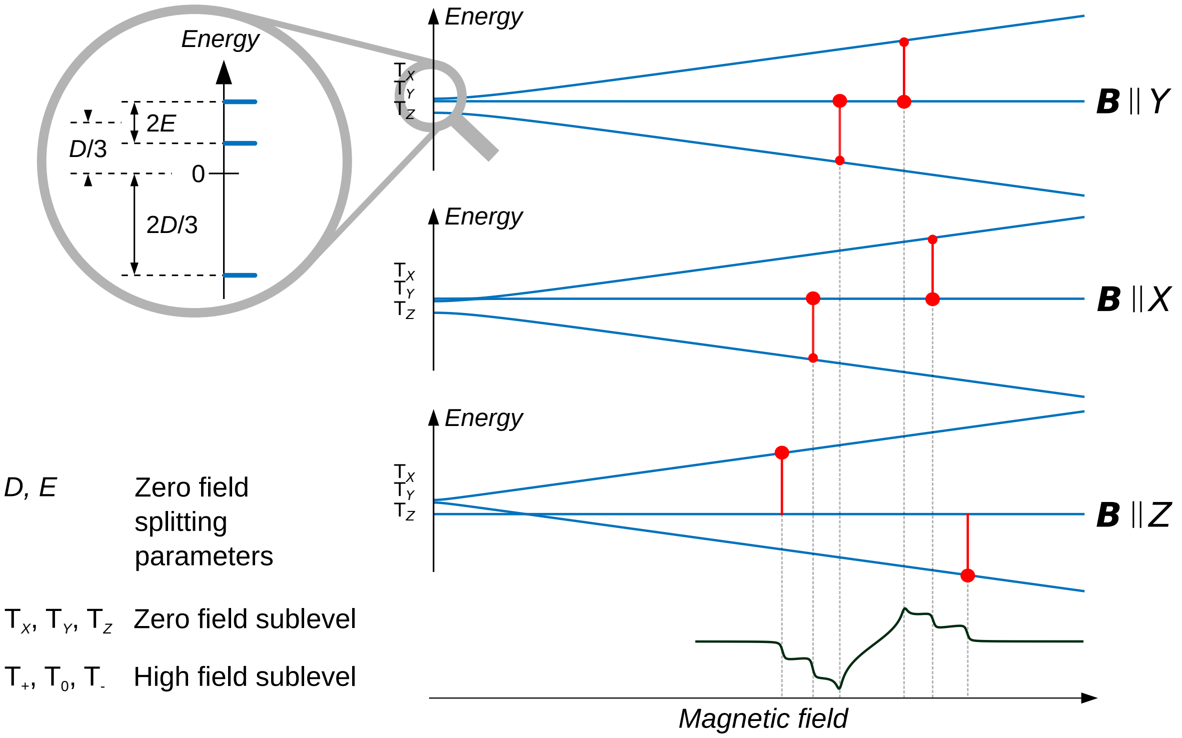

Figure 2.6.: Energy splitting of the triplet sublevels with an external magnetic field. In the absence of an external magnetic field, the energies of the triplet sublevels are given by the ZFS and their eigenfunctions are $|T_x\rangle$, $|T_y\rangle$ and $|T_z\rangle$. Their corresponding zero-field populations in this case are $p_z = 0$ and $p_x = p_y = 0.5$. With a strong magnetic field, the electron Zeeman interaction becomes the dominant contribution of the splitting, the corresponding eigenfunctions are $|T_+\rangle$, $|T_0\rangle$ and $|T_-\rangle$. The three orientations shown are those with the magnetic field parallel to one of the axes of the ZFS tensor. The transitions between the different triplet levels are displayed in red and their respective contribution to the spectrum are indicated by the dotted lines. The black spectrum is obtained by adding up all different orientations from the ZFS tensor to the magnetic field. This Figure was inspired by [82].

Only the triplet sublevels not parallel to the external magnetic field experience an energetic change, whereas the energy of the parallel sublevel remains unchanged. As derived in equation (2.13), the strength of the Zeeman splitting is depends on the g factor. A transition takes place if the splitting between two triplet sublevels matches the energy of the incident MWs. A larger g value leads to a smaller splitting and the transition is shifted to lower magnetic field. The opposite is true for a smaller g value. Anisotropy of the g factor would affect the spectral shape, since the strength of the Zeeman splitting would depend on the orientation of the molecules with respect to the external magnetic field. This effect only becomes relevant for strong magnetic fields [94] and can be neglected in the context of this work. The specific orientations depicted in Figure 2.6 lead to the extreme values of the spectrum. In absence of a magnetic field, the triplet sublevel populations are given by p_x, p_y and p_z, the previously mentioned zero-field populations. To minimize the necessary simulation parameters, the smallest population is often set to zero [95]. By applying a magnetic field, the population of the non-affected sublevel stays the same. The populations of both other sublevels are mixed up and equally distributed. Depending on the resulting population distribution, emissive (E) or absorptive (A) signals are detected.

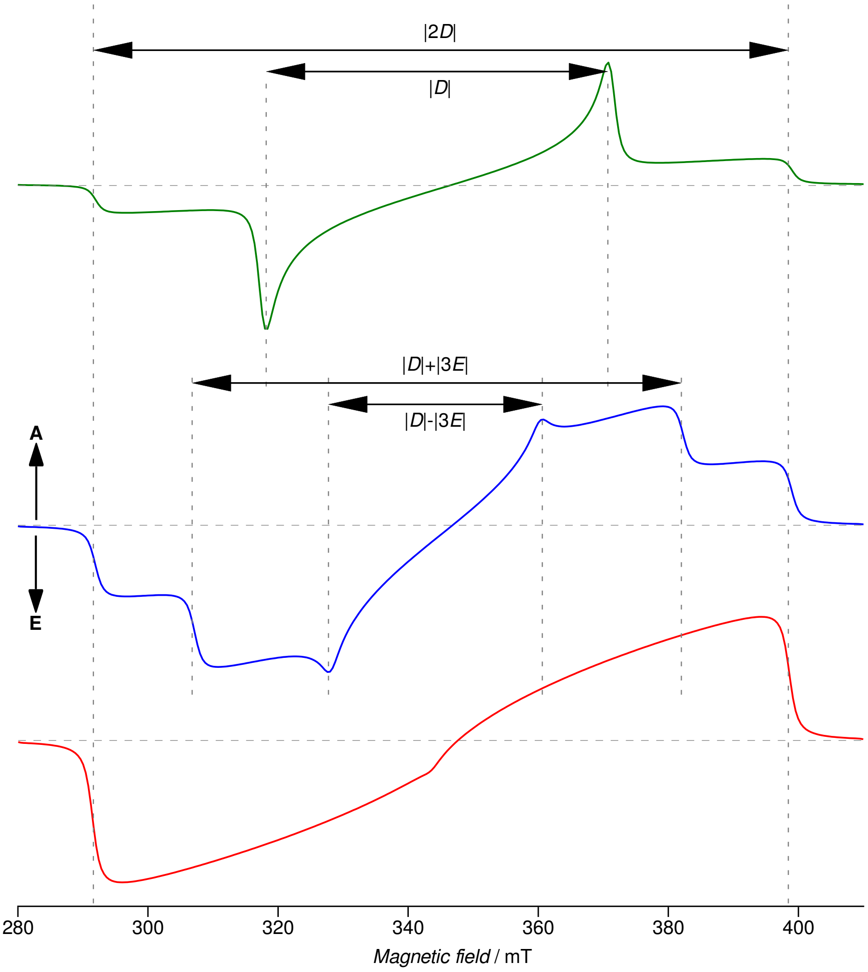

Figure 2.7.: Simulated TREPR spectra with different rhombicities. From top to bottom the spectra were simulated with $E = 0$ (green), $0 < E < \frac{D}{3}$ (blue) and $E = \frac{D}{3}$ (red). The same D value has been used for all spectra. This is reflected in the same overall spectral width being equal to $2D$. For the first spectrum (green) one would speak of an axial one because D_y and D_x are equal. A rhombic spectrum (red) is one were D_z is equal with one of the other tensor components (depending on the sign of D). With an increasing ratio $\frac{E}{D}$, the rhombicity of the spectrum also increases.

Apart from the populations, the ZFS parameters D and E dominate the shape of the triplet spectra. The strength of the dipolar coupling is given by D and can directly be extracted from the overall spectral width as indicated in Figure 2.7. A strong dipolar coupling would result in a large spectrum and *vice versa*. Taking into account equation (2.25), correlating D with the distance between both electron spins, one can attribute a broader TREPR spectrum to a more localised triplet exciton. This is only possible if the investigated molecules are sufficiently similar and if no SOC effects are involved. The parameter E can be extracted from the distance between the two inner peaks, but only if D is previously known. Since the parameter E is always linked to D (see equation (2.24)) it is more reasonable to look at the rhombicity $\frac{E}{D}$ instead of the absolute value of E. The impact of the rhombicity on the spectra is depicted in Figure 2.7. At this point it shall be mentioned that the parameters mostly responsible for the spectral shape, the zero-field populations and the ZFS parameters, are all field-independent.

The last parameters which need to be addressed are the two different line widths used to simulate TREPR spectra. Both line shapes are compared in the left panel of Figure 2.8. The Lorentzian linewidth represents a homogeneous line broadening originating from the lifetime of the excited state. The Gaussian linewidth represents an inhomogeneous broadening, which can have many origins like non-resolved hyperfine couplings [93], anisotropies in the environment [36] or other effects following a Gaussian distribution. In fact, a Gaussian curve can be constructed from Lorentzian curves following a Gaussian distribution as shown on the right side of Figure 2.8. The single Lorentzian curves represent all the different states contributing to the Gaussian distribution.

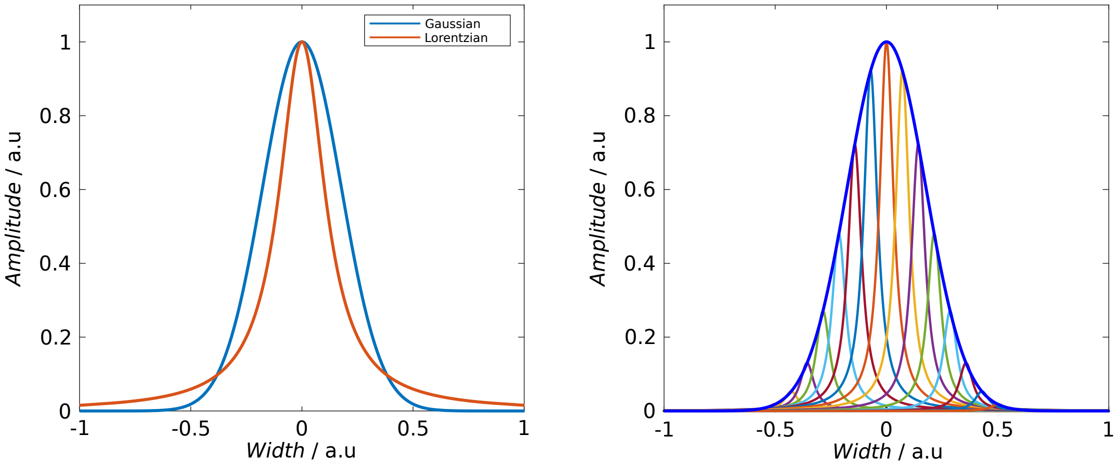

Figure 2.8.: Shape of Lorentzian and Gaussian curves on the left and Lorentzian curves following a Gaussian distribution leading to a Gaussian curve on the right. Both curves on the left are normalised on the same height with a width of one. 15 Lorentzian curves with a width of 0.3 and a height following a Gaussian distribution were used to show how they add up to a Gaussian curve.

As shown in Figure 2.8 Lorentzian and Gaussian lineshapes can best be distinguished at their center and wings. Lorentzians are narrower in their center and have broader wings, leading to a larger overall width. Due to this difference in width, both lineshapes can best be differentiated at the edges of EPR Signal. For the simulations of spectra including both lineshapes a Voigt profile, with contributions from Gaussians and Lorentzians is used [77, 96].

3. Computational chemistry

The following section provides a brief overview of the most important concepts behind the performed DFT calculations. For more general details about this topic, the references [72, 73, 97] can be consulted. More details about the calculation of EPR properties can be found in reference [98]. The described theory doesn't cover relativistic effects since they are not relevant in the context of this work.

3.1. Wavefunction methods

The energy E of a quantum mechanical system can be calculated via the time-independent Schrödinger equation [70, 99]

$$\hat{H}\Psi = E\Psi \tag{3.1}$$

with the Hamilton operator $\hat{H}$ and the wavefunction Ψ. This eigenvalue equation leads to non-continuum energy levels of the considered system [70]. The Hamiltonian contains all terms contributing to the total energy of the system, namely the kinetic energies T and the potential energies V. If energies of molecules are calculated, the Hamiltonian can be written as

$$\hat{H} = \hat{T}_{\mathrm{n}} + \hat{V}_{\mathrm{nn}} + \hat{T}_{\mathrm{e}} + \hat{V}_{\mathrm{ne}} + \hat{V}_{\mathrm{ee}}\,, \tag{3.2}$$

with the kinetic energies of nuclei and electrons $\hat{T}_{\mathrm{n}}$ and $\hat{T}_{\mathrm{e}}$ and the potential energies consisting of the Coulomb attraction between nuclei and electrons $\hat{V}_{\mathrm{ne}}$ and the repulsion among identically charged particles $\hat{V}_{\mathrm{ee}}$ and $\hat{V}_{\mathrm{nn}}$ [73]. In the Born–Oppenheimer (BO) approximation [100], movement of the electrons and nuclei are separated from each other. If the electrons are observed, the nuclei are considered to be immobile. In this approximation, the effect of $\hat{T}_{\mathrm{n}}$ on the electronic wavefunction can be neglected due to the slower movement, and $\hat{V}_{\mathrm{nn}}$ can be calculated separately because it depends on the coordinates of the nuclei and is constant for a given geometry [97]. The remaining electronic part of the Hamiltonian $\hat{H}_{\mathrm{e}}$ consists of the last three operators from equation (3.2) [73]. Except for the repulsion between the electrons, the other terms of $\hat{H}_{\mathrm{e}}$ can be written as sum over one-electron operators $\hat{h}$

$$\hat{H}_{\mathrm{e}} = \sum_{i}^{N} \hat{h}(i) + \hat{V}_{ee} \tag{3.3}$$

Different approaches to construct a suitable electronic wavefunction for a many-particle system have been developed [101]. Like the electronic Hamiltonian that is split into one-electron terms, the common idea is to construct the complete wavefunction Ψ from one-electron-spin wavefunctions ϕ, refered to as molecular orbtails (MO) or spin orbitals. The latter are constructed from a spatial $\psi(r)$ and a spin part $\alpha(\omega)$ or $\beta(\omega)$. They can be associated with spin up and spin down, respectively, described in a more detailed way in section 2.1.1. Slater first found an expression for the complete wavefunction [102], which also satisfies the Pauli principle [103]. The latter demands an asymmetric behaviour of the wavefunction with respect to the exchange of fermions, in this case the electrons. The wavefunction for N electrons is then expressed by the Slater determinant [102]

$$\Psi_{\mathrm{SD}} = (N!)^{-\frac{1}{2}} \begin{vmatrix} \phi_1(1) & \phi_2(1) & \phi_3(1) & \dots & \phi_N(1) \\ \phi_1(2) & \phi_2(2) & \phi_3(2) & \dots & \phi_N(2) \\ \vdots & \vdots & \vdots & \ddots & \vdots \\ \phi_1(N) & \phi_2(N) & \phi_3(N) & \dots & \phi_N(N) \end{vmatrix} . \tag{3.4}$$

The prefactor $(N!)^{-\frac{1}{2}}$ serves as normalisation.

3.1.1. Hartree–Fock theory

Hartree–Fock (HF) equations are obtained by applying the Hamiltonian from equation (3.3) on a single Slater determinant as wavefunction [104] and minimising the resulting energy. The underlying method for energy minimisation is the variational principle [104, 105]. It states that for a given Hamiltonian, the used trial wavefunction will always give an equal or higher expectation energy than the real one [73]. From the term treating the electron–electron interaction in equation (3.2), two terms depending on a single electron wavefunction are derived. Thus eigenvalue equations for the energies of the single electrons ϵ_i can be formulated

$$\hat{F}\phi_i = \epsilon_i \phi_i \, , \tag{3.5}$$

with the single electron Fock operator

$$\hat{F}(1) = \hat{h}(1) + \sum_j^N (\hat{J}_j(1) - \hat{K}_j(1)) \, . \tag{3.6}$$

The two terms originating from the electron–electron interaction are the Coulomb operator $\hat{J}$ and the exchange operator $\hat{K}$. Those operators describe the interaction between the electrons in the HF theory, in more detailed, the interaction of one electron with a mean-field constructed from all other electrons, known as mean-field approximation [106, 107]. Applied to a wavefunction, those two operators give

$$\hat{J}_i(1)|\phi_j(2)\rangle = \langle\phi_i(1)|\frac{1}{|\boldsymbol{r}_{12}|}|\phi_i(1)\rangle|\phi_j(2)\rangle \, , \tag{3.7}$$

and

$$\hat{K}_i(1)|\phi_j(2)\rangle = \langle\phi_i(1)|\frac{1}{|\boldsymbol{r}_{12}|}|\phi_j(1)\rangle|\phi_i(2)\rangle \, , \tag{3.8}$$

with the vector $\boldsymbol{r}_{12}$ between the two electrons. The operator $\hat{K}$ additionally switches the spatial coordinate of the orbitals, hence the name exchange. It is a purely quantum-mechanical phenomenon and only appears for systems including electrons with the same spin ($\alpha(\omega)$ or $\beta(\omega)$). Additional exchange is also the only energy difference between a singlet and triplet state, and therefore reflects the energetic difference between those as mentioned in section 2.1.3. By introducing a linear combination of atomic orbitals (LCAO) as approximation for a MO, the latter can be expressed as

$$\phi_i = \sum_{\mu} c_{\mu i} \chi_{\mu} \tag{3.9}$$

with atomic orbitals (AOs) χ_μ and their corresponding expansion coefficients $c_{\mu i}$. Applied on the HF equations the matrix eigenvalue equation

$$\mathbf{Fc} = \mathbf{Sc}\boldsymbol{\epsilon}\,, \tag{3.10}$$

known as Roothaan–Hall [108, 109] equation is obtained. The elements of the Fock matrix $\mathbf{F}$ are given by $F_{ab} = \langle \chi_a | \hat{F} | \chi_b \rangle$ and those of the overlap matrix $\mathbf{S}$ by $S_{ab} = \langle \chi_a | \chi_b \rangle$. Matrix $\mathbf{c}$ contains all the AOs expansion coefficients introduced in equation (3.9) and matrix $\boldsymbol{\epsilon}$ the energy eigenvalues of the MOs. By diagonalising the Fock matrix, the orbital energies and corresponding expansion coefficients are obtained. But those coefficients are also needed to initially construct operators $\hat{K}$ and $\hat{J}$ and thus $\hat{F}$. This leads to the problem that the solution and the equation depend on each other.

Self-consistent field method

One way to solve this problem is the self-consistent field (SCF) method [106]. The initial orbital coefficients $c_{\mu i}$ are intelligently guessed and the Fock matrix $\hat{F}$ is constructed. The energies of the MOs are minimised via the variational method, which provides new orbital coefficients. Out of those a new Fock matrix can be formed. This loop is repeated until the initial and final energies are similar enough according to the chosen convergence criteria. Then the calculation is finished. A scheme with the different steps is shown in Figure 3.1.

Basis sets

During the SCF procedure, a lot of integrals have to be calculated. To speed it up, Gaussian functions [110] were introduced. They are easy to integrate and the multiplication of two Gaussian functions can be written as single Gaussian function. In order to obtain a good approximation of the wavefunction, many Gaussian functions are combined. For the different atoms and tasks, many basis set combinations have been constructed; an overview can be found in reference [111]. More details about the use of Gaussian functions to substitute the orbitals are given in reference [72].

Resolution of identity

During the SCF procedure, calculating the Coulomb part exactly takes a lot of time. The most time-consuming parts are the four-center-two-electron integrals, occurring in the expression of the total energy of a system. By applying auxiliary basis sets, those integrals are reduced to three centers, making calculations much faster with only a small loss in accuracy [112, 113]. To

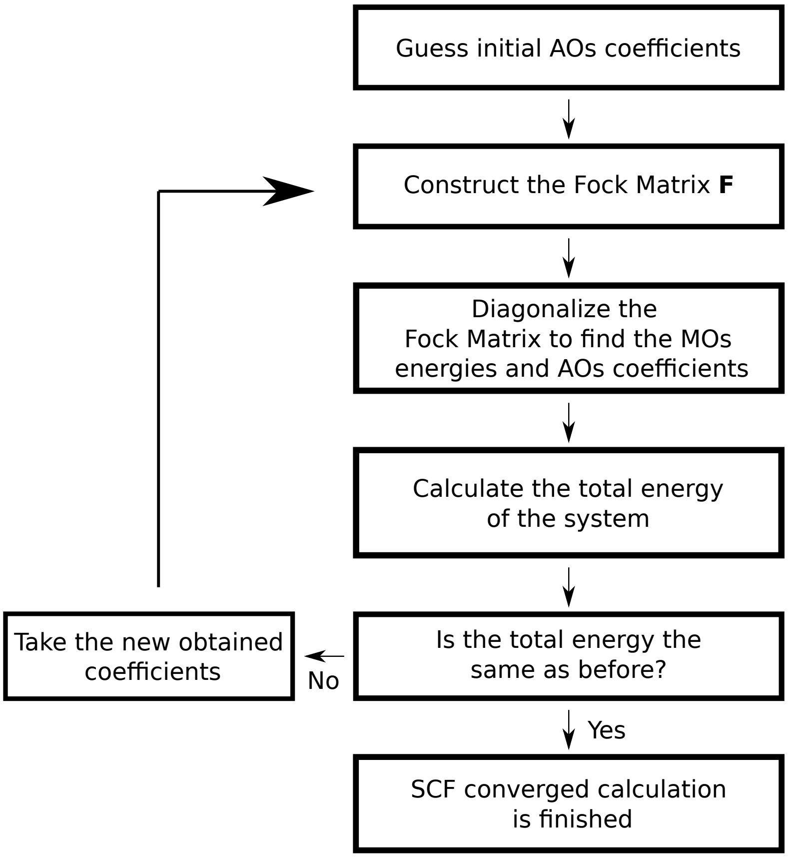

Figure 3.1.: Illustration of the single steps in the SCF procedure. Inspired by a Figure from [73].

take the exact exchange into account in DFT calculations using hybrid functionals (see section 3.2.2), an additional chain of spheres approximation is used [114].

Correlation

With a single Slater determinant as wavefunction and a given basis set, the energies obtained by the HF method are limited to the so-called HF limit, representing the lowest achievable energy. To obtain more accurate results, the mean-field approximation needs to be extended by adding the correlation energy for better description of the electron–electron repulsion. It represents the difference in energy between the HF limit and the energy of the real system in a non-relativistic approach. Various methods have been developed to calculate the correlation energy [72], but none of them is applied in this work.

3.2. Density functional theory

HF calculations are very time-consuming and not very accurate [115]. Therefore they are not suitable for large molecules. To develop a much faster method, it was tried to calculate molecular properties based on the electron density $\rho(\mathbf{r})$. The first big step was done by Hohenberg and Kohn proving that with a given ground-state electron density only one Hamiltonian can be constructed, or more precisely its part describing the potential energy [116]. It is known as the Hohenberg–Kohn existence theorem. Based on this theorem, the development of functionals providing most accurate energies based on electron densities started.

3.2.1. Kohn–Sham formalism

The second big step was the development by Kohn and Sham [117] briefly described in this section. The basic idea is to find the electron density of the interacting (real) system by using a non-interacting system as starting point. To do so, the terms for the kinetic energy of the non-interacting electrons $T_{\mathrm{ni}}[\rho(\boldsymbol{r})]$, the electron–nuclei attraction $V_{\mathrm{ne}}[\rho(\boldsymbol{r})]$ and the mean-field approximation for the Coulomb repulsion $J_{\mathrm{ee}}[\rho(\boldsymbol{r})]$ are expressed as functionals of the electron density [73]. The difference in kinetic energy between the interacting and non-interacting system is captured in the term $\Delta T[\rho(\boldsymbol{r})]$ and all remaining corrections to the electron–electron interaction in $\Delta V_{\mathrm{ee}}[\rho(\boldsymbol{r})]$. So the energy of a system can be written as

$$E[\rho(\mathbf{r})] = T_{\mathrm{ni}}[\rho(\boldsymbol{r})] + V_{\mathrm{ne}}[\rho(\boldsymbol{r})] + J_{\mathrm{ee}}[\rho(\boldsymbol{r})] + \Delta T[\rho(\boldsymbol{r})] + \Delta V_{\mathrm{ee}}[\rho(\boldsymbol{r})]\,. \tag{3.11}$$

Those two last terms are unknown and put together as the exchange-correlation energy $E_{\mathrm{xc}}[\rho(\boldsymbol{r})]$. In a next step, the orbital picture is reintroduced by describing the total electronic density with the Kohn–Sham (KS)-MOs χ_i. The sum over all bra kets of those orbitals defines the electron density. Equation 3.11 can be rewritten as

$$\begin{aligned} E[\rho(\boldsymbol{r})] = \sum_i^N \left(\left\langle \chi_i \right| -\frac{1}{2}\nabla^2 \left| \chi_i \right\rangle - \left\langle \chi_i \right| \sum_n^{\text{nuclei}} \frac{Z_n}{|\boldsymbol{r}_i - \boldsymbol{r}_n|} \left| \chi_i \right\rangle \right) \\ + \sum_i^N \left\langle \chi_i \right| \frac{1}{2} \int \frac{\rho(\boldsymbol{r}')}{|\boldsymbol{r}_i - \boldsymbol{r}'|}\,\mathrm{d}\boldsymbol{r}' \left| \chi_i \right\rangle + E_{\mathrm{xc}}[\rho(\boldsymbol{r})] \end{aligned}\,. \tag{3.12}$$

With this equation the same procedure as in HF theory can be applied to find the KS-MOs providing the lowest energy. First the one-electron KS operator can be obtained from equation 3.12 by minimising the energy with the density. The resulting KS operator is

$$\hat{h}_i^{\mathrm{KS}} = -\frac{1}{2}\nabla_i^2 - \sum_n^{\text{nuclei}} \frac{Z_n}{|\boldsymbol{r}_i - \boldsymbol{r}_n|} + \int \frac{\rho(\boldsymbol{r}')}{|\boldsymbol{r}_i - \boldsymbol{r}'|}\,\mathrm{d}\boldsymbol{r}' + V_{\mathrm{xc}}(\boldsymbol{r}_i)\,, \tag{3.13}$$

with

$$V_{\mathrm{xc}} = \frac{\delta E_{\mathrm{xc}}}{\delta \rho}\,. \tag{3.14}$$

By using the LCAO approximation and trying to find the KS-AO coefficients leading to the lowest energy, the same problem as in the HF theory occurs. The potential part of $\hat{h}_i^{\mathrm{KS}}$ depends on the KS-AO coefficients. Again the SCF method needs to be applied to obtain self-consistent KS-MOs and energies.

3.2.2. Exchange and correlation functionals

The last remaining issue to be solved is the treatment of the exchange-correlation functional E_{xc}. Since it contains all unknown terms (which can not be calculated exactly), finding a solution relies on approximations. Those are often tailored to the requirements of the investigated system. Thus many different exchange-correlation functionals have been developed and the three most popular approaches shall be briefly described here.

Local density approach (LDA)

In an early approach, the model of the uniform electron gas was used to construct some functionals for the exchange and correlation energies. Dirac first found an expression to calculate the exchange energy of such a gas [118]; it was later improved by Slater [119] delivering more accurate results. Functionals describing the correlation energy were later designed by using quantum Monte–Carlo simulations [120]. Both energies thereby depend on the local electron density at a given point. Such functionals are often used to calculate inorganic solids, in general metals, since the electron gas is a suitable model to describe metallic bonds. For molecules where the electronic density is not uniform, more advanced approximations had to be developed [73].

Generalised gradient approach (GGA)

To get more accurate results, not only the density at a given point but also its fluctuations need to be considered. The way used to capture the variation of the electron density is to look at its gradient. Most GGA functionals are built on top of the LDA functional, with added terms including the gradients of the exchange and correlation energies. One of the most prominent GGA exchange functional was developed by Becke [121]. The functional has been optimised by adding empirical parameters fitting the experimentally known exchange energies of the six noble gas atoms. It is typically abbreviated with “B” or “B88” . For the correlation energy, an often used functional was developed by Perdew, termed “P86” [122]. It is based on the electron gas and contains no empirical parameters. Another widely used correlation functional is the one of Lee, Yang, and Parr, abbreviated “LYP” [123]. It contains empirical parameters adapted to the He atom. To calculate the exchange-correlation energy, a widespread combination is the BP86 functional using the Becke exchange and Perdew correlation. It is possible to mix any correlation and exchange functionals in order to find a good solution for the investigated problem.

Hybrid approach

The next step in development was to add an empirical amount of HF exchange to the exchange functional. Since HF theory describes the exchange term exactly, this hybrid approach led to very good results but with additional computing time. Becke used his B88 with additional HF exchange and added three empirical parameters to weight both exchange and correlation terms [124]. Those parameters were fitted to the atomisation energies of several molecules [124]. The famous and most oftenly used functional B3LYP was created that way. It gives good results for calculating the properties of molecules and is also often used in this work.

Dispersion correction

Missing in the mentioned approximations of E_{xc} is the contribution from dispersion originating from London forces [125]. Those are important for weakly bound systems, large polymers or if the system of interest consists of several molecules. Different ways have been developed; a good overview is given in reference [126].

3.3. Calculation of TREPR-related properties

3.3.1. Spin density distributions

Open-shell systems require the α and β orbitals to be treated independently from each other in order to describe the exchange interaction occurring between two electrons with the same spin more accurately. This interaction leads to a lowering of the orbitals occupied with electrons of the same spin [97]. One would refer to such a calculation as unrestricted; they are more time-consuming since twice as many orbitals need to be calculated. The spin-density distribution of an open-shell state can directly be constructed from the spacial difference between α and β electrons. It is also possible to define the amount of spin density associated with a specific atom, the most common way was introduced by Mulliken [127]. For an open-shell state, the sum of all spin densities should be equal to the number of unpaired electrons. Artificially small deviations occur very often and are called spin contamination of the system [97]. They are difficult to avoid and can be tolerated as long as they lie within in a certain range [128].

3.3.2. Zero-field-splitting parameters

As mentioned in section 2.1.3 two different phenomena contribute to the ZFS, the dipole–dipole interaction and the second-order SOC. For organic molecules the latter can be neglected [67, 129]. A more convenient way to write equation (2.22) is

$$\hat{H}_{\mathrm{DD}} = \frac{g_{\mathrm{e}}^2 \alpha^2}{8} \left[\frac{\hat{\boldsymbol{S}}_1 \cdot \hat{\boldsymbol{S}}_2}{|\boldsymbol{r}_{12}|^3} - \frac{3(\hat{\boldsymbol{S}}_1 \cdot \boldsymbol{r}_{12})(\hat{\boldsymbol{S}}_2 \cdot \boldsymbol{r}_{12})}{|\boldsymbol{r}_{12}|^5} \right], \tag{3.15}$$

where α is the fine-structure constant. Expressed in the more common tensorial representation shown in equation (2.23), the elements of the tensor can be calculated by [65]:

$$D_{kl} = \frac{g_{\mathrm{e}}^2 \alpha^2}{4S(2S-1)} \langle \Psi | \frac{|\boldsymbol{r}_{12}|^2 \delta_{kl} - 3 r_{12,k} r_{12,l}}{|\boldsymbol{r}_{12}|^5} \left[2\hat{S}_z(1)\hat{S}_z(2) - \hat{S}_x(1)\hat{S}_x(2) - \hat{S}_y(1)\hat{S}_y(2) \right] | \Psi \rangle , \tag{3.16}$$

using first order perturbation theory. The indices k and l represent the three spatial variables x, y and z. The equations derived by McWeeny and Mizuno [130] provide manageable solutions within the DFT framework. The tensor elements can be expressed by

$$
\begin{aligned}
D_{kl} = \frac{g_\mathrm{e}^2\alpha^2}{4S(2S-1)} \sum_{\mu\nu}\sum_{\kappa\tau} \mathbf{P}^{\alpha-\beta}_{\mu\nu}\mathbf{P}^{\alpha-\beta}_{\kappa\tau} \Bigg[& \langle\mu\nu| \frac{3r_{12,k}r_{12,l} - |\boldsymbol{r}_{12}|^2\delta_{kl}}{|\boldsymbol{r}_{12}|^5} |\kappa\tau\rangle \\
& -\langle\mu\kappa| \frac{3r_{12,k}r_{12,l} - |\boldsymbol{r}_{12}|^2\delta_{kl}}{|\boldsymbol{r}_{12}|^5} |\nu\tau\rangle \Bigg],
\end{aligned}
\tag{3.17}
$$

where μ, ν, κ and τ denote different basis functions and $\mathbf{P}^{\alpha-\beta}_{\mu\nu}$ are elements of the spin-density-difference matrix [131].

3.3.3. Excitation wavelengths

To calculate excitation energies, the KS DFT approach needs to be extended by a time dependency. This enables one to describe photo excitation by an electric field that can be turned on at a given time. Time-dependent DFT (TDDFT) was first theoretically proven by Runge and Gross [132] and became quickly popular. If the external electric field is small compared to the field induced by the nuclear charges, it can be treated as perturbation. From time-dependent perturbation theory one gets the eigenvalue equation [133, 134]

$$
\begin{pmatrix} \mathbf{A} & \mathbf{B} \\ \mathbf{B*} & \mathbf{A*} \end{pmatrix} \begin{pmatrix} \boldsymbol{X} \\ \boldsymbol{Y} \end{pmatrix} = \omega \begin{pmatrix} 1 & 0 \\ 0 & -1 \end{pmatrix} \begin{pmatrix} \boldsymbol{X} \\ \boldsymbol{Y} \end{pmatrix},
\tag{3.18}
$$

with the excitation frequency ω, the corresponding eigenvectors $\boldsymbol{X}$ and $\boldsymbol{Y}$ and the matrices $\mathbf{A}$ and $\mathbf{B}$ with their elements

$$
A_{ia,jb} = \delta_{ij}\delta_{ab}(\epsilon_a - \epsilon_i) + 2\langle ia|jb\rangle - a_x\langle ij|ab\rangle + (1-a_x)\langle ia|f_\mathrm{xc}|jb\rangle
\tag{3.19}
$$

and

$$
B_{ia,jb} = 2\langle ia|jb\rangle - a_x\langle ib|aj\rangle + (1-a_x)\langle ia|f_\mathrm{xc}|jb\rangle
\tag{3.20}
$$

with integrals given in the common chemist's notation [97]

$$
\langle ia|jb\rangle = \int\int \chi_i^*(1)\chi_a(1)\frac{1}{\boldsymbol{r}_{12}}\chi_j^*(2)\chi_b(2)\mathrm{d}\boldsymbol{r}_1\mathrm{d}\boldsymbol{r}_2\,.
\tag{3.21}
$$

Indices i and j denote occupied orbitals and a, b virtual ones, coefficient a_x is the amount of used HF exchange defined by the chosen hybrid functional. Matrix $\mathbf{A}$ contains from left to right, the energy differences between the occupied and virtual orbitals, two terms attributed to electron–electron interaction and the response of the exchange-correlation energy to the perturbation. This last term contains f_xc, the so-called exchange correlation kernel. Within the highly used adiabatic linear-density approximation (ALDA), the time dependency of the kernel is removed. It can be written as

$$
f_\mathrm{xc}^\mathrm{ALDA}(\boldsymbol{r}_1, \boldsymbol{r}_2) = \frac{\delta E_\mathrm{xc}}{\delta\rho(\boldsymbol{r}_1)\delta\rho(\boldsymbol{r}_2)}\,.
\tag{3.22}
$$

Matrix **B** only provides small corrections and within the Tamm–Dancoff approximation (TDA) it is neglected [134]. Equation (3.18) is then simplified to

$$\mathbf{A}\boldsymbol{X}_{\text{TDA}} = \omega_{\text{TDA}}\boldsymbol{X}_{\text{TDA}} \, . \tag{3.23}$$

From those calculations, natural-transition orbitals (NTOs) can be built out of MOs involved in the different transitions. Detailed information can be found in references [134, 135].

Part III.

Publications

4. Overview and introduction to the publications

Materials in the focus of this work are copolymers consisting of different donor and acceptor moieties. A variety of modifications more closely described for each single publication below was investigated in order to get more insights into the electronic structure, morphology and pathways for triplet-state formation and how modifications on the molecular structure affect them. To do so methods with a molecular resolution are needed. Previous work [41] has proven that TREPR spectroscopy with its molecular resolution is a suitable method, but interpretation of obtained data is challenging and sometimes inconclusive. To improve knowledge gained from TREPR spectra, temperature-dependent UV-VIS spectroscopy and quantum-chemical (DFT) calculations on single molecules were included into the research routine.

TREPR experiments were performed on frozen solutions and thin films at 80 K with excitation wavelength at the maximum of the CT band. Obtained spectra were analysed via the TREPR toolbox and fitted with the TSim [41, 92] program which relies on Easyspin [136] simulation routines (TREPR toolbox [137], TSim [138] Easyspin [139] are all available for free). All three programs are written in the programming language MATLAB [140]. From the simulations ZFS parameters D and E, g factor, ZF populations p_1, p_2 and p_3, and Gaussian and Lorentzian linewidths $\Gamma_{\mathrm{G,L}}$ are obtained.

Since TREPR experiments were performed at low temperature, knowledge about possible aggregation and changes of absorptive behaviour was crucial for futher data analysis and interpretation. Temperature-dependent UV-VIS spectroscopy is a method giving access to those informations. Spectra of dissolved samples were recorded and temperature was gradually decreased until the sample froze. Hints for possible aggregation can be found in changes of spectral shape [141, 142] and a suitable excitation wavelength for TREPR experiment can directly be extracted from the maximum of an absorptive band.

Information about aggregation, more precisely over how many molecules the triplet exciton tends to be delocalised, was important as starting point for DFT calculations. On the basis of those findings suitable initial molecular structures for DFT calculations could be constructed. No signs of aggregation were found in UV-VIS spectra, so DFT calculations were perfomed on individual fragments in vacuum using the ORCA [143] program package. Complexity and extent of the calculations increased over the course of this work. First the singlet and triplet ground state geometries of different rotamers were energetically optimised using different combinations of functionals and basis sets. Vibrational analysis was used afterwards to see if a minimum in energy was found. Spin-density distribution of the triplet states was used to identify the localisation of the triplet exciton. Second the orientation of the ZFS tensor **D** and the corresponding values of the ZFS parameters D and E were calculated on the triplet-state geometries with different combinations of functionals and basis sets as well. Finally, TDDFT calculations giving insight into the orbitals involved during light excitation were performed.

Tools for quantitative and qualitative analysis of DFT data have been developed. More information are given in the description of the respective publications. The dihedral angles between the D and A moieties of the polymer had to be calculated with respect to the molecules curvature (publications 1, 2 and 3). Calculated spin density on the single D and A moieties needed to be quantified to enable intermolecular comparisons. Additionally the Mulliken spin density on each atom was plotted to examine its overall symmetry (publications 1, 2, 3, 5 and 6). Finally to analyse and compare the orientation of the calculated **D** tensor a suitable reference coordinate system had to be found (publications 2 and 3). Only this extensive DFT-data analysis enabled the interpretation the interpretation of the experimental parameters.

Publication 1: From the building block to the polymer I (PCDTBT) In this publication the impact of the growing chain length on the electronic structure and the molecular geometry of PCDTBT has been investigated. Solutions of the units A, D-A, D-A-D and the polymer (respectively TBT, Cbz-TBT, Cbz-TBT-Cbz and PCDTBT) in *o*-DCB were spectroscopically analysed as described above. Singlet and triplet ground state were geometry optimised via DFT calculations with a series of combinations of functionals and basis sets, showing BP86:Def2-SVP [121, 122, 144] to be superior to the mostly used B3LYP:6-31G** [123, 124, 145, 146] for this particular polymer system. UV-VIS spectra showed a red-shift of the CT band with a growing polymer chain, indicating an increasing delocalisation of the singlet exciton. TREPR data showed a growing rhombicity and delocalisation of the triplet exciton with increasing chain length. All spectra could be simulated with one triplet species, using no Gaussian linewidth. DFT calculations predicted a flat molecular structure for all molecules and a triplet exciton mainly localised on one TBT unit. Temperature-dependent UV-VIS spectra showed no hints of aggregation, and together with the exclusively Lorentzian linewidth of the simulations fitted to the TREPR data, one could deduce that the environment of the molecules is very homogeneous. By comparing the optimised geometries with the rhombicity of the TREPR spectra a link between increasing rhombicity and growing curvature of the otherwise flat molecules could be found. Despite the increasing delocalisation of the triplet exciton with a growing molecular chain, the donor–acceptor interaction between thiophene and benzothiadiazol was found to be dominant even in the polymer, breaking down the electronic structure to a small unit. A conclusion that could not be made by means of optical spectroscopy. Given that TBT dominates the electronic structure of PCDTBT, one should rather speak of a thiophene-benzothiadiazole than a carbazole derivate [14, 15].

Publication 2: From the building block to the polymer II (hex-PCDTBT) The hexylated version of PCDTBT, with hexyl side chains attached to the two thiophenes of the TBT unit, was subject of the second publication. Through the knowledge of the the non-hexylated polymer, gained from the first publication, the side-chain impact could directly be identified. The same ansatz as in the first paper was chosen, the growing polymer chain and impact of the alkylation on the electronic structure and molecular geometries were explored that way. Solutions of the units A, D-A, D-A-D and the polymer (respectively hexTBT, Cbz-hexTBT, Cbz-hexTBT-Cbz and hexPCDTBT) in *o*-DCB were analysed via TREPR and UV-VIS spectroscopy as described above. DFT calculations have been performed the same way with additional **D** tensor calculations on both variations of the molecules. TREPR data showed stagnation on increasing triplet exciton delocalisation at the length of D-A-D unit and rhombicity first in- then decreasing, with a maximum at the D-A-D unit. DFT calculations predicted a twist in the former flat geometry between the D and A units. Due to those twists strong localisation of the triplet exciton on a single A unit was found. **D** tensor calculations showed a nearly identical orientation for all molecules and a positive sign of the ZFS parameters. Similar conclusions to the first paper could be drawn. The comparison between UV-VIS and TREPR data led to the same result, no hints for aggregation. Also it was found that the A unit dominates the electronic structure of the polymer.

From the obtained twist in the molecular backbone due to hexylation hindering conjugation, the stagnation of the triplet exciton delocalisation at the D-A-D unit could be explained. The same effect is also responsible for the overall larger delocalisation in the non-hexylated system, with the single A unit as exception. The positive sign of the ZFS parameter D enabled us to assign the ZF populations to their corresponding tensorial axes. A correlation between the largest population located in direction of the bonding axis between the thiophene and the benzothiadiazole could be identified. More detailed analysis of the dihedral angles between adjacent moieties in the polymer chain provided hints for the triplet exciton flattening its environment.

Publication 3: Side-chain impact on morphology and electronic structure Influence of the degree of hexylation of PCDTBT onto the morphology and electronic structure of PCDTBT was topic of the third publication. Knowledge about the electronic structure of the non- and fully-hexylated polymer gained from the previous publications were the prerequisite for this study. Solutions and drop-cast films of the polymer with systematically increased degree of hexylation were analysed with TREPR spectroscopy, the films were recorded at different orientations with respect to the external magnetic field and globally fitted. Additional magnetophotoselection experiments have been performed on the polymer and its repeat unit. Complementary DFT calculations of the geometries of chains with different degrees of hexyation and their **D** tensor were carried out to get more insights into changes of the molecular structure. A larger delocalisation of the triplet exciton was detected for the drop-cast polymers compared to those in solution, what could be correlated with a more planar polymer backbone when deposited on substrate. With increasing degree of hexylation the triplet exciton delocalisation became smaller, in line with the increasing dihedral angles in the polymer backbone obtained by DFT calculations. The combined results from the magnetophotoselection experiment, DFT calculations and angular-dependent TREPR spectra obtained for thin films led to the conclusion that, even being amorphous, PCDTBT shows a face-on orientation on the substrate.

Publication 4: Pathways for triplet-state formation In a former study [37] the influcence of the excitation wavelength of Cbz-TBT, the repeat unit of PCDTBT, was investigated. By exciting with energies lower than the CT absorption band a direct singlet–tripet excitation could be found. In the first publication it was shown that TBT is dominating the electronic structure of the PCDTBT polymer. The TBT unit can also be found in different other polymers [147, 148], which is why in this publication the same experiments as for the Cbz-TBT were repeated for the TBT. TREPR spectra with different excitation wavelengths were recorded directly one after the other without touching the sample. Even for excitation wavelengths outside the CT band, where no absorption should take place, triplet states were detected with a maximum amount per photon at the red-shifted from CT band. Thus a direct $S_0 \rightarrow T$ excitation takes place also in the smaller unit. Parameters extracted from the spectral simulations were identical for all triplet states formed via ISC from the excited singlet state, while those originating from direct $S_0 \rightarrow T$ excitation showed clear differences for different wavelengths. Those results hint towards different triplet states being populated by the direct excitation. By comparing both studies, a slower decomposition could be found for Cbz-TBT. This shows that the Cbz unit which only plays a minor role for the electronic structure is very important for the photostability of the polymer.

Publication 5: Electronic structure of two competing acceptors The effects on the electronic structure by inserting the acceptor benzothiadiazole into the alternating donor–acceptor copolymer PNDIT2 was explored in this paper. By inserting the mentioned acceptor between both thiophenes the polymer PNDITBT is obtained. Comparison of the TREPR spectra of the three polymers PNDIT2, PNDITBT and PCDTBT show first hints, that the donor–acceptor interaction in the TBT unit dominates similarly to the situation found for PCDTBT as described in the first publication. The results of DFT calculations of the triplet ground state geometries, spin delocalisation and $\mathbf{D}$ tensors, confirm this suggestion. The calculated properties resemble those obtained for PCDTBT and by assigning the ZF populations to their corresponding tensorial axes, it was also found that the main population was located along the binding axis between donor and acceptor.

Publication 6: Electronic structure of a polymer—know your building block Topic of the publication was the influence of different linkage between donor and acceptor units. Investigated molecules are the two potential repeat units of PNDIT2, NDI-T2 and T-NDI-T. Both represent different electronic structures in terms of donor–acceptor constellations. Recorded UV-VIS spectra of both molecules looked very similar, whereas TREPR spectra showed a major difference in spectral shape and revealed the similarity between NDI-T2 and PNDIT2. DFT calculations of NTOs of the singlet states and spin-density distributions of the triplet states confirmed those results. Also a stronger CT character could be associated with NDI-T2. The similarities, in the simulation parameters obtained from TREPR spectra, between T-NDI-T and former reported T2-NDI-T2 [38], and between NDI-T2 and PNDIT2 gave new insights into the electronic structure of the polymer. Even though being symmetric, the electronic structure of the polymer is clearly dominated by an asymmetric chromophore.

The latest version of the manuscript can be found in the appendix, since it is not yet accepted.

5. List of publications and author contributions

5.1. TBT entirely dominates the electronic structure of the conjugated copolymer PCDTBT: Insights from time-resolved electron paramagnetic resonance spectroscopy

Clemens Matt, Deborah L. Meyer, Florian Lombeck, Michael Sommer and Till Biskup: TBT Entirely Dominates the Electronic Structure of the Conjugated Copolymer PCDTBT: Insights from Time-Resolved Electron Paramagnetic Resonance Spectroscopy. *Macromolecules*, 51 (2018), pp. 4341–4349 (DOI: 10.1021/acs.macromol.8b00791)

Contributions of all authors:

Clemens Matt: conception and study design, data aquisition (DFT, TREPR and UV-VIS), data analysis, contributions to manuscript and manuscript review

Deborah L. Meyer: data aquisition (TREPR), data analysis, and manuscript review

Florian Lombeck: sample synthesis and manuscript review

Michael Sommer: conception and study design and manuscript review

Till Biskup: conception and design of study, data acquisition (TREPR and UV-VIS), data analysis, main contribution to the manuscript and manuscript review

Macromolecules

Article

Cite This: *Macromolecules* 2018, 51, 4341−4349

TBT Entirely Dominates the Electronic Structure of the Conjugated Copolymer PCDTBT: Insights from Time-Resolved Electron Paramagnetic Resonance Spectroscopy

Clemens Matt,[†] Deborah L. Meyer,[†] Florian Lombeck,[‡] Michael Sommer,[‡] and Till Biskup*,[†]

[†]Institut für Physikalische Chemie, Albert-Ludwigs-Universität Freiburg, Albertstraße 21, 79104 Freiburg, Germany
[‡]Institut für Makromolekulare Chemie, Albert-Ludwigs-Universität Freiburg, Stefan-Meier-Straße 31, 79104 Freiburg, Germany

Supporting Information

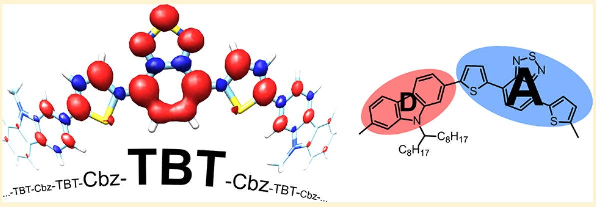

ABSTRACT: Insight into the electronic structure of conjugated polymers used for organic electronics applications is of outstanding importance. Time-resolved electron paramagnetic resonance spectroscopy of light-induced triplet excitons provides access to the electronic structure with molecular resolution. Systematically investigating building blocks of increasing length and comparing the results with the polymer deepens our understanding of the structure−function relationship in organic semiconductors. Applying this approach to the copolymer poly[*N*-9′-heptadecanyl-2,7-carbazole-*alt*-5,5-(4′,7′-di-2-thienyl-2′,1′,3′-benzothiadiazole)] (PCDTBT) known for its efficiency and device stability reveals the electronic structure of the polymer as well as each of the smaller building blocks to be dominated entirely by the TBT moiety. Hence, the usual description of PCDTBT as a carbazole derivative is somewhat misleading. Furthermore, delocalization extends along the backbone, over at least two repeat units, and is consistent for singlet and triplet excitons, quite in contrast to other push−pull systems previously investigated. DFT calculations of the spin density distribution agree well with the experimental results and show the BP86 functional to be superior to B3LYP in the given context. The polymer and all its building blocks show a remarkable homogeneity that by ruling out aggregation phenomena is ascribed to a rather rigid and planar backbone geometry.

■ INTRODUCTION

Organic electronics is an exciting field with great impact in all areas of electronics,[1] from light-energy conversion in organic photovoltaics[2,3] to flexible transistors[4] to sensors.[5,6] The common ground of this widespread field of potential applications is to use organic materials, mostly polymers, as a replacement for conventional inorganic (silicon-based) semiconductors. Potential advantages of these materials are their mechanical flexibility, low cost due to solution printing, and the nearly infinite possibility of tailoring molecules by means of organic synthesis for each special application. In order to fully exploit the last-mentioned advantage, it is important to gain a fundamental understanding of the inner workings of these organic semiconductors. Two key aspects have been identified: morphology[7] and electronic structure.[8] Whereas many well-established methods are available to probe morphology of conjugated polymers, direct access to the electronic structure is much more difficult to achieve. Necessary are spectroscopic tools with molecular resolution that are capable of directly probing the electronic structure of the polymer.

As most applications in organic electronics involve excited states, charges, and charge carriers, electron paramagnetic resonance (EPR) spectroscopy is highly suited to investigate these materials, allowing one to directly detect paramagnetic states and to reveal their spin multiplicity, besides its clearly superior molecular resolution compared to optical methods. Time-resolved EPR (TREPR) spectroscopy,[9,10] in particular, is a powerful tool to characterize the various excited species that are created after light excitation of organic molecules, such as triplet excitons[11−13] and charge-transfer complexes.[14] Illuminating conjugated polymers hence not only leads to excited states but sheds light on some of the most important aspects of device efficiency in organic electronics as well. The interplay between electronic structure, morphology, flexibility, and local ordering, while at the heart of structure−function relationship of organic electronic materials, is still barely understood. TREPR spectroscopy has proven valuable to gain further insight,[12,15] and since the resulting spectra are also highly sensitive to the orientation of the molecule, it can even give insights into sample morphology on a microscopic scale, in both (frozen) solution[13] and thin film.[11]

To get a deeper insight into the electronic structure of a conjugated polymer, looking at building blocks with increasing backbone length has been proven useful.[15] Here, we apply this strategy to the copolymer poly[*N*-9′-heptadecanyl-2,7-carbazole-*alt*-5,5-(4′,7′-di-2-thienyl-2′,1′,3′-benzothiadiazole)] (PCDTBT),[16,17] mostly used as donor material in organic photovoltaics with high internal quantum efficiency of nearly

Received: April 13, 2018
Revised: May 21, 2018
Published: May 31, 2018

DOI: 10.1021/acs.macromol.8b00791
Macromolecules 2018, 51, 4341−4349

100%[18] and its stability under ambient conditions, leading to an increased lifetime of devices of several years.[19−22] Taken together, these characteristics have led to considering PCDTBT a benchmark polymer replacing P3HT in this respect.[23] Previously, we could already show the polymer PCDTBT to exhibit quite some long-range overall ordering and determine the backbone to be oriented face-on on a flat surface,[11] beneficial for charge injection. Furthermore, we could demonstrate that spin-forbidden direct $T \leftarrow S_0$ excitation plays a major role in the polymer repeat unit, CbzTBT.[12] To get a deeper insight into the electronic structure of the polymer, here, we investigate a series of building blocks of PCDTBT and the polymer itself (see Figure 1 for chemical structures) using TREPR spectroscopy of their triplet excitons, complemented with steady-state absorption spectroscopy and quantum-chemical calculations of the spin density distribution in the triplet state using density-functional theory (DFT).

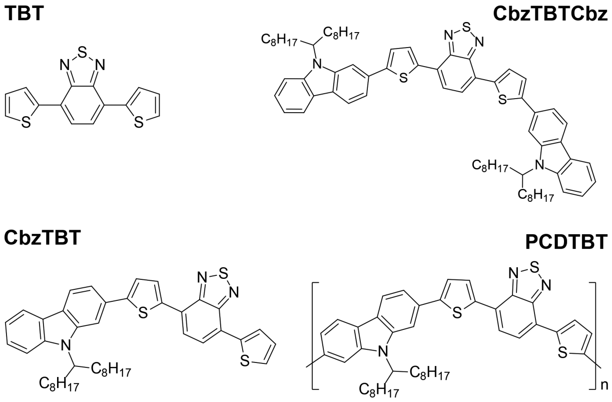

Figure 1. Chemical structure of PCDTBT and its building blocks. The polymer repeat unit Cbz-TBT forms a push−pull system comprising a carbazole (Cbz) and a dithienylbenzothiadiazole (TBT) unit, the latter being itself a push−pull system.

For PCDTBT, a systematic study focusing on optical spectroscopy and DFT calculations has already been performed,[24] besides a number of theoretical investigations.[25,26] However, optical spectra offer only limited insight into the electronic structure, clearly inferior to the molecular resolution of EPR spectroscopy. Besides that, the repeat unit investigated by Banerjee et al. had a phenyl substituent present on one side obviously substantially contributing to the electronic structure of its excited states. Hence, this does not entirely reflect the situation in the “true” repeat unit nor the polymer. Furthermore, here, we investigate additionally a symmetric building block, CbzTBTCbz, larger than the actual polymer repeat unit, providing further insight.

■ RESULTS

Absorption Spectra. Steady-state absorption spectra were recorded for all building blocks and the polymer (cf. Figure 2). Each of the substances investigated in this study shows two distinct absorption bands: a high-energy band that can be attributed to a π−π* transition and a low-energy band usually termed charge transfer (CT) band that is due to the weak intramolecular CT character of the push−pull system comprising benzothiadiazole and the two flanking thiophenes. The CT band shows a progression toward longer wavelengths with increasingly extended conjugated system.

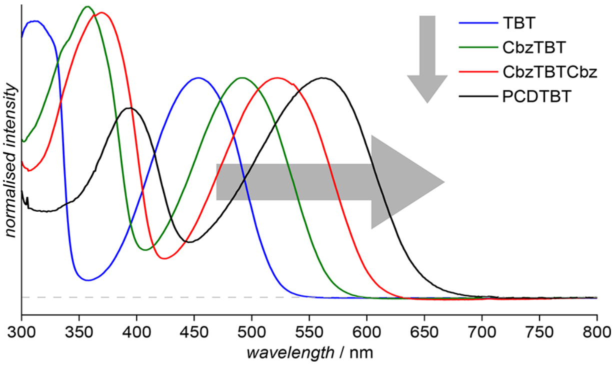

Figure 2. Absorption spectra of PCDTBT and its building blocks. Each spectrum consists of two bands: a π−π* band (mostly) in the near-UV region and a prominent band in the visible region, assigned to the partial charge-transfer character of the molecule and hence termed CT band. Obviously, the CT band increasingly shifts toward greater wavelengths with increasing length of the backbone. For easier comparison, spectra have been normalized to the same CT band height.

The absorption spectra do not show any sign of aggregation of the model compounds in solution, and they were not sensitive to the concentration used (data not shown). To rule out any aggregation due to cooling (as necessary for EPR spectroscopic investigations, see below), we performed temperature-dependent absorption measurements for all substances investigated. None of them showed any sign of aggregation in the solvent used (*o*-dichlorobenzene, *o*-DCB). Note that due to *o*-DCB not forming a transparent glass upon freezing, optical absorption spectra can only be recorded down to the freezing point of the solution. For details and actual spectra, see the Supporting Information.

TREPR Spectra. If optically excited either in the CT band or in the π−π* transition, PCDTBT and its building blocks readily form short-lived triplet states that manifest themselves as characteristic spectra in TREPR spectroscopy (Figure 3). These

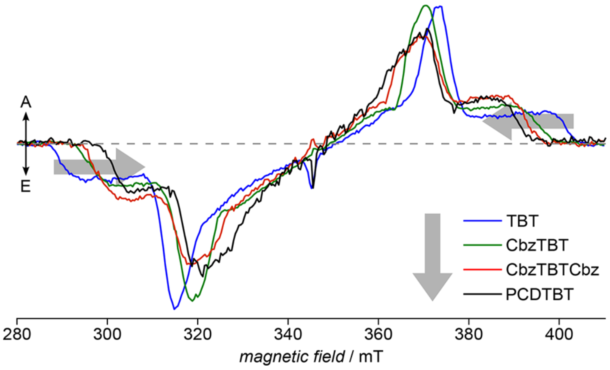

Figure 3. TREPR spectra of PCDTBT and its building blocks. Each sample has been excited in the respective CT band absorption maximum (cf. Figure 2). Obviously, the overall spectral width decreases with increasing length of the backbone. Spectra are averages over 200 ns, centered about 500 ns after the laser flash (in the maximum of the signal), and have been normalized to same absolute area under the respective curves. Each spectrum could be reproduced by spectral simulations taking a single triplet species into account (cf. Figure 4). For full two-dimensional data sets see the Supporting Information.

spectra are entirely dominated by the zero-field splitting (ZFS) interaction resulting from the dipolar coupling of the two unpaired electron spins of the triplet state. Accordingly, the absolute values for the two characteristic parameters D and E of the corresponding interaction tensor can be directly extracted from the signal (for details, see the Supporting Information). Here, $|D|$ can be generally related to the average distance between the two spins, and thus to the delocalization of the spin density on the molecule, and $|E|$ to the deviation of the spin density distribution from an axial symmetry, hence the degree of rhombicity. Therefore, TREPR spectra of triplet states allow for directly accessing the electronic structure of the triplet state of the underlying molecule. The light-induced triplet states are initially created with their three sublevels populated far from thermal equilibrium. This gives rise to a large signal enhancement of the corresponding TREPR spectra that show signals in enhanced absorption (A) and emission (E). This signal enhancement allows to omit the lock-in detection scheme used in conventional cw-EPR spectroscopy and therefore to increase time resolution up to about 10 ns.

For all building blocks and the polymer, TREPR spectra have been recorded at low temperature (80 K) and the resulting spectra fitted assuming a single triplet species for each spectrum. Figure 4 gives an overview of both the spectra obtained and their respective simulations. All spectra each can be fully described assuming a single triplet species as demonstrated by the nearly perfectly fitting spectral simulations (cf. Figure 4). For simulation parameters cf. Table 1, and for details of the simulation procedure, see the Supporting Information.

Already from the TREPR spectra it is quite obvious that TBT dominates the overall spectral shape and that, on first sight, only the total width changes with increasing backbone length, consistent with an increased delocalization of the triplet exciton. Note that due to the inverse cubed distance dependence of the dipolar interaction between the two electron spins in the triplet state, narrower EPR spectra mean a larger average distance between the two spins, hence larger exciton delocalization.

A series of further aspects seem notable already on first inspection of the experimentally obtained data: The rhombicity $|E|/|D|$, although overall pretty small and close to a fully axial triplet state, increases with increasing backbone length (cf. Table 1). Additionally, only Lorentzian line broadening (Γ_L) is necessary to account for the data. This hints upon a very homogeneous environment of the electron spins of the triplet exciton on the polymer chain and is in remarkable contrast to other polymers, namely PNDIT2.[13,15] Furthermore, the line width of the TREPR signals is rather narrow compared to triplet states of other conjugated polymers.[13,27]

Although it is notoriously difficult to quantify signal intensities in TREPR spectroscopy due to both a series of hard to control experimental parameters and general considerations (for details, see the Supporting Information), we note that signal intensity, and hence the triplet yield, seems to decrease with increasing chain length. Although this effect cannot be quantified, it reflects nevertheless a commonly observed situation: polymers tend to show a lower triplet yield than their respective building blocks.

The sharp signals in the center of the TREPR spectra are not due to the triplet state. Such features are regularly seen for other conjugated polymers as well (and often much stronger there, e.g., P3HT and PTB7), and possible origins are either stable radicals (due to “defects”) or light-induced charge-separated states.[14,28,29] However, they are notoriously difficult to properly assign and do not contribute to nor hamper the overall interpretation of our data. Hence, they are not discussed any further hereafter.

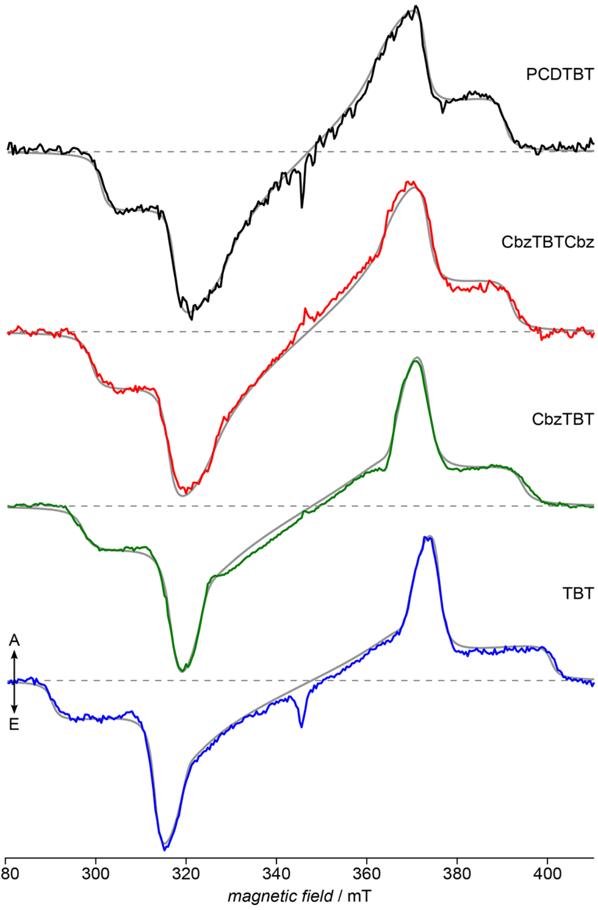

Figure 4. TREPR spectra of PCDTBT and its building blocks together with spectral simulations. Each spectrum could be reproduced by spectral simulations taking a single triplet species into account and shown as gray lines. For simulation parameters cf. Table 1, and for details of the fitting procedure see the Supporting Information. The small features in the center of the spectra at about 345 mT are not due to the triplet state and will not be accounted for here.

DFT Calculations: Geometry and Spin Density Distribution. To gain further insight, all building blocks and a tetramer as model for the polymer chain have been investigated by DFT calculations on the theory level BP86/Def2-SVP. First, the geometry for each molecule has been optimized in its triplet state (cf. Figure 5 and Table 2), and afterward the Mulliken spin density distribution of the triplet state has been calculated (cf. Figure 6). Additionally, calculations have been performed using B3LYP/6-31G** as functional and basis set and the results compared to those obtained for BP86/Def2-SVP that are shown here. For details of the calculations and results for B3LYP/6-31G**, see the Supporting Information.

The trans orientation of the sulfur atoms of the thiophenes with respect to the benzothiadiazole moiety is in accordance with the literature showing that this configuration is the

Table 1. Simulation Parameters for the Spectral Simulations of the TREPR Spectra Shown in Figure 3[a]

	λ_{ex}/nm	$|D|$/MHz	$|E|$/MHz	$|E|/|D|$	Γ_L/mT	$p_{1,2,3}$
TBT	454	1550 ± 2.2	70 ± 1.0	0.045	2.36 ± 0.09	0, 0.182, 0.818
CbzTBT	492	1362 ± 2.5	76 ± 1.4	0.056	3.42 ± 0.13	0, 0.138, 0.862
CbzTBTCbz	522	1303 ± 3.6	101 ± 1.7	0.078	2.96 ± 0.16	0, 0.309, 0.691
PCDTBT	550	1254 ± 3.0	101 ± 1.4	0.081	2.39 ± 0.13	0, 0.351, 0.649

[a] λ_{ex} is the excitation wavelength used (maximum of the CT band), D and E are the parameters of the zero-field splitting tensor of the dipolar interaction, Γ_L is the Lorentzian line width, and $p_{1,2,3}$ are the populations of the three triplet sublevels. For actual simulations and details of the fitting procedure see the Supporting Information.

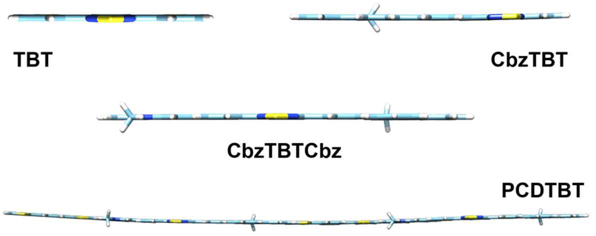

Figure 5. Side view of the optimized geometries of the triplet states of PCDTBT and its building blocks. Geometries have been optimized for the triplet state on the theory level BP86/Def2-SVP. For a view perpendicular to the aromatic plane, cf. Figure 6. As obvious from this side view, all molecules are rather flat, with dihedral angles between the aromatic planes of Cbz and TBT, respectively, close to zero. For values of these dihedral angles, cf. Table 2.

Table 2. Angles between the Aromatic Planes of Cbz and TBT Moieties Obtained from Geometry Optimization in the Triplet State[a]

	BP86/Def2-SVP	B3LYP/6-31G**
CbzTBT	1.1	1.9
CbzTBTCbz	0.3	0.8
	0.7	5.9
PCDTBT	1.0	13.8
	2.9	19.8
	1.4	11.7
	1.1	9.1
	0.5	10.1
	0.2	12.2
	1.0	17.7

[a] The Cbz and TBT moieties are in themselves pretty flat. Angles are given in degrees and for the cis–trans configuration as shown in Figure 6. Note the dramatic differences between BP86 and B3LYP, particularly for the polymer fragment. For details of how these angles have been obtained see the Supporting Information.

energetically most favorable,[30] although other reports have shown a cis–trans conformation to dominate in TBT crystals.[31]

All building blocks and the polymer chain itself are rather flat (cf. Figure 5 and Table 2), with the polymer showing a characteristic s-curvature of the otherwise flat backbone (Figure 6), consistent with previous reports for the geometries of the singlet state.[24,25] Whereas the TBT unit is known to be strictly planar,[30,31] for the dihedral angles between the thiophenes of the TBT and the adjacent carbazole moiety, different angles between about 26° and close to zero can be found in the literature.[24,26,32] Note, however, the striking differences between BP86 and B3LYP for our own calculations that will be discussed in detail below.

Already at a first glance, the calculated spin-density distribution (Figure 6) coincides nicely with the experimentally observed increasing delocalization with extended backbone (cf. Figures 2 and 3). Similarly, the role of the TBT moiety entirely dominating the electronic structure even of the polymer is reflected in the spin density nearly exclusively being localized there. Whereas these kinds of plots of the spin density on top of the molecular structure give a good impression of the overall picture, different approaches are necessary for a more detailed understanding.

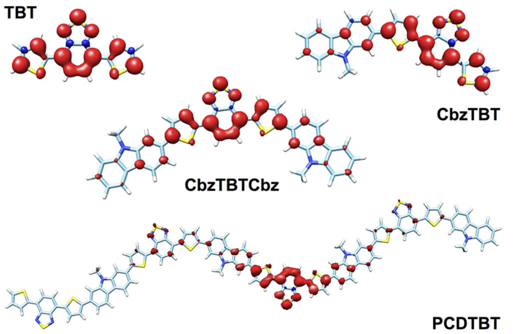

Figure 6. Spin density distribution for the triplet states of PCDTBT and its building blocks. Geometries have been optimized for the triplet state on the theory level BP86/Def2-SVP and spin densities displayed for a threshold level of ±0.002 (building blocks) and ±0.001 (PCDTBT). Red denotes positive and blue negative spin density.

To quantify the spin-density distribution of the triplet state and gain further insight, we compare the values of the spin densities for each nucleus of the TBT moiety for the three building blocks and the polymer fragment with $n = 4$ (Figure 7). For most of the nuclei, a monotonic decrease with increasing backbone length can be readily observed. Note that with exception of the intrinsically asymmetric molecule CbzTBT, both other building blocks and to a large extend the polymer fragment as well show a fairly symmetric distribution of spin density over the TBT moiety. The largest part of the spin density is located on the benzothiadiazole part of the TBT moiety. For the asymmetric building block CbzTBT, the carbazole moiety was attached to the left of the TBT moiety, hence on the carbon atom labeled "C1" in Figure 7.

■ DISCUSSION

Delocalization Extends with Backbone Length. Both singlet and triplet excitons are increasingly delocalized with increasing chain length, as evidenced by the increased red-shift of the optical absorption (CT band) of the molecules for the singlet exciton and the decrease in the D value of the dipolar interaction between the two unpaired electrons of the triplet state (Figure 8). Whereas this is according to "chemical intuition" and has been observed for some polymers,[28] such consistent monotonic increase in delocalization for both singlet

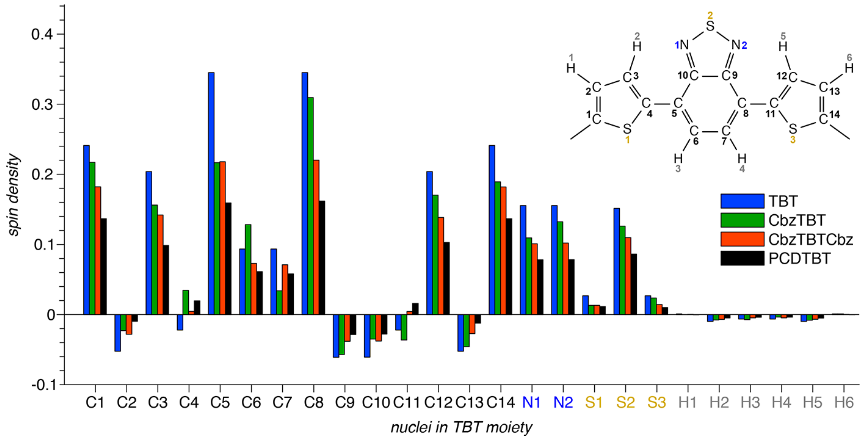

Figure 7. Quantitative analysis of the spin density distribution for the triplet states of PCDTBT and its building blocks. Depicted are the values for the spin densities for each of the TBT atoms in the four fragments of different size displayed in Figure 6. The inset shows the numbering of the atoms used as axis labels.

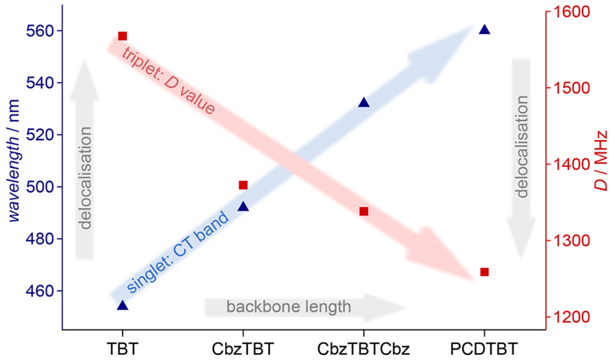

Figure 8. Delocalization of singlet and triplet excitons of PCDTBT and its building blocks. Both singlet and triplet excitons show a consistent trend toward greater delocalization with increasing backbone length. Note that the width of the TREPR spectra of the triplet states is determined by the dipolar interaction between the two spins, characterized by D. Because of the inverse cubed distance dependence of D, it decreases with increasing delocalization and distance between the two electron spins in the triplet state.

and triplet excitons is not necessarily observed for all conjugated polymers, particularly not for other push−pull systems such as PNDIT2.[15]

PCDTBT does not form highly ordered stacked structures and is normally referred to as amorphous[33] and only exhibiting short-range order,[34] although a rather high degree of ordering and orientation are present in thin films.[11] Therefore, delocalization in both solution and thin film most probably takes place along the backbone, not perpendicular to it. Our experimental data for both singlet and triplet excitons suggest a delocalization over at least two repeat units, in line with the literature showing the $S_1 \leftarrow S_0$ transition to consist of two contributions delocalized over about two and three TBT units, respectively.[25] For the triplet exciton, our spin density data (cf. Figure 6) suggest as well an extension over three TBT units, based on the cutoff value used. Given the singlet exciton normally to be more delocalized compared to the triplet exciton, the extent of the latter gives only a lower boundary for the singlet exciton delocalization.

Comparing our results to those obtained for the homopolymer P3HT showing a basically identical rhombicity, but at the same time a larger D value ($|D_{\mathrm{P3HT}}| \approx 1570$ MHz, see Supporting Information for details), it is tempting to speculate about a larger triplet exciton delocalization in the copolymer PCDTBT as compared to the homopolymer P3HT. This would be consistent with the optical absorption spectra showing a clear red-shift of PCDTBT compared to P3HT. For the latter, detailed TREPR studies of oligomers of different length[28] combined with extensive theoretical calculations[35] show the triplet exciton to extend over at least four thiophene rings. In contrast, the charged polaron seems to extend over 13 thiophene rings, as probed by hyperfine spectroscopy.[36] Assuming a delocalization of the triplet exciton in P3HT over about four rings would amount to a distance of approximately 14 Å, a value in between the extend of TBT (having a nearly identical D value, $|D_{\mathrm{TBT}}| \approx 1550$ MHz) and CbzTBT. However, great care must be taken comparing the D values of polymers with markedly different electronic structure, and quite generally, the estimation of the triplet extension by means of a simple dipole model is not useful in these systems due to their complex spin density distribution, as already clearly mentioned by Bennati et al.[28,35] Therefore, comparing the values of the ZFS parameters between entirely different systems is far from being straightforward. Nevertheless, for fragments of different length of one and the same polymer system this is clearly possible as long as one can reasonably assume the ZFS tensor not to reorient within the molecular coordinate system.[37] Given the near-identical electronic structure, as evidenced by the values for the rhombicity, triplet sublevel populations, and line width, this seems clearly fulfilled in PCDTBT. Hence, the decrease in D can be attributed to a successively larger delocalization of the triplet exciton, consistent with the increasing red-shift of the optical absorption data hinting toward the same trend for the singlet exciton.

As mentioned above, the consistent monotonic increase of the delocalization of both singlet and triplet exciton with increasing length of the conjugated backbone, though consistent with the naive picture connecting length of the conjugated system with delocalization, is not necessarily observed in polymers consisting of alternating donor and acceptor moieties, as has been recently shown for PNDIT2.[15] There, although the triplet state geometries are more flat as compared to their singlet state counterparts, delocalization of the triplet exciton is rather restricted to about 1.5 repeat units, hence rendering electronic structure in this particular case more important than planarity. For the n-type semiconducting polymer PNDIT2 consisting of a push−pull system comprising NDI and bithophene, the electronic structure of the polymer is dominated by the strong interaction between NDI and bithiophene, as has recently been shown by TREPR-spectroscopic investigation of its triplet excitons.[15] Quite in contrast, the electronic structure of PCDTBT is nearly entirely dominated by the TBT unit, in itself a push−pull system, with the carbazole moiety merely providing additional space for extending the conjugated system (see detailed discussion below).

TBT Dominates the Electronic Structure. As can be seen quite clearly from the high similarity of the TREPR spectra of the building blocks and the polymer (Figure 4), TBT dominates the electronic structure of PCDTBT as well as all the building blocks. Although this has been previously discussed mainly based on DFT calculations,[24,25] it cannot easily be deduced from optical absorption data, although they are consistent with this observation. This is one particular strength of TREPR with its molecular resolution and sensitivity to the direct environment of the unpaired electron spins, and the great similarity of all triplet excitons from TBT up to the polymer is not only obvious from the TREPR spectra but also reflected in the simulation parameters as well (Table 1).

The experimental results suggest that to some extent PCDTBT can be seen as "extended" version of the TBT monomer. On the other hand, even the triplet exciton is clearly delocalized over more than one repeat unit. Further insight comes from calculating the spin density distribution. Within the TBT, nearly half of the spin density is located on the benzothiadiazole core, with substantial constributions from the two nitrogens and the sulfur of the thiadiazole part, whereas the sulfurs of the flanking thiophenes are nearly devoid of spin density, consistent with the situation in polythiophenes.[35] The carbazole, in contrast, merely acts as "bridge" between adjacent TBT units, possessing comparably little spin density.

The dominant nature of the TBT unit seems to be conserved with other substituents than carbazole as well, even with those generally known to be acceptors, such as NDI. In this case, TBT even seems to reverse the acceptor character of NDI into a donor.[38] Our own preliminary work on PNDITBT is in line with this notion, showing a rather axial electronic structure of the triplet exciton, as compared to the rather rhombic situation in PNDIT2.[15]

Rhombicity Increases with Backbone Length, Reflecting Curvature. As mentioned already, the overall rhombicity is pretty small, close to the fully axial case. This is in stark contrast to other push−pull polymers, namely PNDIT2 with a nearly fully rhombic symmetry of the triplet state.[15] On the other hand, the triplet spectra of the homopolymer P3HT exhibit a very similar rhombicity (see Supporting Information for details), whereas the delocalization of the triplet exciton in P3HT seems far more restricted, carefully judging from the D value of the ZFS ($|D_{\mathrm{P3HT}}| \approx 1570$ MHz, but see discussion above). Furthermore, the rhombicity increases with increasing size of the molecules (Figure 9). This increase in rhombicity nicely coincides with the elongated conjugated system and could be well explained by the s-curvature of the backbone that has been discussed as characteristic for PCDTBT before.[25] Given the rather flat backbone, the only parameter accounting for the rhombicity, i.e., a spin density distribution different in symmetry in all three directions of space, is the curvature of the backbone. The degree and "frequency" of the curvature of a flat polymer backbone have been shown to be crucial for π−π stacking and solubility.[39] CbzTBTCbz is already much closer to the curvature of the polymer chain in comparison to the shorter building blocks, as can be seen from the optimized geometries (Figure 6), hence the pretty close rhombicity values for CbzTBTCbz and PCDTBT. Besides the curvature, the backbone should be otherwise pretty flat in order to give this highly axial symmetry of the triplet exciton as evident by the small value of $|E|$ as compared to $|D|$.

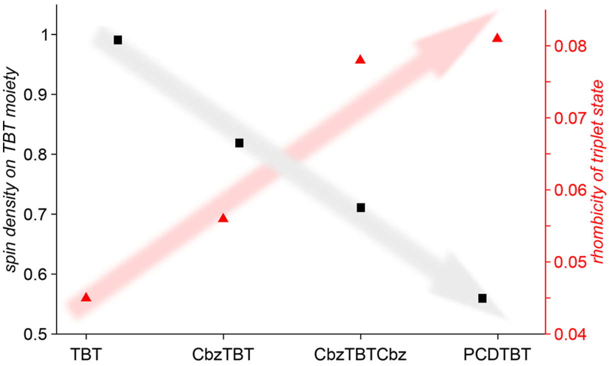

Figure 9. Comparison of spin density on the TBT moiety with rhombicity of the triplet exciton for PCDTBT and its building blocks. As can be seen from the plots in Figure 6, spin density is always centered about one single TBT moiety, even in the polymer. Plotted here is the relative amount of total spin density on the TBT moiety for the triplet excitons of PCDTBT and its building blocks (black squares). The monotonic decrease of the relative amount is consistent with the experimental data, showing clearly an increase in delocalization with increasing chain length. A similar trend can be seen for the overall rhombicity of the triplet exciton. It monotonically increases with the length of the conjugated backbone (red triangles).

Line Broadening Reveals Highly Homogeneous System. The small overall line width and the possibility to account for the experimental data using only Lorentzian line widths, as previously already realized for the polymer repeat unit, CbzTBT,[12] point toward a highly homogeneous environment of the molecules. Temperature-dependent absorption measurements show no aggregation to take place until freezing of the solution (for details see the Supporting Information). Ruling out aggregation, another possible explanation is a rather rigid backbone and an overall very flat geometry. Such a situation has been described for the homopolymer P3HT and its oligomers.[28,35] Whereas P3HT is known to form highly oriented microcrystalline domains, quite different than PCDTBT, our previous results on PCDTBT show the polymer to clearly orient itself with quite high overall ordering when dropcast as rather thick film on a flat substrate.[11] However, "accidental" forming of fibrillar structures in PCDTBT can be ruled out, as previous studies have shown the difficulties of purposefully crystallizing PCDTBT.[40]

Generally speaking, there are a number of contributions to the inhomogeneous line width of triplet states, namely unresolved hyperfine interactions, variable mean distances between the two electrons in the triplet state for different sites, and slightly different conformations for different sites. Given the small overall number of protons per TBT moiety and the very small amount of spin density on them (six protons, cf. Figure 7), we are pretty confident with ruling out hyperfine couplings as a potential cause of inhomogeneous broadening in this polymer. This is in line with the notion that we could not detect any ^{1}H-ENDOR signal for the triplet state using pulsed EPR spectroscopy. For the other nuclei (C, N, S), the natural abundances of isotopes with a nuclear spin unequal zero are very low, or in the case of ^{14}N with $I = 1$, the normally quite anisotropic couplings and quadrupole effects result in very small contributions to the broadening of EPR lines. The other two contributions, variations in the interspin distance of the two unpaired electron spins in the triplet state, and hence a distribution of D values, and conformational flexibility, cannot easily be separated.

However, the absence of any inhomogeneous line broadening, or at least the possibility to fit spectral simulations to the experimental data with similar quality if omitting inhomogeneous line broadening entirely, would be consistent with a rather rigid polymer backbone and in turn a small conformational flexibility between different sites. This is in line with the very flat geometry obtained for the triplet states of all fragments investigated using the BP86 functional and would be another argument to prefer BP86 over B3LYP for the molecules investigated here, besides the more consistent results regarding the exciton delocalization (see detailed discussion below).

DFT Calculations Are Consistent with Experimental Data. We would like to point out that the results of our DFT calculations are pretty much in line with the experimental results. The calculations performed on the BP86/Def2-SVP level of theory nicely reproduce the increased delocalization, shown here as relative amount of spin density on the TBT moiety with increasing backbone length (Figure 9). Furthermore, the calculated geometries of the triplet states show a pretty flat backbone nicely consistent with the highly homogeneous line width of the TREPR data.

To compare our results with other data from the literature, we performed similar calculations using B3LYP/6-31G** as functional and basis set, respectively. Interestingly, these calculations cannot as nicely reproduce the decrease in spin density on TBT experimentally validated by TREPR and consistently obtained from calculations using BP86/Def2-SVP. For details of the calculations, see the Supporting Information. Additionally, the geometries obtained with B3LYP/6-31G** exhibit small, but still substantial, dihedral angles between the adjacent aromatic planes of the alternating TBT and Cbz moieties (Table 2). This should be reflected in a substantial contribution from inhomogeneous line broadening in the TREPR spectra as well as an increased rhombicity. Both are clearly absent, hence pointing toward the geometries and spin density distributions obtained using BP86/Def2-SVP being more compatible to the experimental results. Hence, BP86 seems to be much better suited for calculating spin densities and geometries of triplet states for PCDTBT and its building blocks. Any generalization, however, cannot easily be drawn from these results. Nevertheless, it seems quite important to have experimental results readily available that can test different functionals and basis sets used in DFT for consistency between theory and experiment.

CONCLUSIONS

In summary, we have demonstrated the TBT moiety to dominate the electronic structure of the entire polymer. This is in stark contrast to other push–pull systems investigated so far (see PNDIT2 for comparison) and points toward TBT being a strong acceptor. Therefore, referring to PCDTBT as a carbazole derivative, though chemically entirely correct, seems slightly misleading. Furthermore, the delocalization of both singlet and triplet excitons extends over at least two repeat units, with DFT calculations suggesting three repeat units for the triplet state. Comparing our results with those previously obtained for the n-type polymer PNDIT2, it is obvious that push–pull systems behave tremendously different depending on the D and A moieties involved. Hence, generalization from one system to another seems rather difficult, and great care should be taken. Additionally, the results from TREPR spectroscopy, particularly the rather small and exclusively homogeneous line broadening, clearly point toward a rather rigid backbone of PCDTBT and its building blocks and a flat overall geometry, consistent with DFT results. Comparing our experimental results with DFT calculations using two different functionals and basis sets reveals BP86/Def2-SVP to be superior over the widely used B3LYP/6-31G** with regard to geometries and spin-density distributions of triplet states, at least for PCDTBT and its building blocks investigated here.

Taken together, we could show that TREPR spectroscopy in combination with building blocks of polymers available for investigation is an excellent tool to reveal the electronic structure of a polymer and due to its molecular resolution clearly superior to optical methods. In combination with temperature-dependent optical spectroscopy and accompanied by quantum-chemical calculations, this provides detailed insight into the geometry and morphology of the polymer as well. Such investigations are highly necessary to properly understand the all-important structure–function relationship of conjugated polymers used for organic electronics applications.

EXPERIMENTAL SECTION

Synthesis. TBT and CbzTBTCbz have been synthesized according to ref 41 and CbzTBT according to ref 12. PCDTBT has M_n/M_w of 22/68 kg/mol (high-temperature SEC at 150 °C in TCB vs PS standards) and was synthesized according to ref 16.

Optical Spectroscopy. All samples were dissolved in *o*-dichlorobenzene. Absorption spectra were recorded using a commercial UV/vis spectrometer (Shimadzu UV-2450, UV-1601PC) in combination with the corresponding software (UV Probe version 3.42). Measurements at ambient temperatures were performed with standard path length cuvettes (1 cm). Temperature series were recorded using a cryostat (Optistat DN2) in combination with a temperature controller (MercuryiTC, both Oxford Instruments) and using liquid nitrogen as a coolant. These measurements were performed using 1 mm path length cuvettes.

EPR Instrumentation. All samples were dissolved in *o*-dichlorobenzene. All TREPR experiments were performed at 80 K using a setup described previously.[11,12] Optical excitation at the respective wavelengths was carried out using an optical parametric oscillator (OPO) pumped by an Nd:YAG laser. The repetition rate of the laser was set to 10 Hz and the final pulse energy (after the OPO) to 1 mJ. Further experimental parameters (except where explicity given) are as follows: microwave frequency, 9.700 GHz; microwave power, 2 mW (20 dB attenuation, source power 200 mW); frequency-mixer detection; video amplifier set to 42 dB amplification and 25 MHz bandwidth; between 850 and 1400 averages per point.

Spectral Simulations. All simulations of triplet spectra were performed using the pepper routine from the EasySpin software package[42] available for MATLAB. Details of both the simulations and the fitting procedure are given in the Supporting Information.

DFT Calculations. All calculations were performed using ORCA 3.0.3[43] using the BP86[44,45] and B3LYP[46,47] functionals and the Def2-SVP[48] and 6-31G**[49,50] basis sets, respectively. The solvent has been accounted for by the COSMO model.[51] Initial geometries of the molecules were created using Avogadro 1.1.1.[52] Spin density plots were created using UCSF Chimera 1.11.2.[53]

DOI: 10.1021/acs.macromol.8b00791
Macromolecules 2018, 51, 4341−4349

■ ASSOCIATED CONTENT

Ⓢ Supporting Information

The Supporting Information is available free of charge on the ACS Publications website at DOI: 10.1021/acs.macromol.8b00791.

> Details of the EPR instrumentation, TREPR spectra of triplet states including full 2D data sets, details for the spectral simulations of TREPR spectra, the triplet spectrum of P3HT for comparison, comments on quantifying TREPR signal intensities, temperature-dependent absorption spectra of PCDTBT and its building blocks, details of the optimized geometries including angles between TBT and Cbz moieties, as well as DFT calculations (geometries and spin densities) using B3LYP/6-31G** and details of the quantitative analysis of the spin density distributions (PDF)

■ AUTHOR INFORMATION

Corresponding Author

*(T.B.) E-mail till.biskup@physchem.uni-freiburg.de; Ph +49 (0)761 20367801; Fax +49 (0)761 2036222.

ORCID

Michael Sommer: 0000-0002-2377-5998

Till Biskup: 0000-0003-2913-0004

Present Address

M.S.: Lehrstuhl Polymerchemie, Technische Universität Chemnitz, Straße der Nationen 62, 09111 Chemnitz, Germany.

Notes

The authors declare no competing financial interest.

■ ACKNOWLEDGMENTS

The authors thank the German Research Foundation (DFG, Grant BI-1249/3-1 to T.B., SPP1355 to M.S., and IRTG Soft Matter Science 1645, Project SO-1213/8-1 to M.S.) and Albert-Ludwigs-Universität Freiburg (Innovationsfonds Forschung to T.B. and M.S.) for financial support and S. Weber for continuous support.

■ REFERENCES

(1) Forrest, S. R. Excitons and the lifetime of organic semiconductor devices. *Philos. Trans. R. Soc., A* **2015**, *373*, 20140320.

(2) Darling, S. B.; You, F. The case for organic photovoltaics. *RSC Adv.* **2013**, *3*, 17633−17648.

(3) Yeh, N.; Yeh, P. Organic solar cells: their developments and potentials. *Renewable Sustainable Energy Rev.* **2013**, *21*, 421−431.

(4) Facchetti, A. Seminconductors for organic transistors. *Mater. Today* **2007**, *10*, 28−37.

(5) Janata, J.; Josowicz, M. Conducting polymers in electronic chemical sensors. *Nat. Mater.* **2003**, *2*, 19−24.

(6) Katz, H. E.; Huang, J. Thin-film organic electronic devices. *Annu. Rev. Mater. Res.* **2009**, *39*, 71−92.

(7) Jackson, N. E.; Savoie, B. M.; Marks, T. J.; Chen, L. X.; Ratner, M. A. The next breakthrough for organic photovoltaics? *J. Phys. Chem. Lett.* **2015**, *6*, 77−84.

(8) Scharber, M. C.; Mühlbacher, D.; Koppe, M.; Denk, P.; Waldauf, C.; Heeger, A. J.; Brabec, C. J. Design rules for donors in bulk-heterojunction solar cells—towards 10% energy-conversion efficiency. *Adv. Mater.* **2006**, *18*, 789−794.

(9) Forbes, M. D.; Jarocha, L. E.; Sim, S.; Tarasov, V. F. Time-resolved electron paramagnetic resonance spectroscopy: history, technique, and application to supramolecular and macromolecular chemistry. *Adv. Phys. Org. Chem.* **2013**, *47*, 1−83.

(10) Biskup, T. Time-resolved EPR of radical pair intermediates in cryptochromes. *Mol. Phys.* **2013**, *111*, 3698−3703.

(11) Biskup, T.; Sommer, M.; Rein, S.; Meyer, D. L.; Kohlstädt, M.; Würfel, U.; Weber, S. Ordering of PCDTBT revealed by time-resolved electron paramagnetic resonance spectroscopy of its triplet excitons. *Angew. Chem., Int. Ed.* **2015**, *54*, 7707−7710.

(12) Meyer, D. L.; Lombeck, F.; Huettner, S.; Sommer, M.; Biskup, T. Direct S_0→T excitation of a conjugated polymer repeat unit: unusual spin-forbidden transitions probed by time-resolved electron paramagnetic resonance spectroscopy. *J. Phys. Chem. Lett.* **2017**, *8*, 1677−1682.

(13) Meyer, D. L.; Matsidik, R.; Huettner, S.; Sommer, M.; Biskup, T. Solvent-mediated aggregate formation of PNDIT2: Decreasing the available conformational subspace by introducing locally highly ordered domains. *Phys. Chem. Chem. Phys.* **2018**, *20*, 2716−2723.

(14) Behrends, J.; Sperlich, A.; Schnegg, A.; Biskup, T.; Teutloff, C.; Lips, K.; Dyakonov, V.; Bittl, R. Direct detection of photoinduced charge transfer complexes in polymer fullerene blends. *Phys. Rev. B: Condens. Matter Mater. Phys.* **2012**, *85*, 125206.

(15) Meyer, D. L.; Matsidik, R.; Sommer, M.; Biskup, T. Electronic structure trumps planarity: Unexpected narrow exciton delocalisation in PNDIT2 revealed by time-resolved EPR spectroscopy. *Adv. Electron. Mater.* **2018**, *4*, 1700385.

(16) Blouin, N.; Michaud, A.; Leclerc, M. A low-bandgap poly(2,7-carbazole) derivative for use in high-performance solar cells. *Adv. Mater.* **2007**, *19*, 2295−2300.

(17) Blouin, N.; Michaud, A.; Gendron, D.; Wakim, S.; Blair, E.; Neagu-Plesu, R.; Belletête, M.; Durocher, G.; Tao, Y.; Leclerc, M. Toward a rational design of poly(2,7-carbazole) derivatives for solar cells. *J. Am. Chem. Soc.* **2008**, *130*, 732−742.

(18) Park, S. H.; Roy, A.; Beaupré, S.; Cho, S.; Coates, N.; Moon, J. S.; Moses, D.; Leclerc, M.; Lee, K.; Heeger, A. J. Bulk heterojunction solar cells with internal quantum efficiency approaching 100%. *Nat. Photonics* **2009**, *3*, 297−303.

(19) Cho, S.; Seo, J. H.; Park, S. H.; Beaupré, S.; Leclerc, M.; Heeger, A. J. A thermally stable semiconducting polymer. *Adv. Mater.* **2010**, *22*, 1253−1257.

(20) Sun, Y.; Takacs, C. J.; Cowan, S. R.; Seo, J. H.; Gong, X.; Roy, A.; Heeger, A. J. Efficient, air-stable bulk heterojunction polymer solar cells using MoO_x as the anode interfacial layer. *Adv. Mater.* **2011**, *23*, 2226−2230.

(21) Peters, C. H.; Sachs-Quintana, I. T.; Kastrop, J. P.; Beaupré, S.; Leclerc, M.; McGehee, M. D. High efficiency polymer solar cells with long operating lifetimes. *Adv. Energy Mater.* **2011**, *1*, 491−494.

(22) Kong, J.; Song, S.; Yoo, M.; Lee, G. Y.; Kwon, O.; Park, J. K.; Back, H.; Kim, G.; Lee, S. H.; Suh, H.; Lee, K. Long-term stable polymer solar cells with significantly reduced burn-in loss. *Nat. Commun.* **2014**, *5*, 5688.

(23) Beaupré, S.; Leclerc, M. PCDTBT: en route for low cost plastic solar cells. *J. Mater. Chem. A* **2013**, *1*, 11097−11105.

(24) Banerji, N.; Gagnon, E.; Morgantini, P.-Y.; Valouch, S.; Mohebbi, A. R.; Seo, J.-H.; Leclerc, M.; Heeger, A. J. Breaking down the problem: optical transitions, electronic structure, and photoconductivity in conjugated polymer PCDTBT and in its separate building blocks. *J. Phys. Chem. C* **2012**, *116*, 11456−11469.

(25) Risko, C.; McGehee, M. D.; Brédas, J.-L. A quantum-chemical perspective into low optical-bandgap polymers for highly-efficient organic solar cells. *Chem. Sci.* **2011**, *2*, 1200−1218.

(26) Franco, F., Jr. Computational study on the structural and optoelectronic properties of a cabazole-benzothiadiazole based conjugated oligomer with various alkyl side-chain lengths. *Mol. Simul.* **2017**, *43*, 222−227.

(27) Niklas, J.; Beaupré, S.; Leclerc, M.; Xu, T.; Yu, L.; Sperlich, A.; Dyakonov, V.; Poluektov, O. G. Photoinduced dynamics of charge separation: from photosynthesis to polymer−fullerene bulk heterojunctions. *J. Phys. Chem. B* **2015**, *119*, 7407−7416.

(28) Bennati, M.; Grupp, A.; Mehring, M.; Bäuerle, P. Pulsed EPR spectroscopy of the photoexcited triplet states of thiophene oligomers in frozen solution. *J. Phys. Chem.* **1996**, *100*, 2849−2853.

(29) Sperlich, A.; Kraus, H.; Deibel, C.; Blok, H.; Schmidt, J.; Dyakonov, V. Reversible and irreversible interactions of poly(3-hexylthiophene) with oxygen studied by spin-sensitive methods. *J. Phys. Chem. B* **2011**, *115*, 13513−13518.

(30) Bhatta, R. S.; Tsige, M. Understanding structural and electronic properties of dithienyl benzothiadiazole and its complex with C70. *Polymer* **2015**, *75*, 73−77.

(31) Nielsen, C. B.; White, A. J. P.; McCulloch, I. Effect of fluorination of 2,1,3-benzothiadiazole. *J. Org. Chem.* **2015**, *80*, 5045−5048.

(32) Kim, J.; Kwon, Y. S.; Shin, W. S.; Moon, S.-J.; Park, T. Carbazole-based copolymers: effects of conjugation breaks and steric hindrance. *Macromolecules* **2011**, *44*, 1909−1919.

(33) Beiley, Z. M.; Hoke, E. T.; Noriega, R.; Dacuña, J.; Burkhard, G. F.; Bartelt, J. A.; Salleo, A.; Toney, M. F.; McGehee, M. D. Morphology-dependent trap formation in high performance polymer bulk heterojunction solar cells. *Adv. Energy Mater.* **2011**, *1*, 954−962.

(34) Lu, X.; Hlaing, H.; Germack, D. S.; Peet, J.; Jo, W. H.; Andrienko, D.; Kremer, K.; Ocko, B. M. Bilayer order in a polycarbazole-conjugated polymer. *Nat. Commun.* **2012**, *3*, 795.

(35) Bennati, M.; Németh, K.; Surján, P. R.; Mehring, M. Zero-field-splitting and π-electron spin densities in the lowest excited triplet state of oligothiophenes. *J. Chem. Phys.* **1996**, *105*, 4441−4447.

(36) Aguirre, A.; Gast, P.; Orlinskii, S.; Akimoto, I.; Groenen, E. J. J.; El Mkami, H.; Goovaerts, E.; Van Doorslaer, S. Multifrequency EPR analysis of the positive polaron in I_2-doped poly(3-hexylthiophene) and in poly[2-methoxy-5-(3,7-dimethyloctyloxy)]-1,4-phenylenevinylene. *Phys. Chem. Chem. Phys.* **2008**, *10*, 7129−7138.

(37) Tait, C. E.; Neuhaus, P.; Anderson, H. L.; Timmel, C. R. Triplet state delocalization in a conjugated porphyrin dimer probed by transient electron paramagnetic resonance techniques. *J. Am. Chem. Soc.* **2015**, *137*, 6670−6679.

(38) Gu, C.; Hu, W.; Yao, J.; Fu, H. Naphthalenediimide-benzothiadiazole copolymer semiconductors: rational molecular design for air-stable ambipolar charge transport. *Chem. Mater.* **2013**, *25*, 2178−2183.

(39) Rieger, R.; Beckmann, D.; Mavrinskiy, A.; Kastler, M.; Müllen, K. Backbone curvature in polythiophenes. *Chem. Mater.* **2010**, *22*, 5314−5318.

(40) Wang, H.-W.; Pentzer, E.; Emrick, T.; Russell, T. P. Preparation of low band gap fibrillar structures by solvent-induced crystallization. *ACS Macro Lett.* **2014**, *3*, 30−34.

(41) Lombeck, F.; Marx, F.; Strassel, K.; Kunz, S.; Lienert, C.; Komber, H.; Friend, R.; Sommer, M. To branch or not to branch: C−H selectivity of thiophene-based donor−acceptor−donor monomers in direct arylation polycondensation exemplified by PCDTBT. *Polym. Chem.* **2017**, *8*, 4738−4745.

(42) Stoll, S.; Schweiger, A. EasySpin, a comprehensive software package for spectral simulation and analysis in EPR. *J. Magn. Reson.* **2006**, *178*, 42−55.

(43) Neese, F. The ORCA program package. *Wiley Interdiscip. Rev.-Comput. Mol. Sci.* **2012**, *2*, 73−78.

(44) Becke, A. D. Density-functional exchange−energy approximation with correct asymptotic behavior. *Phys. Rev. A: At., Mol., Opt. Phys.* **1988**, *38*, 3098−3100.

(45) Perdew, J. P. Density-functional approximation for the correlation energy of the inhomogeneous electron gas. *Phys. Rev. B: Condens. Matter Mater. Phys.* **1986**, *33*, 8822−8824.

(46) Becke, A. D. Density-functional thermochemistry. III. The role of exact exchange. *J. Chem. Phys.* **1993**, *98*, 5648−5652.

(47) Lee, C.; Yang, W.; Parr, R. G. Development of the Colle-Salvetti correlation-energy formula into a functional of the electron density. *Phys. Rev. B: Condens. Matter Mater. Phys.* **1988**, *37*, 785−789.

(48) Weigend, F.; Ahlrichs, R. Balanced basis sets of split valence, triple zeta valence and quadruple zeta valence quality for H to Rn: Design and assessment of accuracy. *Phys. Chem. Chem. Phys.* **2005**, *7*, 3297−3305.

(49) Petersson, G. A.; Bennett, A.; Tensfeldt, T. G.; Al-Laham, M. A.; Shirley, W. A.; Mantzaris, J. A complete basis set model chemistry. I. The total energies of closed-shell atoms and hydrides of the first-row elements. *J. Chem. Phys.* **1988**, *89*, 2193−2218.

(50) Petersson, G. A.; Al-Laham, M. A. A complete basis set model chemistry. II. Open-shell systems and the total energies of the first-row atoms. *J. Chem. Phys.* **1991**, *94*, 6081−6090.

(51) Sinnecker, S.; Rajendran, A.; Klamt, A.; Diedenhofen, M.; Neese, F. Calculation of solvent shifts on electronic g-tensors with the conductor-like screening model (COSMO) and its self-consistent generalization to real solvents (direct COSMO-RS). *J. Phys. Chem. A* **2006**, *110*, 2235−2245.

(52) Hanwell, M. D.; Curtis, D. E.; Lonie, D. C.; Vandermeersch, T.; Zurek, E.; Hutchison, G. R. Avogadro: an advanced semantic chemical editor, visualization, and analysis platform. *J. Cheminf.* **2012**, *4*, 17.

(53) Pettersen, E. F.; Goddard, T. D.; Huang, C. C.; Couch, G. S.; Greenblatt, D. M.; Meng, E. C.; Ferrin, T. E. UCSF Chimera—A visualization system for exploratory research and analysis. *J. Comput. Chem.* **2004**, *25*, 1605−1612.

TBT entirely dominates the electronic structure of the conjugated copolymer PCDTBT: Insights from time-resolved electron paramagnetic resonance spectroscopy

— Supporting Information —

Clemens Matt, Deborah L. Meyer, Florian Lombeck, Michael Sommer, and Till Biskup[*]

Contents

---

[*] till.biskup@physchem.uni-freiburg.de

EPR Instrumentation

TREPR spectroscopy with a time resolution of up to 10 ns allows for real-time observation, *e.g.*, of short-lived radical-pair and triplet states generated by pulsed laser excitation. In contrast to conventional continuous-wave EPR spectroscopy, which usually involves magnetic-field modulation to improve the signal-to-noise ratio, TREPR is recorded in a high-bandwidth direct-detection mode, so as not to constrain the time resolution of the experiment. Consequently, positive and negative signal amplitudes in TREPR correspond to enhanced absorptive (A) and emissive (E) electron-spin polarisations of the EPR transitions, respectively.

All TREPR experiments were performed at 80 K using a commercial EPR spectrometer (Bruker ESP380E) in conjunction with a Bruker microwave bridge (ER 046 MRT) equipped with a low-noise high-bandwidth video amplifier. The sample was placed in a synthetic-quartz (Suprasil) sample tube (3 mm inner diameter) and irradiated in a dielectric-ring resonator (Bruker ER 4118X-MD5), which was immersed in a helium gas-flow cryostat (Oxford CF-935) cooled with liquid nitrogen. The temperature was regulated to ±0.1 K by a temperature controller (Oxford ITC-503). The time resolution of the experimental setup was in the 10 ns range. A microwave frequency counter (Hewlett-Packard HP 5352B) was used to monitor the microwave frequency.

Optical excitation at the respective wavelengths was carried out with an optical parametric oscillator (OPO) system (Opta BBO-355-vis/IR) pumped by an Nd:YAG laser (Spectra Physics, Quanta Ray GCR 190-10) with a pulse width of approximately 6 ns, and a pulse energy of 1 mJ. The repetition rate of the laser was set to 10 Hz. A transient recorder (LeCroy 9354A) with a digitizing rate of 2 ns/11 bit was used to acquire the time-dependent EPR signal. To eliminate the background signal induced by the laser entering the EPR cavity, TREPR signals were accumulated at off-resonance magnetic-field positions (background) and subtracted from those recorded on-resonance. This background signal is completely independent in its shape from both, laser wavelength and magnetic field, and normally long-lived compared to the detected spin-polarised EPR signal. Background subtraction was performed directly in the transient recorder and a background signal repeatedly recorded after each tenth time trace of the experimental data.

Further experimental parameters (except where explicity given) are as follows: Microwave frequency, 9.700 GHz, microwave power: 2 mW (20 dB attenuation, source power 200 mW), frequency-mixer detection, video amplifier set to 42 dB amplification and 25 MHz bandwidth, between 850 and 1400 averages per point.

TREPR spectra of triplet states

As TREPR spectra of spin-polarised triplet states of organic molecules recorded at X-band frequencies and magnetic fields are normally dominated by the zero-field splitting (ZFS) interaction, the hamilton operator used to describe the system reduces dramatically. The only contributions that need to be taken into account are the Hamilton operator for the Zeeman interaction, $\mathcal{H}_{\mathrm{EZ}}$, and the one for the ZFS interaction, $\mathcal{H}_{\mathrm{ZFS}}$:

$$\mathcal{H} = \mathcal{H}_{\mathrm{EZ}} + \mathcal{H}_{\mathrm{ZFS}} = \mathbf{g}\mu_{\mathrm{B}}\vec{S}\vec{B} + \vec{S}\mathbf{D}\vec{S}. \tag{S1}$$

All other contributions can be considered as small perturbations that can be accounted for using (inhomogeneous) line broadening.

The $\mathbf{D}$ tensor in its principal axis system is given to

$$\mathbf{D} = \begin{pmatrix} -\frac{1}{3}D + E & 0 & 0 \\ 0 & -\frac{1}{3}D - E & 0 \\ 0 & 0 & \frac{2}{3}D \end{pmatrix} \tag{S2}$$

where D and E are the zero-field-splitting parameters that can be directly read out from the experimental spectra (cf. Fig. S1). Note that D and E are defined such in the simulation routine used that the relation $|E| \leq |D|/3$ always holds.

Spectral simulations of TREPR spectra of triplet states

All simulations of triplet spectra have been performed using the EasySpin software package [1] available for MATLAB® (MathWorks), and here the routine `pepper`. Parameters included were the $\mathbf{g}$ and $\mathbf{D}$ tensor and the triplet sublevel populations (in zero field). Line broadening (Γ) was included using a combination of Lorentzian (Γ_{L}) and Gaussian (Γ_{G}) lines. For all simulations, the $\mathbf{g}$ tensor was assumed to be isotropic, with $g_{\mathrm{iso}} = 2.002$, and the population p_1 was set to zero. This left the parameters D and E of the zero-field splitting tensor $\mathbf{D}$, the populations p_2 and p_3, and the two line widths Γ_{L} and Γ_{G} as the only free parameters that were adjusted. In the case of NDI the parameters E of the zero-field splitting tensor $\mathbf{D}$ was set two zero and was not adjusted by a fitting process.

Fitting of the spectral simulations to the experimental data was done with the routine `lsqcurvefit` from the MATLAB® Optimization Toolbox™ using the trust-region-reflective least squares algorithm.

The nonlinear least-square solver finds the m coefficients $\vec{a}$ that solve the problem

$$\min_{\vec{a}} \sum_i (f(x_i;\vec{a}) - y_i)^2 \tag{S3}$$

with y_i being the measured data and $f(x_i;\vec{a})$ the fitting function $f : \mathbb{R}^m \to \mathbb{R}^n$ with the same size n as the measured data y_i

Error estimation of the fitting parameters was carried out by using the Jacobian matrix $\mathbf{J}$. J_{ij} is the partial derivative of the fitting function $f(x_i;\vec{a})$ with respect to a_j at the solution a_0.

$$J_{ij}(\vec{a}_0) := \left(\frac{\partial f(x_i;\vec{a})}{\partial a_j}(\vec{a}_0)\right)_{i=1\ldots n, j=1\ldots m} \tag{S4}$$

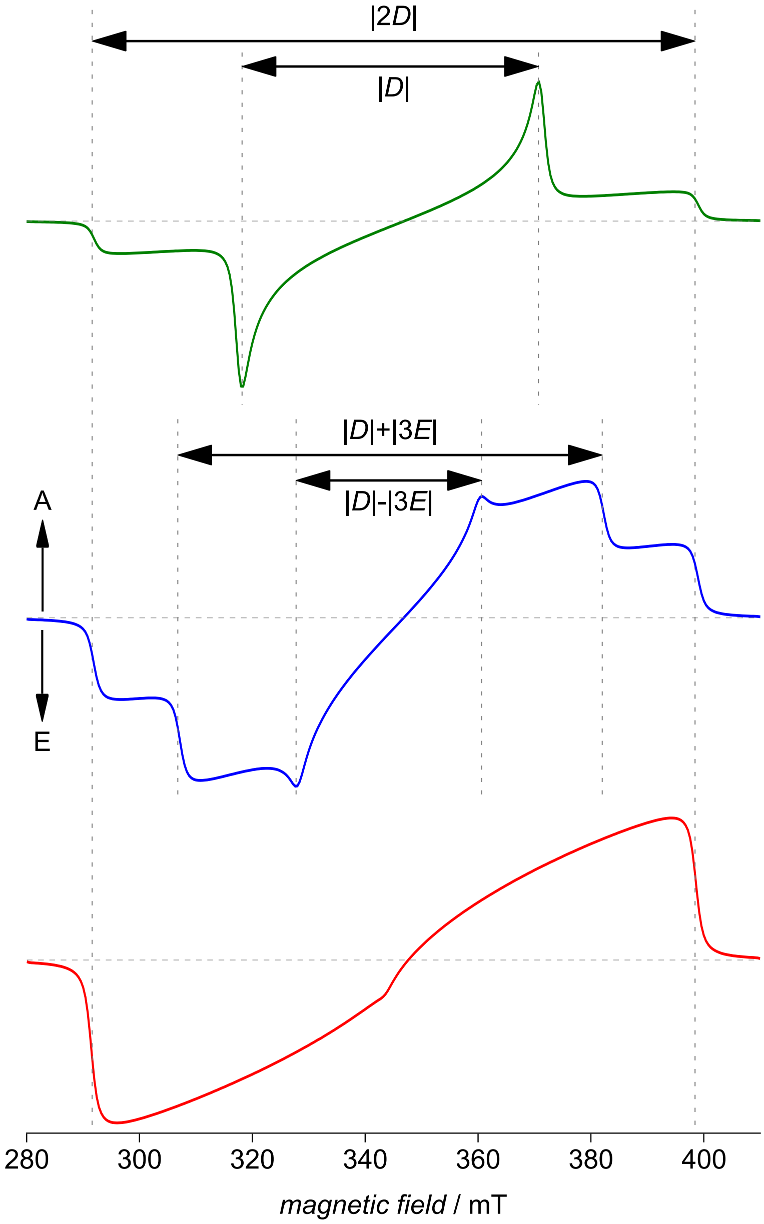

Figure S1: Characteristics of TREPR spectra of (photo-generated) triplet states. Three characteristic situations for the ratio of the two parameters D and E of the ZFS tensor are depicted here: the fully axial case (top, green), an intermediate case (blue, centre) and a fully rhombic case (red, bottom). Spectra were calculated using EasySpin. [2] The zero-field populations $p_{1,2,3}$ of the three triplet sublevels are far from thermal equilibrium, due to optical excitation and the inherent anisotropy of the intersystem crossing processes. Therefore, signals consist of both, absorptive (A) and emissive (E) contributions.

$$\mathbf{J}(\vec{a}_0) = \begin{pmatrix} \frac{\partial f(x_1;\vec{a})}{\partial a_1}(\vec{a}_0) & ... & \frac{\partial f(x_1;\vec{a})}{\partial a_m}(\vec{a}_0) \\ ... & & \\ \frac{\partial f(x_n;\vec{a})}{\partial a_1}(\vec{a}_0) & ... & \frac{\partial f(x_n;\vec{a})}{\partial a_m}(\vec{a}_0) \end{pmatrix} \tag{S5}$$

The variances of the coefficients a_j are given by the diagonal elements of the covariance matrix, $\mathbf{C}$, i.e. $\sigma_{a_j}^2 = C_{jj}$, where $\mathbf{C}$ is the inverse of the matrix $\mathbf{H}$, variously referred to as the curvature or Hessian matrix.

The Hessian matrix was approximated by a series expansion, which is terminated after the first rank:

$$H_{jk} = \frac{1}{2}\frac{\partial^2 \chi^2(\vec{a})}{\partial a_j \partial a_k} \approx \sum_{i=1}^{n} \frac{1}{\sigma_i^2} \frac{\partial f(x_i;\vec{a})}{\partial a_j} \frac{\partial f(x_i;\vec{a})}{\partial a_k}$$

Hence the Jacobian matrix can be used to approximate the Hessian if σ_i^2 is chosen to be equal for all points,

$$\mathbf{H} \approx \frac{1}{\sigma_i^2}\, \mathbf{J}^T \cdot \mathbf{J}. \tag{S6}$$

To speed up calculation time for the matrix product $\mathbf{J}^T \cdot \mathbf{J}$, an economy-size QR decomposition of $\mathbf{J}$ was carried out, reducing the dimension of $\mathbf{R}$ to the size of $\vec{a}$:

$$\mathbf{J} = \mathbf{Q} \cdot \mathbf{R}. \tag{S7}$$

In the following matrix multiplication, $\mathbf{Q}$ vanishes by multiplication with $\mathbf{Q}^T$:

$$(\mathbf{J}^T \cdot \mathbf{J})^{-1} = (\mathbf{R}^T \cdot \mathbf{R})^{-1} = \mathbf{R}^{-1} \cdot (\mathbf{R}^T)^{-1} = \mathbf{R}^{-1} \cdot (\mathbf{R}^{-1})^T \tag{S8}$$

In MATLAB®, this implementation leads to high computational speed and only minor numerical errors. The corresponding code would be as follows:

```
[~,R] = qr(jacobian,0);
```

The diagonal elements of the approximated $\mathbf{H}^{-1}$ can easily be calculated by element-wise squaring followed by summation over the rows of $\mathbf{R}$. Since σ_i^2 is chosen to be equal for all points, the errors for the fit parameters are given by:

```
stdDev = sqrt(variance * sum(inv(R).^2,2));
```

The fitting algorithm `lsqcurvefit` can optionally return the residuals as additional output argument, here termed `residuals`. Hence the variance of the residuals obtained as

```
variance = var(residuals);
```

was used as σ^2 for all points.

TREPR signal decay and triplet lifetime

The kinetics of TREPR signals of triplet states are rather complicated, involving spin relaxation, decay of spin polarisation, and decay of the actual triplet state, usually via intersystem crossing back into the singlet ground state. Hence, only a lower limit of the triplet lifetime can be extracted from the TREPR time profiles, based on the simple fact that regardless of all other processes, TREPR signals will only be observable as long as there exists a triplet state.

As can be seen from the full 2D datasets of all four compounds investigated in this study (Fig. S2), TREPR signals decay on the time scale of several microseconds. However, it is highly likely that this decay is dominated by the microwave power and other experimental parameters and that the actual triplet state lifetime extends well into tens or even hundreds of microseconds.

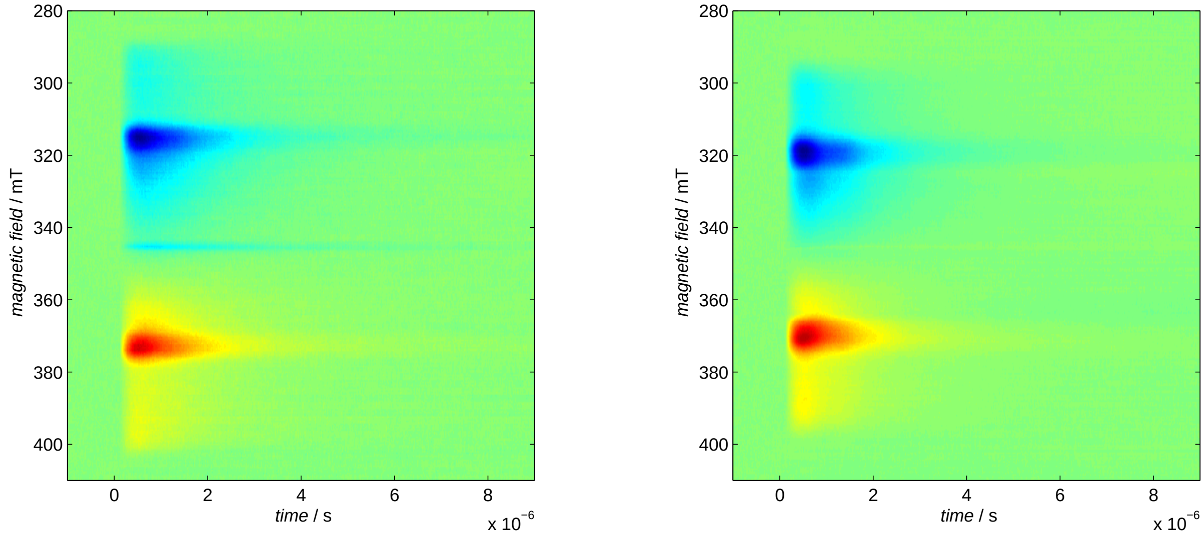

(a) TBT

(b) CbzTBT

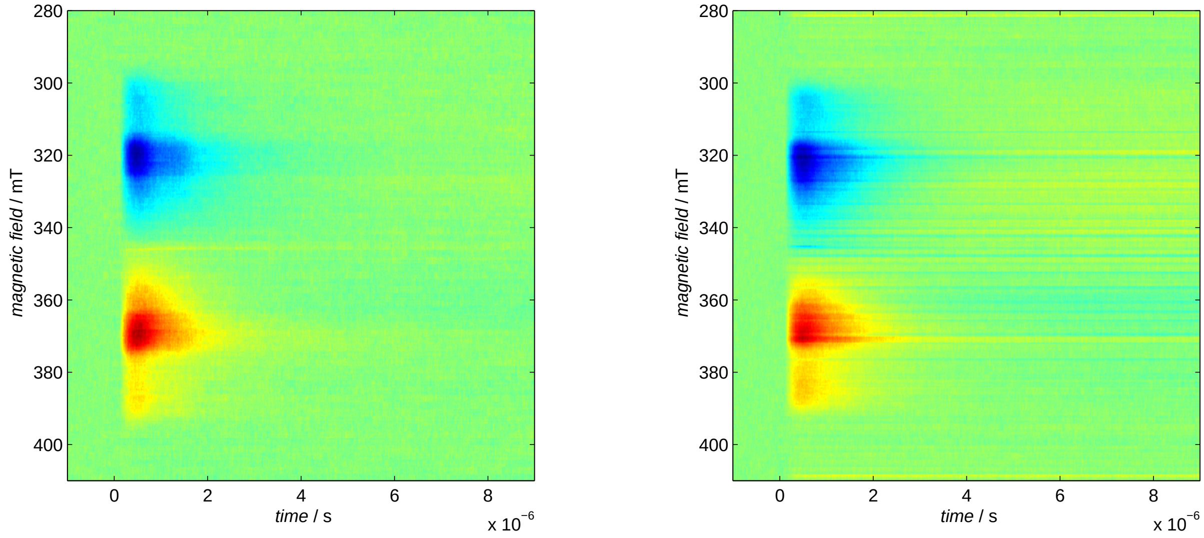

(c) CbzTBTCbz

(d) PCDTBT

Figure S2: Full 2D TREPR datasets of all compounds investigated in this study. Blue colour denotes emissive, red colour enhanced absorptive polarisation. For experimental details see main text.

Signal intensities of TREPR spectra

Normally, TREPR spectra cannot be analysed in a quantitative fashion, as signal intensity strongly depends on a series of experimental and device parameters. Even more fundamentally, these spectra consist of overlapping contributions of differently polarised (emissive or absorptive) lines that partially compensate each other, making the resulting signals particularly sensitive to even slight changes in the electronic structure of the investigated system. In case of an identical setup, the same operators and repeated experiments yielding comparable results, a relative comparison resulting in a general trend might be possible, particularly given the only modest changes in overall signal shape, as with the data presented here. However, no quantification of the triplet yield in terms of quantum efficiencies can be drawn from the TREPR data.

Temperature-dependent absorption spectra

To rule out effects of aggregation, temperature-dependent absorption spectra have been recorded for all substances investigated. The results are shown in Fig. S3. Due to the solvent, *o*-dichlorobenzene, not forming a transparent glass upon freezing, spectra could only be recorded until the solution froze out. As obvious from the spectra, none of the substances investigated showed any sign of aggregation under the conditions used here.

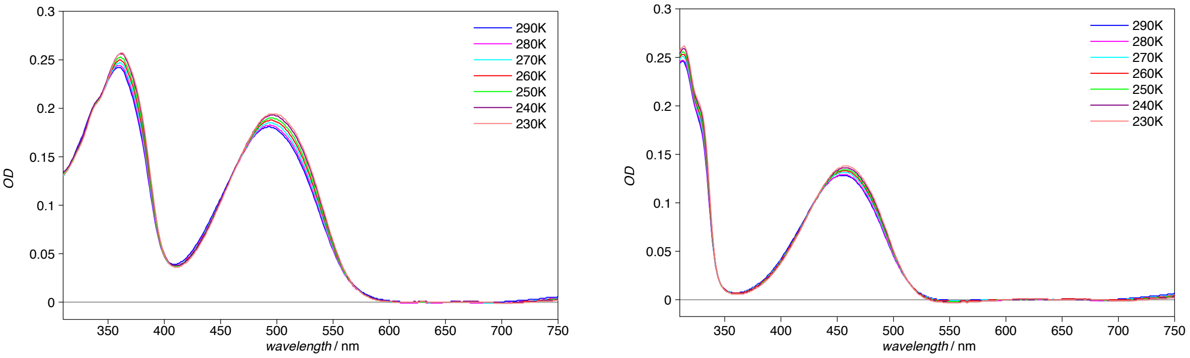

(a) TBT

(b) CbzTBT

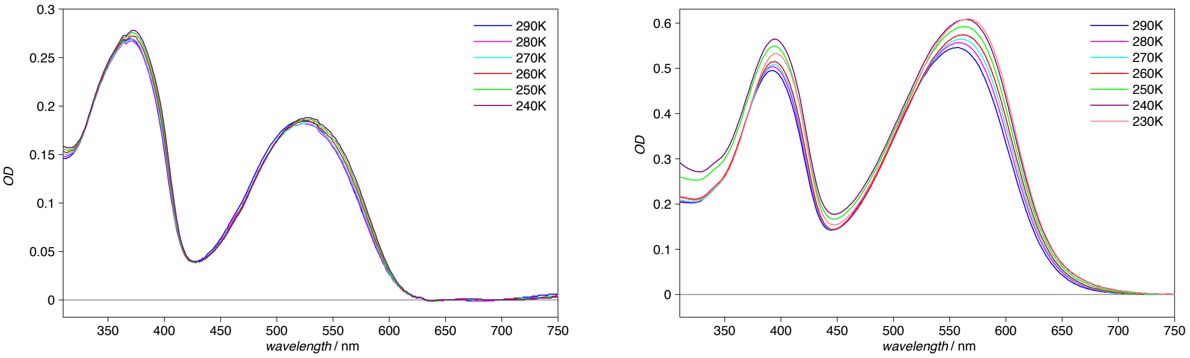

(c) CbzTBTCbz

(d) PCDTBT

Figure S3: Temperature-dependent absorption spectra of all compounds investigated in this study. Due to the solvent, *o*-dichlorobenzene, not forming a transparent glass upon freezing, spectra could only be recorded until the solution froze out.

Determining the angles between TBT and Cbz moieties

As the aromatic planes of the TBT and Cbz moieties can be twisted against each other in all three directions, the tilting cannot be ascribed fully by single dihedral angle between adjacent atoms. Hence, coordinate systems have been created in both aromatic planes and the angles between the x, y, and z axes compared to those of the planar structure.

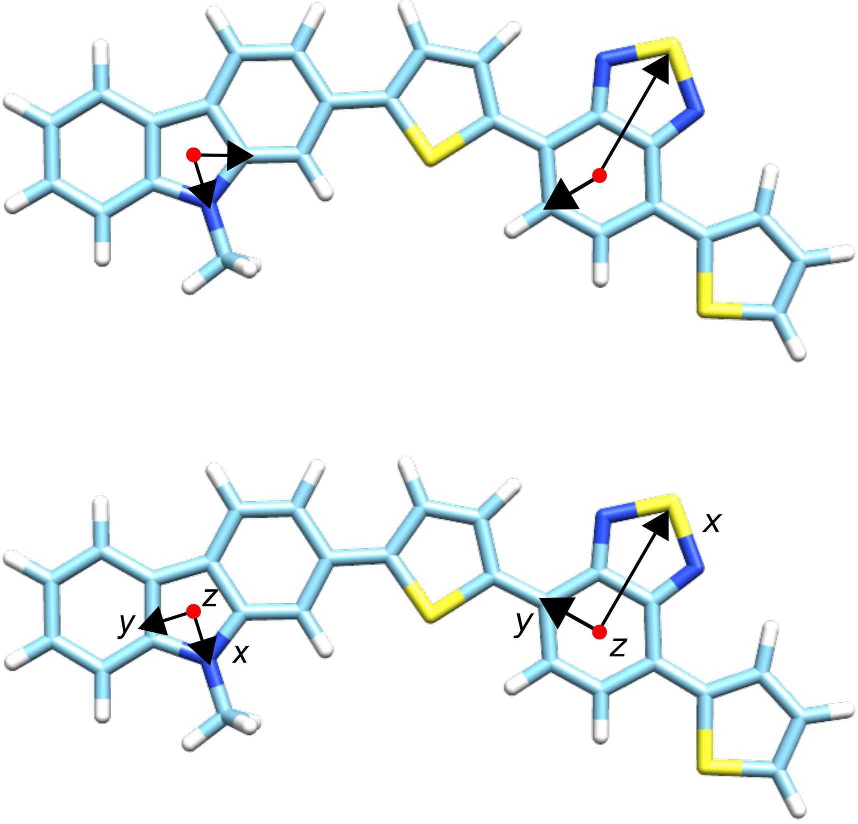

Figure S4: Illustration of constructing the vectors that have been used for determining the angles between TBT and Cbz moieties. The top panel shows the two vectors spanning the aromatic planes, whereas the complete coordinate systems in Cbz and TBT are shown in the bottom panel.

In a first step, the center of both, benzene and pyrroline rings have been calculated (red dot in Fig. S4) and the vectors from there to the S and N atom, respectively, created that form the x axis of the coordinate system. A second vector has been created pointing from the centre of the aromatic plane to one of the atoms in the aromatic plane to span this plane (Fig. S4, top). The cross product of these two vectors led to the z axis of the coordinate system. In the following, the cross product of the vectors for the x and z axis could be used to create the y axis and hence complete the coordinate system (Fig. S4, bottom).

As the cross product always generates one of two possible vectors being orthogonal to the two vectors multiplied, displaying all vectors was necessary to check that the correct vector has been found. If not, the two vectors for the cross product have to be swapped.

Table S1: Angles between the aromatic planes of Cbz and TBT moieties obtained from geometry optimisation in the triplet state. The Cbz and TBT moieties are in themselves pretty flat. Angles Angles are given in degrees and for the cis-trans configuration as shown in Fig. S5. Note the dramatic differences between BP86 and B3LYP, particularly for the polymer fragment.

	BP86/Def2-SVP	B3LYP/6–31G**
CbzTBT	1.1	1.9
CbzTBTCbz	0.3	0.8
	0.7	5.9
PCDTBT	1.0	13.8
	2.9	19.8
	1.4	11.7
	1.1	9.1
	0.5	10.1
	0.2	12.2
	1.0	17.7

For convenience, the angles for the cis-trans configuration given already in the main text are shown in Tab. S1 for both types of calculations performed, with BP86/Def2-SVP and B3LYP/6-31G**. As can be readily seen, geometries optimised using BP86/Def2-SVP are very flat, whereas particularly for the polymer, B3LYP/6-31G** predicts a twist in the backbone that seems not to be in line with our experimental results. For a detailed discussion, the reader is referred to the main text.

Quantitative analysis of spin density distributions

Whereas spin density plots on the optimised geometries of the molecules are very valuable to give an overall impression, they are less useful for a quantitative comparison.

ORCA normalises the calculated spin densities internally such that the sum of all spin densities equals to the number of spins involved. In case of a triplet state with two unpaired electron spins, this sum equals to two.

To calculate the relative amount of spin density on the TBT moiety, $r^{\mathrm{abs}}_{\mathrm{TBT}}(\mathrm{M})$, for all compounds, M, investigated, the spin density on the TBT moiety, $\rho_{\mathrm{TBT}}(\mathrm{M})$, has been divided by the spin density on the entire molecule, $\rho_{\mathrm{M}}(\mathrm{M})$ as follows:

$$r^{\mathrm{abs}}_{\mathrm{TBT}}(\mathrm{M}) = \frac{\sum |\rho_{\mathrm{TBT}}(\mathrm{M})|}{\sum |\rho_{\mathrm{M}}(\mathrm{M})|} \leq 1\,.$$

As spin densities can have positive and negative sign, the absolute values have been taken in this case, hence the notation r^{abs}. The resulting values can be found in Tab. S2 and graphically displayed in Fig. S5 and in Fig. S8.

To get further insight, spin densities have been compared for the TBT unit in each of the

Table S2: Relative amount of spin density on the TBT moiety as calculated with BP86 and B3LYP functionals. Note that due to omitting the two protons in TBT where the Cbz moieties are substituted in larger fragments, the relative amount of spin density on the TBT moiety does not amount to exactly one in case of the TBT molecule alone (first row).

	BP86/Def2-SVP	B3LYP/6–31G**
TBT	0.99	0.99
CbzTBT	0.82	0.83
CbzTBTCbz	0.71	0.73
PCDTBT	0.56	0.70

compounds in form of a histogram (Fig. S7). Therefore, spin densities of the TBT unit have to be normalised to the amount of spin density on the TBT moiety in the TBT compound, $\rho_{\mathrm{TBT}}(\mathrm{TBT})$, relative to the amount of spin density on the TBT moiety in the actual compound, $\rho_{\mathrm{TBT}}(\mathrm{M})$, and this time, the sign of the spin densities has to be taken into account:

$$r_{\mathrm{TBT}}(\mathrm{M}) = \frac{\sum \rho_{\mathrm{TBT}}(\mathrm{M})}{\sum \rho_{\mathrm{TBT}}(\mathrm{TBT})} \leq 1\,.$$

Note that, in our case, $\sum \rho_{\mathrm{TBT}}(\mathrm{TBT})$ does not amount to two, as one would naively expect, as the two protons present in TBT that are substituted successively in the larger compounds are not taken into account for calculating the ratio of the spin densities, but do possess some non-vanishing, although rather small, spin density. Hence this rather complicated way of calculating this ratio.

Having the two ratios of spin density on the TBT moiety as compared to the entire molecule at hand, we can proceed to calculate the correction factor $r_{\mathrm{corr}}(\mathrm{M})$ for the spin density values for the TBT moiety of a given compound:

$$r_{\mathrm{corr}}(\mathrm{M}) = \frac{r^{\mathrm{abs}}_{\mathrm{TBT}}(\mathrm{M})}{r_{\mathrm{TBT}}(\mathrm{M})}$$

and with this, the corrected spin density for the TBT moiety of a given compound amounts to:

$$\rho^{\mathrm{corr}}_{\mathrm{TBT}}(\mathrm{M}) = r_{\mathrm{corr}}(\mathrm{M}) \cdot \rho_{\mathrm{TBT}}(\mathrm{M})\,.$$

The values for $\rho^{\mathrm{corr}}_{\mathrm{TBT}}(\mathrm{M})$ for each of the atoms have been displayed in the respective histograms.

Comparison of calculations with BP86 and B3LYP

As mentioned in the main text, geometry optimisations and spin density calculations of all compounds investigated have been performed both, with BP86/Def2-SVP [2–4] and B3LYP/6–31G** [5–8] as functional and basis set, respectively, and the results compared with each other. For all calculations, ORCA 3.0.3 [9] has been used. The solvent has been accounted for by the COSMO model [10]. Initial geometries of the molecules were created using Avogadro 1.1.1 [11]. Spin density plots were created using UCSF Chimera 1.11.2 [12].

Geometry optimisations in triplet state

For all four compounds investigated, geometry optimisations of their respective triplet states have been performed. The two sets of calculations differ clearly in the degree of planarity of the resulting geometries, as can be readily seen from a side view parallel to the aromatic planes (Fig. S5). For actual numbers of the dihedral angles between adjacent aromatic planes of Cbz and TBT moieties, cf. Tab. S1.

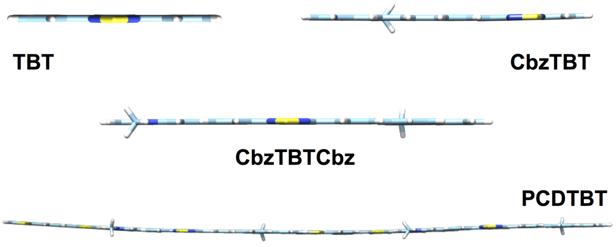

(a) BP86/Def2-SVP

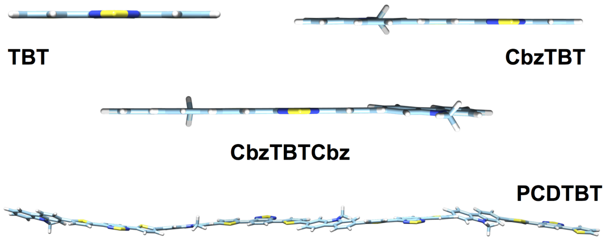

(b) B3LYP/6-31G**

Figure S5: Side-view of the optimised geometries of the triplet states of PCDTBT and its building blocks. Geometries have been optimised for the triplet state on the theory level BP86/Def2-SVP and B3LYP/6–31G**, respectively. For a view perpendicular to the aromatic plane, cf. Fig. S6. As obvious from this side-view, all molecules are rather flat for BP86/Def2-SVP, with dihedral angles between the aromatic planes of Cbz and TBT, respectively, close to zero, whereas B3LYP/6–31G** results in clear distortions. For actual values of these dihedral angles, cf. Tab. S1.

Whereas the geometries calculated using BP86/Def2-SVP are basically flat, for B3LYP/6–31G**, particularly the polymer fragment with $n = 4$ shows clear distortions with dihedral angles up to approx. 20%.

Spin density distributions

For all compounds investigated, after geometry optimisation in the triplet state the Mulliken spin density distribution has been calculated (cf. Fig. S6). Note that we have used different threshold levels for the spin density for the three building blocks on the one hand and the polymer fragment on the other hand, to highlight the spread of spin density in the latter including the two TBT units next to the central TBT unit carrying the large majority of the spin density.

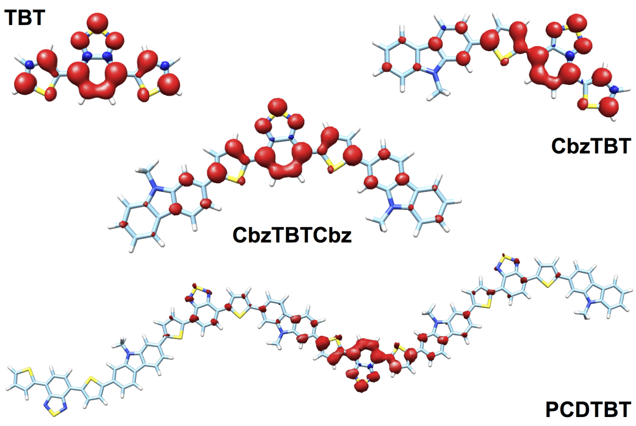

(a) BP86/Def2-SVP

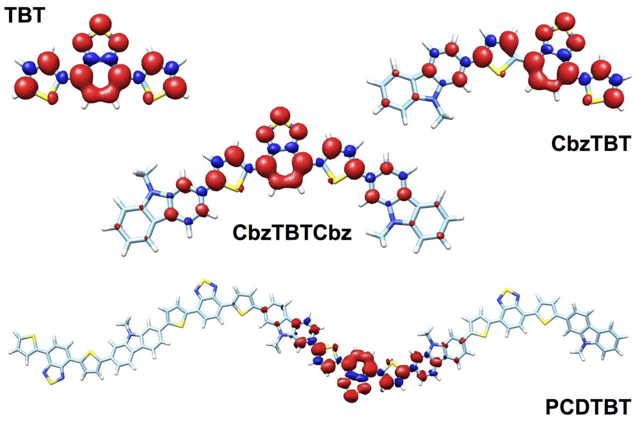

(b) B3LYP/6-31G**

Figure S6: Spin density distribution for the triplet states of PCDTBT and its building blocks. Geometries have been optimised for the triplet state on the theory level BP86/Def2-SVP and B3LYP/6–31G**, respectively, and spin densities displayed for a threshold level of ±0.002 (building blocks) and ±0.001 (PCDTBT). Red denotes positive and blue negative spin density.

Already from these pictures of the spin density as iso-surface on the geometries, one can see some differences, particularly for the polymer fragment with $n = 4$, showing less spin density outside the "core" CbzTBTCbz unit with the maximum of spin density located on the central TBT for B3LYP/6–31G** as compared to BP86/Def2-SVP. Besides that, we note that more intense negative spin density values are obtained for B3LYP/6–31G** as compared to BP86/Def2-SVP for all molecules.

Whereas these overview plots of the spin density give a very direct access to the overall picture, they are less useful to really quantify and compare the spin densities between fragments of different length.

Hence, we followed the approach layed out above to quantify the spin-density distribution of the triplet state and compare the values of the spin densities for each nucleus of the TBT moiety for the three building blocks and the polymer fragment with $n = 4$ (Figure S7).

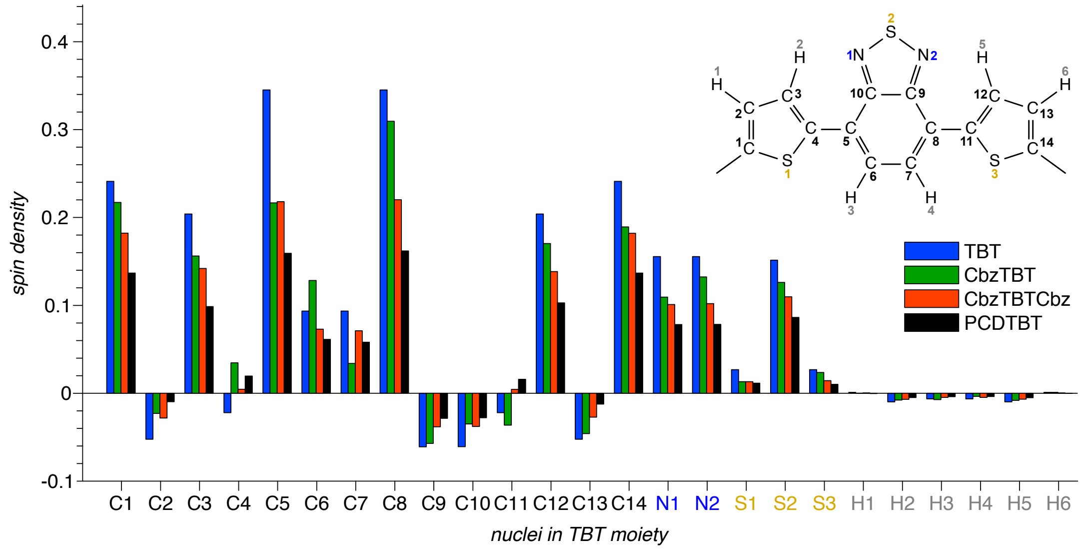

(a) BP86/Def2-SVP

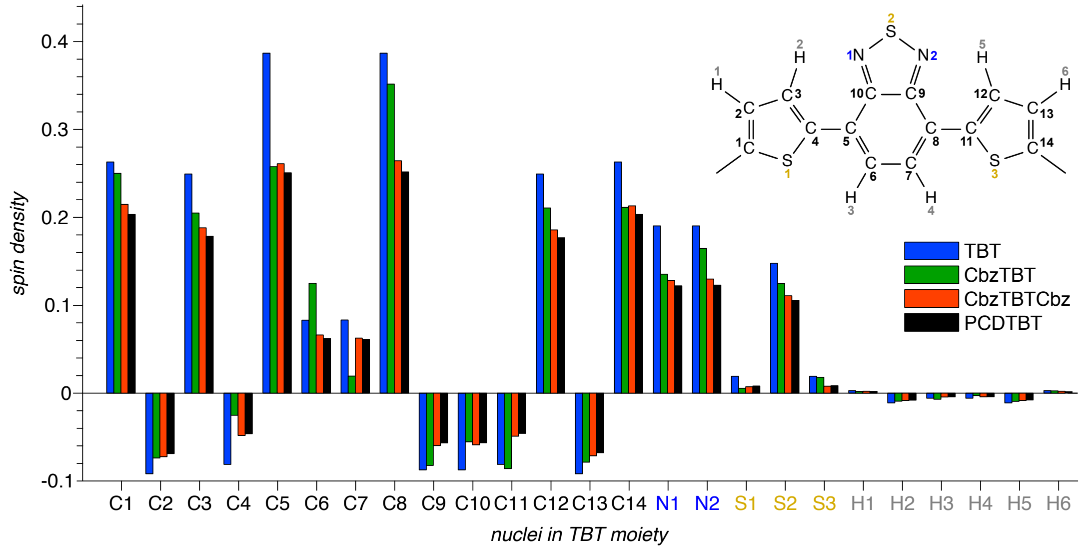

(b) B3LYP/6-31G**

Figure S7: Quantitative analysis of the spin density distribution for the triplet states of PCDTBT and its building blocks. Depicted are the values for the spin densities for each of the TBT atoms in the four fragments of different size shown in Fig. S5. The inset shows the numbering of the atoms used as axis labels.

Here again, clear differences are obvious for the calculations performed with BP86/Def2-SVP and those performed with B3LYP/6–31G**. The clear trend observed experimentally, namely an increase in delocalisation with increasing backbone length, is nicely reproduced by BP86/Def2-SVP, but not as well by B3LYP/6–31G**. This can readily be seen by comparing the spin density values of the different atoms of the TBT moieties for different fragment lengths in the histograms in Fig. S7. Here, again, the larger values for the negative spin densities obtained with B3LYP/6–31G** as compared to BP86/Def2-SVP can be seen.

To further help with comparing the spin density located on the TBT moiety for different fragment lengths, we plot the normalised spin density on TBT as a function of fragment length (Fig. S8). From this plot it is obvious that the spin density calculated using BP86/Def2-SVP nicely coincides with the experimental data obtained by TREPR spectroscopy, whereas this is not the case for B3LYP/6-31G**. Hence, BP86/Def2-SVP seems better suited for investigating spin densities and comparing the obtained values to experimental results on triplet exciton delocalisation at least for the polymer system investigated here.

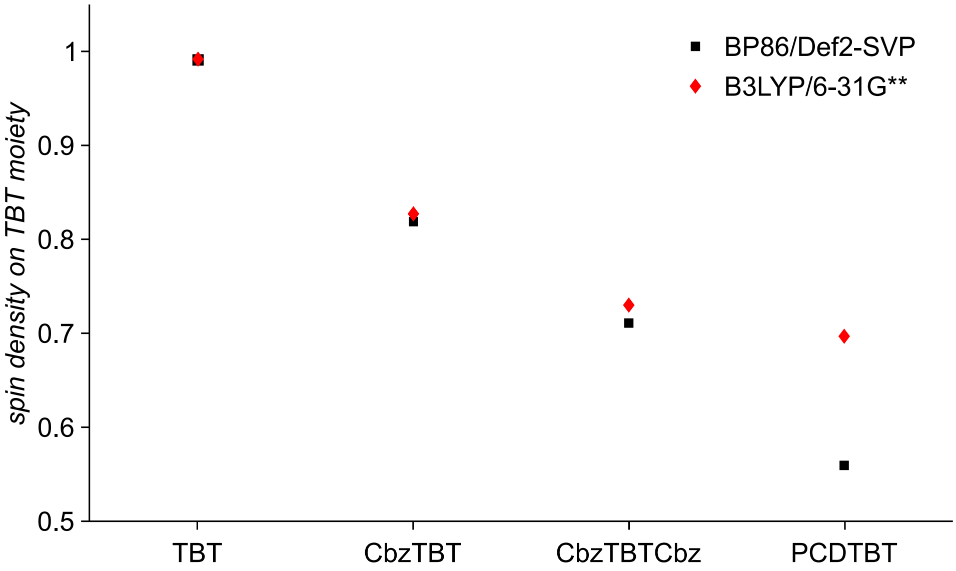

Figure S8: Relative amount of spin density on the TBT moiety as calculated with BP86 and B3LYP functionals. Whereas the spin density calculated using BP86/Def2-SVP nicely coincides with the experimental data obtained by TREPR spectroscopy, this is not the case for B3LYP/6-31G**.

TREPR signal of P3HT triplet state

As mentioned in the main text, P3HT shows as well triplet excitons upon illumination that have a comparable axiality ($|E|/|D| \approx 0.082$) compared with those of PCDTBT and its building blocks. Hence we show here the experimental data and a corresponding spectral simulation assuming a single triplet species for P3HT recorded under comparable conditions to the data for PCDTBT and its building blocks (cf. Fig. S9). For the simulation parameters used cf. Tab. S3.

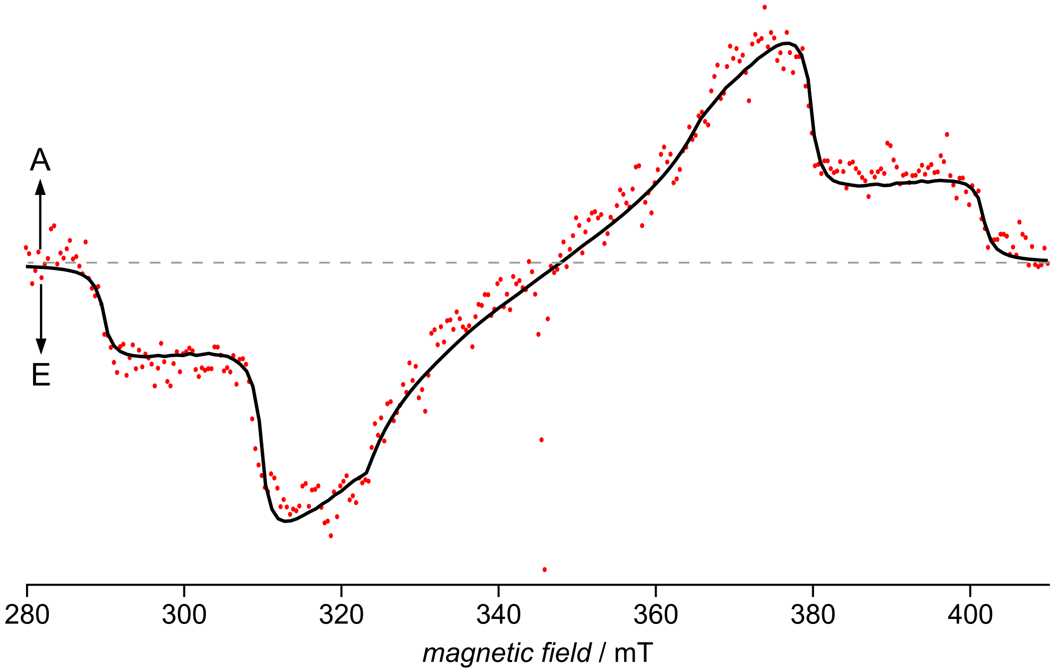

Figure S9: TREPR spectrum of P3HT together with a spectral simulation based on a single triplet exciton species and no partial orientation (full powder averaging). Experimental parameters: Microwave: 9.692 GHz, 2 mW; Video amplifier: 42 dB, 25 MHz bandwidth; 200 averages.

Table S3: Simulation parameters obtained by fitting the triplet spectrum of P3HT. The initial values for the zero-field-splitting parameters D and E were obtained graphically, the **g** tensor was assumed to be isotropic. For the line width, both Gaussian and Lorentzian linewidths are given.

g_x	g_y	g_z
2.002	2.002	2.002
p_1	p_2	p_3
0.317	0.335	0.348
D / MHz	E / MHz	Γ / mT
1569	129	1.0, 2.2

References

[1] Stefan Stoll and Arthur Schweiger. EasySpin, a comprehensive software package for spectral simulation and analysis in EPR. *J. Magn. Reson.*, 178:42–55, 2006.

[2] A. D. Becke. Density–functional exchange–energy approximation with correct asymptotic behavior. *Phys. Rev. A*, 38:3098–3100, 1988.

[3] John P. Perdew. Density–functional approximation for the correlation energy of the inhomogeneous electron gas. *Phys. Rev. B*, 33:8822–8824, 1986.

[4] Florian Weigend and Reinhart Ahlrichs. Balanced basis sets of split valence, triple zeta valence and quadruple zeta valence quality for H to Rn: Design and assessment of accuracy. *Phys. Chem. Chem. Phys.*, 7:3297–3305, 2005.

[5] Axel D. Becke. Density-functional thermochemistry. III. The role of exact exchange. *J. Chem. Phys.*, 98:5648–5652, 1993.

[6] Chengteh Lee, Weitao Yang, and Robert G. Parr. Development of the Colle-Salvetti correlation-energy formula into a functional of the electron density. *Phys. Rev. B*, 37:785–789, 1988.

[7] G. A. Petersson, Andrew Bennett, Thomas G. Tensfeldt, Mohammad A. Al-Laham, William A. Shirley, and John Mantzaris. A complete basis set model chemistry. I. The total energies of closed-shell atoms and hydrides of the first-row elements. *J. Chem. Phys.*, 89:2193–2218, 1988.

[8] G. A. Petersson and Mohammad A. Al-Laham. A complete basis set model chemistry. II. Open-shell systems and the total energies of the first-row atoms. *J. Chem. Phys.*, 94:6081–6090, 1991.

[9] Frank Neese. The ORCA program package. *Wiley Interdiscip. Rev.-Comput. Mol. Sci.*, 2:73–78, 2012.

[10] Sebastian Sinnecker, Arivazhagan Rajendran, Andreas Klamt, Michael Diedenhofen, and Frank Neese. Calculation of solvent shifts on electronic g-tensors with the conductor-like screening model (COSMO) and its self-consistent generalization to real solvents (direct COSMO-RS). *J. Phys. Chem. A*, 110:2235–2245, 2006.

[11] Marcus D. Hanwell, Donald E. Curtis, David C. Lonie, Tim Vandermeersch, Eva Zurek, and Geoffrey R. Hutchison. Avogadro: an advanced semantic chemical editor, visualization, and analysis platform. *J. Cheminformatics*, 4:17, 2012.

[12] Eric F. Pettersen, Thomas D. Goddard, Conrad C. Huang, Gregory S. Couch, Daniel M. Greenblatt, Elaine C. Meng, and Thomas E. Ferrin. UCSF Chimera—a visualization system for exploratory research and analysis. *J. Comput. Chem.*, 25:1605–1612, 2004.

5.2. Impact of Side Chains of Conjugated Polymers on Electronic Structure: A Case Study

Clemens Matt, Florian Lombeck, Michael Sommer and Till Biskup: Impact of Side Chains of Conjugated Polymers on Electronic Structure: A Case Study. *Polymers*, 11 (2019), pp. 870 (DOI: 10.3390/polym11050870)

Contributions of all authors:

Clemens Matt: conception and study design, data aquisition (DFT, TREPR and UV-VIS), data analysis, contributions to manuscript and manuscript review

Florian Lombeck: sample synthesis and manuscript review

Michael Sommer: conception and study design and manuscript review

Till Biskup: conception and design of study, data acquisition (TREPR and UV-VIS), data analysis, main contribution to the manuscript and manuscript review

polymers

MDPI

Article

Impact of Side Chains of Conjugated Polymers on Electronic Structure: A Case Study

Clemens Matt [1], **Florian Lombeck** [2], **Michael Sommer** [2,†] **and and Till Biskup** [1,*]

[1] Institut für Physikalische Chemie, Albert-Ludwigs-Universität Freiburg, Albertstraße 21, 79104 Freiburg, Germany; clemens.matt@physchem.uni-freiburg.de

[2] Institut für Makromolekulare Chemie, Albert-Ludwigs-Universität Freiburg, Stefan-Meier-Straße 31, 79104 Freiburg, Germany; Florian.Lombeck@Hahn-Schickard.de (F.L.); michael.sommer@chemie.tu-chemnitz.de (M.S.)

* Correspondence: till.biskup@physchem.uni-freiburg.de

† Current address: Institut für Chemie, Technische Universität Chemnitz, Straße der Nationen 62, 09111 Chemnitz, Germany.

Received: 28 February 2019; Accepted: 8 May 2019; Published: 13 May 2019

Abstract: Processing from solution is a crucial aspect of organic semiconductors, as it is at the heart of the promise of easy and inexpensive manufacturing of devices. Introducing alkyl side chains is an approach often used to increase solubility and enhance miscibility in blends. The influence of these side chains on the electronic structure, although highly important for a detailed understanding of the structure-function relationship of these materials, is still barely understood. Here, we use time-resolved electron paramagnetic resonance spectroscopy with its molecular resolution to investigate the role of alkyl side chains on the polymer PCDTBT and a series of its building blocks with increasing length. Comparing our results to the non-hexylated compounds allows us to distinguish four different factors determining exciton delocalization. Detailed quantum-chemical calculations (DFT) allows us to further interpret our spectroscopic data and to relate our findings to the molecular geometry. Alkylation generally leads to more localized excitons, most prominent only for the polymer. Furthermore, singlet excitons are more delocalized than the corresponding triplet excitons, despite the larger dihedral angles within the backbone found for the singlet-state geometries. Our results show TREPR spectroscopy of triplet excitons to be well suited for investigating crucial aspects of the structure-function relationship of conjugated polymers used as organic semiconductors on a molecular basis.

Keywords: side chains; electronic structure; triplet states; electron paramagnetic resonance; delocalization

1. Introduction

Semiconductors have revolutionized our way of life and are currently ubiquitous materials for various devices and applications. However, most of these devices still consist of inorganic compounds, mostly silicon. While robust, these inorganic semiconducting devices are rather inflexible and limit the possible fields of application. Organic semiconductors, i.e., semiconductors based on organic molecules, mostly conjugated polymers, are very promising candidates for dramatically changing the way we apply the devices built upon them [1–3]. The big advantages of organic semiconductors over their more conventional inorganic counterparts are their mechanical flexibility [4–7], simple and inexpensive processing from solution [8], and variability due to well-developed protocols of synthetic chemistry. This renders wearable electronics [9,10], as well as large-area electronic devices [11] and flexible displays [12] viable, to name just a few potential applications.

While organic semiconductors still lag behind their inorganic counterparts in many respects, they have gained considerable interest in both academia and industry [13–15] and are now even competitive in some areas of electronics [16,17]. Potential and real applications range from Organic Photovoltaics (OPV) [18,19], Organic Light-Emitting Diodes (OLEDs) [20], and Organic Field-Effect Transistors (OFETs) [21] to sensors [2,22]. Key for their successful application is a fundamental understanding of the structure-function relationship of these materials. For OPV materials, two key aspects have been identified that can be extended to other applications as well: morphology [23] and electronic structure [24]. Many different methods are available to probe the morphology of conjugated polymers, at least in films. Recently, we demonstrated (time-resolved) Electron Paramagnetic Resonance (EPR) spectroscopy [25–27] to be able to probe both film [28] and solution [29] morphology with molecular resolution. In contrast to morphology, direct access to the electronic structure of conjugated polymers is much more difficult to achieve. Spectroscopic tools with molecular resolution capable of directly probing the electronic structure of the polymer are of high demand.

Key to the simple and inexpensive manufacturing of organic semiconductor devices is solution processing of the components [30]. Hence, their solubility is of particular importance. To control both molecular weight and dispersity, premature precipitation of the polymer synthesized should be avoided. Introducing linear or branched alkyl side chains is an approach often followed to enhance solubility [31–36]. However, its potential impact on the electronic structure of the backbone is neither trivial nor well-understood. Generally, investigating the building blocks of increasing backbone length has been proven useful to gain deeper insight into the electronic structure of conjugated polymers [37–39]. In this study, we apply this approach to the hexylated version of the common copolymer PCDTBT (poly[*N*-9′-heptadecanyl-2,7-carbazole-*alt*-5,5-(4′,7′-di-2-thienyl-2′,1′,3′-benzothiadiazole)]) [40,41], investigating both the polymer hexPCDTBT, as well as three building blocks with increasing backbone length (Figure 1). The polymer repeat unit consists of a Carbazole (Cbz) moiety acting as Donor (D) and a hexylated dithienyl-benzothiadiazole (hexTBT) moiety serving as Acceptor (A). We note that hexTBT in itself is a push-pull system comprised of the central benzothiadiazole acceptor and the two flanking (hexylated) thiophene donors. For simplicity, we will refer to Cbz and hexTBT as Donor (D) and Acceptor (A) hereafter.

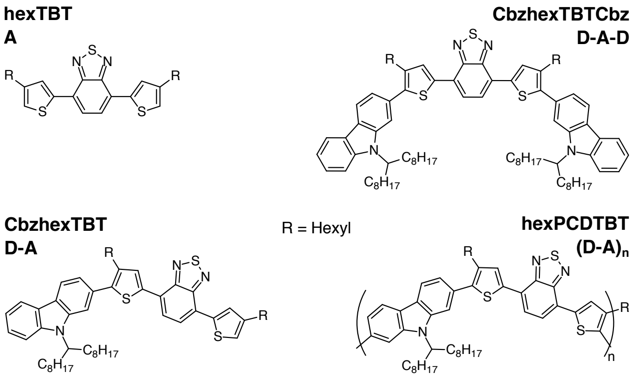

Figure 1. Chemical structure of hexPCDTBT and its building blocks. The polymer repeat unit Carbazole (Cbz)-hexTBT forms a push-pull system comprising a Carbazole (Cbz) as donor and a hexylated Dithienyl-Benzothiadiazole (TBT) unit as the acceptor, the latter being itself a push-pull system. For simplicity, the TBT acceptor unit will be abbreviated with "A" and the Cbz donor unit with "D" hereafter.

PCDTBT is well known for its high power conversion efficiencies up to 7–8% [42] combined with robustness and air-stability over a long time [43–47], but also for its tendency to form carbazole homocouplings [48]. Recently, we demonstrated this polymer to form rather ordered structures in drop-cast films [28]. This came quite to our surprise, as the polymer is known for its amorphous morphology [49], not readily forming crystals [50]. Furthermore, an overall face-on orientation with respect to the substrate was deduced, which is advantageous for charge carrier injection or extraction in OLED or OPV devices, respectively [51–54]. Additionally, we investigated the impact of side chains on the film morphology using a series of PCDTBT polymers with increasing degree of alkyl side chains, allowing us to distinguish between effects on electronic structure and morphology [55].

Introducing additional hexyl side chains at the TBT unit has been shown to increase backbone torsion and luminescence, effectively converting it from a material for photovoltaics to one for OLEDs [56]. Regarding the thermal properties, additional hexyl side chains reduce the glass transition temperature T_g from 127 °C (PCDTBT) to 93 °C for the fully-hexylated version hexPCDTBT. At the same time, a sometimes very weak melting point of PCDTBT at 235 °C vanishes upon hexylation [56]. Here, we combine synthetic chemistry giving access to a series of building blocks of different lengths with Time-Resolved EPR (TREPR) spectroscopy allowing for molecular resolution and detailed mapping of the electronic structure and extended quantum-chemical (DFT) calculations. Comparing our results on the hexylated molecules with those obtained earlier for the non-hexylated ones [39] allows us to map the influence of the additional alkyl chains on the electronic structure of the molecules with unprecedented accuracy. Given the wide-spread use of branched or linear alkyl side chains to enhance solubility and miscibility [33–36], the results obtained are highly relevant far beyond the actual polymer system investigated here.

2. Materials and Methods

Synthesis

All molecules and materials were synthesized according to published procedures as described in detail elsewhere. hexTBT was synthesized according to [57]. CbzhexTBT was synthesized according to [58]. CbzhexTBTCbz was synthesized according to [59]. hexPCDTBT was synthesized according to [56].

Optical spectroscopy

All samples were dissolved in *o*-dichlorobenzene. Absorption spectra were recorded using a commercial UV-Vis spectrometer (Shimadzu UV-2450, UV-1601PC) in combination with the corresponding software (UV Probe Version 3.42, all Shimadzu, Kyoto). Measurements at ambient temperatures were performed with standard path length cuvettes (1 cm). Temperature series were recorded using a cryostat (Optistat DN2) in combination with a temperature controller (MercuryITC, both Oxford Instruments, Abingdon) and using liquid nitrogen as a coolant. These measurements were performed using 1-mm path length cuvettes.

EPR Instrumentation

All samples were dissolved in *o*-dichlorobenzene. All TREPR experiments were performed at 80 K using a setup described previously [28,58]. Optical excitation at the respective wavelengths was carried out using an Optical Parametric Oscillator (OPO) pumped by a Nd:YAG laser. The repetition rate of the laser was set to 10 Hz and the final pulse energy (after the OPO) to 1 mJ. Further experimental parameters (except where explicity given) were as follows: Microwave frequency, 9.700 GHz, microwave power: 2 mW (20 dB attenuation, source power 200 mW), frequency-mixer detection, video amplifier set to a 42-dB amplification and a 25-MHz bandwidth, between 850 and 1400 averages per point.

Spectral simulations

All simulations of triplet spectra were performed using the `pepper` routine from the EasySpin software package [60] available for MATLAB® (MathWorks, Natick, MA). Details of both the simulations and the fitting procedure are given in the Supplementary Materials.

DFT calculations

All calculations were performed using ORCA 3.0.3 [61] using the BP86 [62,63] and B3LYP [64,65] functionals and the Def2-SVP [66] and 6-31G** [67,68] basis sets, respectively. For ***D*** tensor calculations, the EPR-II basis set [69] was used. The solvent has been accounted for by the COSMO model [70]. Initial geometries of the molecules were created using Avogadro 1.1.1 [71]. Spin density plots were created using UCSF Chimera 1.11.2 [72]. Extracting dihedral angles and tensor geometries from the calculations was performed using MATLAB routines written specifically for this purpose.

3. Results

3.1. Absorption Spectra

For all building blocks and the polymer, steady-state absorption spectra have been recorded at room temperature in solution (Figure 2). For each of the molecules, the spectrum consisted of a prominent absorption band in the visible region, due to its (partial) Charge-Transfer (CT) character usually termed the CT band, and a second band in the near-UV region that can be ascribed predominantly to a π–π* transition [37]. Obviously, the CT band increasingly shifts towards larger wavelengths with increasing length of the backbone. Whereas this red-shift is nearly identical for going from **A** to **D-A** and from **D-A** to **D-A-D**, it is dramatically reduced for proceeding from **D-A-D** to the polymer, **(D-A)$_\mathbf{n}$**.

Additionally, we note that the intensity of the π–π* transition is always higher than the CT band. Furthermore, there is no trend proceeding from **A** to **(D-A)$_\mathbf{n}$**. Rather, for **A** and **(D-A)$_\mathbf{n}$**, the π–π* transition is only slightly stronger than the CT band, about 20%, whereas for **D-A** and **D-A-D**, the π–π* transition is more than 1.5× more intense. It is tempting to assign these differences to a different degree of charge-transfer character of the (singlet) exciton in the respective molecule.

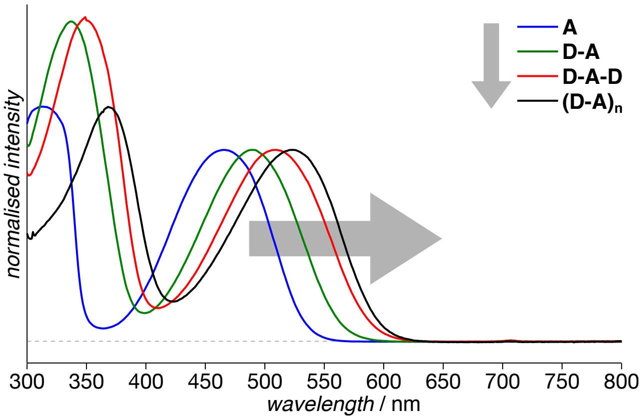

Figure 2. Absorption spectra of hexPCDTBT and its building blocks. Each spectrum consists of two bands, a π–π* band (mostly) in the near-UV region and a prominent band in the visible region, assigned to the partial Charge-Transfer character of the molecule and hence termed CT band. Obviously, the CT band increasingly shifts towards greater wavelengths with increasing length of the backbone. For easier comparison, spectra have been normalized to the same CT band height.

Besides giving insight into the electronic structure and delocalization of the singlet exciton, these steady-state absorption spectra are useful to determine the excitation wavelength for TREPR spectroscopy. Due to the fast spin relaxation of the strongly-coupled electron spins within a triplet state, TREPR spectra of these molecules need to be recorded in solid state under cryogenic conditions (see details below and in the Supplementary Materials). To rule out aggregation taking place upon cooling and to impact our interpretation of the EPR data, we recorded temperature-dependent absorption spectra for each of the four compounds investigated (see the Supplementary Materials for actual spectra). Due to the solvent, *o*-dichlorobenzene (*o*-DCB), not forming a transparent glass upon freezing, these spectra could only be recorded down to the freezing point. The choice of solvent can quite dramatically influence the behavior of the molecules [29]. From the temperature-dependent spectra, we can clearly rule out any aggregation taking place upon slow cooling. Hence, we are pretty sure the sample morphology in solution was preserved, i.e., fully-solvated molecules, upon shock-freezing our EPR samples prior to measuring.

3.2. TREPR Spectra

Upon excitation at the maximum of the respective CT band, all compounds investigated here readily showed EPR spectra that can be clearly and unequivocally assigned to a single triplet species each (cf. Figure 3). One particular strength of EPR spectroscopy in general and TREPR spectroscopy in particular is not only its exclusive sensitivity to paramagnetic states, but also the clear distinction possible between triplet states and coulombically-bound polaron pairs, often termed charge-transfer complexes or radical pairs [25,73]. Both states consist of two unpaired electron spins interacting with each other via dipolar and exchange coupling. The interaction strength strongly depends on the average distance r between the two electron spins. In the case of a triplet state with the two electrons residing on the same chromophore, hence in close vicinity, the resulting EPR spectrum is usually entirely dominated by the dipolar interaction that can directly be estimated from the spectra (see the Supplementary Materials for details). A radical pair with its much larger separation of the two electron spins exhibited a much weaker dipolar and exchange interaction, the latter often negligible. Hence, its spectral width is dramatically reduced as compared to a triplet state [25,73].

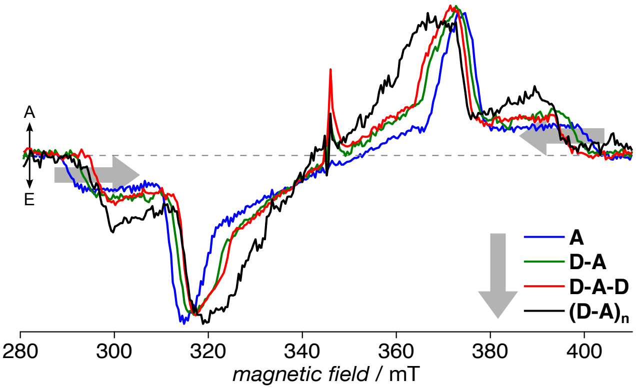

Figure 3. TREPR spectra of hexPCDTBT and its building blocks. Each sample has been excited in the respective CT band absorption maximum, cf. Figure 2. Obviously, the overall spectral width decreases with increasing length of the backbone. Spectra are averages over 200 ns, centered about 500 ns after the laser flash (in the maximum of the signal), and have been normalized to same absolute area under the respective curves. Each spectrum could be reproduced by spectral simulations taking a single triplet species into account (cf. Figure 4). For full two-dimensional datasets, see the Supplementary Materials.

The spin Hamilton operator for an organic triplet state in the presence of an external magnetic field can be written as:

$$\hat{\mathcal{H}} = g_e \beta_e \boldsymbol{B}^{\mathrm{T}} \cdot \hat{S} + \hat{S}^{\mathrm{T}} \cdot \boldsymbol{D} \cdot \hat{S} \,. \tag{1}$$

Here, the first term describes the electron Zeeman interaction and the second term the Zero-Field Splitting (ZFS) interaction with the corresponding interaction tensor:

$$\boldsymbol{D} = \begin{pmatrix} -\frac{1}{3}D + E & 0 & 0 \\ 0 & -\frac{1}{3}D - E & 0 \\ 0 & 0 & \frac{2}{3}D \end{pmatrix} . \tag{2}$$

In the frame of the $\boldsymbol{D}$ tensor, the second term can be rewritten in terms of the two scalar ZFS parameters D and E. The spin–spin contributions to these two parameters are defined as:

$$D = \frac{3D_z}{2} = \frac{3}{4}\left(\frac{\mu_0}{4\pi}\right)(g_e\beta_e)^2\left\langle\frac{r^2-3z^2}{r^5}\right\rangle, \tag{3}$$

$$E = \frac{D_x - D_y}{2} = \frac{3}{4}\left(\frac{\mu_0}{4\pi}\right)(g_e\beta_e)^2\left\langle\frac{x^2-y^2}{r^5}\right\rangle. \tag{4}$$

The angular brackets denote integration over the triplet state wave function, i.e., the spatial distribution of the two unpaired electrons of the triplet state. Different conventions can be found in the literature, and we followed here the convention used by EasySpin [60] for the order of the $\boldsymbol{D}$ tensor values, namely $|D_z| > |D_y| > |D_x|$, assuming, inter alia, $|E| \leq |D|/3$ [74] and $E/D > 0$. This is in contrast to [75] with respect to the order of D_x and D_y. However, this affects only the assignment of the x and y axes of the $\boldsymbol{D}$ tensor, not the order of the triplet energy levels or the assignment of the populations to these levels depending on the sign of D. "The sign of E depends on the specific assignment of the axes X and Y and thus has no physical meaning except in terms of the convention that we have chosen" ([75], p. 167).

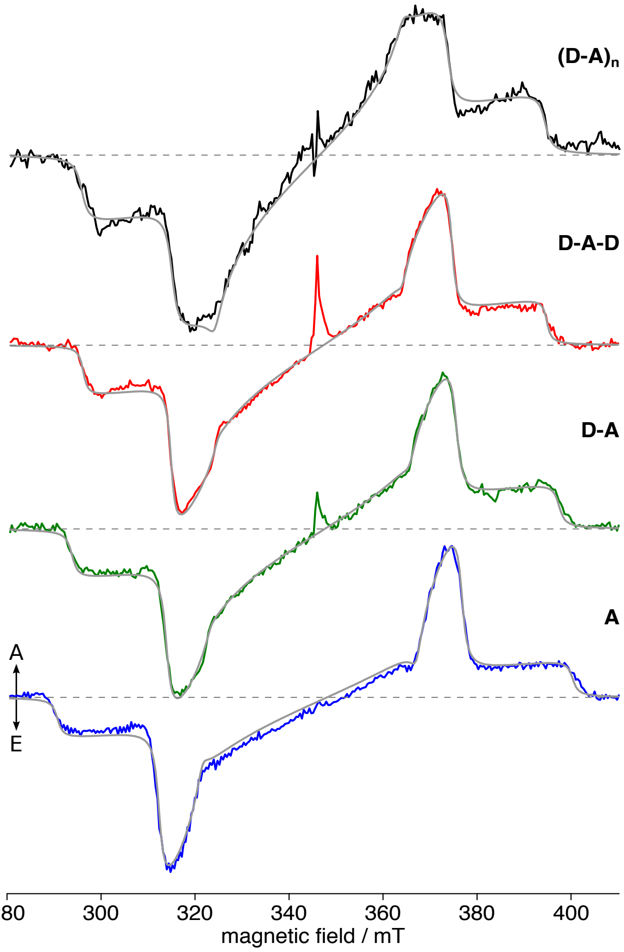

Figure 4. TREPR spectra of hexPCDTBT and its building blocks together with spectral simulations. Each spectrum could be reproduced by spectral simulations taking a single triplet species into account and shown as grey lines. For simulation parameters, cf. Table 1, for details of the fitting procedure see the Supplementary Materials. The small features in the center of the spectra at about 345 mT are not due to the triplet state and will not be accounted for here.

The small features visible in the center of some of the TREPR spectra are clearly not due to the triplet state. Their origin remains largely unknown, and different explanations have been brought forward in the past, ranging from photoinduced stable radicals, i.e., defects, to short-lived charge-transfer states, i.e., radical pairs, to species with higher spin multiplicity such as interacting triplet states. As they do not impair our tripet state simulations nor the interpretation of our data, they will not be discussed any further here.

Table 1. Simulation parameters for the spectral simulations of the TREPR spectra shown in Figure 4. λ_{ex} is the excitation wavelength used (maximum of the CT band); D and E are the parameters of the zero-field splitting tensor of the dipolar interaction; Γ_{L} is the Lorentzian line width; and $p_{1,2,3}$ are the populations of the three triplet sublevels, respectively, ordered in ascending energy. For details of the fitting procedure, see the Supplementary Materials.

Compound	λ_{ex} (nm)	$\lvert D\rvert$ (MHz)	$\lvert E\rvert$ (MHz)	$\lvert E\rvert/\lvert D\rvert$	Γ_{L} (mT)	$p_{1,2,3}$
A	466	1539 ± 2.5	88 ± 1.1	0.057	1.72 ± 0.10	0.000, 0.152, 0.848
D-A	490	1457 ± 2.1	91 ± 0.9	0.062	1.84 ± 0.11	0.000, 0.256, 0.744
D-A-D	509	1387 ± 1.9	96 ± 0.8	0.069	1.38 ± 0.07	0.000, 0.264, 0.736
(D-A)$_\mathbf{n}$	518	1384 ± 3.1	87 ± 1.4	0.063	2.12 ± 0.15	0.000, 0.436, 0.564

The TREPR spectra of each of the four compounds can be simulated taking into account a single triplet species each, as evident from the near-perfect fits (Figure 4). For simulation parameters, cf. Table 1. We note that each spectrum could be nicely reproduced taking into account only homogeneous (Lorentzian) line broadening, hinting at an overall very homogeneous environment of the exciton. Additionally, no population in the lowest-lying triplet sublevel, p_1, was necessary to reproduce the spectra. The overall trend of decreasing dipolar interaction with increasing backbone extent, as evident from the narrowing of the spectra (Figure 3), is reflected in the simulation parameters, as well. Furthermore, the triplet sublevel populations showed a trend of increasing p_2 with respect to p_3. However, no other consistent trends similar to the situation in the non-hexylated system [39] can be found. The rhombicity $\lvert E\rvert/\lvert D\rvert$ increased slightly from **A** to **D-A-D**, but reduced again for **(D-A)$_\mathbf{n}$**. Whereas the overall spectral width and the $\lvert D\rvert$ values were nearly identical for **D-A-D** and **(D-A)$_\mathbf{n}$**, the latter exhibited an overall somewhat different electronic structure, reflected in changes in the spectral shape. Nevertheless, the general spectral shape of all compounds remained rather similar, with an overall quite small rhombicity close to fully axial spectra, a small and only homogeneous line broadening, and a consistent order of the triplet sublevel populations with $p_1 < p_2 < p_3$.

Generally, the value of $\lvert D\rvert$ can be assigned to the average distance between the two unpaired electron spins within the triplet state and therefore the triplet exciton delocalization, and $\lvert E\rvert$ to its rhombicity, hence deviation from a fully-axial symmetry. Given the slightly different rhombicity for **D-A-D** and **(D-A)$_\mathbf{n}$**, the identical values for $\lvert D\rvert$ within experimental error for these two compounds did not necessarily imply a fully-identical exciton delocalization. However, the trend already observed for the singlet exciton from the absorption spectra (Figure 2) was retained: Whereas a clear progression towards delocalization can be observed from **A** to **D-A-D**, the effect was much smaller for the polymer **(D-A)$_\mathbf{n}$**.

3.3. DFT Calculations

To gain further insight, a series of quantum-chemical calculations has been performed for each of the building blocks and two oligomer fragments with $n = 4$ and $n = 7$. Molecular geometries have been optimized both for singlet and triplet states, and for triplet states, the spin-density distribution, as well as the $\boldsymbol{D}$ tensors have been calculated. Furthermore, we compared two different functionals and basis sets.

First, for each of the building blocks and the oligomer fragments with $n = 4$ and $n = 7$, geometry optimizations have been performed for both singlet and triplet state and with two combinations of the functional and basis set, namely BP86/Def2-SVP and B3LYP/6-31G**. Note that the hexyl side chains have been fully accounted for in the calculations, whereas the branched alkyl chain attached to the nitrogen of the Cbz moiety has been omitted to save computational time. To validate this approach, we calculated geometries for the **D-A** fragment with and without branched alkyl chains on the Cbz moiety and found the dihedral angles between the aromatic planes of D and A to be mutually identical, in line with previous theoretical investigations obtained for the non-hexylated polymer [76]. For the spin-density distribution, four sets of calculations have been performed, with both combinations of the functional and basis set for both geometries. The combination fitting best to the experimental results is the one using the geometries optimized on the BP86/Def2-SVP level of theory and performing single-point calculations for the spin-density distribution with B3LYP/6-31G**. $\boldsymbol{D}$ tensors have been calculated as well for both geometries, but via single-point calculations performed on the B3LYP/EPR-II level of theory often used for calculating EPR parameters. In our previous study of non-hexylated PCDTBT and its building blocks [39], we have already shown the geometries obtained on the BP86/Def2-SVP level of theory to be more consistent with the experimental results. The same is true for the hexylated compounds studied here. Therefore, in the following, only the results from calculations based on these geometries are shown. For the results obtained for the other geometries, see the Supplementary Materials.

Figure 5 gives a first impression of the geometries obtained for the triplet state. In any case, the acceptor moiety (hexTBT) in itself is planar, as well as the donor moiety (Cbz), and only between D and A, there is a quite substantial torsion, in line with previous analysis [56]. In order to obtain useful information of the planarity of the geometries, we calculated the dihedral angles between the aromatic planes of D and A, respectively (Table 2). For details of how these angles have been calculated, see the Supplementary Materials. Interestingly, for both combinations of functionals and basis sets (BP86/Def2-SVP and B3LYP/6-31G**), the geometries obtained for the triplet state were more planar as compared to those of the singlet state. This is in line with previous results obtained for an entirely different conjugated polymer, PNDIT2 [38]. Furthermore, we note that for the triplet state, the angles adjacent to the acceptor moiety carrying most of the spin density were smaller than average. This means that the triplet state locally planarizes the polymer backbone. To exclude possible boundary effects due to the hexTBT moiety carrying the maximum spin density in the fragment with $n = 4$ being located towards one end of the chain, calculations for a fragment with $n = 7$ have been performed as well. Note that the longer fragment with $n = 7$ had a D moiety on both ends. Both polymer fragments showed a consistent behavior.

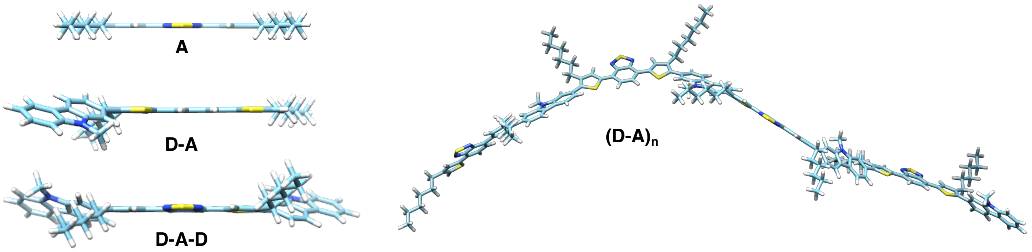

Figure 5. Side-view of the optimized geometries of the triplet states of hexPCDTBT and its building blocks. Geometries have been optimized for the triplet state on the theory level BP86/Def2-SVP. For a view perpendicular to the aromatic plane, cf. Figure 6. The D and A moieties in themselves are rather flat, whereas the aromatic planes of D and A moieties are tilted by substantial dihedral angles, respectively. For values of these dihedral angles, cf. Table 2.

Table 2. Dihedral angles between the aromatic planes of the Cbz and hexTBT moieties obtained from geometry optimization in both the singlet and triplet state. The Cbz and hexTBT moieties are planar. Angles are given in degrees and for the cis-trans configuration as shown in Figure 6. All geometries have been optimized on the BP86/Def2-SVP level of theory. Note that the longer fragment with $n = 7$ has a D moiety on both ends. Bold numbers for the triplet state geometries denote the angles directly adjacent to the A moiety carrying the maximum spin density. The spin density is always centered on one A moiety, cf. Figure 6. For details of how these angles have been obtained, see the Supplementary Materials.

Compound	State	Dihedral Angles													
D-A	singlet	35.4													
	triplet	**27.0**													
D-A-D	singlet	37.2	35.8												
	triplet	**28.7**	**27.0**												
(D-A)$_4$	singlet	36.2	31.7	39.3	34.3	35.2	35.1	35.4							
	triplet	36.6	34.3	38.1	30.3	**22.5**	**25.2**	34.0							
(D-A)$_7$-D	singlet	38.2	37.3	38.7	36.0	41.3	32.5	36.4	32.9	33.4	33.0	38.2	38.3	35.2	34.9
	triplet	39.3	34.7	36.5	31.8	**23.3**	**24.5**	32.4	36.5	43.2	39.3	35.7	34.7	35.5	36.1

The spin density of the triplet states was centered on a single acceptor moiety for each of the building blocks and the polymer fragments (Figure 6), consistent with our previous results obtained for the non-hexylated polymer [39]. Hence, TBT seems to dominate the electronic structure of the polymer entirely, in line with the minor changes in the overall spectral shape of the TREPR data of the respective triplet states (Figure 4).

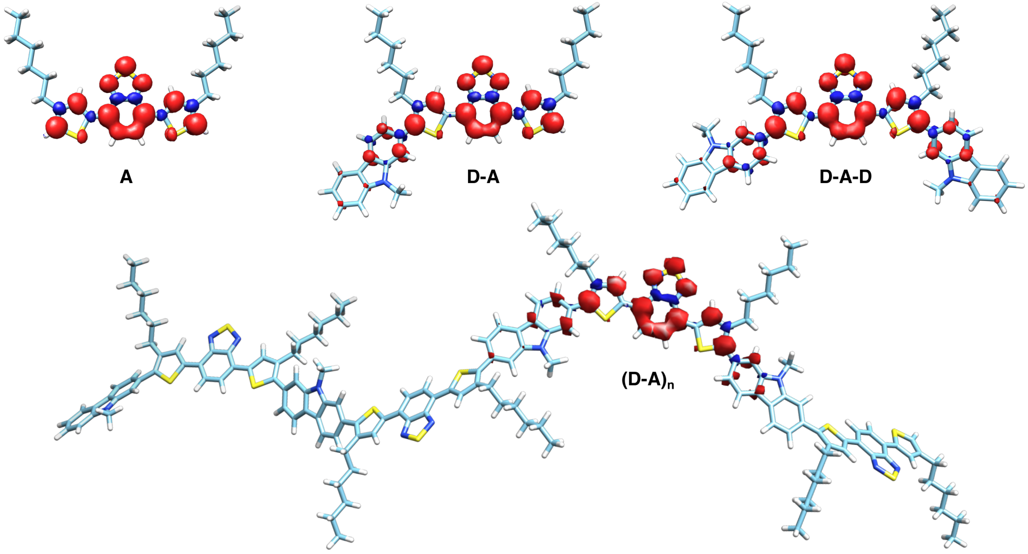

Figure 6. Spin-density distribution for the triplet states of hexPCDTBT and its building blocks. Geometries have been optimized for the triplet state on the theory level BP86/Def2-SVP and spin densities calculated on the theory level B3LYP/6-31G**. The latter have been displayed for a threshold level of ±0.002 (building blocks) and ±0.001 (polymer). Red denotes positive and blue negative spin density.

Whereas graphical representations of the spin densities as in Figure 6 provide an overall picture of their distribution upon a molecule, further analysis requires careful quantification of the information obtained. Therefore, we calculated the relative amount of spin density of the dominating acceptor unit, ρ_{TBT}, for each of the fragments with varying backbone length. For actual values, cf. Table 3, and for details of how this information has been obtained, see the Supplementary Materials. Furthermore, we quantified the spin density on each of the atoms of the dominating acceptor unit (Figure 7). The latter allowed us to investigate in more detail the asymmetry introduced by adding a single donor moiety to one end of the acceptor. Note that in this case, the donor moiety was attached to the left of the acceptor moiety, hence on the carbon atom labeled "C1" in Figure 7.

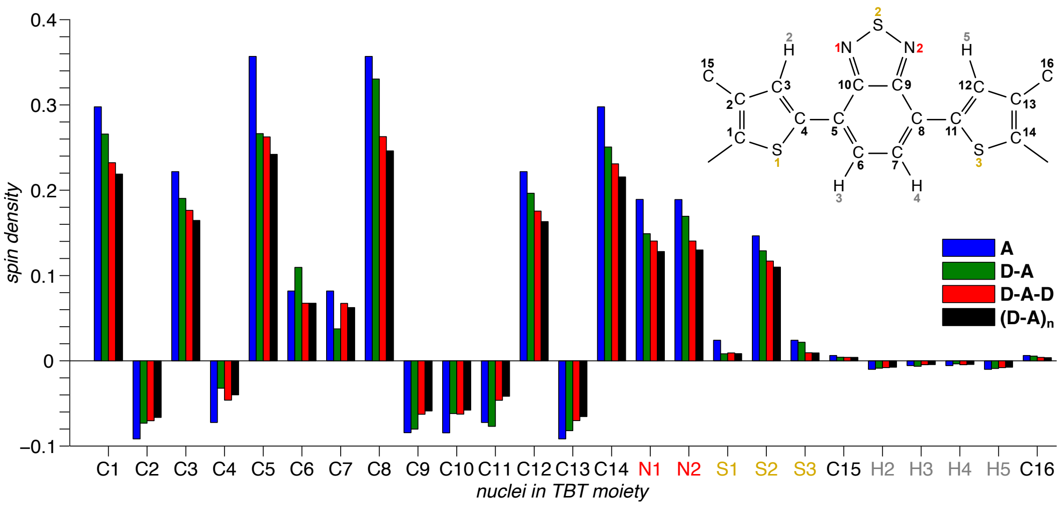

Figure 7. Quantitative analysis of the spin-density distribution for the triplet states of hexPCDTBT and its building blocks. Depicted are the values for the spin densities for each of the hexTBT atoms in the four fragments of different sizes displayed in Figure 6. The inset shows the numbering of the atoms used as axis labels. The hexyl chains are attached at positions C15 and C16. For the asymmetric building block, **D-A**, the D unit was attached to the left of the A unit, hence on the carbon atom labeled "C1".

Although ***D*** tensors are known to be notoriously difficult to calculate using DFT methods, at least the calculated absolute values for the D and E parameter to deviate dramatically from experimental results, quantum-chemical calculations may well provide additional insight into the orientation of the ***D*** tensor within the molecular frame [77]. Hence, we calculated the ***D*** tensor for each of the compounds for both geometries (using the BP86/Def2-SVP and B3LYP/6-31G** level of theory, respectively) using B3LYP as the functional and EPR-II as the basis set. Interestingly, all calculated tensors exhibited a mutually-identical orientation within the molecular frame, with their x and y axes within the aromatic plane of the acceptor moiety and the z axis perpendicular to it. The x axis points perpendicular to the axis connecting thiophene-benzothiadiazole and the y axis along this connection (Figure 8). Assigning the ***D*** tensor axes is based on the usual convention $|D_z| > |D_y| > |D_x|$, assuming, inter alia, $|E| \leq |D|/3$ [74] and $E/D > 0$. Note that this convention follows EasySpin [60], but is in contrast to [75] with respect to the order of D_x and D_y. However, this affects only the assignment of the x and y axes of the ***D*** tensor, not the order of the triplet energy levels or the assignment of the populations to the these levels depending on the sign of D. The molecular reference frame is given in Figure 8 (right), with the x and y axes as well within the aromatic plane of the acceptor moiety and the z axis perpendicular to it, accordingly. The deviations (dihedral angles) of the ***D*** tensor axes from the molecular reference frame are given in Table 3.

Whereas generally, the ***D*** tensor axes were collinear with the molecular reference frame as depicted in Figure 8, only for the asymmetric **D-A** building block, a slight tilt of the x and y axes by a few degrees towards the donor moiety can be seen. Whereas the angles given in Table 3 were calculated for the geometry obtained using the BP86/Def2-SVP level of theory, they were mutually identical for the geometry obtained using B3LYP/6-31G**. The same is true for the non-hexylated compounds for which the ***D*** tensors have been calculated, as well. Here, the deviation of the x and y axes from the molecular reference frame for the asymmetric repeat unit was slightly larger, amounting to about four degrees, each. See the Supplementary Materials for further details.

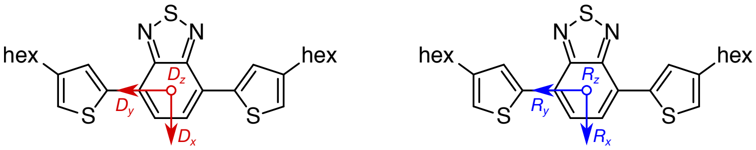

Figure 8. Orientation of the calculated ***D*** tensor within the TBT acceptor moiety and molecular reference frame. For each of the fragments investigated, the ***D*** tensor is basically oriented in the same way, as shown on the left. Assuming a right-handed coordinate system, the z component is pointing towards the paper plane. Only for the asymmetric repeat unit **D-A**, a slight deviation from the molecular reference frame (R_i with $i = \{x, y, z\}$, right) of a few degrees has been obtained from the DFT calculations. The deviation from the reference frame is given as three dihedral angles, α, β, and γ, for each of the three axes, x, y, and z, respectively. For actual values of these angles, see Table 3.

Table 3. Comparison of calculated and experimental ***D*** tensors, as well as their orientation within the molecular reference frame. ***D*** tensors for each of the compounds have been calculated using the B3LYP/EPR-II level of theory. Values for $|D|$ and $|E|$ are given in MHz. For the orientation of the ***D*** tensor with respect to the molecular reference frame R_i with $i = \{x, y, z\}$, cf. Figure 8. The angles α, β, and γ (in degrees) refer to the deviation of the corresponding ***D*** tensor axes from the molecular reference frame. Only for the asymmetric repeat unit **D-A**, a slight deviation from the molecular reference frame has been obtained, with the x and y axis tilted towards the additional D moiety. ρ_{TBT} denotes the relative amount of spin density on the dominating A moiety. Note that for the calculated values, the oligomer fragment with $n = 4$ has been used. The experimental values have been extracted from the simulations shown in Figure 4, cf. Table 1.

Compound	$\lvert D\rvert$	$\lvert E\rvert$	$\lvert E\rvert/\lvert D\rvert$	$\lvert D\rvert$	$\lvert E\rvert$	$\lvert E\rvert/\lvert D\rvert$	α	β	γ	ρ_{TBT}
	Calculated			**Experimental**						
A	808	179	0.22	1539	88	0.06	0.0	0.0	0.0	1.00
D-A	736	173	0.24	1457	91	0.06	2.3	2.3	0.2	0.92
D-A-D	688	170	0.25	1387	96	0.07	0.1	0.2	0.2	0.88
(D-A)$_n$	675	173	0.26	1384	87	0.06	0.2	0.0	0.2	0.85

As can be seen from Table 3, as well, the calculated $|D|$ values were about half of the size of those experimentally obtained. The opposite is true for the $|E|$ values, where the calculations overestimated the parameter by about a factor of two. Hence, the rhombicity $|E|/|D|$ of the calculated tensors dramatically deviated from those experimentally obtained. Given that the $|D|$ and $|E|$ values can be determined very accurately from the experimental EPR data, this clearly demonstrates the limits of the current approaches of DFT calculations for these types of parameters. At least the overall trend of decreasing $|D|$ values for increasing fragment length is reflected in the calculated values. A smaller $|D|$ value means a weakened dipolar interaction interpreted as increasing separation of the two unpaired electron spins of the triplet state and hence a larger delocalization of the exciton. The sign of the D values calculated using ORCA is always positive. Based on other studies [77] comparing in more detail experimentally-obtained signs of D with results from calculations, we are quite confident that assigning a positive sign to D is justified in our case, resulting in an oblate spin-density distribution. This allows assigning the populations $p_{1,2,3}$ to triplet energy levels $T_{x,y,z}$ using the conventions given above.

4. Discussion

Besides discussing the results described above, they will be compared to the results obtained in a previous study on the non-hexylated polymer and its building blocks [39]. This approach allows us to reveal the details of the impact the alkyl chains have on the electronic structure of the molecules and to distinguish the different aspects that are influenced, such as electronics and sterics. For a direct comparison of both spectra and parameters of the hexylated and non-hexylated system, the reader is referred to the Supplementary Materials.

4.1. Acceptor Dominates Electronic Structure

As obvious particularly from the TREPR spectra (Figure 4), the TBT acceptor moiety entirely dominates the electronic structure even of the polymer. Overall, the TREPR spectrum obtained for the polymer clearly resembles that of the acceptor alone, with only very minor changes in the overall shape and a narrower appearance due to increased delocalization of the exciton. This is in line with both the absorption spectra showing a dominating CT band in the visible range for all compounds investigated and our previous study on the non-hexylated polymer [39]. Hence, the same applies here, namely that referring to the polymer as a carbazole derivative, although chemically entirely correct, does not really reflect the situation in terms of its electronic structure.

DFT calculations of the spin-density distribution (Figure 6) further support the dominating role the acceptor moiety plays for the electronic structure of the polymer, as well as all the building blocks. Even for the polymer, about 85 percent of the total spin density resides on a single TBT moiety (ρ_{TBT} in Table 3). This is more than in case of the non-hexylated polymer and can be explained by the smaller delocalization of the triplet exciton on the hexylated polymer, as evident from comparing the $|D|$ values and spectral widths. The detailed quantitative investigation of the spin density for each of the atoms of the acceptor moiety (Figure 7) reveals the Benzothiadiazole (BT) moiety to dominate within the TBT unit, carrying about half of the total spin density. Furthermore, this histogram reveals that for all compounds investigated, the spin density is distributed highly symmetrical upon the TBT unit, with one notable exception. The intrinsically-asymmetric polymer repeat unit, **D-A**, shows an asymmetric spin density pattern particularly for the central BT, with alternating increased and diminished spin density for adjacent atoms. As can be seen from Figure 6, the spin density advances to the flanking carbazole moieties, in line with an increased delocalization with extended backbone length.

4.2. Exciton Delocalization Extends with Backbone Length

Both singlet and triplet excitons exhibit an increasing delocalization with extended backbone length, as obvious from optical (Figure 2) and TREPR data (Figure 3) and the simulation parameters for the latter (Table 1). To help with extracting trends and with comparing the data obtained for the hexylated system with those of the non-hexylated system [39], the crucial parameters have been plotted in Figure 9. Whereas the absorption maximum of the CT band is a measure for the delocalization of the singlet exciton, the D parameter obtained by fitting simulations to the EPR spectra can be related to the spread of the triplet exciton. As D follows an inverse cubed distance dependence, $D^{-1/3}$ has been plotted.

A number of conclusions can be drawn immediately from the data presented in Figure 9. Whereas singlet and triplet exciton delocalization followed the same overall trend for both, non-hexylated and hexylated compounds, the delocalization of the triplet excitons was much more affected by the hexylation than that of the singlet excitons, with the delocalization of the bare acceptor unit being equal. As both, D and A moieties were in themselves pretty flat, the only difference between the hexylated and the non-hexylated compounds was the dihedral angle between the aromatic planes of D and A. Hence, we ascribed the overall stronger localization of the excitons for the hexylated polymer to the backbone torsion. Furthermore, this torsion seems to affect the delocalization of the triplet exciton much stronger than that of the singlet exciton.

The exciton delocalization on the bare acceptor unit deserves a special comment. Whereas for the singlet exciton, hexylation leads to a clearly visible red-shift of the CT band of 12 nm and thus an increased delocalization, the D values for the corresponding triplet exciton were nearly identical. We attributed the increased delocalization of the singlet exciton upon hexylation to the +I effect of the hexyl side chains. Furthermore, it seems to have a much stronger influence on the singlet exciton as compared to the triplet exciton. This is in line with the nearly negligible spin density residing on the carbon atoms (C16 and C16, Figure 7) of the hexyl side chains.

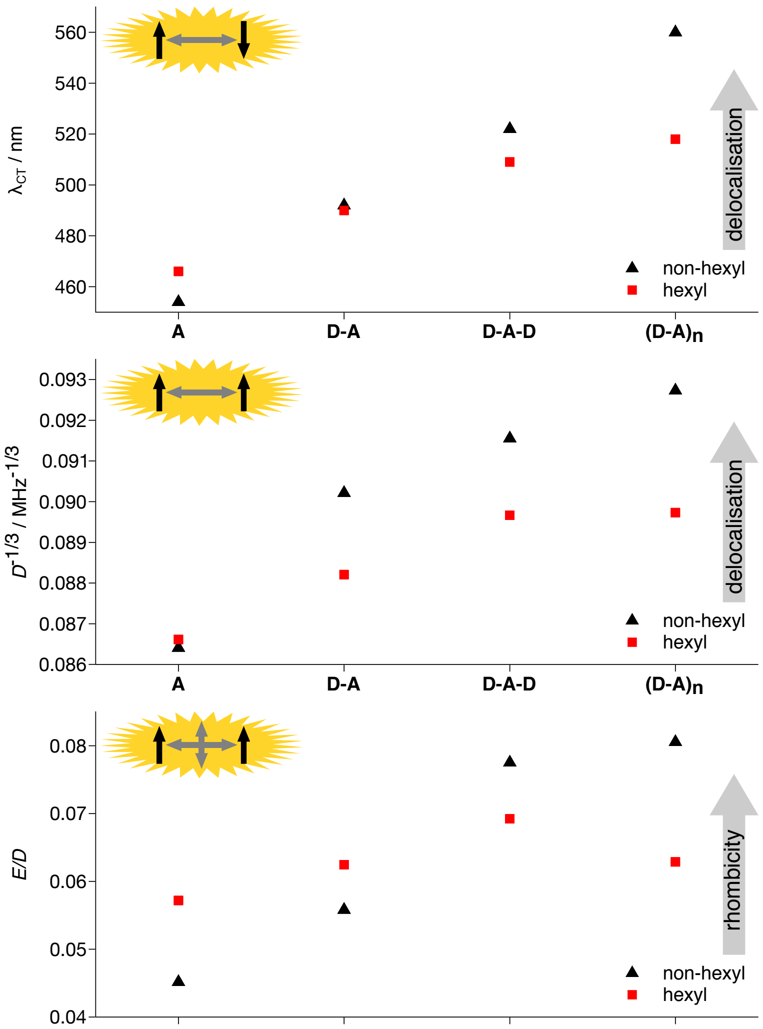

Figure 9. Comparison of the characteristics of singlet and triplet excitons for hexPCDTBT and PCDTBT and their respective building blocks. Delocalization of the singlet excitons (top) and triplet excitons (middle) follow overall the same trend, i.e., increasing delocalization with increasing backbone extent. In both cases, the relative differences were much larger for the non-hexylated compounds. For the rhombicity of the triplet exciton (bottom), a clear trend is only visible for the non-hexylated compounds, with rhombicity increasing with backbone extent.

Additionally, while the non-hexylated compounds followed a monotonic trend with nearly identical slope for the exciton delocalization of both, singlet and triplet excitons, for the hexylated compounds, the increase in delocalization when proceeding from **D-A-D** to **(D-A)$_n$** was clearly reduced. Particularly for the triplet exciton, the *D* values for **D-A-D** and **(D-A)$_n$** were identical within experimental error. Nevertheless, the **D-A-D** fragment did not reflect the situation in the polymer. Whereas sharing a similar extent of the triplet exciton, both rhombicity and, more importantly, triplet sublevel populations were different, resulting in a clearly altered spectral shape (cf. Figure 4).

For the polymer, not only the band gap, but the HOMO level, as well, has been obtained experimentally in a previous study using Ultraviolet Photoelectron Spectroscopy (UPS) [56]. From these data, it is obvious that hexylation affects almost exclusively the HOMO level, but not the LUMO level.

4.3. Twisting the Backbone Reduces Curvature

A characteristic of the PCDTBT polymer is its flat and s-shaped backbone [78] that has been used to interpret the monotonic increase in rhombicity of the triplet exciton with increasing backbone length [39]. Interestingly, no such trend can be seen for the rhombicity of the spin-density distribution of the triplet excitons for the hexylated compounds. Directly comparing the rhombicity of hexylated and non-hexylated compounds (Figure 9, lower panel) shows that its values were higher for the hexylated compounds only for **A** and **D-A**, but smaller for **D-A-D** and **(D-A)$_\mathbf{n}$**. Additionally, the rhombicity slightly decreased again when proceeding from **D-A-D** to **(D-A)$_\mathbf{n}$**. We interpreted this in light of the sidechain-induced backbone torsion obvious from the geometry-optimized fragments (Table 2). Note that hexylation only introduces backbone torsion between adjacent D and A units, not within the A unit itself, which remains flat. Hence the sidechain-induced backbone torsion masks the backbone curvature dominating in the non-hexylated polymer. This is reflected in the rhombicity of PCDTBT being much larger than that of hexPCDTBT.

4.4. Triplet Excitons Planarize the Polymer Backbone

A very interesting trend can be deduced from the dihedral angles obtained from the optimized geometries (Table 2): The triplet excitons seem to locally planarize the polymer backbone. An overall more planar geometry for triplet-state geometries as compared to singlet-state geometries has been described before for a different polymer system, PNDIT2 [38]. The same seems true for the building blocks of hexylated PCDTBT investigated here. On average, the dihedral angles for the **D-A** and **D-A-D** fragments were smaller by about eight degrees for the triplet state compared to the singlet state. The effect was even more dramatic in the polymer, with a reduction in dihedral angles of ≤ 10 degrees. Particularly for the longer polymer fragment with $n = 7$, where the A moiety carrying the maximum spin density is located well within the chain, additionally, a small reduction of the dihedral angles next to those directly adjacent to the dominant A moiety can be observed. While being a rather minor effect, it may well explain the difference in electronic structure of the triplet exciton of **D-A-D** and **(D-A)$_\mathbf{n}$** evident from the difference in triplet sublevel populations and spectral shape. In the shorter fragment with $n = 4$, such a conclusion would not have been possible due to potential boundary effects, as the dominant A moiety carrying the maximum of spin density is located close to one chain end of the fragment.

We show here only the dihedral angles from geometry optimization performed on the BP86/Def2-SVP level of theory, which is clearly superior over B3LYP/6-31G** for this purpose. Nevertheless, we did perform geometry optimizations for all fragments (excluding the fragment with $n = 7$) using B3LYP/6-31G** as the functional and basis set, respectively. These geometries show the same overall trend in terms of a local planarization due to the triplet state. For details and actual values, see the Supplementary Materials.

For the non-hexylated polymer and its building blocks, no such trend could be deduced due to the dihedral angles between adjacent D and A moieties being always close to zero, in line with an overall pretty flat polymer backbone and a dominating s-shaped curvature.

4.5. Different Functionals/Basis Sets for Geometry Optimizations and Spin Density Calculations

In our previous detailed study of the non-hexylated PCDTBT system [39], we did both geometry optimization and spin density calculations on the BP86/Def2-SVP level of theory. This gave consistent results, and already there, we could show BP86/Def2-SVP to be superior over B3LYP/6-31G** for geometry optimization, as judged from consistency with the experimental data. The situation was slightly different for the hexylated compounds, where BP86/Def2-SVP resulted in a spin-density distribution being too delocalized. Nevertheless, the angles from geometry optimization were reasonable. Therefore, we used BP86/Def2-SVP for geometry optimization and performed single-point calculations for the spin-density distribution on the B3LYP/6-31G** level of theory. Note that for calculating magnetic resonance parameters, namely $\boldsymbol{D}$ tensors, we used EPR-II as the basis set, as it is well known to be suited for those types of calculations.

4.6. ***D*** *Tensor Calculations: Challenging But Informative*

As is obvious from comparing calculated and experimentally-determined values for $|D|$ and $|E|$ (Table 3), calculating these parameters by using DFT calculations remains challenging. Nevertheless, the calculations revealed details that cannot easily be obtained experimentally, such as the relative orientation of the $\boldsymbol{D}$ tensor within the molecule (Figure 8) and the sign of the D parameter.

As mentioned above, the sign of the D values calculated using ORCA is always positive. Other studies [77] compared experimentally-obtained signs of D with experimental values in more detail, showing excellent agreement between calculations and experiments in this respect. Therefore, we are quite confident that we can assign a positive sign to D in our case. Experimental validation would require EPR measurements at low temperatures [79], optically-detected EPR [80–82], static magnetic susceptibility measurements [83], or alternatively comparison with other magnetic interaction parameters, preferably hyperfine couplings, if their sign is known [84]. None of these is simply accessible, the latter most probably impossible for the system under investigation, as preliminary ENDOR (electron nuclear double resonance) measurements did not result in any usable signal intensity. Assuming a positive sign for D based on the DFT calculations resulted in an oblate spin-density distribution and allowed assigning the populations $p_{1,2,3}$ to triplet energy levels $T_{x,y,z}$ using the conventions given above. The relative arrangement of the three triplet energy levels for $D > 0$ and $E/D > 0$ is given in Figure 10. As the three triplet sublevel populations obtained by spectral simulations were always sorted in ascending order of triplet sublevel energy, we can therefore make the following assignments: $p_1 \rightarrow p_z$, $p_2 \rightarrow p_x$, and $p_3 \rightarrow p_y$. For convenience, a summary of the simulation parameters with these assignments is presented in Table 4.

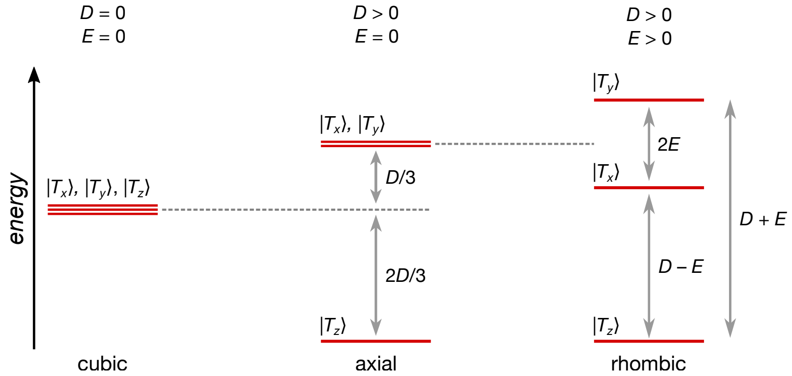

Figure 10. Relative position of the triplet energy sublevels for three characteristic cases. In the case of the compounds investigated here, the situation termed "rhombic" with $E \neq 0$ is the relevant one. In this case, all three triplet sublevels can be distinguished by their position in the experimental EPR data. As the three zero-field populations $p_{1,2,3}$ from the simulations are ordered in ascending energy level, they can be assigned to $p_{z,x,y}$, respectively, assuming $D > 0$ as obtained from the DFT calculations.

Table 4. Simulation parameters for the spectral simulations of the TREPR spectra shown in Figure 4. λ_{ex} is the excitation wavelength used (maximum of the CT band); D and E are the parameters of the zero-field splitting tensor of the dipolar interaction; Γ_{L} is the Lorentzian line width; and $p_{1,2,3}$ are the populations of the three triplet sublevels, respectively, ordered in ascending energy. For actual simulations and details of the fitting procedure, see the Supplementary Materials.

Compound	$\|D\|$ **(MHz)**	$\|E\|$ **(MHz)**	$\|E\|/\|D\|$	p_x	p_y	p_z
A	1539 ± 2.5	88 ± 1.1	0.057	0.152	0.848	0.000
D-A	1457 ± 2.1	91 ± 0.9	0.062	0.256	0.744	0.000
D-A-D	1387 ± 1.9	96 ± 0.8	0.069	0.264	0.736	0.000
(D-A)$_\mathbf{n}$	1384 ± 3.1	87 ± 1.4	0.063	0.436	0.564	0.000

Based on the assignment of a positive sign to D from DFT calculations and given the information of the orientation of the $\boldsymbol{D}$ tensor within the molecule, we can draw some conclusions from the zero-field triplet sublevel populations obtained by spectral simulations. The vanishing contribution of p_z associated with the D_z component oriented perpendicular to the aromatic plane, in line with magnetophotoselection experiments on the (non-hexylated) **D-A** fragment [55], can be rationalized based on the spin-density distribution obtained from DFT calculations. However, we would not try to deduce, in reverse, a positive sign of D only based on a disk-like (oblate) spin-density distribution of a planar aromatic system.

Having assigned the x and y axes of the $\boldsymbol{D}$ tensor based on our convention stated above (Figure 8), we can proceed with a more detailed analysis of the remaining p_x and p_y populations. As a general trend, the longer the fragment, the larger the population is found along the x direction, perpendicular to the backbone. In compound **A**, the dominant Intersystem Crossing (ISC) took place along the y axis connecting the two donor thiophenes with the central BT moiety. This is in line with the rather strong donor-acceptor character of the TBT unit [37]. For both **D-A** and **D-A-D**, nearly identical populations p_x and p_y were revealed, with a clearly higher contribution along the x axis, perpendicular to the backbone. This can be rationalized by the curvature introduced by the additional D moieties bearing some spin density, as apparent from the spin-density distribution (Figure 6). Obviously, the additional D moiety in the **D-A-D** fragment only leads to an increased delocalization by extending the conjugated system, but not to an alteration in the orbitals contributing to the ISC. Carefully comparing the TREPR spectra of both compounds shows the only change to be the overall width, hence delocalization. The changes in populations from **A** to **D-A** can be similarly seen in a slight change in spectral shape.

As mentioned already above, proceeding from **D-A-D** to **(D-A)$_\mathbf{n}$** comes along with a notable change in the overall spectral shape, reflected in the altered triplet sublevel populations $p_{x,y}$, although the overall widths (and hence, the D value) of both spectra were identical within experimental error. The increased contribution to the ISC along the molecular x direction, perpendicular to the backbone, can be rationalized by the smaller dihedral angles between D and A moieties in **(D-A)$_\mathbf{n}$** compared to **D-A-D** (Table 2). The triplet exciton seems to flatten the local polymer backbone, most prominently directly adjacent to the central A moiety carrying the maximum spin density, but even extending to the next dihedral angles on each side. This comparably more planar geometry allows for a better conjugation and hence more contribution of the two D moieties, besides increasing the local curvature and thus the contribution to the ISC along the x direction.

The detailed discussion of the electronic structure and in particular the origins of the altered zero-field triplet sublevel populations for **D-A-D** and **(D-A)$_\mathbf{n}$** above has been based on assigning a positive sign to D obtained from DFT calculations. However, even without determining or assigning the sign of D, the differences in populations observed experimentally reveal them to be a very sensitive probe for the local environment of the triplet exciton. This shows the power of TREPR spectroscopy to reveal even subtle differences in electronic structure and to assign them to a change in (local) geometry of the polymer backbone.

4.7. Four Distinct Factors Determining Exciton Delocalization

By comparing both non-hexylated and hexylated polymer and the respective building blocks, four distinct factor determining exciton delocalization and triplet exciton rhombicity can be distinguished (Figure 11): electronics (+I effect), curvature of the polymer backbone, conjugation length, and dihedral angles between D and A moieties due to sterics.

For the non-hexylated system, only increasing conjugation length of the polymer backbone and increasing curvature were relevant and have both a large effect when proceeding from one compound to the next-larger one (cf. Figure 9). In all cases, both, delocalization and rhombicity increased monotonically from smallest to largest fragment investigated. This changes somewhat for the hexylated system. Here, increased conjugation length is still the driving force behind the larger delocalization with enhanced backbone length. However, this effect diminished when proceeding from **D-A-D** to **(D-A)$_n$**, with a slightly enhanced delocalization length of the singlet exciton and a near-identical size of the triplet exciton for both molecules. The smaller increase of the rhombicity from **A** to **D-A-D** for the hexylated vs. non-hexylated system can be attributed to the dihedral angles between the D and A moieties in the former, leading to a smaller curvature of the backbone. This effect is slightly reversed for the polymer due to the triplet exciton planarizing locally the polymer backbone, and to a much larger extent than in the smaller fragments. The increased delocalization of the hexylated **A** moiety compared to its non-hexylated counterpart is at first sight surprising. However, it can be ascribed to the +I effect dominating more for the singlet exciton than the triplet exciton. In the case of the triplet exciton for the polymer repeat unit **D-A**, the +I effect gets compensated for by sterical effects of the hexyl side chains resulting in substantial dihedral angles between the D and A moiety. Generally, singlet exciton delocalization seems less affected by dihedral angles and a twisted backbone than triplet excitons. This is in line with previous results on PNDIT2 showing overall more planar geometries of the triplet geometries, but much stronger restricted triplet exciton delocalization as compared to the corresponding singlet excitons [38]. In the symmetric fragment **D-A-D**, finally, sterics reduced the overall curvature in the case of the hexylated compound, resulting in a smaller overall rhombicity of its triplet exciton as compared to the non-hexylated counterpart. The same is true for comparing the two polymers, although here, the effect of reduced impact of the backbone curvature was more pronounced, in line with the smaller dihedral angles found for the polymer compared to **D-A-D**.

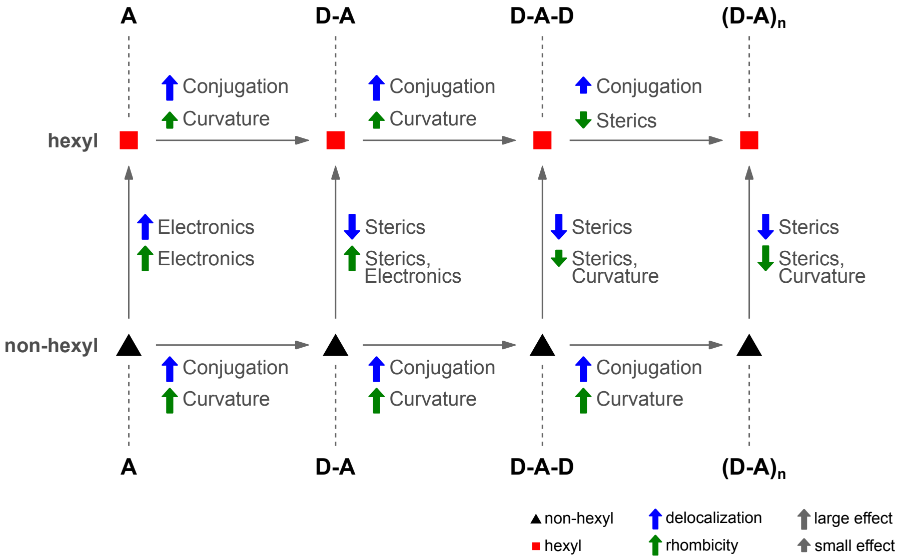

Figure 11. Factors determining the delocalization and triplet exciton rhombicity of the excited states of PCDTBT and its building blocks. Four distinct contributions can be differentiated: electronics (+I effect), the curvature of the polymer backbone, conjugation length, and sterics due to dihedral angles between the D and A moieties.

Taken together, introducing alkyl side chains, mostly for better solubility and enhanced miscibility with other components, can have a wealth of effects on both the morphology and electronic structure of the underlying polymer that can only be distinguished and investigated in detail by comparing both alkylated and non-alkylated polymers, as well as their respective building blocks of different length.

5. Conclusions

In summary, we have investigated the effect of adding alkyl side chains to the electronic structure of the underlying polymer in great detail. For PCDTBT, alkylation generally leads to more localized excitons, but most prominent only for the polymer. Furthermore, singlet excitons seem to be more delocalized than the corresponding triplet excitons, despite the larger dihedral angles between the

D and A moieties found for the singlet-state geometries. Using a series of building blocks with increasing length leads to a fundamental understanding of the electronic structure and allows for discriminating different effects, namely electronics (+I effect), curvature, conjugation length, and sterics (backbone twist). Finally, DFT calculation of $\boldsymbol{D}$ tensors, while still rather limited in terms of the D and E values obtained, reveals the sign of the D value. This allows us to assign the populations to triplet sublevels and to the geometry of the molecule, providing additional insight into the impact even slight modifications of the backbone geometry have on the electronic structure of the excitons. This renders TREPR spectroscopy of triplet excitons well-suited to investigate crucial aspects of the structure-function relationship of conjugated polymers used as organic semiconductors on a molecular basis.

Supplementary Materials: The following are available online at http://www.mdpi.com/2073-4360/11/5/870/s1: EPR instrumentation, details of spectral simulations, Figure S1: Characteristics of TREPR spectra of (photo-generated) triplet states, Figure S2: Full 2D TREPR datasets, Figure S3: Temperature-dependent absorption spectra, Figure S4: Comparison of absorption spectra of non-hexylated and hexylated compounds, Figure S5: Comparison of TREPR spectra of non-hexylated and hexylated compounds, Table S1: Simulation parameters for spectral simulations of TREPR spectra, Figure S6: Scheme for the dihedral angles between D and A moieties, Table S2: Dihedral angles for non-hexylated and hexylated compounds, Table S3: Absolute amount of spin density on the TBT moiety for non-hexylated and hexylated compounds, Figure S7: Optimized geometries, Figure S8: Orientation of the calculated $\boldsymbol{D}$ tensor and molecular reference frame, Table S4: Calculated and experimental $\boldsymbol{D}$ tensors for non-hexylated and hexylated compounds.

Author Contributions: Conceptualization, M.S. and T.B.; data curation, T.B.; formal analysis, C.M., F.L., M.S., and T.B.; funding acquisition, M.S. and T.B.; investigation, C.M. and T.B.; methodology, M.S. and T.B.; project administration, M.S. and T.B.; resources, C.M., F.L., and T.B.; software, C.M.; supervision, M.S. and T.B.; validation, C.M., F.L., M.S., and T.B.; visualization, C.M. and T.B.; writing, original draft, T.B.; writing, review and editing, C.M., F.L., M.S., and T.B.

Funding: This research was funded by German Research Foundation (DFG) Grant Number BI-1249/3-1, Albert-Ludwigs-Universität Freiburg (Innovationsfonds Forschung), and Wissenschaftliche Gesellschaft Freiburg. The APC was funded by the German Research Foundation (DFG) and the University of Freiburg in the funding program Open Access Publishing.

Acknowledgments: C.M. and T.B. thank D. Meyer for an extensive interface for conveniently fitting EPR spectra of triplet states, J. Popp for artwork (Table of contents figure), T. Koslowski for providing computational resources, and S. Weber for support.

Conflicts of Interest: The authors declare no conflict of interest.

Abbreviations

The following abbreviations are used in this manuscript:

A	Acceptor
Cbz	Carbazole
COSMO	Conductor-like Screening Model
CT	Charge Transfer
D	Donor
DFT	Density Functional Theory
ENDOR	Electron Nuclear Double Resonance
EPR	Electron Paramagnetic Resonance
ISC	Intersystem Crossing
PCDTBT	Poly[*N*-9′-heptadecanyl-2,7-carbazole-*alt*-5,5-(4′,7′-di-2-thienyl-2′,1′,3′-benzothiadiazole)]
PNDIT2	Poly{[*N*,*N*′-bis(2-octyldodecyl)-naphthalene-1,4,5,8-bis(dicarboximide)-2,6-diyl]-*alt*-5,5′-(2,2′-bithiophene)}
TBT	Dithienyl-Benzothiadiazole
TREPR	Time-Resolved Electron Paramagnetic Resonance
ZFS	Zero-Field Splitting

References

1. Forrest, S.R. The path to ubiquitious and low-cost organic electronic appliances on plastic. *Nature* **2004**, *428*, 911–918. [CrossRef]
2. Katz, H.E.; Huang, J. Thin-film organic electronic devices. *Ann. Rev. Mater. Res.* **2009**, *39*, 71–92. [CrossRef]
3. Sirringhaus, H. 25th anniversary article: Organic field-effect transistors: The path beyond amorphous silicon. *Adv. Mater.* **2014**, *26*, 1319–1335. [CrossRef]
4. Lewis, J. Material challenge for flexible organic devices. *Mater. Today* **2006**, *9*, 38–45. [CrossRef]
5. Logothetidis, S. Flexible organic electronic devices: Materials, process and applications. *Mater. Sci. Eng. B Solid State Mater. Adv. Technol.* **2008**, *152*, 96–104. [CrossRef]
6. Rogers, J.A.; Someya, T.; Huang, Y. Materials and mechanics for stretchable electronics. *Science* **2010**, *327*, 1603–1607. [CrossRef]
7. Ling, H.; Liu, S.; Zheng, Z.; Yan, F. Organic flexible electronics. *Small Meth.* **2018**, *2*, 1800070. [CrossRef]
8. Berggren, M.; Nilsson, D.; Robinson, N.D. Organic materials for printed electronics. *Nat. Mater.* **2007**, *6*, 3–5. [CrossRef] [PubMed]
9. Choi, C.; Lee, Y.; Cho, K.W.; Koo, J.H.; Kim, D.H. Wearable and implantable soft bioelectronics using two-dimensional materials. *Acc. Chem. Res.* **2019**, *52*, 73–81. [CrossRef]
10. Wang, C.; Wang, C.; Huang, Z.; Xu, S. Materials and structures toward soft electronics. *Adv. Mater.* **2018**, *30*, 1801368. [CrossRef]
11. Arias, A.C.; MacKenzie, J.D.; McCulloch, I.; Rivnay, J.; Salleo, A. Materials and applications for large area electronics: Solution-based approaches. *Chem. Rev.* **2010**, *110*, 3–24. [CrossRef]
12. Xu, R.P.; Li, Y.Q.; Tang, J.X. Recent advances in flexible organic light-emitting diodes. *J. Mater. Chem. C* **2016**, *4*, 9116–9142. [CrossRef]
13. Heeger, A.J. Semiconducting polymers: The Third Generation. *Chem. Soc. Rev.* **2010**, *39*, 2354–2371. [CrossRef]
14. Darling, S.B.; You, F. The case for organic photovoltaics. *RSC Adv.* **2013**, *3*, 17633–17648. [CrossRef]
15. Forrest, S.R. Excitons and the lifetime of organic semiconductor devices. *Philos. Trans. R. Soc. A Math. Phys. Eng. Sci.* **2015**, *373*, 20140320. [CrossRef] [PubMed]
16. Azzopardi, B.; Emmott, C.J.M.; Urbina, A.; Kresbs, F.C.; Mutale, J.; Nelson, J. Economic assessment of solar electricity production from organic-based photovoltaic modules in a domestic environment. *Energy Environ. Sci.* **2011**, *4*, 3741–3753. [CrossRef]
17. Brabec, C.J.; Durrant, J.R. Solution-processed organic solar cells. *MRS Bull.* **2008**, *33*, 670–275. [CrossRef]
18. Lu, L.; Zheng, T.; Wu, Q.; Schneider, A.M.; Zhao, D.; Yu, L. Recent advances in bulk heterojunction polymer solar cells. *Chem. Rev.* **2015**, *115*, 12666–12731. [CrossRef]
19. Yeh, N.; Yeh, P. Organic solar cells: Their developments and potentials. *Renew. Sust. Energ. Rev.* **2013**, *21*, 421–431. [CrossRef]
20. Sekine, C.; Tsubata, Y.; Yamada, T.; Kitano, M.; Doi, S. Recent progress of high performance polymer OLED and OPV materials for organic printed electronics. *Sci. Technol. Adv. Mater.* **2014**, *15*, 034203. [CrossRef] [PubMed]
21. Faccetti, A. Seminconductors for organic transistors. *Mater. Today* **2007**, *10*, 28–37. [CrossRef]
22. Janata, J.; Josowicz, M. Conducting polymers in electronic chemical sensors. *Nat. Mater.* **2002**, *2*, 19–24. [CrossRef] [PubMed]
23. Jackson, N.E.; Savoie, B.M.; Marks, T.J.; Chen, L.X.; Ratner, M.A. The next breakthrough for organic photovoltaics? *J. Phys. Chem. Lett.* **2015**, *6*, 77–84. [CrossRef] [PubMed]
24. Scharber, M.C.; Mühlbacher, D.; Koppe, M.; Denk, P.; Waldauf, C.; Heeger, A.J.; Brabec, C.J. Design rules for donors in bulk-heterojunction solar cells—towards 10% energy-conversion efficiency. *Adv. Mater.* **2006**, *18*, 789–794. [CrossRef]
25. Biskup, T. Structure–function relationship of organic semiconductors: Detailed insights from time-resolved EPR spectroscopy. *Front. Chem.* **2019**, *7*, 10. [CrossRef]
26. Forbes, M.D.; Jarocha, L.E.; Sim, S.; Tarasov, V.F. Time-resolved electron paramagnetic resonance spectroscopy: History, technique, and application to supramolecular and macromolecular chemistry. *Adv. Phys. Org. Chem.* **2014**, *47*, 1–83.
27. Weber, S. Transient EPR. *eMagRes* **2017**, *6*, 255–270.

28. Biskup, T.; Sommer, M.; Rein, S.; Meyer, D.L.; Kohlstädt, M.; Würfel, U.; Weber, S. Ordering of PCDTBT revealed by time-resolved electron paramagnetic resonance spectroscopy of its triplet excitons. *Angew. Chem. Int. Ed.* **2015**, *54*, 7707–7710. [CrossRef]
29. Meyer, D.L.; Matsidik, R.; Huettner, S.; Sommer, M.; Biskup, T. Solvent-mediated aggregate formation of PNDIT2: Decreasing the available conformational subspace by introducing locally highly ordered domains. *Phys. Chem. Chem. Phys.* **2018**, *20*, 2716–2723. [CrossRef]
30. Yu, G.; Gao, J.; Hummelen, J.C.; Wudl, F.; Heeger, A.J. Polymer photovoltaic cells: Enhanced efficiencies via a network of internal donor-acceptor heterojunctions. *Science* **1995**, *270*, 1789–1791. [CrossRef]
31. Szarko, J.M.; Guo, J.; Liang, Y.; Lee, B.; Rolczynski, B.S.; Strzalka, J.; Xu, T.; Loser, S.; Marks, T.J.; Yu, L.; et al. When function follows form: Effects of donor copolymer side chains on film morphology and BHJ solar cell performance. *Adv. Mater.* **2010**, *22*, 5468–5472. [CrossRef]
32. Lan, S.C.; Chang, C.K.; Lu, Y.H.; Lin, S.W.; Jen, A.K.Y.; Wei, K.H. Side chain structure affects the molecular packing and photovoltaic performance of oligothiophene-based solution-processable small molecules. *RSC Adv.* **2015**, *5*, 67718–67726. [CrossRef]
33. Oberhumer, P.M.; Huang, Y.S.; Massip, S.; James, D.T.; Tu, G.; Albert-Seifried, S.; Beljonne, D.; Cornil, J.; Kim, J.S.; Huck, W.T.S.; et al. Tuning the electronic coupling in a low-bandgap donor–acceptor copolymer via the placement of side-chains. *J. Chem. Phys.* **2011**, *134*, 114901. [CrossRef] [PubMed]
34. Ko, S.; Hoke, E.T.; Pandey, L.; Hong, S.; Mondal, R.; Risko, C.; Yi, Y.; Noriega, R.; McGehee, M.D.; Brédas, J.L.; et al. Controlled conjugated backbone twisting for an increased open-circuit voltage while having a high short-circuit current in poly(hexylthiophene) derivatives. *J. Am. Chem. Soc.* **2012**, *134*, 5222–5232. [CrossRef]
35. Lu, L.P.; Finlayson, C.E.; Kabra, D.; Albert-Seifried, S.; Song, M.H.; Havenith, R.W.A.; Tu, G.; Huck, W.T.S.; Friend, R.H. The influence of side-chain position on the optoelectronic properties of a red-emitting conjugated polymer. *Macromol. Chem. Phys.* **2013**, *214*, 967–974. [CrossRef]
36. Mei, J.; Bao, Z. Side chain engineering in solution-processable conjugated polymers. *Chem. Mater.* **2014**, *26*, 604–615. [CrossRef]
37. Banerji, N.; Gagnon, E.; Morgantini, P.Y.; Valouch, S.; Mohebbi, A.R.; Seo, J.H.; Leclerc, M.; Heeger, A.J. Breaking down the problem: Optical transitions, electronic structure, and photoconductivity in conjugated polymer PCDTBT and in its separate building blocks. *J. Phys. Chem. C* **2012**, *116*, 11456–11469. [CrossRef]
38. Meyer, D.L.; Matsidik, R.; Sommer, M.; Biskup, T. Electronic structure trumps planarity: Unexpected narrow exciton delocalization in PNDIT2 revealed by time-resolved EPR spectroscopy. *Adv. Electron. Mater.* **2018**, *4*, 1700384. [CrossRef]
39. Matt, C.; Meyer, D.L.; Lombeck, F.; Sommer, M.; Biskup, T. TBT entirely dominates the electronic structure of the conjugated copolymer PCDTBT: Insights from time-resolved electron paramagnetic resonance spectroscopy. *Macromolecules* **2018**, *51*, 4341–4349. [CrossRef]
40. Blouin, N.; Michaud, A.; Leclerc, M. A low-bandgap poly(2,7-carbazole) derivative for use in high-performance solar cells. *Adv. Mater.* **2007**, *19*, 2295–2300. [CrossRef]
41. Blouin, N.; Michaud, A.; Gendron, D.; Wakim, S.; Blair, E.; Neagu-Plesu, R.; Belletête, M.; Durocher, G.; Tao, Y.; Leclerc, M. Toward a rational design of poly(2,7-carbazole) derivatives for solar cells. *J. Am. Chem. Soc.* **2008**, *130*, 732–742. [CrossRef]
42. Zhang, Y.; Zhou, H.; Seifter, J.; Ying, L.; Mikhailovsky, A.; Heeger, A.J.; Bazan, G.C.; Nguyen, T.Q. Molecular doping enhances photoconductivity in polymer bulk heterojunction solar cells. *Adv. Mater.* **2013**, *25*, 7038–7044. [CrossRef]
43. Cho, S.; Seo, J.H.; Park, S.H.; Beaupré, S.; Leclerc, M.; Heeger, A.J. A thermally stable semiconducting polymer. *Adv. Mater.* **2010**, *22*, 1253–1257. [CrossRef] [PubMed]
44. Sun, Y.; Takacs, C.J.; Cowan, S.R.; Seo, J.H.; Gong, X.; Roy, A.; Heeger, A.J. Efficient, air-stable bulk heterojunction polymer solar cells using MoO_x as the anode interfacial layer. *Adv. Mater.* **2011**, *23*, 2226–2230. [CrossRef]
45. Peters, C.H.; Sachs-Quintana, I.T.; Kastrop, J.P.; Beaupré, S.; Leclerc, M.; McGehee, M.D. High efficiency polymer solar cells with long operating lifetimes. *Adv. Energy Mater.* **2011**, *1*, 491–494. [CrossRef]
46. Kong, J.; Song, S.; Yoo, M.; Lee, G.Y.; Kwon, O.; Park, J.K.; Back, H.; Kim, G.; Lee, S.H.; Suh, H.; et al. Long-term stable polymer solar cells with significantly reduced burn-in loss. *Nat. Commun.* **2014**, *5*, 5688. [CrossRef]

47. Beaupré, S.; Leclerc, M. PCDTBT: en route for low cost plastic solar cells. *J. Mater. Chem. A* **2013**, *1*, 11097–11105. [CrossRef]
48. Lombeck, F.; Komber, H.; Fazzi, D.; Nava, D.; Kuhlmann, J.; Stegerer, D.; Strassel, K.; Brandt, J.; de Zerio Mendaza, A.D.; Müller, C.; et al. On the effect of prevalent carbazole homocoupling defects on the photovoltaic performance of PCDTBT:$PC_{71}BM$ solar cells. *Adv. Energy Mater.* **2016**, *6*, 1601232. [CrossRef]
49. Beiley, Z.M.; Hoke, E.T.; Noriega, R.; Dacuña, J.; Burkhard, G.F.; Bartelt, J.A.; Salleo, A.; Toney, M.F.; McGehee, M.D. Morphology-dependent trap formation in high performance polymer bulk heterojunction solar cells. *Adv. Energy Mater.* **2011**, *1*, 954–962. [CrossRef]
50. Wang, H.W.; Pentzer, E.; Emrick, T.; Russell, T.P. Preparation of low band gap fibrillar structures by solvent-induced crystallization. *ACS Macro Lett.* **2014**, *3*, 30–34. [CrossRef]
51. Ibraikulov, O.A.; Ngov, C.; Chávez, P.; Bulut, I.; Heinrich, B.; Boyron, O.; Ivanov, K.L.G.D.A.; Swaraj, S.; Méry, S.; Leclerc, N.; et al. Face-on orientation of fluorinated polymers conveyed by long alkyl chains: A prerequisite for high photovoltaic performances. *J. Mater. Chem. A* **2018**, *6*, 12038–12045. [CrossRef]
52. Osaka, I.; Kakara, T.; Takemura, N.; Koganezawa, T.; Takimiya, K. Naphthodithiophene–naphthobisthiadiazole copolymers for solar cells: Alkylation drives the polymer backbone flat and promotes efficiency. *J. Am. Chem. Soc.* **2015**, *135*, 8834–8837. [CrossRef] [PubMed]
53. Rand, B.P.; Cheyns, D.; Vasseur, K.; Giebink, N.C.; Mothy, S.; Yi, Y.; Coropceanu, V.; Beljonne, D.; Cornil, J.; Brédas, J.L.; et al. The impact of molecular orientation on the photovoltaic properties of a phthalocyanine/fullerene heterojunction. *Adv. Funct. Mater.* **2012**, *22*, 2987–2995. [CrossRef]
54. Akaike, K.; Ando, S.; Enozawa, H.; Kosaka, A.; Kajitani, T.; Fukushima, T. An electron-accepting molecular unit exhibiting an orientational preference favorable for organic photovoltaic applications. *Thin Solid Film.* **2015**, *583*, 34–39. [CrossRef]
55. Meyer, D.L.; Schmidt-Meinzer, N.; Rein, S.; Matt, C.; Lombeck, F.; Sommer, M.; Biskup, T. Side-chain engineering of conjugated polymers: Distinguishing its impact on film morphology and electronic structure. *J. Phys. Chem. C* **2019**, submitted.
56. Lombeck, F.; Di, D.; Yang, L.; Meraldi, L.; Athanasopoulos, S.; Credgington, D.; Sommer, M.; Friend, R.H. PCDTBT: From polymer photovoltaics to light-emitting diodes by side-chain-controlled luminescence. *Macromolecules* **2016**, *49*, 9382–9387. [CrossRef]
57. Lombeck, F.; Komber, H.; Gorelsky, S.I.; Sommer, M. Identifying homocouplings as critical side reactions in direct arylation polycondensation. *ACS Macro Lett.* **2014**, *3*, 819–823. [CrossRef]
58. Meyer, D.L.; Lombeck, F.; Huettner, S.; Sommer, M.; Biskup, T. Direct $S_0 \rightarrow T$ excitation of a conjugated polymer repeat unit: Unusual spin-forbidden transitions probed by time-resolved electron paramagnetic resonance spectroscopy. *J. Phys. Chem. Lett.* **2017**, *8*, 1677–1682. [CrossRef]
59. Lombeck, F.; Marx, F.; Strassel, K.; Kunz, S.; Lienert, C.; Komber, H.; Friend, R.; Sommer, M. To branch or not to branch: C–H selectivity of thiophene-based donor–acceptor–donor monomers in direct arylation polycondensation exemplified by PCDTBT. *Polym. Chem.* **2017**, *8*, 4738–4745. [CrossRef]
60. Stoll, S.; Schweiger, A. EasySpin, a comprehensive software package for spectral simulation and analysis in EPR. *J. Magn. Reson.* **2006**, *178*, 42–55. [CrossRef]
61. Neese, F. The ORCA program package. *Wiley Interdiscip. Rev.-Comput. Mol. Sci.* **2012**, *2*, 73–78. [CrossRef]
62. Becke, A.D. Density–functional exchange–energy approximation with correct asymptotic behavior. *Phys. Rev. A* **1988**, *38*, 3098–3100. [CrossRef]
63. Perdew, J.P. Density–functional approximation for the correlation energy of the inhomogeneous electron gas. *Phys. Rev. B* **1986**, *33*, 8822–8824. [CrossRef]
64. Becke, A.D. Density-functional thermochemistry. III. The role of exact exchange. *J. Chem. Phys.* **1993**, *98*, 5648–5652. [CrossRef]
65. Lee, C.; Yang, W.; Parr, R.G. Development of the Colle-Salvetti correlation-energy formula into a functional of the electron density. *Phys. Rev. B* **1988**, *37*, 785–789. [CrossRef]
66. Weigend, F.; Ahlrichs, R. Balanced basis sets of split valence, triple zeta valence and quadruple zeta valence quality for H to Rn: Design and assessment of accuracy. *Phys. Chem. Chem. Phys.* **2005**, *7*, 3297–3305. [CrossRef] [PubMed]

67. Petersson, G.A.; Bennett, A.; Tensfeldt, T.G.; Al-Laham, M.A.; Shirley, W.A.; Mantzaris, J. A complete basis set model chemistry. I. The total energies of closed-shell atoms and hydrides of the first-row elements. *J. Chem. Phys.* **1988**, *89*, 2193–2218. [CrossRef]
68. Petersson, G.A.; Al-Laham, M.A. A complete basis set model chemistry. II. Open-shell systems and the total energies of the first-row atoms. *J. Chem. Phys.* **1991**, *94*, 6081–6090. [CrossRef]
69. Barone, V. Structure, Magnetic Properties and Reactivities of Open-Shell Species From Density Functional and Self-Consistent Hybrid Methods. In *Recent Advances in Density Functional Methods (Part I); Recent Advances in Computational Chemistry*; Chong, D.P., Ed.; World Scientific: Singapore, 1995; Volume 1, Chapter 8, pp. 287–334.
70. Sinnecker, S.; Rajendran, A.; Klamt, A.; Diedenhofen, M.; Neese, F. Calculation of solvent shifts on electronic g-tensors with the conductor-like screening model (COSMO) and its self-consistent generalization to real solvents (direct COSMO-RS). *J. Phys. Chem. A* **2006**, *110*, 2235–2245. [CrossRef] [PubMed]
71. Hanwell, M.D.; Curtis, D.E.; Lonie, D.C.; Vandermeersch, T.; Zurek, E.; Hutchison, G.R. Avogadro: An advanced semantic chemical editor, visualization, and analysis platform. *J. Cheminform.* **2012**, *4*, 17. [CrossRef]
72. Pettersen, E.F.; Goddard, T.D.; Huang, C.C.; Couch, G.S.; Greenblatt, D.M.; Meng, E.C.; Ferrin, T.E. UCSF Chimera—A visualization system for exploratory research and analysis. *J. Comput. Chem.* **2004**, *25*, 1605–1612. [CrossRef]
73. Biskup, T. Time-resolved EPR of radical pair intermediates in cryptochromes. *Mol. Phys.* **2013**, *111*, 3698–3703. [CrossRef]
74. Hall, P.L.; Angel, B.R.; Jones, J.P.E. Dependence of spin Hamiltonian parameters *E* and *D* on labeling of magnetic axes: Application to ESR of high-spin Fe^{3+}. *J. Magn. Reson.* **1974**, *15*, 64–68. [CrossRef]
75. Weil, J.A.; Bolton, J.R. *Electron Paramagnetic Resonance: Elementary Theory and Practical Applications*, 2nd ed.; John Wiley & Sons, Inc.: Hoboken, NJ, USA, 2007.
76. Franco, F., Jr. Computational study on the structural and optoelectronic properties of a cabazole-benzothiadiazole based conjugated oligomer with various alkyl side-chain lengths. *Mol. Simul.* **2017**, *43*, 222–227. [CrossRef]
77. Akimov, A.; Masitov, A.; Korchagin, D.; Chapyshev, S.; Misochko, E.; Savitsky, A. W-band EPR studies of high-spin nitrenes with large spin-orbit contribution to zero-field splitting. *J. Chem. Phys.* **2015**, *143*, 084313. [CrossRef] [PubMed]
78. Risko, C.; McGehee, M.D.; Brédas, J.L. A quantum-chemical perspective into low optical-bandgap polymers for highly-efficient organic solar cells. *Chem. Sci.* **2011**, *2*, 1200–1218. [CrossRef]
79. Hornig, A.W.; Hyde, J.S. Paramagnetic resonance in triplet naphthalene at liquid helium temperatures. *Mol. Phys.* **1963**, *6*, 33–41. [CrossRef]
80. Schuch, H.; Seiff, F.; Furrer, R.; Möbius, K.; Dinse, K.P. Direkte Bestimmung des absoluten Vorzeichens des Triplett-Nullfeld-Parameters *D* mit hochauflösender optischer Detektion von ESR. *Z. Naturforsch. A* **1974**, *29*, 1543–1547. [CrossRef]
81. Hochstrasser, R.M.; Lin, T.S. Magnetic and electric field spectra of organic crystals: Optical measurements of zero-field splittings. *J. Chem. Phys.* **1968**, *49*, 4929–4945. [CrossRef]
82. Tinti, D.S.; Kothandaraman, G.; Harris, C.B. Determination of the absolute sign of the electron spin dipolar and nuclear quadrupolar interactions in molecular excited triplet states. *J. Chem. Phys.* **1973**, *59*, 190–193. [CrossRef]
83. Yamaguchi, Y.; Sakamoto, N. Exchange interactions and magnetic susceptibilities of Ni^{2+} in $KMgF_3$ and K_2MgF_4. *J. Phys. Soc. Jpn.* **1969**, *27*, 1444–1450. [CrossRef]
84. Tait, C.E.; Neuhaus, P.; Anderson, H.L.; Timmel, C.R. Triplet state delocalization in a conjugated porphyrin dimer probed by transient electron paramagnetic resonance techniques. *J. Am. Chem. Soc.* **2015**, *137*, 6670–6679. [CrossRef] [PubMed]

Supplementary Materials: Side Chain Engineering of PCDTBT: Impact on Electronic Structure

Clemens Matt [1], Florian Lombeck [2], Michael Sommer [2,†], and Till Biskup [1,*]

Contents

1. EPR Instrumentation

TREPR spectroscopy with a time resolution of up to 10 ns allows for real-time observation, *e.g.*, of short-lived radical-pair and triplet states generated by pulsed laser excitation. In contrast to conventional continuous-wave EPR spectroscopy, which usually involves magnetic-field modulation to improve the signal-to-noise ratio, TREPR is recorded in a high-bandwidth direct-detection mode, so as not to constrain the time resolution of the experiment. Consequently, positive and negative signal amplitudes in TREPR correspond to enhanced absorptive (A) and emissive (E) electron-spin polarisations of the EPR transitions, respectively.

All TREPR experiments were performed at 80 K using a commercial EPR spectrometer (Bruker ESP380E) in conjunction with a Bruker microwave bridge (ER 046 MRT) equipped with a low-noise high-bandwidth video amplifier. The sample was placed in a synthetic-quartz (Suprasil) sample tube (3 mm inner diameter) and irradiated in a dielectric-ring resonator (Bruker ER 4118X-MD5), which was immersed in a helium gas-flow cryostat (Oxford CF-935) cooled with liquid nitrogen. The temperature was regulated to ±0.1 K by a temperature controller (Oxford ITC-503). The time resolution of the experimental setup was in the 10 ns range. A microwave frequency counter (Hewlett-Packard HP 5352B) was used to monitor the microwave frequency.

Optical excitation at the respective wavelengths was carried out with an optical parametric oscillator (OPO) system (Opta BBO-355-vis/IR) pumped by an Nd:YAG laser (Spectra Physics, Quanta Ray GCR 190-10) with a pulse width of approximately 6 ns, and a pulse energy of 1 mJ. The repetition rate of the laser was set to 10 Hz. A transient recorder (LeCroy 9354A) with a digitizing rate of 2 ns/11 bit was used to acquire the time-dependent EPR signal. To eliminate the background signal induced by the laser entering the EPR cavity, TREPR signals were accumulated at off-resonance magnetic-field positions (background) and subtracted from those recorded on-resonance. This background signal is completely independent in its shape from both, laser wavelength and magnetic field, and normally long-lived compared to the detected spin-polarised EPR signal. Background subtraction was performed directly in the transient recorder and a background signal repeatedly recorded after each tenth time trace of the experimental data.

Further experimental parameters (except where explicity given) are as follows: Microwave frequency, 9.700 GHz, microwave power: 2 mW (20 dB attenuation, source power 200 mW), frequency-mixer detection, video amplifier set to 42 dB amplification and 25 MHz bandwidth, between 850 and 1400 averages per point.

2. TREPR spectra of triplet states

As TREPR spectra of spin-polarised triplet states of organic molecules recorded at X-band frequencies and magnetic fields are normally dominated by the zero-field splitting (ZFS) interaction, the hamilton operator used to describe the system reduces dramatically. The only contributions that need to be taken into account are the Hamilton operator for the Zeeman interaction, $\mathcal{H}_{\mathrm{EZ}}$, and the one for the ZFS interaction, $\mathcal{H}_{\mathrm{ZFS}}$:

$$\hat{\mathcal{H}} = \hat{\mathcal{H}}_{\mathrm{EZ}} + \hat{\mathcal{H}}_{\mathrm{ZFS}} = g_e \beta_e \boldsymbol{B}^{\mathrm{T}} \cdot \hat{\boldsymbol{S}} + \hat{\boldsymbol{S}}^{\mathrm{T}} \cdot \boldsymbol{D} \cdot \hat{\boldsymbol{S}} \,. \tag{1}$$

All other contributions can be considered as small perturbations that can be accounted for using (inhomogeneous) line broadening.

The $\boldsymbol{D}$ tensor in its principal axis system is given to

$$\boldsymbol{D} = \begin{pmatrix} -\frac{1}{3}D + E & 0 & 0 \\ 0 & -\frac{1}{3}D - E & 0 \\ 0 & 0 & \frac{2}{3}D \end{pmatrix} \tag{2}$$

where D and E are the zero-field-splitting parameters that can be directly read out from the experimental spectra (cf. Fig. S1). Note that D and E are defined such in the simulation routine used that the relation $|E| \leq |D|/3$ always holds.

3. Spectral simulations of TREPR spectra of triplet states

All simulations of triplet spectra have been performed using the EasySpin software package [1] available for MATLAB® (MathWorks), and here the routine `pepper`. Parameters included were the $\boldsymbol{g}$ and $\boldsymbol{D}$ tensor and the triplet sublevel populations (in zero field). Line broadening (Γ) was included using a combination of Lorentzian (Γ_{L}) and Gaussian (Γ_{G}) lines. For all simulations, the $\boldsymbol{g}$ tensor was assumed to be isotropic, with $g_{\mathrm{iso}} = 2.002$. This left the parameters D and E of the zero-field splitting tensor $\boldsymbol{D}$, the populations p_1, p_2, and p_3, and the two line widths Γ_{L} and Γ_{G} as the only free parameters that were adjusted.

Fitting the spectral simulations to the experimental data was done with the routine `lsqcurvefit` from the MATLAB® Optimization Toolbox™ using the trust-region-reflective least squares algorithm.

The nonlinear least-square solver finds the m coefficients $\boldsymbol{a}$ that solve the problem

$$\min_{\boldsymbol{a}} \sum_i (f(x_i; \boldsymbol{a}) - y_i)^2 \tag{3}$$

with y_i being the measured data and $f(x_i; \boldsymbol{a})$ the fitting function $f : \mathbb{R}^m \to \mathbb{R}^n$ with the same size n as the measured data y_i

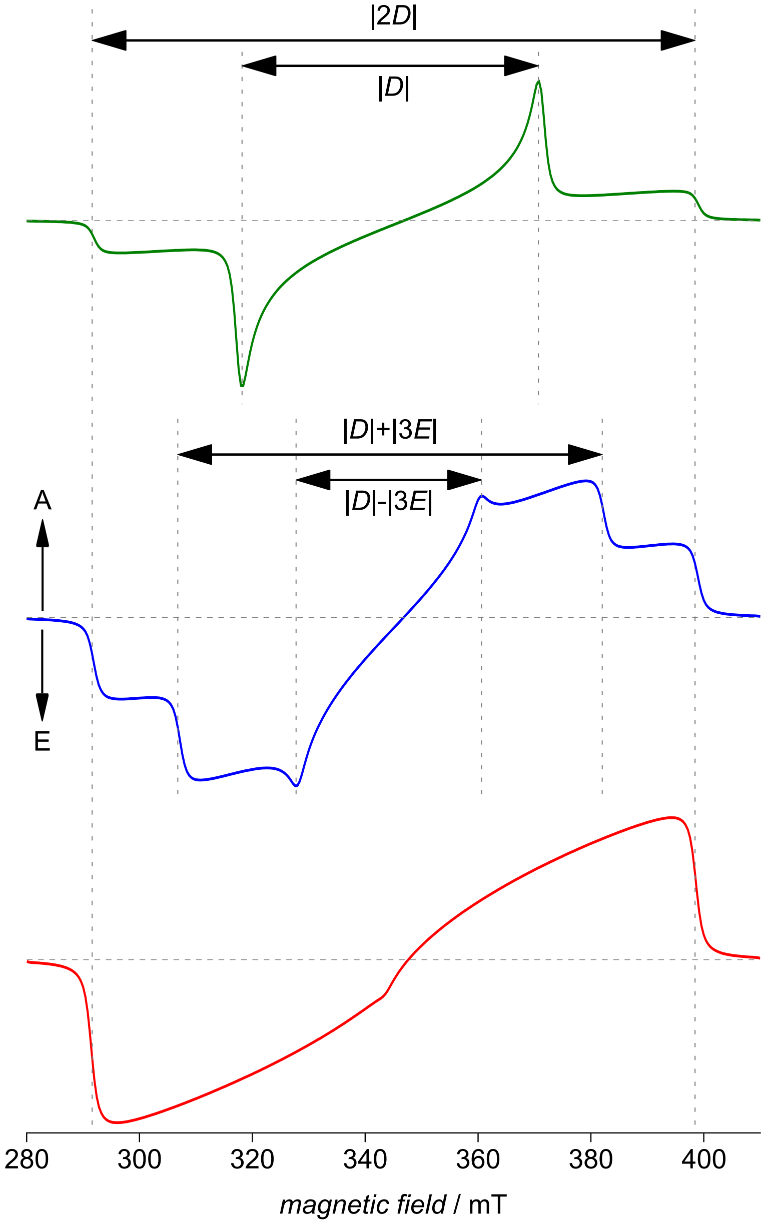

Figure S1. Characteristics of TREPR spectra of (photo-generated) triplet states. Three characteristic situations for the ratio of the two parameters D and E of the ZFS tensor are depicted here: the fully axial case (top, green), an intermediate case (blue, centre) and a fully rhombic case (red, bottom). Spectra were calculated using EasySpin. [2] The zero-field populations $p_{1,2,3}$ of the three triplet sublevels are far from thermal equilibrium, due to optical excitation and the inherent anisotropy of the intersystem crossing processes. Therefore, signals consist of both, absorptive (A) and emissive (E) contributions.

Error estimation of the fitting parameters was carried out by using the Jacobian matrix **J**. J_{ij} is the partial derivative of the fitting function $f(x_i;\boldsymbol{a})$ with respect to a_j at the solution a_0.

$$J_{ij}(\boldsymbol{a}_0) := \left(\frac{\partial f(x_i;\boldsymbol{a})}{\partial a_j}(\boldsymbol{a}_0)\right)_{i=1...n,j=1...m} \tag{4}$$

$$\mathbf{J}(\boldsymbol{a}_0) = \begin{pmatrix} \frac{\partial f(x_1;\boldsymbol{a})}{\partial a_1}(\boldsymbol{a}_0) & ... & \frac{\partial f(x_1;\boldsymbol{a})}{\partial a_m}(\boldsymbol{a}_0) \\ ... & & \\ \frac{\partial f(x_n;\boldsymbol{a})}{\partial a_1}(\boldsymbol{a}_0) & ... & \frac{\partial f(x_n;\boldsymbol{a})}{\partial a_m}(\boldsymbol{a}_0) \end{pmatrix} \tag{5}$$

The variances of the coefficients a_j are given by the diagonal elements of the covariance matrix, **C**, i.e. $\sigma^2_{a_j} = C_{jj}$, where **C** is the inverse of the matrix **H**, variously referred to as the curvature or Hessian matrix.

The Hessian matrix was approximated by a series expansion, which is terminated after the first rank:

$$H_{jk} = \frac{1}{2}\frac{\partial^2\chi^2(\boldsymbol{a})}{\partial a_j \partial a_k} \approx \sum_{i=1}^{n} \frac{1}{\sigma_i^2}\frac{\partial f(x_i;\boldsymbol{a})}{\partial a_j}\frac{\partial f(x_i;\boldsymbol{a})}{\partial a_k}$$

Hence the Jacobian matrix can be used to approximate the Hessian if σ_i^2 is chosen to be equal for all points,

$$\mathbf{H} \approx \frac{1}{\sigma_i^2}\,\mathbf{J}^{\mathrm{T}} \cdot \mathbf{J}. \tag{6}$$

To speed up calculation time for the matrix product $\mathbf{J}^{\mathrm{T}} \cdot \mathbf{J}$, an economy-size QR decomposition of **J** was carried out, reducing the dimension of **R** to the size of $\boldsymbol{a}$:

$$\mathbf{J} = \mathbf{Q} \cdot \mathbf{R}. \tag{7}$$

In the following matrix multiplication, **Q** vanishes by multiplication with $\mathbf{Q}^{\mathrm{T}}$:

$$(\mathbf{J}^{\mathrm{T}} \cdot \mathbf{J})^{-1} = (\mathbf{R}^{\mathrm{T}} \cdot \mathbf{R})^{-1} = \mathbf{R}^{-1} \cdot (\mathbf{R}^{\mathrm{T}})^{-1} = \mathbf{R}^{-1} \cdot (\mathbf{R}^{-1})^{\mathrm{T}} \tag{8}$$

In MATLAB®, this implementation leads to high computational speed and only minor numerical errors. The corresponding code would be as follows:

```
[~,R] = qr(jacobian,0);
```

The diagonal elements of the approximated $\mathbf{H}^{-1}$ can easily be calculated by element-wise squaring followed by summation over the rows of **R**. Since σ_i^2 is chosen to be equal for all points, the errors for the fit parameters are given by:

```
stdDev = sqrt(variance * sum(inv(R).^2,2));
```

The fitting algorithm `lsqcurvefit` can optionally return the residuals as additional output argument, here termed `residuals`. Hence the variance of the residuals obtained as

```
variance = var(residuals);
```

was used as σ^2 for all points.

4. TREPR signal decay and triplet lifetime

The kinetics of TREPR signals of triplet states are rather complicated, involving spin relaxation, decay of spin polarisation, and decay of the actual triplet state, usually via intersystem crossing back into the singlet ground state. Hence, only a lower limit of the triplet lifetime can be extracted from the TREPR time profiles, based on the simple fact that regardless of all other processes, TREPR signals will only be observable as long as there exists a triplet state.

As can be seen from the full 2D datasets of all four compounds investigated in this study (Fig. S2), TREPR signals decay on the time scale of several microseconds. However, it is highly likely that this decay is dominated by the microwave power and other experimental parameters and that the actual triplet state lifetime extends well into tens or even hundreds of microseconds.

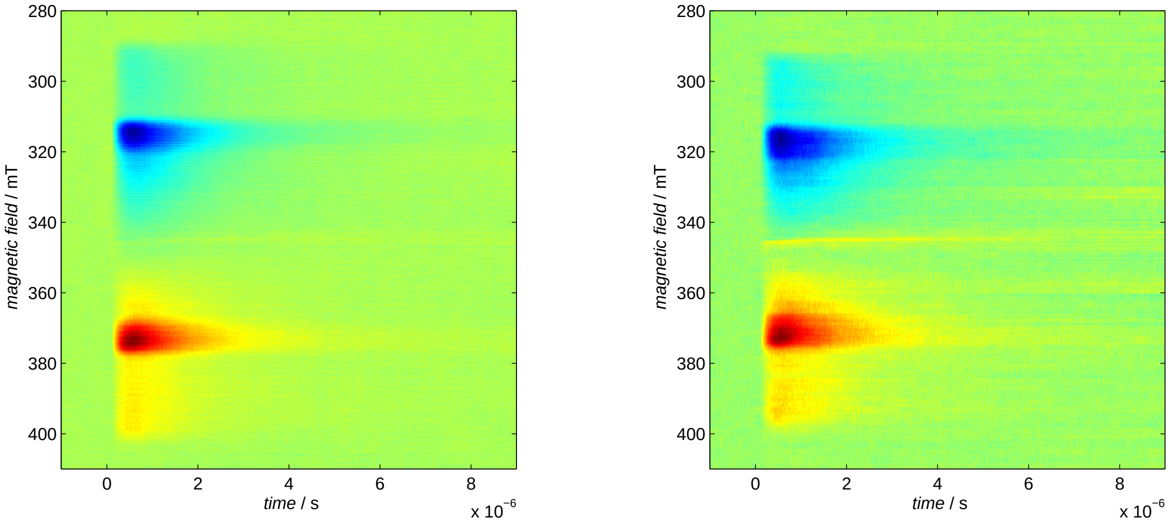

(a) **A** (hexTBT) (b) **D-A** (CbzhexTBT)

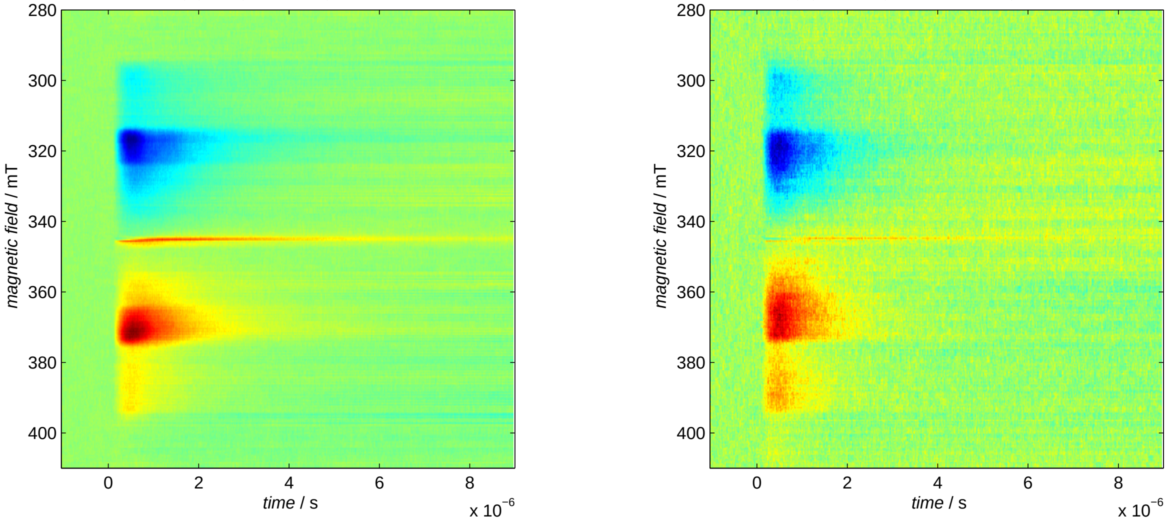

(c) **D-A-D** (CbzhexTBTCbz) (d) **(D-A)$_n$** (hexPCDTBT)

Figure S2. Full 2D TREPR datasets of all compounds investigated in this study. Blue colour denotes emissive, red colour enhanced absorptive polarisation. For experimental details see main text.

5. Temperature-dependent absorption spectra

To rule out effects of aggregation, temperature-dependent absorption spectra have been recorded for all substances investigated. The results are shown in Fig. S3. Due to the solvent, *o*-dichlorobenzene, not forming a transparent glass upon freezing, spectra could only be recorded until the solution froze out. As obvious from the spectra, none of the substances investigated showed any sign of aggregation under the conditions used here.

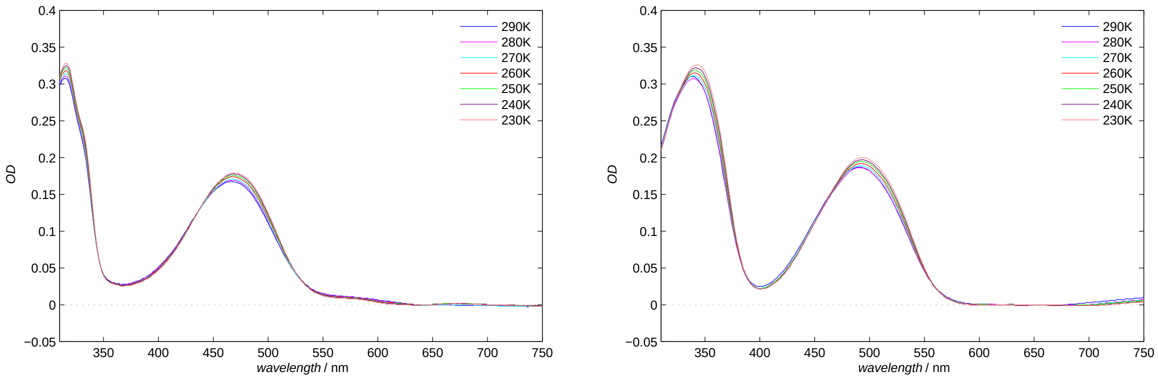

(a) **A** (hexTBT) (b) **D-A** (CbzhexTBT)

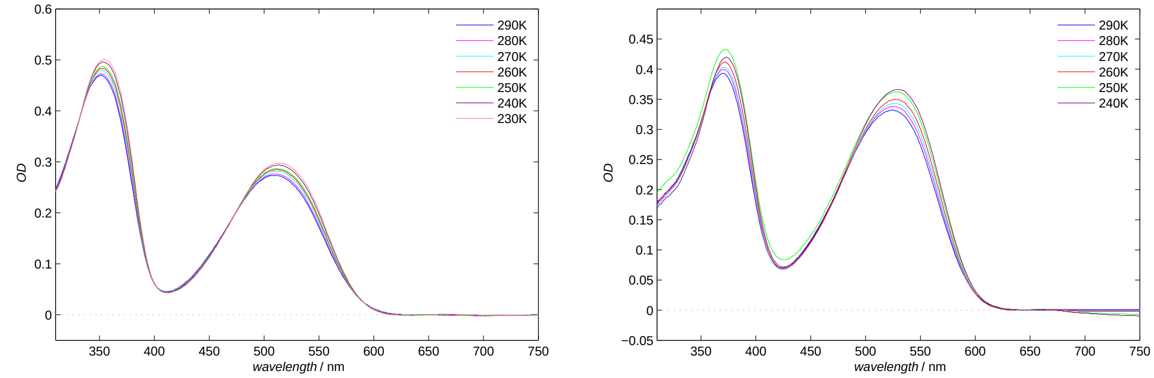

(c) **D-A-D** (CbzhexTBTCbz) (d) **(D-A)$_n$** (hexPCDTBT)

Figure S3. Temperature-dependent absorption spectra of all compounds investigated in this study. Due to the solvent, *o*-dichlorobenzene, not forming a transparent glass upon freezing, spectra could only be recorded until the solution froze out.

6. Comparison of non-hexylated and hexylated compounds

The non-hexylated polymer and its building blocks have been investigated previously [2]. For a detailed discussion of the differences and commonalities between the two systems, hexylated and non-hexylated, see the main text. Here, both steady-state absorption spectra (Fig. S4) as well as TREPR data (Fig. S5), are presented face to face for ease of comparison. Additionally, Tab. S1 summarises the simulation parameters for the spectral simulations of both systems.

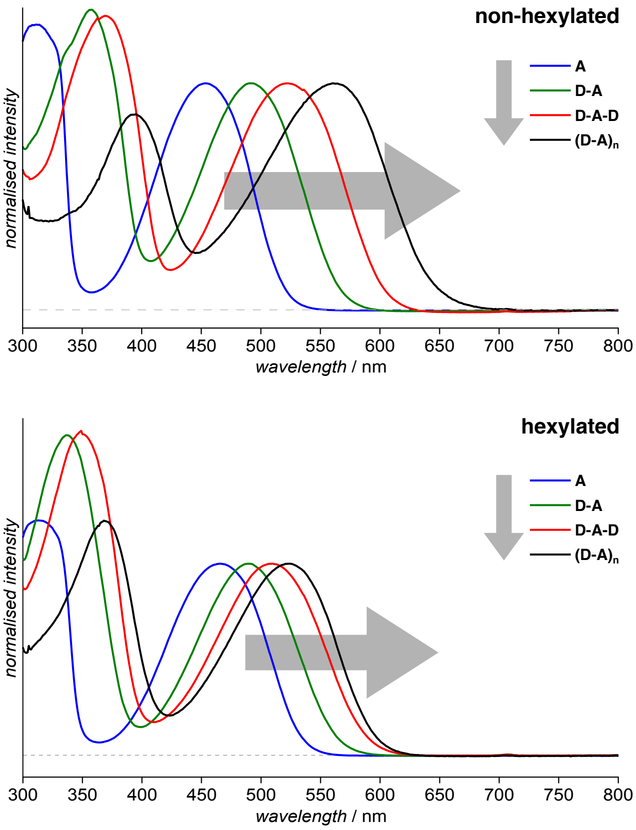

Figure S4. Comparison of the steady-state absorption spectra of the non-hexylated and hexylated compounds. All spectra have been recorded at room temperature in standard path length cuvettes in *o*-dichlorobenzene. Data for the non-hexylated compounds (top) taken from Ref. [2].

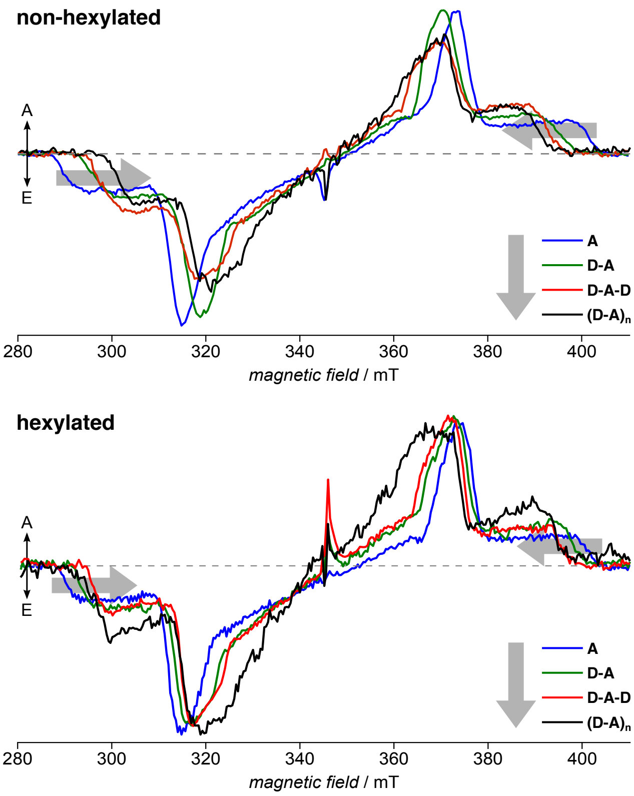

Figure S5. Comparison of the TREPR spectra of the non-hexylated and hexylated compounds. All spectra have been recorded at 80 K with the identical setup described above. Samples have been excited with wavelengths corresponding to the maximum of their respective CT band. Data for the non-hexylated compounds (top) taken from Ref. [2].

Table S1. Simulation parameters for the spectral simulations of the TREPR spectra shown in Fig. S5. λ_{ex} is the excitation wavelength used (maximum of the CT band), D and E are the parameters of the zero-field splitting tensor of the dipolar interaction, Γ_{L} is the Lorentzian line width, and $p_{1,2,3}$ are the populations of the three triplet sublevels, respectively. For actual simulations see the main text and Ref. [2], for details of the fitting procedure see above.

	λ_{ex}/nm	$\lvert D\rvert$/MHz	$\lvert E\rvert$/MHz	$\lvert E\rvert/\lvert D\rvert$	Γ_{L}/mT	$p_{1,2,3}$
			non-hexylated			
A	454	1550 ± 2.2	70 ± 1.0	0.045	2.36 ± 0.09	0.000, 0.182, 0.818
D-A	492	1362 ± 2.5	76 ± 1.4	0.056	3.42 ± 0.13	0.000, 0.138, 0.862
D-A-D	522	1303 ± 3.6	101 ± 1.7	0.078	2.96 ± 0.16	0.000, 0.309, 0.691
(D-A)$_\mathbf{n}$	550	1254 ± 3.0	101 ± 1.4	0.081	2.39 ± 0.13	0.000, 0.351, 0.649
			hexylated			
A	466	1539 ± 2.5	88 ± 1.1	0.057	1.72 ± 0.10	0.000, 0.152, 0.848
D-A	490	1457 ± 2.1	91 ± 0.9	0.062	1.84 ± 0.11	0.000, 0.256, 0.744
D-A-D	509	1387 ± 1.9	96 ± 0.8	0.069	1.38 ± 0.07	0.000, 0.264, 0.736
(D-A)$_\mathbf{n}$	518	1384 ± 3.1	87 ± 1.4	0.063	2.12 ± 0.15	0.000, 0.436, 0.564

7. Determining the angles between TBT and Cbz moieties

As the aromatic planes of the TBT and Cbz moieties can be twisted against each other in all three directions, the tilting cannot be ascribed fully by single dihedral angle between adjacent atoms. Hence, coordinate systems have been created in both aromatic planes and the angles between the x, y, and z axes compared to those of the planar structure.

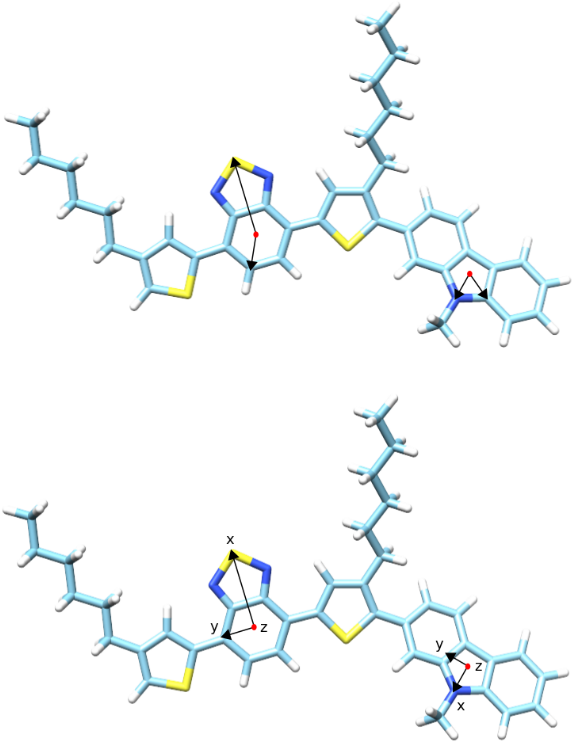

Figure S6. Illustration of constructing the vectors that have been used for determining the angles between TBT and Cbz moieties. The top panel shows the two vectors spanning the aromatic planes, whereas the complete coordinate systems in Cbz and TBT are shown in the bottom panel.

In a first step, the center of both, benzene and pyrroline rings have been calculated (red dot in Fig. S6) and the vectors from there to the S and N atom, respectively, created that form the x axis of the coordinate system. A second vector has been created pointing from the centre of the aromatic plane to one of the atoms in the aromatic plane to span this plane (Fig. S6, top). The cross product of these two vectors led to the z axis of the coordinate system. In the following, the cross product of the vectors for the x and z axis could be used to create the y axis and hence complete the coordinate system (Fig. S6, bottom).

As the cross product always generates one of two possible vectors being orthogonal to the two vectors multiplied, displaying all vectors was necessary to check that the correct vector has been found. If not, the two vectors for the cross product have to be swapped.

For convenience, the angles for the cis-trans configuration given already in the main text are shown in Tab. S2 for both types of calculations performed, with BP86/Def2-SVP and B3LYP/6-31G**. As can be readily seen, geometries optimised using BP86/Def2-SVP are very flat, whereas particularly for the polymer, B3LYP/6-31G** predicts a twist in the backbone that seems not to be in line with our experimental results. For a detailed discussion, the reader is referred to the main text.

Table S2. Dihedral angles between the aromatic planes of Cbz and hexTBT moieties obtained from geometry optimisation in both, singlet and triplet state. The Cbz and hexTBT moieties are in themselves pretty flat. Angles are given in degrees and for the cis-trans configuration. Note that the longer fragment with $n = 7$ has a D moiety on both ends. Bold numbers for the triplet state geometries denote the angles directly adjacent to the A moiety carrying the maximum spin density. The spin density is always centred on one A moiety.

compound	state	dihedral angles													
		non-hexylated, BP86/Def2-SVP													
D-A	singlet	3.0													
	triplet	**1.1**													
D-A-D	singlet	1.0	3.2												
	triplet	**0.7**	**0.4**												
(D-A)$_4$	singlet	0.9	0.6	1.6	3.9	3.1	3.5	1.4							
	triplet	1.0	0.2	**0.5**	**1.1**	1.4	2.9	1.0							
		non-hexylated, B3LYP/6-31G**													
D-A	singlet	16.6													
	triplet	**7.2**													
D-A-D	singlet	16.7	16.7												
	triplet	**0.8**	**5.9**												
(D-A)$_4$	singlet	14.2	14.5	20.4	17.0	20.0	12.2	14.2							
	triplet	17.2	12.2	**10.1**	**9.0**	11.7	19.8	13.8							
		hexylated, BP86/Def2-SVP													
D-A	singlet	35.4													
	triplet	**27.0**													
D-A-D	singlet	37.2	35.8												
	triplet	**28.7**	**27.0**												
(D-A)$_4$	singlet	36.2	31.7	39.3	34.3	35.2	35.1	35.4							
	triplet	36.6	34.3	38.1	30.3	**22.5**	**25.2**	34.0							
(D-A)$_7$-D	singlet	38.2	37.3	38.7	36.0	41.3	32.5	36.4	32.9	33.4	33.0	38.2	38.3	35.2	34.9
	triplet	39.3	34.7	36.5	31.8	**23.3**	**24.5**	32.4	36.5	43.2	39.3	35.7	34.7	35.5	36.1
		hexylated, B3LYP/6-31G**													
D-A	singlet	38.4													
	triplet	**34.4**													
D-A-D	singlet	40.8	40.1												
	triplet	**36.1**	**36.0**												
(D-A)$_4$	singlet	43.5	35.6	39.0	37.3	46.0	39.9	32.5							
	triplet	38.3	38.0	**35.7**	**36.3**	39.7	39.2	33.3							

8. Quantitative analysis of spin density distributions

Whereas spin density plots on the optimised geometries of the molecules are very valuable to give an overall impression, they are less useful for a quantitative comparison.

ORCA normalises the calculated spin densities internally such that the sum of all spin densities equals to the number of spins involved. In case of a triplet state with two unpaired electron spins, this sum equals to two.

To calculate the relative amount of spin density on the TBT moiety, $r^{\mathrm{abs}}_{\mathrm{TBT}}(\mathrm{M})$, for all compounds, M, investigated, the spin density on the TBT moiety, $\rho_{\mathrm{TBT}}(\mathrm{M})$, has been divided by the spin density on the entire molecule, $\rho_{\mathrm{M}}(\mathrm{M})$ as follows:

$$r^{\mathrm{abs}}_{\mathrm{TBT}}(\mathrm{M}) = \frac{\sum |\rho_{\mathrm{TBT}}(\mathrm{M})|}{\sum |\rho_{\mathrm{M}}(\mathrm{M})|} \leq 1\,.$$

As spin densities can have positive and negative sign, the absolute values have been taken in this case, hence the notation r^{abs}. The resulting values can be found in Tab. S3 and graphically displayed in Fig. S7.

Table S3. Absolute amount of spin density on the TBT moiety as calculated with BP86 and B3LYP functionals on both geometries. Geometries have been optimised on the BP86/Def2-SVP and B3LYP/6-31G** level of theory, and spin densities calculated for both geometries and both functional/basis set combinations.

Geometry	Spin Density	**A**	**D-A**	**D-A-D**	**(D-A)$_{\mathrm{n}}$**
		non-hexyl			
BP86/Def2-SVP	BP86/Def2-SVP	1.00	0.87	0.77	0.52
BP86/Def2-SVP	B3LYP/6–31G**	1.00	0.89	0.84	0.80
B3LYP/6–31G**	BP86/Def2-SVP	1.00	0.88	0.78	0.71
B3LYP/6–31G**	B3LYP/6–31G**	1.00	0.90	0.85	0.84
		hexyl			
BP86/Def2-SVP	BP86/Def2-SVP	1.00	0.91	0.86	0.72
BP86/Def2-SVP	B3LYP/6–31G**	1.00	0.92	0.88	0.85
B3LYP/6–31G**	BP86/Def2-SVP	1.00	0.92	0.86	0.86
B3LYP/6–31G**	B3LYP/6–31G**	1.00	0.94	0.90	0.91

To get further insight, spin densities have been compared for the TBT unit in each of the compounds in form of a histogram. Therefore, spin densities of the TBT unit have to be normalised to the amount of spin density on the TBT moiety in the TBT compound, $\rho_{\mathrm{TBT}}(\mathrm{TBT})$, relative to the amount of spin density on the TBT moiety in the actual compound, $\rho_{\mathrm{TBT}}(\mathrm{M})$, and this time, the sign of the spin densities has to be taken into account:

$$r_{\mathrm{TBT}}(\mathrm{M}) = \frac{\sum \rho_{\mathrm{TBT}}(\mathrm{M})}{\sum \rho_{\mathrm{TBT}}(\mathrm{TBT})} \leq 1\,.$$

Note that, in our case, $\sum \rho_{\mathrm{TBT}}(\mathrm{TBT})$ does not amount to two, as one would naively expect, as the two protons present in TBT that are substituted successively in the larger compounds are not taken into account for calculating the ratio of the spin densities, but do possess some non-vanishing, although rather small, spin density. Hence this rather complicated way of calculating this ratio.

Having the two ratios of spin density on the TBT moiety as compared to the entire molecule at hand, we can proceed to calculate the correction factor $r_{\text{corr}}(\text{M})$ for the spin density values for the TBT moiety of a given compound:

$$r_{\text{corr}}(\text{M}) = \frac{r_{\text{TBT}}^{\text{abs}}(\text{M})}{r_{\text{TBT}}(\text{M})}$$

and with this, the corrected spin density for the TBT moiety of a given compound amounts to:

$$\rho_{\text{TBT}}^{\text{corr}}(\text{M}) = r_{\text{corr}}(\text{M}) \cdot \rho_{\text{TBT}}(\text{M})\,.$$

The values for $\rho_{\text{TBT}}^{\text{corr}}(\text{M})$ for each of the atoms have been displayed in the respective histograms.

9. Comparison of calculations with BP86 and B3LYP

As mentioned in the main text, geometry optimisations and spin density calculations of all compounds investigated have been performed both, with BP86/Def2-SVP [3–5] and B3LYP/6–31G** [6–9] as functional and basis set, respectively, and the results compared with each other. For all calculations, ORCA 3.0.3 [10] has been used. The solvent has been accounted for by the COSMO model [11]. Initial geometries of the molecules were created using Avogadro 1.1.1 [12]. Spin density plots were created using UCSF Chimera 1.11.2 [13].

For all four compounds investigated, geometry optimisations of their respective triplet states have been performed. The two sets of calculations differ clearly in the degree of planarity of the resulting geometries, as can be readily seen from a side view parallel to the aromatic planes (Fig. S7). For actual numbers of the dihedral angles between adjacent aromatic planes of Cbz and TBT moieties, cf. Tab. S2.

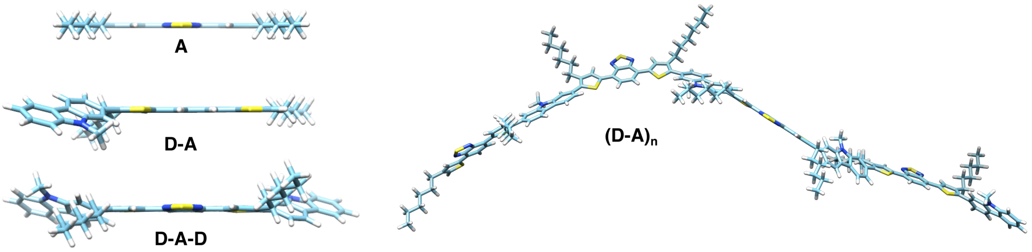

(a) BP86/Def2-SVP

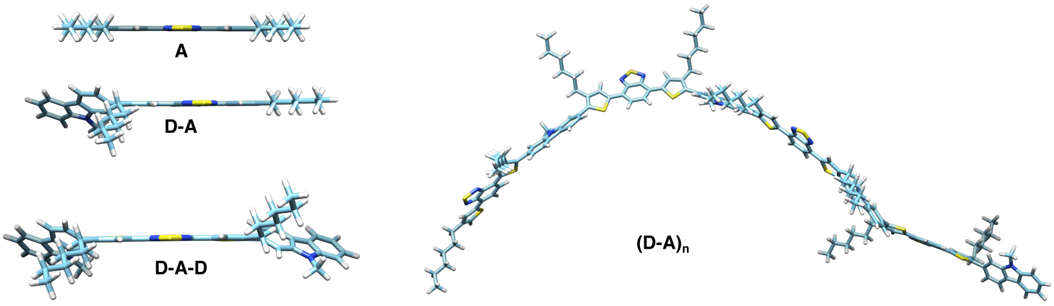

(b) B3LYP/6-31G**

Figure S7. Side-view of the optimised geometries of the triplet states of PCDTBT and its building blocks. Geometries have been optimised for the triplet state on the theory level BP86/Def2-SVP and B3LYP/6–31G**, respectively. As obvious from this side-view, all molecules are rather flat for BP86/Def2-SVP, with dihedral angles between the aromatic planes of Cbz and TBT, respectively, close to zero, whereas B3LYP/6–31G** results in clear distortions. For actual values of these dihedral angles, cf. Tab. S2.

Whereas the geometries calculated using BP86/Def2-SVP are basically flat, for B3LYP/6–31G**, particularly the polymer fragment with $n = 4$ shows clear distortions with dihedral angles up to approx. 20%.

10. *D* tensor calculation

We calculated the ***D*** tensor for each of the compounds for both geometries (using BP86/Def2-SVP and B3LYP/6-31G** level of theory, respectively) using B3LYP as functional and EPR-II [14] as basis set. Interestingly, all calculated tensors exhibit a mutually identical orientation within the molecular frame, with their x and y axes within the aromatic plane of the acceptor moiety and the z axis perpendicular to it. The x axis points perpendicular to the axis connecting thiophene–benzothiadiazole and the y axis along this connection (Figure S8). Assigning the ***D*** tensor axes is based on the usual convention $|D_z| > |D_y| > |D_x|$, assuming, *inter alia*, $|E| \leq |D|/3$ [15] and $E/D > 0$.

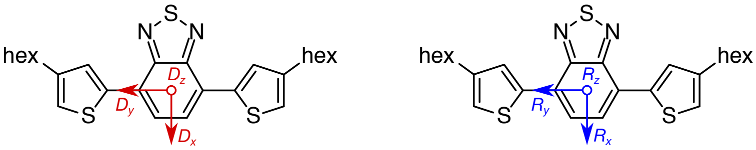

Figure S8. Orientation of the calculated *D* tensor within the TBT acceptor moiety and molecular reference frame. For each of the fragments investigated, the ***D*** tensor is basically oriented in the same way, as shown on the left. Assuming a right-handed coordinate system, the z component is pointing towards the paper plane. Only for the asymmetric repeat unit **D-A** a slight deviation from the molecular reference frame (R_i with $i = \{x, y, z\}$, right) of a few degrees has been obtained from the DFT calculations. The deviation from the reference frame is given as three dihedral angles, α, β, and γ, for each of the three axes, x, y, and z, respectively. For actual values of these angles see Table S4.

The molecular reference frame is given in Figure S8 (right), with the x and y axes as well within the aromatic plane of the acceptor moiety and the z axis perpendicular to it, accordingly. The deviations (dihedral angles) of the ***D*** tensor axes from the molecular reference frame are given in Table S4.

Table S4. Comparison of calculated and experimental *D* tensors as well as their orientation within the molecular reference frame. ***D*** tensors for each of the compounds have been calculated using the B3LYP/EPR-II level of theory. Values for $|D|$ and $|E|$ are given in MHz. For the orientation of the ***D*** tensor with respect to the molecular reference frame R_i with $i = \{x, y, z\}$ cf. Figure S8. The angles α, β, and γ (in degrees) refer to the deviation of the corresponding ***D*** tensor axes from the molecular reference frame. Only for the asymmetric repeat unit **D-A**, a slight deviation from the molecular reference frame has been obtained, with the x and y axis tilted towards the additional D moiety. Note that for the calculated values, the oligomer fragment with $n = 4$ has been used.

compound	$\|D\|$	$\|E\|$	$\|E\|/\|D\|$	$\|D\|$	$\|E\|$	$\|E\|/\|D\|$	α	β	γ
		calculated			experimental				
				non-hexylated, geometry: BP86/Def2-SVP					
A	847	179	0.21	1550	70	0.06	0.0	0.0	0.0
D-A	730	180	0.25	1362	76	0.06	4.0	4.1	0.5
D-A-D	662	174	0.26	1303	101	0.07	0.1	0.2	0.2
(D-A)$_\mathbf{n}$	662	180	0.27	1254	101	0.06	0.0	0.1	0.1
				non-hexylated, geometry: B3LYP/6-31G**					
A	857	183	0.21	1550	70	0.06	0.0	0.0	0.0
D-A	740	182	0.25	1362	76	0.06	3.9	3.9	0.3
D-A-D	671	176	0.26	1303	101	0.07	0.1	0.1	0.1
(D-A)$_\mathbf{n}$	665	176	0.26	1254	101	0.06	0.1	0.0	0.1
				hexylated, geometry: BP86/Def2-SVP					
A	808	179	0.22	1539	88	0.06	0.0	0.0	0.0
D-A	736	173	0.24	1457	91	0.06	2.3	2.3	0.2
D-A-D	688	170	0.25	1387	96	0.07	0.1	0.2	0.2
(D-A)$_\mathbf{n}$	675	173	0.26	1384	87	0.06	0.2	0.0	0.2
				hexylated, geometry: B3LYP/6-31G**					
A	818	177	0.22	1539	88	0.06	0.0	0.0	0.0
D-A	766	176	0.23	1457	91	0.06	1.7	1.7	0.0
D-A-D	726	174	0.24	1387	96	0.07	0.2	0.4	0.4
(D-A)$_\mathbf{n}$	736	176	0.24	1384	87	0.06	0.1	0.2	0.3

1. Stoll, S.; Schweiger, A. EasySpin, a comprehensive software package for spectral simulation and analysis in EPR. *J. Magn. Reson.* **2006**, *178*, 42–55.
2. Matt, C.; Meyer, D.L.; Lombeck, F.; Sommer, M.; Biskup, T. TBT entirely dominates the electronic structure of the conjugated copolymer PCDTBT: Insights from time-resolved electron paramagnetic resonance spectroscopy. *Macromolecules* **2018**, *51*, 4341–4349.
3. Becke, A.D. Density–functional exchange–energy approximation with correct asymptotic behavior. *Phys. Rev. A* **1988**, *38*, 3098–3100.
4. Perdew, J.P. Density–functional approximation for the correlation energy of the inhomogeneous electron gas. *Phys. Rev. B* **1986**, *33*, 8822–8824.
5. Weigend, F.; Ahlrichs, R. Balanced basis sets of split valence, triple zeta valence and quadruple zeta valence quality for H to Rn: Design and assessment of accuracy. *Phys. Chem. Chem. Phys.* **2005**, *7*, 3297–3305.
6. Becke, A.D. Density-functional thermochemistry. III. The role of exact exchange. *J. Chem. Phys.* **1993**, *98*, 5648–5652.
7. Lee, C.; Yang, W.; Parr, R.G. Development of the Colle-Salvetti correlation-energy formula into a functional of the electron density. *Phys. Rev. B* **1988**, *37*, 785–789.
8. Petersson, G.A.; Bennett, A.; Tensfeldt, T.G.; Al-Laham, M.A.; Shirley, W.A.; Mantzaris, J. A complete basis set model chemistry. I. The total energies of closed-shell atoms and hydrides of the first-row elements. *J. Chem. Phys.* **1988**, *89*, 2193–2218.
9. Petersson, G.A.; Al-Laham, M.A. A complete basis set model chemistry. II. Open-shell systems and the total energies of the first-row atoms. *J. Chem. Phys.* **1991**, *94*, 6081–6090.
10. Neese, F. The ORCA program package. *Wiley Interdiscip. Rev.-Comput. Mol. Sci.* **2012**, *2*, 73–78.
11. Sinnecker, S.; Rajendran, A.; Klamt, A.; Diedenhofen, M.; Neese, F. Calculation of solvent shifts on electronic g-tensors with the conductor-like screening model (COSMO) and its self-consistent generalization to real solvents (direct COSMO-RS). *J. Phys. Chem. A* **2006**, *110*, 2235–2245.
12. Hanwell, M.D.; Curtis, D.E.; Lonie, D.C.; Vandermeersch, T.; Zurek, E.; Hutchison, G.R. Avogadro: an advanced semantic chemical editor, visualization, and analysis platform. *J. Cheminformatics* **2012**, *4*, 17.
13. Pettersen, E.F.; Goddard, T.D.; Huang, C.C.; Couch, G.S.; Greenblatt, D.M.; Meng, E.C.; Ferrin, T.E. UCSF Chimera—A visualization system for exploratory research and analysis. *J. Comput. Chem.* **2004**, *25*, 1605–1612.
14. Barone, V. Structure, Magnetic Properties and Reactivities of Open-Shell Species From Density Functional and Self-Consistent Hybrid Methods. In *Recent Advances in Density Functional Methods (Part I)*; Chong, D.P., Ed.; World Scientific: Singapore, 1995; Vol. 1, *Recent Advances in Computational Chemistry*, chapter 8, p. 287–334.
15. Hall, P.L.; Angel, B.R.; Jones, J.P.E. Dependence of spin Hamiltonian parameters E and D on labeling of magnetic axes: application to ESR of high-spin Fe^{3+}. *J. Magn. Reson.* **1974**, *15*, 64–68.

5.3. Side-Chain Engineering of Conjugated Polymers: Distinguishing Its Impact on Film Morphology and Electronic Structure

Deborah L. Meyer, Noah Schmidt-Meinzer, Clemens Matt, Stephan Rein, Florian Lombeck, Michael Sommer and Till Biskup: Side-Chain Engineering of Conjugated Polymers: Distinguishing Its Impact on Film Morphology and Electronic Structure. *J. Phys. Chem. C*, 123 (2019), pp. 20071–20083 (DOI: 10.1021/acs.jpcc.9b02835)

Contributions of all authors:

Deborah L. Meyer: conception and study design, data aquisition (TREPR), data analysis, contributions to manuscript and manuscript review

Noah Schmidt-Meinzer: data aquisition (TREPR) and data analysis

Clemens Matt: data aquisition (DFT), data analysis, contributions to manuscript and manuscript review

Stephan Rein: Software development for data analysis

Florian Lombeck: sample synthesis and manuscript review

Michael Sommer: conception and study design and manuscript review

Till Biskup: conception and design of study, data acquisition (TREPR and UV-VIS), data analysis, main contribution to the manuscript and manuscript review

THE JOURNAL OF
PHYSICAL CHEMISTRY C

Article

Cite This: J. Phys. Chem. C 2019, 123, 20071−20083

pubs.acs.org/JPCC

Side-Chain Engineering of Conjugated Polymers: Distinguishing Its Impact on Film Morphology and Electronic Structure

Deborah L. Meyer,[†] Noah Schmidt-Meinzer,[†] Clemens Matt,[†] Stephan Rein,[†] Florian Lombeck,[‡] Michael Sommer,[§] and Till Biskup*[,†,∥]

[†]Institut für Physikalische Chemie, Albert-Ludwigs-Universität Freiburg, Albertstraße 21, 79104 Freiburg, Germany
[‡]Institut für Makromolekulare Chemie, Albert-Ludwigs-Universität Freiburg, Stefan-Meier-Straße 31, 79104 Freiburg, Germany
[§]Lehrstuhl Polymerchemie, Technische Universität Chemnitz, Straße der Nationen 62, 09111 Chemnitz, Germany

Supporting Information

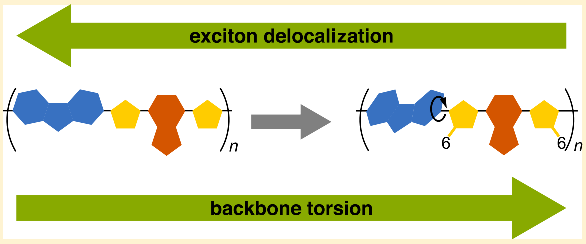

ABSTRACT: Solution processing of conjugated polymers is key for low-cost processing of organic electronic devices. To improve solubility, introducing alkyl side chains is a commonly employed approach, known for its impact on film morphology. The morphology of polymer films is a key aspect of the structure−function relationship in organic electronic devices with a strong impact on their overall efficiency. Although planarity of conjugated backbones is advantageous for exciton and charge carrier mobilities and the overall degree of order, it leads to aggregation in solution. This reduces solubility but can result in interesting structures. Side-chain-mediated backbone torsion, in contrast, greatly enhances solubility, facilitating synthesis and control of molecular weight, but often impairs performance. Detailed insight into the impact of side chains on both morphology and electronic structure is therefore of high demand. We demonstrate time-resolved electron paramagnetic resonance spectroscopy to be perfectly suited to probe the orientation as well as the overall degree of order in conjugated polymer films, while simultaneously revealing details of the electronic structure. By systematically studying the impact of additional side chains, we distinguish their impact on the film morphology and electronic structure. Additional side chains decrease exciton delocalization but not the overall degree of order in the film. Delocalization is therefore only connected to backbone planarity. Using magnetophotoselection experiments, we additionally present clear evidence for the preferential face-on orientation of the amorphous polymer backbone on the substrate. This is crucial for the efficiency of both organic photovoltaic devices and organic light-emitting diodes.

INTRODUCTION

Printed electronics have gained considerable interest in both industry and academia[1−3] and are now, in some fields, competing with their inorganic, mostly silicon-based, counterparts.[4,5] The promises are low-cost[6−8] and high-throughput production of light-weight, flexible, and large-area electronics devices,[9] including organic photovoltaics (OPVs),[10,11] organic field-effect transistors,[12] and organic light-emitting diodes (OLEDs).[13] One key aspect is solution processing,[14] and hence solubility of the polymers used is of high importance. Furthermore, to control both molecular weight and dispersity, premature precipitation of the polymer being synthesized should be avoided. One approach often followed is to introduce branched or linear alkyl side chains[15−18] that will generally enhance solubility, while not or only very slightly affecting the electronic structure of the isolated backbone.[19] Additionally, alkyl side chains help compatibilizing the polymer with both fullerenes and other polymers, enhancing miscibility that needs to be fine-tuned for the efficiency of blends.[20]

Generally, there is always a trade-off between planarity and solubility. Planarity is key to both exciton and charge carrier mobilities as well as the overall order. At the same time, it renders polymers increasingly insoluble, hampering synthesis and control of molecular weight and dispersity. Backbone torsion, e.g., by introducing alkyl side chains, greatly increases solubility and facilitates synthesis but normally at the expense of mobility and order. However, this picture might be overly simplistic, and the detailed structure−function relationship of conjugated polymers is far more complicated.[21] Do additional side chains lead to a decrease in the overall order of polymer films, most probably degrading charge carrier mobility? Or is delocalization only locally affected by dihedral angles between adjacent units? To shed light on these questions, we systematically investigated a series of polymers with increasing number of hexyl side chains (Figure 1) using time-resolved electron paramagnetic resonance (TREPR) spectroscopy[22,23] supported by quantum-chemical calculations.

Received: March 26, 2019
Revised: July 26, 2019
Published: July 29, 2019

DOI: 10.1021/acs.jpcc.9b02835
J. Phys. Chem. C 2019, 123, 20071−20083

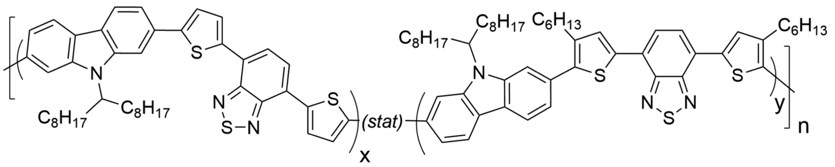

Figure 1. Chemical structure of poly[*N*-9′-heptadecanyl-2,7-carbazole-*alt*-5,5-(4′,7′-di-2-thienyl-2′,1′,3′-benzothiadiazole)] (PCDTBT) with different degrees of hexylation. Hexyl side chains on the thiophene−benzothiadiazole−thiophene (TBT) moiety have been statistically introduced during synthesis. In this study, five polymers with hexylation ratio R_{hex} corresponding to $R_{\text{hex}} = y = 0, 0.3, 0.5, 0.7, 1$ and $x = 1 - y$, respectively, have been investigated. The polymers are termed P0−P100 hereafter.

Poly[*N*-9′-heptadecanyl-2,7-carbazole-*alt*-5,5-(4′,7′-di-2-thienyl-2′,1′,3′-benzothiadiazole)] (PCDTBT) is a common copolymer, consisting of alternating thiophene−benzothiadiazole−thiophene (TBT) and carbazole (Cbz) repeat units,[24,25] renowned not only for its robustness and air stability over long time[26−30] and high power conversion efficiencies of up to 7−8%[31] but also for its tendency to form carbazole homocouplings.[32] Recently, we could show that this polymer orients its backbone toward the substrate in drop-cast films.[33] This is quite surprising given that the polymer is known for its rather amorphous morphology[34] and does not readily form crystals.[35] Furthermore, an overall face-on orientation with respect to the substrate was deduced. This is advantageous for charge carrier injection or extraction in OLED or OPV devices, respectively.[36−39] Here, we use the power of TREPR spectroscopy of triplet excitons to simultaneously reveal both the orientation of the polymer backbone with respect to the surface and the overall degree of ordering within the film.[33] The advantage of TREPR spectroscopy over other methods is its capability to show the overall picture, hence ordering within the film, combined with molecular resolution, i.e., sensitivity to the immediate surrounding of the exciton and its delocalization. Furthermore, it does not rely on semicrystalline domains for detecting the overall ordering in, e.g., thin films.

Particularly in light of hexylated PCDTBT exhibiting electroluminescence,[40] rendering it a very interesting material for OLEDs, a detailed investigation of the triplet excitons is of great importance. Due to spin statistics,[41] triplet states are unavoidable in OLED devices. Therefore, a detailed knowledge of their electronic structure is key for further optimizing materials for more efficient devices. Here, TREPR spectroscopy is a perfect fit, given its inherent sensitivity to paramagnetic states, its capability to unequivocally discriminate triplet states from other paramagnetic species, and its molecular resolution.[42] The availability of polymers with different degrees of hexylation allows for a systematic approach, whereas accompanying quantum-chemical calculations give insight into the geometry and spin-density distribution. Taken together, this helps us unravel intricate details of the all-important structure−function relationship of semiconducting polymers, in particular the effects of introducing additional side chains not only on morphology but also on the electronic structure, with high relevance for further application.

■ RESULTS

Absorption Spectra. PCDTBT with five different degrees of hexylation (cf. Figure 1), termed P0−P100 hereafter, has been investigated. For all five polymers, absorption spectra in solution at room temperature have been recorded (cf. Figure 2). All substances investigated in this study show two distinct absorption bands: a high-energy band that can be attributed to a π−π* transition and a low-energy band usually termed the charge-transfer (CT) band that is due to the weak intramolecular CT character of the push−pull system comprising benzothiadiazole and the two flanking thiophenes. For a more detailed investigation of the optical spectra and corroborating quantum-chemical calculations see the work by Banerji et al.[43] Recently, we could show TBT to entirely dominate the electronic structure even of the polymer by investigating P0 and a series of its building blocks using TREPR spectroscopy.[44]

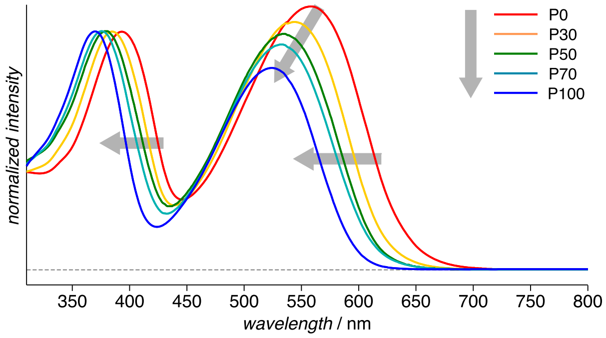

Figure 2. Absorption spectra of solutions of PCDTBT with different degrees of hexylation. Two trends are obvious: The absorption shifts toward shorter wavelength for increasing hexylation, hinting at an increased localization of the singlet exciton, and concomitantly, the relative intensity of the CT band in the visible region decreases compared to the $S_n \leftarrow S_0$ band in the near-UV region. All polymers have been measured at room temperature in *o*-dichlorobenzene (*o*-DCB) solution.

The absorption spectra do not show aggregation. To rule out aggregation due to cooling (as necessary for electron paramagnetic resonance (EPR) spectroscopic investigations, see below), we recently performed temperature-dependent absorption measurements on P0, confirming the absence of aggregation in the solvent used (*o*-dichlorobenzene, *o*-DCB).[44] We note that the choice of solvent is often not determined by its spectroscopic properties, e.g., forming glasses upon cooling, but by the processing requirements for both synthesis and device manufacturing.

Even from the first inspection of the optical spectra (Figure 2), two trends are obvious: The absorption shifts toward shorter wavelength for increasing hexylation, hinting at an increased localization of the singlet exciton, and concomitantly, the relative intensity of the CT band in the visible region decreases compared to the $S_n \leftarrow S_0$ band in the near-UV region. This weakening of the CT band intensity hints at a weakened CT character of the respective polymer that could be explained by an increasing steric hindrance upon hexylation, thus diminishing the orbital overlap between the highest occupied molecular orbital and the lowest unoccupied molecular orbital giving rise to the (partial) CT character.

Table 1. Simulation Parameters for the TREPR Spectra of Frozen Solutions of PCDTBT with Different Degrees of Hexylation[a]

polymer	R_{hex}	λ_{ex}	$\lvert D\rvert$	$\lvert E\rvert/\lvert D\rvert$	p_1	p_2	p_3	Γ_{G}	Γ_{L}
P0	0	557	1264	0.078	0.123	0.353	0.523	2.00	2.17
P30	0.3	544	1283	0.076	0.053	0.393	0.554	0.79	2.41
P50	0.5	533	1297	0.075	0.073	0.427	0.501	1.48	2.02
P70	0.7	531	1328	0.077	0.163	0.411	0.429	0.20	2.94
P100	1	522	1370	0.066	0.069	0.386	0.546	1.21	2.39

[a] For the actual spectra, cf. Figure 3. R_{hex} is the degree of hexylation, λ_{ex} (in nm) is the excitation wavelength used (maximum of the CT band, cf. Figure 2), D and E (in MHz) are the parameters of the zero-field splitting tensor of the dipolar interaction, $\Gamma_{\text{G,L}}$ (in mT) are the Gaussian and Lorentzian line widths, and $p_{1,2,3}$ are the populations of the three triplet sublevels. For details of the simulation and fitting procedure, see the Supporting Information (SI).

Besides giving insight into the electronic structure of the polymers and their respective singlet excitonic state, the steady-state absorption spectra are of practical use in determining the excitation wavelength for the subsequent TREPR measurements. Both frozen solution and drop-cast film samples have been excited with wavelengths corresponding to the maximum of their respective CT band. For actual values, cf. Tables 1 and 2.

TREPR Spectra of Frozen Solutions. For obtaining a first overview of the effects of increasing hexylation on the respective triplet excitons, TREPR spectra of a frozen solution of each of the five polymers have been recorded (Figure 3). As already detailed above, each polymer has been optically excited with a wavelength corresponding to the respective maximum of its CT band. Due to fast spin−spin relaxation in triplet states consisting of two unpaired, strongly coupled electron spins, TREPR spectra of triplet states usually need to be recorded at cryogenic temperatures in the solid state. Hence, all TREPR spectra shown in this study have been recorded at 80 K. The spectra of all five polymers can be clearly attributed to a single triplet species each and simulated accordingly (gray curves in Figure 3; for simulation parameters cf. Table 1). These spectra are entirely dominated by the dipolar interaction of the two unpaired, strongly coupled electron spins of the triplet exciton. The small and narrow emissive feature appearing at the center in some of the spectra, however, is clearly not due to the triplet state. Possible origins will be discussed below in more detail.

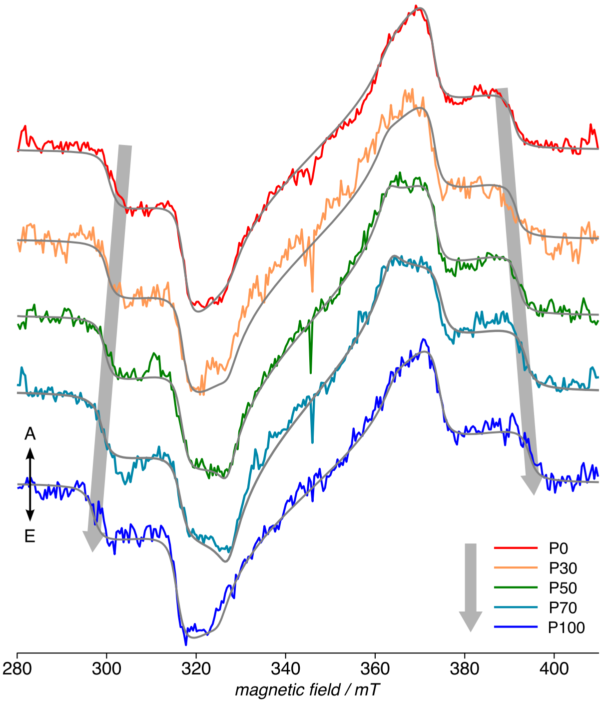

Figure 3. TREPR spectra of frozen solutions of PCDTBT in *o*-DCB with different degrees of hexylation together with spectral simulations (gray lines). The spectra broaden slightly with increasing hexylation, consistent with an increased localization of the triplet exciton. For the simulation parameters, cf. Table 1, and for details of the simulation and fitting procedure, see the Supporting Information.

The spectra broaden slightly with increasing hexylation, as depicted by the gray arrows in Figure 3, consistent with an increased localization of the triplet exciton. This is in accordance with the simulation parameters obtained from spectral simulations (Table 1) showing an increasing value for D, directly connected to the strength of the dipolar interaction and hence the width of the TREPR spectra. Generally, D has an inverse cubed distance dependence. For a detailed explanation of the general shape of TREPR spectra of triplet states see the Supporting Information and the recent reviews by Weber[23] and Biskup.[42] Besides the obvious trend for the D parameter of the dipolar interaction, no clear trends can be seen within the simulation parameters. The overall rhombicity of the spectra, given as $\lvert E\rvert/\lvert D\rvert$, is rather small, as already known for P0 and its building blocks.[44] Interestingly, the rhombicity is clearly the smallest for P100. The line widths, both Gaussian and Lorentzian, are rather small as well, and all triplet sublevel populations follow the same overall trend, $p_1 < p_2 < p_3$. Note that the signs of $\lvert D\rvert$ and $\lvert E\rvert$ have not been and cannot be determined from our data, hence populations have been given for positive values of D and E. We note that neither the signs of D and E nor further assignments of the populations are relevant for our further analysis.

TREPR Spectra of Films Drop-Cast on Quartz Substrates. From a previous study,[33] it is known that P0 shows a rather strong degree of ordering and clear orientation of its backbone if cast as a film on a flat substrate. To be more precise, P0 shows preferential orientation perpendicular to the surface plane but no orientation within this plane. The high degree of ordering is reflected in the small Gaussian line width pointing at an overall very homogeneous local environment of the triplet excitons. Here we use the same approach followed previously and drop-cast films on substrates. Whereas in the previous study, we used poly(ethylene terephthalate) as the substrate, here we used synthetic quartz glass plates offering a number of advantages. Most relevant in this study are their stiffness and, therefore, more accurate positioning within the quartz glass tube and hence within the EPR spectrometer.

For each of the five polymers, a film has been drop-cast on a substrate and afterward measured in an angular-dependent fashion with TREPR spectroscopy for five different orientations with respect to the external magnetic field. A representative example, P30, is shown in Figure 4. For the full set of spectra of the other polymers see the Supporting Information. The overall picture for all five polymer films with different degrees of hexylation is quite similar. They show clear orientational effects and all can be simulated (gray lines in Figure 4) in a global fashion assuming a single triplet species. It remains a very interesting question as to why an amorphous polymer should show an overall rather strong order and orientation of its backbones perpendicular to the substrate plane when cast as a film on a substrate. We cannot answer this question on a mechanistic level at present. However, there are a number of arguments why TREPR spectroscopy probes the whole film morphology rather than very minor triplet contributions at the interface. For a detailed discussion, the interested reader is referred to the SI.

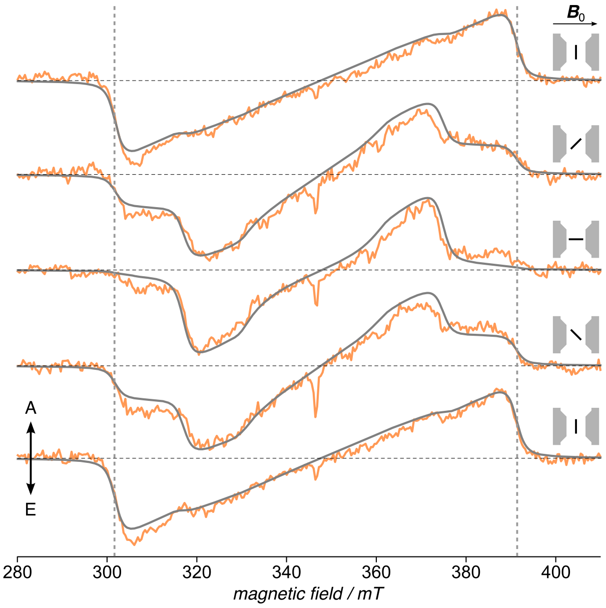

Figure 4. Angular-dependent TREPR spectra of a thin film of P30 drop-cast on a quartz glass substrate, together with spectral simulations (gray lines). Spectra have been globally fitted for all five positions at once with one set of parameters. From the simulations, the orientation of the $\boldsymbol{D}$ tensor relative to the substrate plane as well as the overall degree of order can be extracted. Insets to the right show the orientation of the substrate with respect to the external magnetic field, $\boldsymbol{B}_0$. Vertical dashed lines represent the two D_z positions, immediately revealing D_z to be perpendicular to the substrate plane. Samples have been excited with nonpolarized light.

To help the reader, instead of angular positions, pictograms of the magnet of the EPR spectrometer have been used in Figure 4 to indicate the position of the substrate with respect to the external magnetic field. The vertical dashed line highlights the D_z position, resulting from the z component of the dipolar coupling tensor $\boldsymbol{D}$ being parallel or antiparallel to the magnetic field. Already from a first inspection, the orientation of D_z with respect to the substrate surface plane can be deduced. Given that the signal corresponding to the D_z position is maximal for the substrate being perpendicular to the magnetic field (top most and bottom most traces in Figure 4), D_z is necessarily oriented perpendicular to the substrate plane. Similar to previous observations for P0,[33] we note a C_{2v} symmetry, with both possible positions of the substrate tilted 45° toward the magnetic field resulting in identical spectral shape. Similarly to the D_z positions being most prominent for the substrate plane oriented perpendicular to the external magnetic field $\boldsymbol{B}_0$, both inner positions D_x and D_y are most prominent for the substrate plane oriented parallel toward $\boldsymbol{B}_0$. Although D_x and D_y cannot be easily assigned here, they are definitely the two inner positions. This means that both positions are located within the substrate plane. This is a necessity from geometrical arguments, knowing that D_z is oriented perpendicular to the substrate plane, as all three components together form an orthogonal Cartesian coordinate system. This arrangement means that information on the orientation of D_x and D_y within the substrate plane cannot be obtained. The polymer is only oriented with respect to the surface plane but not within it. This is expected, given that the film has been made by drop-casting.

Simulation and Fitting Strategy for TREPR Spectra of Films. To obtain information on both delocalization (via the dipolar interaction parameter D) and the overall degree of order, we used a similar simulation and fitting strategy to that in our previous study, revealing strong ordering and orientation in P0.[33] The crucial aspect here is a global fitting approach, i.e., fitting one set of parameters concurrently to all spectra obtained for one and the same sample for different positions with respect to the external magnetic field. This assumes the angular positions or at least their relative changes with respect to each other to be known and all other parameters to be identical for each position for one and the same sample.

Table 2. Simulation Parameters for the Angular-Dependent TREPR Spectra of Films of PCDTBT with Different Degrees of Hexylation Drop-Cast on Quartz Glass Substrates[a]

polymer	R_{hex}	λ_{ex}	$\lvert D \rvert$	$\lvert E \rvert/\lvert D \rvert$	p_1	p_2	p_3	Γ_{G}	Γ_{L}	σ
P0	0	557	1238	0.088	0.181	0.328	0.491	1.45	2.18	0.60
P30	0.3	544	1254	0.097	0.180	0.353	0.468	2.19	2.15	0.59
P50	0.5	533	1272	0.085	0.002	0.367	0.631	1.73	3.26	0.73
P70	0.7	531	1290	0.093	0.190	0.336	0.400	5.23	2.95	0.83
P100	1	522	1356	0.074	0.249	0.324	0.427	0.70	4.33	0.64

[a] For the actual spectra, cf. Figure 4 and the Supporting Information. R_{hex} is the degree of hexylation, λ_{ex} (in nm) is the excitation wavelength used (maximum of the CT band, cf. Figure 2), D and E (in MHz) are the parameters of the zero-field splitting tensor of the dipolar interaction, $\Gamma_{\text{G,L}}$ (in mT) are the Gaussian and Lorentzian line widths, $p_{1,2,3}$ are the populations of the three triplet sublevels, and σ (in rad) is the width of the Gaussian used to weight the powder average. For details of the simulation and fitting procedure, see the Supporting Information.

Partial orientation has been accounted for by applying a weighting to one direction of the powder averaging using a Gaussian with standard deviation σ. Compared to other approaches, this gives a rather intuitive measure for the overall degree of order. The smaller the value for σ, the higher the degree of order. Generally, weighting could be performed along both angles of the powder averaging. Here, only weighting along one angle has been applied. This is due to the polymer only being oriented with respect to the substrate plane but not within it. In addition, we used Latin-hypercube sampling to obtain more reliable fits, sampling a rather large parameter hypersurface, thus preventing the fitting algorithm from prematurely ending up in local minima. For the actual simulations, a routine has been implemented in the programming language Python, following published approaches[45] but focusing particularly on the need to account for partial orientation. Therefore, it makes use of the intrinsic symmetry of the spin Hamilton operator, while retaining the possibility of easily applying a weighting to the powder average. Details of this simulation routine will be published elsewhere.

The results obtained from globally fitting the spectral simulations to the experimental data can be found in Table 2 for each of the five polymers. For the parameter, $|D|$, of the dipolar interaction, a similar trend can be observed to that already described for the spectra obtained in frozen solutions (Figure 3 and Table 1), namely, an increase in the value of D for increasing hexylation. Directly comparing the D values for spectra obtained in frozen solutions and in films, we note a generally smaller value for the film samples (cf. Figure 9 in the Discussion section). The rhombicity though, whereas still rather small, is clearly larger in the film samples as compared to frozen solutions. Both Gaussian and Lorentzian line widths are again rather small, with one notable exception being the Gaussian (inhomogeneous) line width of P70. Finally, for the parameter σ, i.e., the width of the Gaussian used to weight the powder average, we note a maximum again for P70, followed by a clear drop for P100. Taken together, a consistent trend of increasing D with increasing hexylation can be extracted from the simulation parameters. At the same time, the ordering parameter σ seems not to follow a similar trend, with only P50 and P70 clearly deviating from the others. Finally, the inhomogeneous line width for P70 clearly stands out, although it is still not exceptionally large compared to the values obtained for other polymers.[46,47]

Density Functional Theory (DFT) Calculations. To get further insight into both the geometry and the spin-density distribution of the polymers with varying degrees of hexylation, density functional theory (DFT) calculations have been performed for fragments of P0, P50, and P100. For these three cases, model oligomers can be constructed in a quite straightforward manner, assuming for P50 a strictly alternating sequence of building blocks. Due to the statistical approach used for synthesis, investigating model structures for the other two polymers probed experimentally in this study, namely, P30 and P70, would be computationally much more demanding. Not only would longer oligomer chain lengths be necessary, but also taking into account different variants of sequences due to the statistical distribution.

Both geometries and spin-density distributions for all three oligomer models investigated are shown in Figure 5. As known already for P0 and its building blocks,[44] TBT nearly entirely dominates the electronic structure of the polymer, as reflected by the spin density situated with its majority on a single TBT moiety. Additionally, the dihedral angles between each adjacent Cbz and TBT moiety along the chain have been calculated and are given in Table 3. For details of how these angles have been computed, see ref 44 and the SI. Last but not least, the relative amount of spin density, ρ_{TBT}, on the dominating TBT has been calculated and is given as well in Table 3.

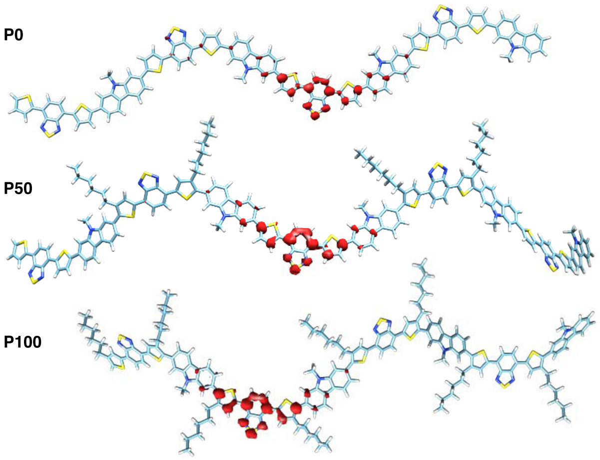

Figure 5. Spin-density distribution for the triplet states of PCDTBT fragments with different degrees of hexylation. For simplicity, for P50 a strictly alternating sequence of hexylated and non-hexylated units has been used. Geometries have been optimized for the triplet state at the BP86/Def2-SVP level of theory and spin densities are displayed for a threshold level of ±0.001. Red denotes positive and blue negative spin density. Due to a total spin density of +2 for the triplet state, the negative spin density is barely visible.

As expected, for each of the three polymers, spin density is centered mostly on a single TBT unit, in line with previous investigations of P0 and its building blocks[44] as well as with the experimental data, reflecting mostly the situation found for TBT alone. Furthermore, the dihedral angles are much smaller for P0, show a clear alternation for P50 with alternating hexylated and non-hexylated TBT units, and are at a consistent maximum for P100. Interestingly though, the polymer backbone appears to be more planar directly adjacent to the TBT unit on which the maximum spin density resides.

Small Emissive Signal at the Center. As already mentioned, both solution spectra and spectra from thin films show sometimes a small, emissive signal at the center, at $g \approx 2$. Although this signal definitely does not belong to the triplet state and does not impair the overall interpretation of our results, it deserves some comments. First of all, it is angular-dependent, as apparent from the spectra recorded for the drop-cast film of P30, Figure 4. This rules out a migrating exciton as a possible origin. Furthermore, the angular dependence is clearly different from that of the triplet state. Although the maximum appears to be at an angle of 45° toward the external magnetic field, the actual value is hard to reveal, as the resolution along the field axis optimized for the triplet spectra is not sufficient to properly resolve this rather narrow signal. Furthermore, it cannot be an artifact due to sample degradation, as its intensity diminishes again for substrates perpendicular to $\boldsymbol{B}_0$ and is of the same size for the first and last spectra recorded. Due to it appearing in emission, it is definitely spin-polarized, hence with the energy levels populated far from the Boltzmann equilibrium. It is very

Table 3. Dihedral Angles between the Aromatic Planes of Cbz and TBT Moieties Obtained from Geometry Optimization in the Triplet State, and Relative Amount of Total Spin Density on the Dominating TBT Unit[a]

polymer	R_{hex}	dihedral angles									ρ_{TBT}
P0	0	1.0	2.9	1.4	**1.1**	**0.5**	0.2	1.0			60.8
P50	0.5	13.2	36.7	34.1	**2.6**	**0.9**	33.3	36.3	16.9	15.1	70.3
P100	1	34.0	**25.2**	**22.5**	30.3	38.1	34.3	36.6			76.7

[a] R_{hex} refers to the degree of hexylation of the polymer. The Cbz and TBT moieties are in themselves pretty flat. Angles are given in degrees and for the cis−trans configuration, as shown in Figure 5. Boldface numbers refer to the two angles directly adjacent to the TBT carrying the center of spin density. The relative amount of total spin density on the dominating TBT unit, ρ_{TBT}, is given in percent. For details of how the dihedral angles and spin densities have been obtained see the Supporting Information.

narrow, comparable to spin-correlated radical pairs observed in both biological systems[48,49] and materials used in organic electronics.[50−53] And last but not least, the time profiles have a similar behavior to those of the triplet states (for full two-dimensional (2D) datasets, see the SI), making a species with the same spin multiplicity highly likely.[54,55] A possible interpretation is, therefore, the presence of two separated but still Coulombically bound charges, resulting from short-lived charge separation within the pristine polymer.

Magnetophotoselection. So far, the preferential face-on orientation of the polymer has been deduced from logical arguments about the orientation of D_z with respect to the molecular plane.[33] To further strengthen these arguments, magnetophotoselection experiments have been performed both with P0 and with its repeat unit, Cbz−TBT. In these experiments, linearly polarized light is used to excite the sample, and spectra are recorded for different orientations of the plane of the polarized light with respect to the external magnetic field.[56,57] Optical excitation is most efficient for optical transition dipole moments lying within the plane of the linearly polarized light. Therefore, this experiment can generally reveal the orientation of the $\boldsymbol{D}$ tensor axes with respect to the optical transition dipole moment.[58] The angular dependence of the optical excitation with respect to the plane of the polarized light only modulates the probabilities of the respective transitions. Hence, only modulations of the signal intensities in the TREPR spectra are expected, not narrow spectra obtained for single crystals, and not even such strong effects as can be seen for the films (Figure 4). The results for the magnetophotoselection experiments on Cbz−TBT and P0 are shown in Figure 6.

To rule out negative side effects due to possible migration of the triplet exciton, polymer P0 and its repeat unit Cbz−TBT have been investigated. In a polymer, the exciton is expected to be mobile to a certain extent, given its long lifetime of at least several microseconds. As the polymer chain is not entirely flat, particularly not in the case of a polymer in a frozen solution, migration of the exciton would sooner or later destroy the angular relationship between the optical transition dipole moment involved in the initial excitation and the resulting excitonic state. Hence, small molecules with their dramatically reduced exciton migration probability will generally show stronger effects than polymers. Furthermore, hexylation seems to reduce the triplet yield, leading to weaker TREPR signals, and hence worse signal-to-noise ratio. This led us to investigate only the non-hexylated compounds. Given the overall high similarity of the signals, we are, nevertheless, confident that the magnetophotoselection results obtained for Cbz−TBT and P0 are applicable to the other polymers investigated here as well.

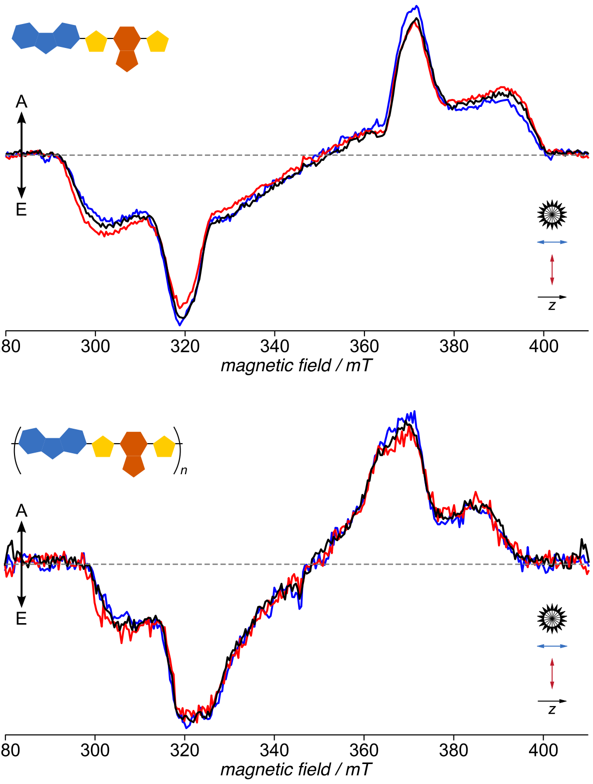

Figure 6. Results of magnetophotoselection experiments for Cbz−TBT (top) and P0 (bottom) in frozen solutions. The enhanced signal intensity of the outer wings for orientation of the polarization plane perpendicular to $\boldsymbol{B}_0$ reveals the D_z-axis to be oriented perpendicular to the optical transition dipole moment. Cbz−TBT and P0 show the same overall trend, whereas for P0, the effect is very minor and only barely visible. Blue and red traces arise from light polarization parallel and perpendicular to the external magnetic field, respectively, whereas the black trace arises from excitation with unpolarized light.

For Cbz−TBT, a clear effect is visible (cf. Figure 6). The enhanced signal intensity of the outer wings for orientation of the polarization plane perpendicular to $\boldsymbol{B}_0$ reveals the D_z-axis to be oriented perpendicular to the optical transition dipole moment. Although Cbz−TBT and P0 show the same overall trend, for P0, the effect is very minor and only barely visible. Nevertheless, the effect can be seen at about 370 mT, where the signals for parallel and perpendicular orientations of the polarization plane of the incident light clearly deviate from each other beyond the signal-to-noise ratio. As the sample was not touched between measurements, we are confident that this observed effect is not an artifact.

■ DISCUSSION

Singlet and Triplet Excitons Show the Same Trends with Increasing Hexylation. From both the steady-state absorption data (Figure 2) and the TREPR data in (frozen) solution (Figure 3), an increased localization of the excitonic state with increasing hexylation can be deduced. The blue shift of the absorption spectra with increasing degree of hexylation can be attributed to an increased energy gap and hence a more localized exciton. Concomitantly, the increased width of the TREPR spectra with increasing degree of hexylation, revealed in an increase in the D value of the triplet state (cf. Table 1), can be directly attributed to a larger localization of the triplet exciton. We note that due to the very similar overall shape of the triplet spectra for the polymers with different degrees of hexylation, any reorientation of the $\boldsymbol{D}$ tensor that would invalidate using D as a measure of delocalization[59] can be ruled out. Hence, at least semiquantitative statements are possible.

A more detailed look at these trends is provided by Figure 7. Here, both wavelength and $D^{-1/3}$ have been plotted versus the degree of hexylation. The reason for plotting $D^{-1/3}$, rather than D, is its distance dependence, $D \propto r^{-3}$. Here, r is the average distance between the two electron spins of the triplet state. Both exciton types show an identical overall trend, namely, an increased exciton localization with increased hexylation. The effect shows two linear regimes for both exciton types, with a change in slope at a hexylation ratio of 0.5, meaning statistically alternating hexylated and non-hexylated building blocks. The strength of the effect of increasing hexylation appears to be opposite for singlet and triplet excitons. Whereas for the singlet excitons, the effect is strongest at the beginning, for triplet excitons, the effect is more pronounced beyond a hexylation ratio of 0.5. This may be explained by the different delocalization lengths of both exciton types.

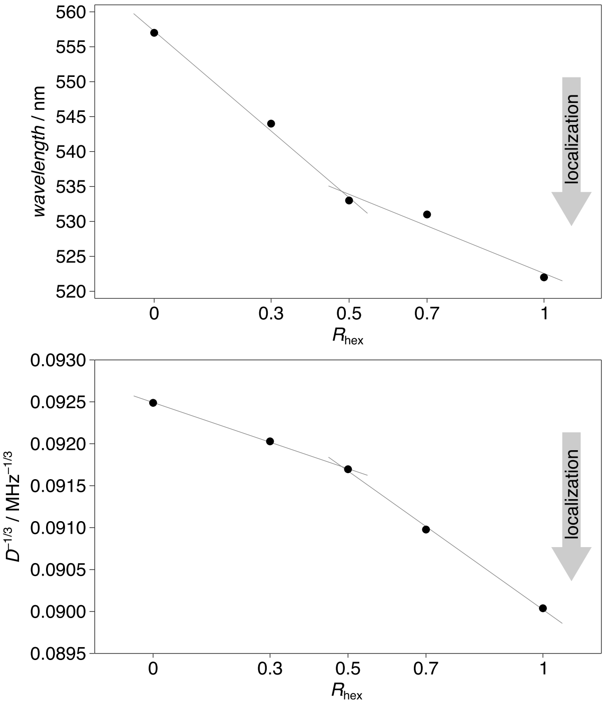

Figure 7. Trend of enhanced localization of both singlet and triplet excitons for increasing hexylation. The overall trend for both exciton types is identical, namely, an increased exciton localization with increased hexylation. The effect shows two linear regimes for both exciton types, with a change in slope at a hexylation ratio of 0.5, meaning statistically alternating hexylated and non-hexylated building blocks. The strength of the effect of increasing hexylation appears to be opposite for singlet and triplet excitons. Whereas for the singlet excitons, the effect is strongest at the beginning, for triplet excitons, the effect is more pronounced beyond a hexylation ratio of 0.5. This may be explained by the different delocalization lengths of both exciton types. For the triplet exciton, $D^{-1/3}$ has been plotted vs the hexylation ratio, R_{hex}, for easier comparison with the wavelength. Note that the error bars would be within the bullets representing the data points. Those who are more familiar with a wave number rather than a wavelength scale are referred to Figure S5 in the SI.

Comparing the delocalization length of singlet and triplet excitons with those of P0 and its building blocks,[44] P100 strongly resembles the symmetric building block, Cbz−TBT−Cbz (cf. Figure 8). For the singlet exciton, the absorption maximum of the CT band is almost identical, although the low-energy shoulder of this absorption band falls off faster as compared to the building block. In the case of the triplet exciton, the situation is not as clear. Although the D values are more similar for P100 and Cbz−TBT, the overall spectral shape and rhombicity of Cbz−TBT−Cbz much better reflect the situation in the hexylated polymer. However, the rather limited signal-to-noise ratio of the TREPR spectra obtained for the polymers makes direct comparison less straightforward.

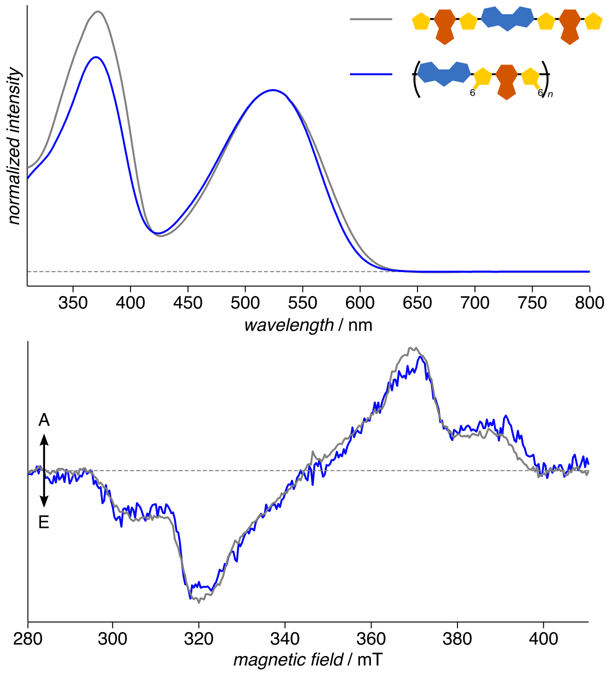

Figure 8. Comparing the exciton delocalization length of P100 with the symmetric building block of P0. In both cases, i.e., singlet and triplet excitons, the delocalization of P100 (blue trace) as reflected in the position of the absorption band and overall width of the spectrum, respectively, pretty much resembles that of the non-hexylated symmetric building block of P0 (gray trace) with carbazole moieties on both ends. This is fully consistent with an increased exciton localization due to enhanced backbone torsion caused by the hexyl side chains.

Film Formation Enhances Delocalization. The overall trend for both morphologies, frozen solution and film, is identical and consistent with the observation for the singlet exciton, namely, an increased exciton localization with increased hexylation (cf. Tables 1 and 2 and Figure 7). Additionally, triplet excitons in films are systematically more delocalized as compared to the identical polymer investigated in solution, as shown in Figure 9 comparing D values for both types of sample preparation. This is attributed to a slight planarization in films upon depositing the polymer on its substrate. Hence, exciton delocalization as measured for solution samples only gives a lower limit of the actual delocalization found in films. The enhanced delocalization in films attributed here to an increased planarization is fully consistent with the overall high order in these films with respect to the surface plane.

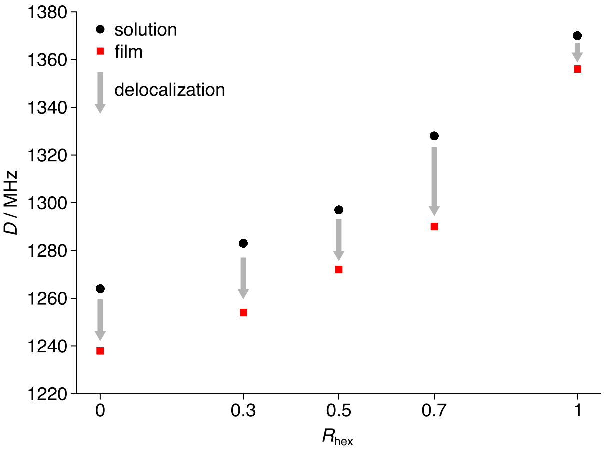

Figure 9. Film morphology enhances triplet exciton delocalization as compared to the situation in solution. The overall trend for both morphologies, frozen solution and film, is identical and consistent with the observation for the singlet exciton, namely, an increased exciton localization with increased hexylation. Additionally, triplet excitons in films are systematically more delocalized as compared to the identical polymer investigated in solution. This is attributed to a slight planarization in films upon depositing the polymer on its substrate.

Hexylation Enhances Backbone Torsion. The results from geometry optimization of the three different oligomer models are in line with previous results, showing hexylation to introduce backbone torsions.[40,60] Besides that, the overall picture of the spin density being situated on the TBT moiety entirely dominating the electronic structure is unaltered as compared to P0 and its building blocks.[44] Previously, we have shown BP86/Def2-SVP to be superior for describing the electronic structure of P0 as compared to the often-used B3LYP/6-31G**. Therefore, we applied the same level of theory here for geometry optimization and calculation of spin densities. The differences in dihedral angles from those calculated previously are most probably due to the different functionals and basis sets used as well as investigation of triplet states in our case, whereas previous studies have calculated geometries only for singlet states. Recently, for another polymer, we demonstrated triplet states to have, in general, more planar geometries than the corresponding singlet states.[46]

To gain further insight, a quantitative approach to the spin-density distribution of the triplet state seems sensible. Therefore, we compare the values of the spin densities for each nucleus of the TBT moiety for the three polymer fragments with different degrees of hexylation (Figure 10). For most of the nuclei, a monotonic increase with increasing hexylation can be readily observed. All polymers show a fairly symmetric distribution of spin density over the TBT moiety. The largest part of the spin density is localized on the benzothiadiazole part of the TBT moiety.

Interestingly, for both P0 and P50, the maximum of the spin density is located on a non-hexylated TBT moiety. Additionally, we note that the dihedral angles adjacent to this TBT unit are systematically, although not always significantly, smaller than the others. In the case of P0, all dihedral angles are very close to zero, hence no statement can be made regarding an increased planarity surrounding the TBT moiety at which the majority of spin density is located.

The relative amount of total spin density on the dominating TBT unit calculated for the different oligomer models is nicely in line with the experimental data obtained by TREPR spectroscopy. The latter show a monotonic increase with increasing hexylation, consistent with a similar increase in the D value (cf. Tables 1 and 2).

Degree of Ordering and Delocalization Are Independent. In a first picture, the overall degree of order with respect to the surface plane revealed by the parameter σ of the simulations of the orientation-dependent TREPR spectra should be connected with the delocalization length as deduced

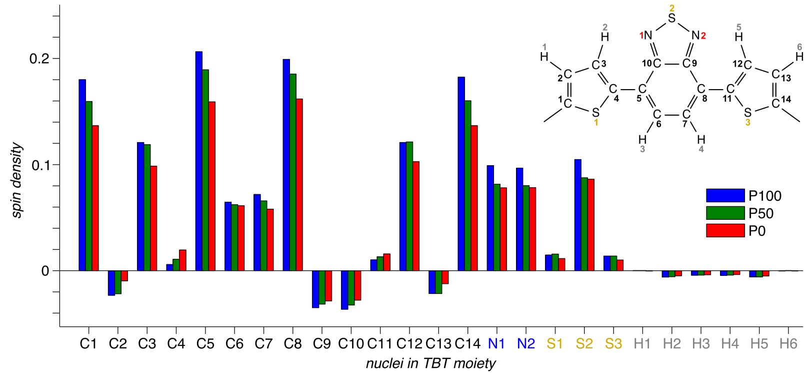

Figure 10. Quantitative analysis of the spin-density distribution for the triplet states of PCDTBT fragments with different degrees of hexylation. Depicted are the values for the spin densities for each of the TBT atoms in the three fragments displayed in Figure 5. The inset shows the numbering of the atoms used as axis labels.

from the D parameter of the dipolar interaction tensor. However, these two parameters are clearly not related for the series of polymers investigated in this study. Upon closer inspection, the situation becomes clearer, as the two parameters reflect entirely different characteristics of the polymer. Delocalization can be attributed to an effective conjugation length that in turn is connected to the planarity of an individual polymer chain fragment. In contrast, the ordering parameter as deduced from the weighting of the powder averaging of the simulations reveals the preferential orientation of the polymer backbone with respect to the surface for the entire film. Hence, the delocalization gives insight into the local order and planarity of an individual polymer chain,[21,61] whereas the ordering parameter reflects the (ir)regular arrangement of the polymer chains within the film with respect to the surface.

P0 is amorphous or very weakly semicrystalline depending on the sample and preparation method.[34,40] A rather unconventional bilayer packing structure has been reported to form at higher temperatures, which further indicates that the classical classification of a polymer as amorphous or semicrystalline may not be useful here.[62] From DSC data of the polymers with different degrees of hexylation,[40] we can deduce all other polymers to be amorphous as well. Given these data and the difficulties arising from trying to crystallize P0,[35] we assume the delocalization to reflect the situation along the polymer chain and the ordering parameter to give insight into the arrangement of the different chains within the film. Note, however, that the TREPR signals result from bulk measurements, i.e., averaging over the entire sample (at least as far as it is within the active volume of the resonator). They are therefore necessarily different from single-chain or single-molecule measurements. It remains an interesting question as to why an amorphous polymer should show an overall order and orientation with respect to the surface plane when cast as a film on a substrate. While we cannot answer this question on a mechanistic level at present, we are sure to investigate the entire film, not just a subset of triplet species located exclusively on the interface between the film and substrate. Note that the preferential orientation is only observed with respect to the surface plane but not within it. Furthermore, similar effects have been observed for a number of different doped polymers cast as rather thick films and investigated using conventional continuous-wave EPR spectroscopy. For a detailed discussion, the reader is referred to the SI.

Delocalization Is Directly Connected to Backbone Planarity. Building on the results from both experiments and quantum-chemical calculations, it is obvious that the extent of exciton delocalization is directly connected to backbone planarity. Relevant in this respect is the planarity of the effectively conjugated segment on which the exciton is located. For the three polymer fragments, optimized geometries and spin densities have been calculated, and the TBT at which the majority of spin density is located exhibits the smallest dihedral angles to the adjacent moieties. Furthermore, the larger delocalization of the polymers in film morphology as compared to their solution counterparts (Figure 9) is another strong hint toward a more planar backbone.

Possible Origin of the Small Emissive Signal at the Center. A few apparent characteristics of the small emissive signal seen at the center of (some of) the triplet signals of PCDTBT shall be discussed, shaping the ground for further investigations. Generally, such features have been observed in other polymers as well.[53,63,64] Possible origins are radical−triplet pairs between a stable radical, e.g., from a defect and a light-induced triplet state, as well as paramagnetic states with higher spin states, such as quintets arising from interacting triplet states.[54,55] For a more detailed discussion of light-induced paramagnetic species with higher spin multiplicity see ref 42.

Given the angular dependence, most probably a species with dipolar coupling between at least two spins is responsible for its origin. Furthermore, as the dipolar interaction dominates the spectral shape and width, a species with two rather far-separated spins—on the order of a few nanometers—is highly likely. In this case, the signal intensity would be mostly determined by the orientation of the vector of the dipolar interaction connecting the two unpaired spins with respect to the external magnetic field. If that were true, the charge separation would be predominantly within the film, not perpendicular to it, consistent with charge separation within polymer chains.

Short-lived charge-separated states have been described and observed for pristine polymers,[65] and it is generally known that, given sufficient excitation energy, such processes do occur, although they do not normally lead to efficient charge separation, hence making binary systems with dedicated donor and acceptor phases necessary for organic photovoltaic devices.[14,66,67]

Further investigations would involve recording spectra over a much narrower field range with higher resolution and probably additional angles with respect to the external magnetic field. However, these investigations, though interesting and promising, are clearly outside the scope of the present study. Note, however, that different materials may well show different origins of their central peak. Therefore, our discussion will not necessarily apply there as well.

Magnetophotoselection Provides Clear Evidence for the Face-On Orientation. The enhanced signal intensity of the outer wings of the triplet spectra for orientation of the polarization plane perpendicular to $\boldsymbol{B}_0$ (cf. Figure 6) reveals the D_z-axis to be oriented perpendicular to the optical transition dipole moment. Cbz−TBT and P0 both show the same overall trend, whereas for P0, the effect is very minor and only barely visible. It is not surprising to see only a very small effect of magnetophotoselection in the polymer. P0 is known to be rather amorphous, at least not to form semicrystalline domains. Hence, given a somewhat twisted polymer backbone, particularly in (frozen) solution, and a finite overall mobility of the triplet exciton on this polymer chain, the initial geometrical relationship between the excitation (hence the transition dipole moment) and the $\boldsymbol{D}$ tensor of the triplet exciton will get lost in due course. This means, on the other hand, that a visible effect of magnetophotoselection in polymers is a clear hint of a rather ordered environment or a very restricted triplet exciton migration.

From previous studies, it is known that the optical transition dipole moment of TBT is located within the aromatic plane.[68] In our previous detailed study of P0 and its building blocks, we revealed TBT to entirely dominate the electronic structure even of the polymer.[44] Therefore, we are quite confident that the transition dipole moment stays within the aromatic plane even for the polymer. Note that the only information necessary in the given context is the orientation either within the aromatic plane or perpendicular to it. Assuming, on these grounds, that the transition dipole moment is situated within

DOI: 10.1021/acs.jpcc.9b02835
J. Phys. Chem. C 2019, 123, 20071−20083

the aromatic plane of the repeat unit, Cbz−TBT, and the polymer, P0, we can deduce the orientation of the polymer on the substrate (Figure 11). Our TREPR data obtained on drop-cast films unequivocally reveal D_z to be orthogonal to the substrate plane, and similarly, our magnetophotoselection studies show D_z to be orthogonal as well to the optical transition dipole moment. Therefore, the aromatic plane is necessarily preferentially oriented in the plane of the substrate, hence the face-on orientation of the polymer backbone. Particularly in OLEDs and organic solar cells, a face-on orientation of the polymer toward the substrate is considered advantageous for charge transport to the electrodes.[36−39]

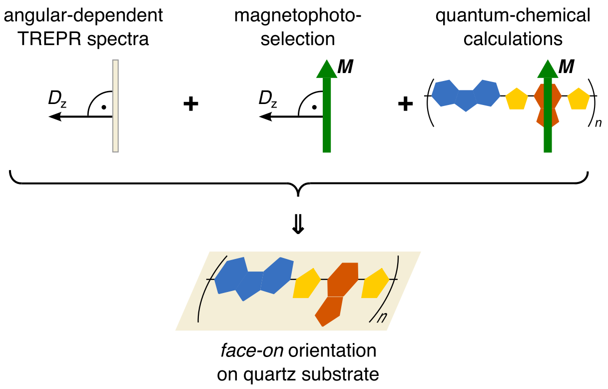

Figure 11. Schematic overview of the different lines of evidence for the face-on orientation of the polymer on the substrate. Angular-dependent TREPR spectra unequivocally assign the *z* component of the ***D*** tensor to be perpendicular to the substrate plane. Magnetophotoselection experiments reveal the *z* component of the ***D*** tensor to be perpendicular to the optical transition dipole moment (green arrow). For TBT, the transition dipole moment vector has been shown by DFT calculations to lie within the aromatic plane. As TBT entirely dominates the electronic structure even of the polymer, taken together, these results clearly reveal the face-on orientation of the polymer on the substrate.

■ CONCLUSIONS

Taken together, applying TREPR spectroscopy to a series of PCDTBT derivatives with systematically increased degree of hexylation, we could gain detailed insight into the effects of side chains on conjugated polymers, distinguishing between its impact on film morphology and electronic structure. For this particular polymer, additional side chains clearly influence both the electronic structure and its solubility and enhance compatibility with complementing components in blends. Furthermore, not only does TREPR spectroscopy allow the film morphology and electronic structure to be probed simultaneously, but it also allows the effects of side-chain engineering on these two crucial aspects of the structure−function relationship to be distinguished. Although the alkyl side chains clearly introduce backbone torsion strongly impacting the exciton delocalization, the overall degree of order is not affected. Thus, we speculate that both exciton and charge carrier mobilities are most probably similar in the hexylated and non-hexylated polymer. The overall degree of order with respect to the surface plane in all polymer films investigated is quite high, in accordance with previous investigations.[33] Thus, although the herein investigated PCDTBT derivatives do not show ordering effects in solution, they exhibit a rather strong degree of order in films. A possible explanation is that the surface induces a strong degree of order in the polymer film that is not restricted to the immediate interface but proceeds through the entire film. Clearly, this is an effect of the preparation method, and further studies on different (model) polymers varying the preparation conditions will help further elucidate the origin of this effect. Furthermore, we demonstrate an overall face-on orientation of the polymer backbone with respect to the surface, advantageous for charge transport to the electrodes. Taken together, with its molecular sensitivity, angular-dependent TREPR spectroscopy on polymer films allows for valuable insight into both morphology and electronic structure of semiconducting polymers. Probing the overall order in the entire polymer films, not easily accessible by other techniques such as X-ray scattering due to the lack of crystallinity of the sample, demonstrates the potential of TREPR spectroscopy of triplet excitons to corroborate the results obtained by other measurement techniques. The overall degree of order and the backbone torsion are revealed to be two independent aspects, with the former being highly relevant to exciton and charge carrier mobilities and charge extraction and injection. Backbone torsion, on the other hand, has a direct impact on the exciton delocalization length and is responsible for efficient charge separation or recombination, respectively. These deepened insights into the intricacies of the structure−function relationship of organic semiconductors are clearly relevant for the design of materials.

■ EXPERIMENTAL SECTION

Synthesis. All polymers were synthesized according to published procedures.[40]

Optical Spectroscopy. All samples were dissolved in *o*-dichlorobenzene in concentrations of 10 mg/mL. Absorption spectra were recorded using a commercial UV/vis spectrometer (UV-1601PC) in combination with the corresponding software (UV Probe version 3.42). Measurements were performed using 1 mm path length cuvettes.

EPR Instrumentation. All samples were dissolved in *o*-dichlorobenzene in concentrations of 10 mg/mL. All TREPR experiments were performed at 80 K using a setup described previously.[33,44] Optical excitation at the respective wavelengths was carried out using an optical parametric oscillator (OPO) pumped by an Nd:YAG laser. The repetition rate of the laser was set to 10 Hz, and the final pulse energy (after the OPO) to 1 mJ. Further experimental parameters (except where explicitly given) are as follows: microwave frequency: 9.700 GHz, microwave power: 2 mW (20 dB attenuation, source power: 200 mW), frequency-mixer detection, video amplifier set to 42 dB amplification and 25 MHz bandwidth, 1000 averages per point. Angular-dependent measurements were performed with help of a goniometer with 1° division attached to the top of the probehead and a pointer connected to the sample rod. The overall accuracy of angles is estimated to be ±5°.

Spectral Simulations. All simulations of triplet spectra were performed using a homemade simulation routine programmed in Python. Details of both the simulations and the fitting procedure are given in the SI.

DFT Calculations. All calculations were performed using ORCA 3.0.3[69] using the BP86[70,71] functional and the Def2-SVP[72] basis set, respectively. The solvent has been accounted for by the COSMO model.[73] Initial geometries of the molecules were created using Avogadro 1.1.1.[74] Spin-density plots were created using UCSF Chimera 1.11.2.[75]

■ ASSOCIATED CONTENT

Ⓢ Supporting Information

The Supporting Information is available free of charge on the ACS Publications website at DOI: 10.1021/acs.jpcc.9b02835.

> Details of the EPR instrumentation, TREPR spectra of triplet states including full 2D datasets, details for the spectral simulations of TREPR spectra, details for determining the dihedral angles of the optimized geometries, Figure 7 with wave numbers rather than wavelengths, and a detailed discussion why TREPR probes the entire films rather than a minority of triplet species residing exclusively on the interface between the film and substrate (PDF)

■ AUTHOR INFORMATION

Corresponding Author

*E-mail: till.biskup@uni-saarland.de. Phone: +49 (0)681 3022741. Fax: +49 (0)681 3024759.

ORCID

Michael Sommer: 0000-0002-2377-5998
Till Biskup: 0000-0003-2913-0004

Present Address

‖Physikalische Chemie und Didaktik der Chemie, Universität des Saarlandes, Campus B2 2, 66123 Saarbrücken, Germany (T.B.).

Notes

The authors declare no competing financial interest.

■ ACKNOWLEDGMENTS

The authors thank the German Research Foundation (DFG, Grant BI 1249/3-1 to T.B.), Albert-Ludwigs-Universität Freiburg (Innovationsfonds Forschung, to T.B.), and Wissenschaftliche Gesellschaft Freiburg (to T.B.) for financial support, M. Herancourt for help with initial experiments, and S. Weber for providing EPR equipment.

■ REFERENCES

(1) Heeger, A. J. Semiconducting polymers: the Third Generation. *Chem. Soc. Rev.* **2010**, *39*, 2354−2371.

(2) Darling, S. B.; You, F. The case for organic photovoltaics. *RSC Adv.* **2013**, *3*, 17633−17648.

(3) Forrest, S. R. Excitons and the lifetime of organic semiconductor devices. *Philos. Trans. R. Soc., A* **2015**, *373*, No. 20140320.

(4) Azzopardi, B.; Emmott, C. J. M.; Urbina, A.; Kresbs, F. C.; Mutale, J.; Nelson, J. Economic assessment of solar electricity production from organic-based photovoltaic modules in a domestic environment. *Energy Environ. Sci.* **2011**, *4*, 3741−3753.

(5) Brabec, C. J.; Durrant, J. R. Solution-processed organic solar cells. *MRS Bull.* **2008**, *33*, 670−275.

(6) Gambhir, A.; Sandwell, P.; Nelson, J. The future costs of OPV - A bottom-up model of material and manufacturing costs with uncertainty analysis. *Sol. Energy Mater. Sol. Cells* **2016**, *156*, 49−58.

(7) Forrest, S. R. The path to ubiquitious and low-cost organic electronic appliances on plastic. *Nature* **2004**, *428*, 911−918.

(8) Mulligan, C. J.; Bilen, C.; Zhou, X.; Belcher, W. J.; Dastoor, P. C. Levelised cost of electricity for organic photovoltaics. *Sol. Energy Mater. Sol. Cells* **2015**, *133*, 26−31.

(9) Li, Y.; Xu, G.; Cui, C.; Li, Y. Flexible and semitransparent organic solar cells. *Adv. Energy Mater.* **2017**, *8*, No. 1701791.

(10) Lu, L.; Zheng, T.; Wu, Q.; Schneider, A. M.; Zhao, D.; Yu, L. Recent advances in bulk heterojunction polymer solar cells. *Chem. Rev.* **2015**, *115*, 12666−12731.

(11) Yeh, N.; Yeh, P. Organic solar cells: their developments and potentials. *Renewable Sustainable Energy Rev.* **2013**, *21*, 421−431.

(12) Facchetti, A. Seminconductors for organic transistors. *Mater. Today* **2007**, *10*, 28−37.

(13) Sekine, C.; Tsubata, Y.; Yamada, T.; Kitano, M.; Doi, S. Recent progress of high performance polymer OLED and OPV materials for organic printed electronics. *Sci. Technol. Adv. Mater.* **2014**, *15*, No. 034203.

(14) Yu, G.; Gao, J.; Hummelen, J. C.; Wudl, F.; Heeger, A. J. Polymer photovoltaic cells: enhanced efficiencies via a network of internal donor-acceptor heterojunctions. *Science* **1995**, *270*, 1789−1791.

(15) Oberhumer, P. M.; Huang, Y.-S.; Massip, S.; James, D. T.; Tu, G.; Albert-Seifried, S.; Beljonne, D.; Cornil, J.; Kim, J.-S.; Huck, W. T. S.; et al. Tuning the electronic coupling in a low-bandgap donor-acceptor copolymer via the placement of side-chains. *J. Chem. Phys.* **2011**, *134*, No. 114901.

(16) Mei, J.; Bao, Z. Side chain engineering in solution-processable conjugated polymers. *Chem. Mater.* **2014**, *26*, 604−615.

(17) Lu, L. P.; Finlayson, C. E.; Kabra, D.; Albert-Seifried, S.; Song, M. H.; Havenith, R. W. A.; Tu, G.; Huck, W. T. S.; Friend, R. H. The influence of side-chain position on the optoelectronic properties of a red-emitting conjugated polymer. *Macromol. Chem. Phys.* **2013**, *214*, 967−974.

(18) Ko, S.; Hoke, E. T.; Pandey, L.; Hong, S.; Mondal, R.; Risko, C.; Yi, Y.; Noriega, R.; McGehee, M. D.; Brédas, J.-L.; et al. Controlled conjugated backbone twisting for an increased open-circuit voltage while having a high short-circuit current in poly(hexylthiophene) derivatives. *J. Am. Chem. Soc.* **2012**, *134*, 5222−5232.

(19) Szarko, J. M.; Guo, J.; Liang, Y.; Lee, B.; Rolczynski, B. S.; Strzalka, J.; Xu, T.; Loser, S.; Marks, T. J.; Yu, L.; et al. When function follows form: effects of donor copolymer side chains on film morphology and BHJ solar cell performance. *Adv. Mater.* **2010**, *22*, 5468−5472.

(20) Lan, S.-C.; Chang, C.-K.; Lu, Y.-H.; Lin, S.-W.; Jen, A. K.-Y.; Wei, K.-H. Side chain structure affects the molecular packing and photovoltaic performance of oligothiophene-based solution-processable small molecules. *RSC Adv.* **2015**, *5*, 67718−67726.

(21) Venkateshvaran, D.; Nikolka, M.; Sadhanala, A.; Lemaur, V.; Zelazny, M.; Kepa, M.; Hurhangee, M.; Kronemeijer, A. J.; Pecunia, V.; Nasrallah, I.; et al. Approaching disorder-free transport in high-mobility conjugated polymers. *Nature* **2014**, *515*, 384−388.

(22) Forbes, M. D.; Jarocha, L. E.; Sim, S.; Tarasov, V. F. Time-resolved electron paramagnetic resonance spectroscopy: history, technique, and application to supramolecular and macromolecular chemistry. *Adv. Phys. Org. Chem.* **2014**, *47*, 1−83.

(23) Weber, S. Transient EPR. *eMagRes* **2017**, *6*, 255−270.

(24) Blouin, N.; Michaud, A.; Leclerc, M. A low-bandgap poly(2,7-carbazole) derivative for use in high-performance solar cells. *Adv. Mater.* **2007**, *19*, 2295−2300.

(25) Blouin, N.; Michaud, A.; Gendron, D.; Wakim, S.; Blair, E.; Neagu-Plesu, R.; Belletête, M.; Durocher, G.; Tao, Y.; Leclerc, M. Toward a rational design of poly(2,7-carbazole) derivatives for solar cells. *J. Am. Chem. Soc.* **2008**, *130*, 732−742.

(26) Cho, S.; Seo, J. H.; Park, S. H.; Beaupré, S.; Leclerc, M.; Heeger, A. J. A thermally stable semiconducting polymer. *Adv. Mater.* **2010**, *22*, 1253−1257.

(27) Sun, Y.; Takacs, C. J.; Cowan, S. R.; Seo, J. H.; Gong, X.; Roy, A.; Heeger, A. J. Efficient, air-stable bulk heterojunction polymer solar cells using MoO_x as the anode interfacial layer. *Adv. Mater.* **2011**, *23*, 2226−2230.

(28) Peters, C. H.; Sachs-Quintana, I. T.; Kastrop, J. P.; Beaupré, S.; Leclerc, M.; McGehee, M. D. High efficiency polymer solar cells with long operating lifetimes. *Adv. Energy Mater.* **2011**, *1*, 491−494.

(29) Kong, J.; Song, S.; Yoo, M.; Lee, G. Y.; Kwon, O.; Park, J. K.; Back, H.; Kim, G.; Lee, S. H.; Suh, H.; et al. Long-term stable polymer solar cells with significantly reduced burn-in loss. *Nat. Commun.* **2014**, *5*, No. 5688.

(30) Beaupré, S.; Leclerc, M. PCDTBT: en route for low cost plastic solar cells. *J. Mater. Chem. A* **2013**, *1*, 11097−11105.

(31) Zhang, Y.; Zhou, H.; Seifter, J.; Ying, L.; Mikhailovsky, A.; Heeger, A. J.; Bazan, G. C.; Nguyen, T.-Q. Molecular doping enhances photoconductivity in polymer bulk heterojunction solar cells. *Adv. Mater.* **2013**, *25*, 7038−7044.

(32) Lombeck, F.; Komber, H.; Fazzi, D.; Nava, D.; Kuhlmann, J.; Stegerer, D.; Strassel, K.; Brandt, J.; de Zerio Mendaza, A. D.; Müller, C.; et al. On the effect of prevalent carbazole homocoupling defects on the photovoltaic performance of PCDTBT:$PC_{71}BM$ solar cells. *Adv. Energy Mater.* **2016**, *6*, No. 1601232.

(33) Biskup, T.; Sommer, M.; Rein, S.; Meyer, D. L.; Kohlstädt, M.; Würfel, U.; Weber, S. Ordering of PCDTBT revealed by time-resolved electron paramagnetic resonance spectroscopy of its triplet excitons. *Angew. Chem., Int. Ed.* **2015**, *54*, 7707−7710.

(34) Beiley, Z. M.; Hoke, E. T.; Noriega, R.; Dacuña, J.; Burkhard, G. F.; Bartelt, J. A.; Salleo, A.; Toney, M. F.; McGehee, M. D. Morphology-dependent trap formation in high performance polymer bulk heterojunction solar cells. *Adv. Energy Mater.* **2011**, *1*, 954−962.

(35) Wang, H.-W.; Pentzer, E.; Emrick, T.; Russell, T. P. Preparation of low band gap fibrillar structures by solvent-induced crystallization. *ACS Macro Lett.* **2014**, *3*, 30−34.

(36) Ibraikulov, O. A.; Ngov, C.; Chávez, P.; Bulut, I.; Heinrich, B.; Boyron, O.; Ivanov, K. L. G. D. A.; Swaraj, S.; Méry, S.; Leclerc, N.; et al. Face-on orientation of fluorinated polymers conveyed by long alkyl chains: a prerequisite for high photovoltaic performances. *J. Mater. Chem. A* **2018**, *6*, 12038−12045.

(37) Osaka, I.; Kakara, T.; Takemura, N.; Koganezawa, T.; Takimiya, K. Naphthodithiophene-naphthobisthiadiazole copolymers for solar cells: alkylation drives the polymer backbone flat and promotes efficiency. *J. Am. Chem. Soc.* **2013**, *135*, 8834−8837.

(38) Rand, B. P.; Cheyns, D.; Vasseur, K.; Giebink, N. C.; Mothy, S.; Yi, Y.; Coropceanu, V.; Beljonne, D.; Cornil, J.; Brédas, J.-L.; et al. The impact of molecular orientation on the photovoltaic properties of a phthalocyanine/fullerene heterojunction. *Adv. Funct. Mater.* **2012**, *22*, 2987−2995.

(39) Akaike, K.; Ando, S.; Enozawa, H.; Kosaka, A.; Kajitani, T.; Fukushima, T. An electron-accepting molecular unit exhibiting an orientational preference favorable for organic photovoltaic applications. *Thin Solid Films* **2015**, *583*, 34−39.

(40) Lombeck, F.; Di, D.; Yang, L.; Meraldi, L.; Athanasopoulos, S.; Credgington, D.; Sommer, M.; Friend, R. H. PCDTBT: from polymer photovoltaics to light-emitting diodes by side-chain-controlled luminescence. *Macromolecules* **2016**, *49*, 9382−9387.

(41) Baldo, M. A.; O'Brien, D. F.; Thompson, M. E.; Forrest, S. R. Excitonic singlet-triplet ratio in a semiconducting organic thin film. *Phys. Rev. B* **1999**, *60*, 14422−14428.

(42) Biskup, T. Structure-function relationship of organic semiconductors: Detailed insights from time-resolved EPR spectroscopy. *Front. Chem.* **2019**, *7*, No. 10.

(43) Banerji, N.; Gagnon, E.; Morgantini, P.-Y.; Valouch, S.; Mohebbi, A. R.; Seo, J.-H.; Leclerc, M.; Heeger, A. J. Breaking down the problem: optical transitions, electronic structure, and photoconductivity in conjugated polymer PCDTBT and in its separate building blocks. *J. Phys. Chem. C* **2012**, *116*, 11456−11469.

(44) Matt, C.; Meyer, D. L.; Lombeck, F.; Sommer, M.; Biskup, T. TBT entirely dominates the electronic structure of the conjugated copolymer PCDTBT: Insights from time-resolved electron paramagnetic resonance spectroscopy. *Macromolecules* **2018**, *51*, 4341−4349.

(45) Stoll, S.; Schweiger, A. EasySpin, a comprehensive software package for spectral simulation and analysis in EPR. *J. Magn. Reson.* **2006**, *178*, 42−55.

(46) Meyer, D. L.; Matsidik, R.; Sommer, M.; Biskup, T. Electronic structure trumps planarity: Unexpected narrow exciton delocalisation in PNDIT2 revealed by time-resolved EPR spectroscopy. *Adv. Electron. Mater.* **2018**, *4*, No. 1700385.

(47) Meyer, D. L.; Matsidik, R.; Huettner, S.; Sommer, M.; Biskup, T. Solvent-mediated aggregate formation of PNDIT2: Decreasing the available conformational subspace by introducing locally highly ordered domains. *Phys. Chem. Chem. Phys.* **2018**, *20*, 2716−2723.

(48) Biskup, T. Time-resolved EPR of radical pair intermediates in cryptochromes. *Mol. Phys.* **2013**, *111*, 3698−3703.

(49) Bittl, R.; Weber, S. Transient radical pairs studied by time-resolved EPR. *Biochim. Biophys. Acta* **2005**, *1707*, 117−126.

(50) Behrends, J.; Sperlich, A.; Schnegg, A.; Biskup, T.; Teutloff, C.; Lips, K.; Dyakonov, V.; Bittl, R. Direct detection of photoinduced charge transfer complexes in polymer fullerene blends. *Phys. Rev. B* **2012**, *85*, No. 125206.

(51) Miura, T.; Aikawa, M.; Kobori, Y. Time-resolved EPR study of electron-hole dissociations influenced by alkyl side chains at the photovoltaic polyalkylthiophene:PCBM interface. *J. Phys. Chem. Lett.* **2014**, *5*, 30−35.

(52) Thomson, S. A. J.; Niklas, J.; Mardis, K. L.; Mallares, C.; Samuel, I. D. W.; Poluektov, O. G. Charge separation and triplet exciton formation pathways in small-molecule solar cells as studied by time-resolved EPR spectroscopy. *J. Phys. Chem. C* **2017**, *121*, 22707−22719.

(53) Yamamoto, Y.; Ako, T.; Tachikawa, T.; Osaka, I.; Kobori, Y. Time-resolved EPR study on photoinduced charge-transfer trap state in thiophene-thiazolothiazole copolymer film. *J. Photopolym. Sci. Technol.* **2017**, *30*, 551−555.

(54) Weiss, L. R.; Bayliss, S. L.; Kraffert, F.; Thorley, K. J.; Anthony, J. E.; Bittl, R.; Friend, R. H.; Rao, A.; Greenham, N. C.; Behrends, J. Strongly exchange-coupled triplet pairs in an organic semiconductor. *Nat. Phys.* **2017**, *13*, 176−181.

(55) Tayebjee, M. J. Y.; Sanders, S. N.; Kumarasamy, E.; Campos, L. M.; Sfeir, M. Y.; McCamey, D. R. Quintet multiexciton dynamics in singlet fission. *Nat. Phys.* **2017**, *13*, 182−188.

(56) Siegel, S.; Judeikis, H. S. A magnetophotoselection study of the polarization of the absorption bands of some structurally related hydrocarbons and heterocyclic molecules. *J. Phys. Chem. A* **1966**, *70*, 2205−2211.

(57) Thurnauer, M. C.; Norris, J. R. The ordering of the zero field triplet spin sublevels in the chlorophylls. A magnetophotoselection study. *Chem. Phys. Lett.* **1977**, *47*, 100−105.

(58) Meyer, D. L.; Matsidik, R.; Fazzi, D.; Sommer, M.; Biskup, T. Probing exciton delocalization in organic semiconductors: Insight from time-resolved electron paramagnetic resonance and magnetophotoselection experiments. *J. Phys. Chem. Lett.* **2018**, *9*, 7026−7031.

(59) Tait, C. E.; Neuhaus, P.; Anderson, H. L.; Timmel, C. R. Triplet state delocalization in a conjugated porphyrin dimer probed by transient electron paramagnetic resonance techniques. *J. Am. Chem. Soc.* **2015**, *137*, 6670−6679.

(60) Kim, J.; Kwon, Y. S.; Shin, W. S.; Moon, S.-J.; Park, T. Carbazole-based copolymers: effects of conjugation breaks and steric hindrance. *Macromolecules* **2011**, *44*, 1909−1919.

(61) Zhang, X.; Bronstein, H.; Kronemeijer, A. J.; Smith, J.; Kim, Y.; Kline, R. J.; Richter, L. J.; Anthopoulos, T. D.; Sirringhaus, H.; Song, K.; et al. Molecular origin of high field-effect mobility in an indacenodithiophene-benzothiadiazole copolymer. *Nat. Commun.* **2013**, *4*, No. 2238.

(62) Lu, X.; Hlaing, H.; Germack, D. S.; Peet, J.; Jo, W. H.; Andrienko, D.; Kremer, K.; Ocko, B. M. Bilayer order in a polycarbazole-conjugated polymer. *Nat. Commun.* **2012**, *3*, No. 795.

(63) Bennati, M.; Grupp, A.; Mehring, M.; Bäuerle, P. Pulsed EPR spectroscopy of the photoexcited triplet states of thiophene oligomers in frozen solution. *J. Phys. Chem. A* **1996**, *100*, 2849−2853.

(64) Sperlich, A.; Kraus, H.; Deibel, C.; Blok, H.; Schmidt, J.; Dyakonov, V. Reversible and Irreversible Interactions of Poly(3-hexylthiophene) with Oxygen Studied by Spin-Sensitive Methods. *J. Phys. Chem. B* **2011**, *115*, 13513−13518.

(65) Huynh, U. N. V.; Basel, T. P.; Ehrenfreund, E.; Li, G.; Yang, Y.; Mazumdar, S.; Vardeny, Z. V. Transient magnetophotoinduced absorption studies of photoexcitations in π-conjugated donor-acceptor copolymers. *Phys. Rev. Lett.* **2017**, *119*, No. 017401.

(66) Tang, C. W. Two-layer organic photovoltaic cell. *Appl. Phys. Lett.* **1986**, *48*, 183−185.

(67) Scharber, M. C.; Sariciftci, N. S. Efficiency of bulk-heterojunction organic solar cells. *Prog. Polym. Sci.* **2013**, *38*, 1929−1940.

(68) Nielsen, C. B.; White, A. J. P.; McCulloch, I. Effect of fluorination of 2,1,3-benzothiadiazole. *J. Org. Chem.* **2015**, *80*, 5045−5048.

(69) Neese, F. The ORCA program package. *Wiley Interdiscip. Rev.: Comput. Mol. Sci.* **2012**, *2*, 73−78.

(70) Becke, A. D. Density-functional exchange-energy approximation with correct asymptotic behavior. *Phys. Rev. A* **1988**, *38*, 3098−3100.

(71) Perdew, J. P. Density-functional approximation for the correlation energy of the inhomogeneous electron gas. *Phys. Rev. B* **1986**, *33*, 8822−8824.

(72) Weigend, F.; Ahlrichs, R. Balanced basis sets of split valence, triple zeta valence and quadruple zeta valence quality for H to Rn: Design and assessment of accuracy. *Phys. Chem. Chem. Phys.* **2005**, *7*, 3297−3305.

(73) Sinnecker, S.; Rajendran, A.; Klamt, A.; Diedenhofen, M.; Neese, F. Calculation of solvent shifts on electronic g-tensors with the conductor-like screening model (COSMO) and its self-consistent generalization to real solvents (direct COSMO-RS). *J. Phys. Chem. A* **2006**, *110*, 2235−2245.

(74) Hanwell, M. D.; Curtis, D. E.; Lonie, D. C.; Vandermeersch, T.; Zurek, E.; Hutchison, G. R. Avogadro: an advanced semantic chemical editor, visualization, and analysis platform. *J. Cheminf.* **2012**, *4*, No. 17.

(75) Pettersen, E. F.; Goddard, T. D.; Huang, C. C.; Couch, G. S.; Greenblatt, D. M.; Meng, E. C.; Ferrin, T. E. UCSF Chimera−A visualization system for exploratory research and analysis. *J. Comput. Chem.* **2004**, *25*, 1605−1612.

Side-Chain Engineering of Conjugated Polymers: Distinguishing Its Impact on Film Morphology and Electronic Structure

— Supporting Information —

Deborah L. Meyer,[a] Noah Schmidt-Meinzer,[a] Clemens Matt,[a] Stephan Rein,[a]
Florian Lombeck,[b] Michael Sommer,[c] Till Biskup[a,d,*]

[a]Institut für Physikalische Chemie, Albert-Ludwigs-Universität Freiburg,
Albertstraße 21, 79104 Freiburg, Germany
[b]Institut für Makromolekulare Chemie, Albert-Ludwigs-Universität Freiburg,
Stefan-Meier-Straße 31, 79104 Freiburg, Germany
[c]Lehrstuhl Polymerchemie, Technische Universität Chemnitz,
Straße der Nationen 62, 09111 Chemnitz, Germany
[d]Physikalische Chemie und Didaktik der Chemie, Universität des Saarlandes,
Campus B2 2, 66123 Saarbrücken, Germany

Contents

---

*till.biskup@uni-saarland.de

EPR instrumentation

TREPR spectroscopy[1] with a time resolution of up to 10 ns allows for real-time observation, *e.g.*, of short-lived radical-pair and triplet states generated by pulsed laser excitation. In contrast to conventional continuous-wave EPR spectroscopy, which usually involves magnetic-field modulation to improve the signal-to-noise ratio, TREPR is recorded in a high-bandwidth direct-detection mode, so as not to constrain the time resolution of the experiment. Consequently, positive and negative signal amplitudes in TREPR correspond to enhanced absorptive (A) and emissive (E) electron-spin polarisations of the EPR transitions, respectively.

All TREPR experiments were performed at 80 K using a commercial EPR spectrometer (Bruker ESP380E) in conjunction with a Bruker microwave bridge (ER 046 MRT) equipped with a low-noise high-bandwidth video amplifier. The sample was placed in a synthetic-quartz (Suprasil) sample tube (3 mm inner diameter) and irradiated in a dielectric-ring resonator (Bruker ER 4118X-MD5), which was immersed in a helium gas-flow cryostat (Oxford CF-935) cooled with liquid nitrogen. The temperature was regulated to ±0.1 K by a temperature controller (Oxford ITC-503). The time resolution of the experimental setup was in the 10 ns range. A microwave frequency counter (Hewlett-Packard HP 5352B) was used to monitor the microwave frequency.

Optical excitation at the respective wavelengths was carried out with an optical parametric oscillator (OPO) system (Opta BBO-355-vis/IR) pumped by an Nd:YAG laser (Spectra Physics, Quanta Ray GCR 190-10) with a pulse width of approximately 6 ns, and a pulse energy of 1 mJ. The repetition rate of the laser was set to 10 Hz. A transient recorder (LeCroy 9354A) with a digitizing rate of 2 ns/11 bit was used to acquire the time-dependent EPR signal. To eliminate the background signal induced by the laser entering the EPR cavity, TREPR signals were accumulated at off-resonance magnetic-field positions (background) and subtracted from those recorded on-resonance. This background signal is completely independent in its shape from both, laser wavelength and magnetic field, and normally long-lived compared to the detected spin-polarised EPR signal. Background subtraction was performed directly in the transient recorder and a background signal repeatedly recorded after each tenth time trace of the experimental data.

Further experimental parameters (except where explicity given) are as follows: Microwave frequency, 9.700 GHz, microwave power: 2 mW (20 dB attenuation, source power 200 mW), frequency-mixer detection, video amplifier set to 42 dB amplification and 25 MHz bandwidth, 1000 averages per point.

TREPR spectra of triplet states

As TREPR spectra of spin-polarised triplet states of organic molecules recorded at X-band frequencies and magnetic fields are normally dominated by the zero-field splitting (ZFS) interaction, the Hamilton operator used to describe the system reduces dramatically. The only contributions that need to be taken into account are the Hamilton operator for the Zeeman interaction, $\mathcal{H}_{\mathrm{EZ}}$,

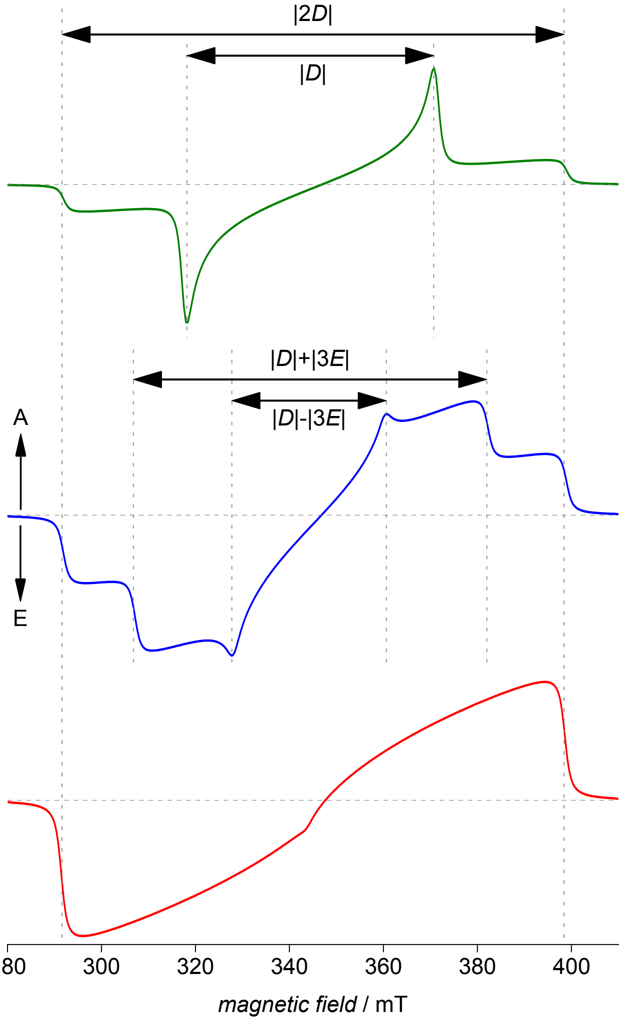

Figure S1: Characteristics of TREPR spectra of (photo-generated) triplet states. Three characteristic situations for the ratio of the two parameters D and E of the ZFS tensor are depicted here: the fully axial case (top, green), an intermediate case (blue, centre) and a fully rhombic case (red, bottom). Spectra were calculated using EasySpin [2]. The zero-field populations $p_{1,2,3}$ of the three triplet sublevels are far from thermal equilibrium, due to optical excitation and the inherent anisotropy of the intersystem crossing processes. Therefore, signals consist of both, absorptive (A) and emissive (E) contributions.

and the one for the ZFS interaction, $\mathcal{H}_{\text{ZFS}}$:

$$\mathcal{H} = \mathcal{H}_{\text{EZ}} + \mathcal{H}_{\text{ZFS}} = \boldsymbol{g}\mu_{\text{B}}\boldsymbol{S}\boldsymbol{B} + \boldsymbol{S}\boldsymbol{D}\boldsymbol{S}. \tag{S1}$$

All other contributions can be considered as small perturbations that can be accounted for using (inhomogeneous) line broadening.

The $\boldsymbol{D}$ tensor in its principal axis system is given to

$$\boldsymbol{D} = \begin{pmatrix} -\frac{1}{3}D + E & 0 & 0 \\ 0 & -\frac{1}{3}D - E & 0 \\ 0 & 0 & \frac{2}{3}D \end{pmatrix} \tag{S2}$$

where D and E are the zero-field-splitting parameters that can be directly read out from the experimental spectra (cf. Fig. S1). Note that D and E are defined such in the simulation routine used that the relation $|E| \leq |D|/3$ always holds.

Spectral simulations of TREPR spectra of triplet states

All simulations of triplet spectra have been performed using a simulation routine implemented in the programming language Python following published procedures [2], but focussing particularly on the need to account for partial orientation, thus making use of the intrinsic symmetry of the spin Hamilton operator while retaining the possibility to easily apply weighting to the powder average. To account for the partial orientation, a Gaussian distribution with standard deviation σ, centred about θ, one of the Euler angles (θ, ϕ), is used to weight the intensities accordingly. Details of this simulation routine will be published elsewhere.

Parameters included were the $\boldsymbol{g}$ and $\boldsymbol{D}$ tensor and the triplet sublevel populations $p_{1,2,3}$ (in zero field). Line broadening (Γ) was included using a convolution of Lorentzian (Γ_L) and Gaussian (Γ_G) lines. For all simulations, the $\boldsymbol{g}$ tensor was assumed to be isotropic, with $g_\mathrm{iso} = 2.002$. This left the parameters D and E of the zero-field splitting tensor $\boldsymbol{D}$, the populations $p_{1,2,3}$, and the two line widths Γ_L and Γ_G, and in case of the partially oriented samples the standard deviation σ and an offset for the angle θ as the only free parameters that were adjusted.

Fitting of the spectral simulations to the experimental data was done using optimisation algorithms provided by the Python SciPy packages [3], and for the Latin Hypercube sampling [4], the Python pyDOE package was used.

TREPR signal decay and triplet lifetime

The kinetics of TREPR signals of triplet states are rather complicated, involving spin relaxation, decay of spin polarisation, and decay of the actual triplet state, usually via intersystem crossing back into the singlet ground state. Hence, only a lower limit of the triplet lifetime can be extracted from the TREPR time profiles, based on the simple fact that regardless of all other processes, TREPR signals will only be observable as long as there exists a triplet state.

As can be seen from the full 2D datasets (Fig. S2), TREPR signals decay on the time scale of several microseconds. However, it is highly likely that this decay is dominated by the microwave power and other experimental parameters and that the actual triplet state lifetime extends well into tens or even hundreds of microseconds.

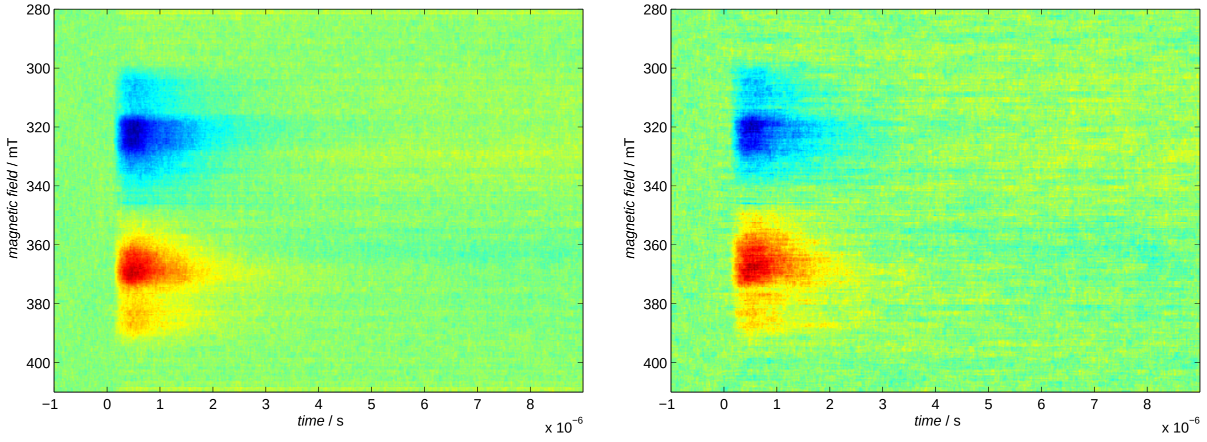

(a) P0 (b) P30

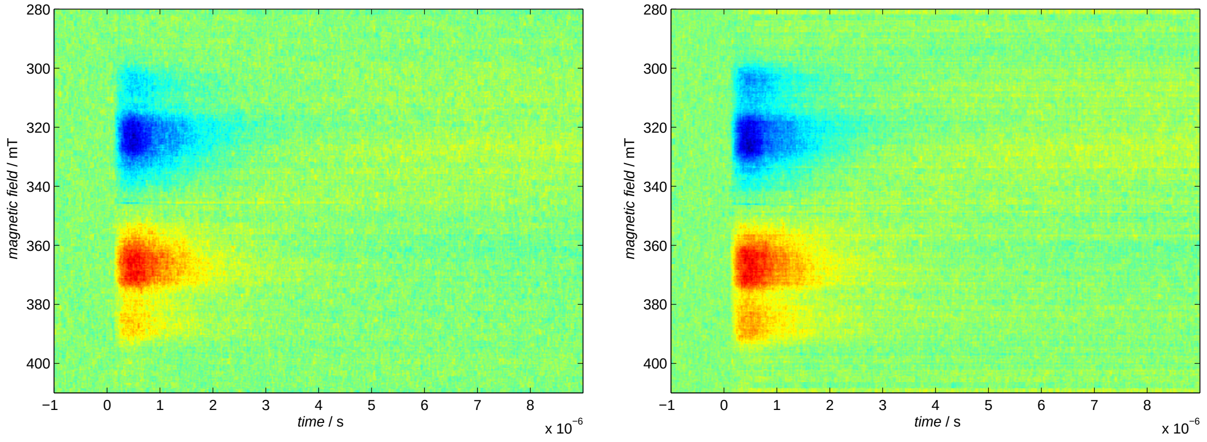

(c) P50 (d) P70

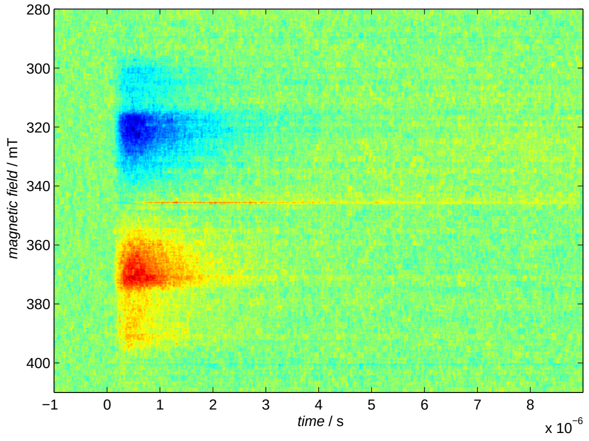

(e) P100

Figure S2: Full 2D TREPR datasets of all compounds investigated in this study. Blue colour denotes emissive, red colour enhanced absorptive polarisation. For experimental details see main text.

TREPR spectra of films drop-cast on quartz glass

For P30, the TREPR spectra of films drop-cast on quartz glass are shown in the main text (Fig. 4). For all other samples, TREPR spectra of the films are shown in Fig. S3.

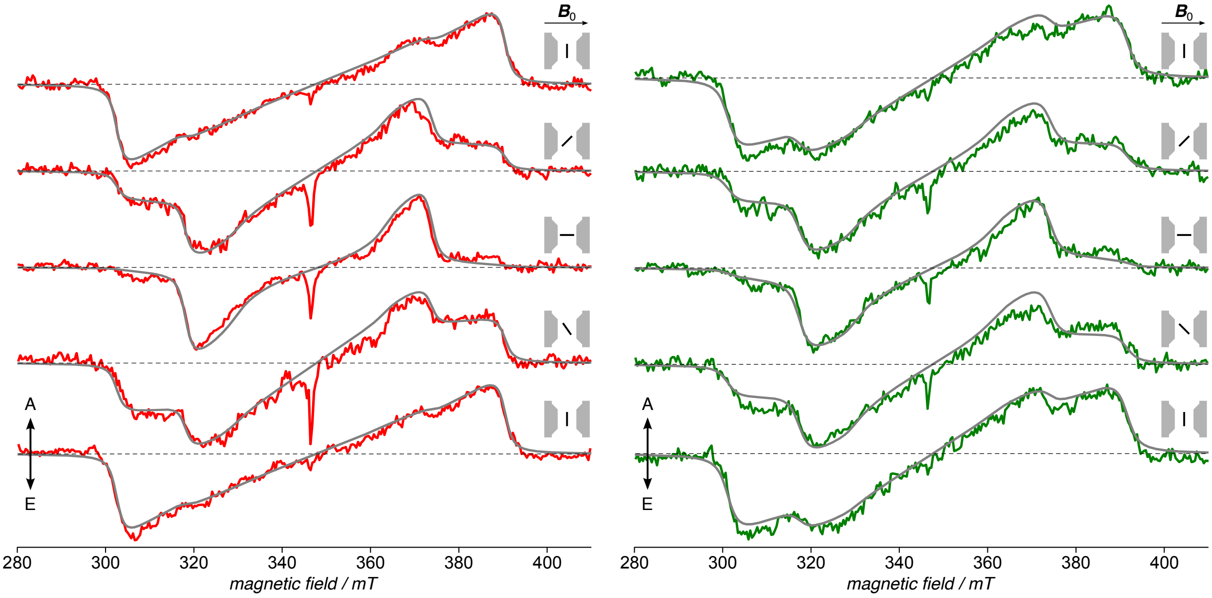

(a) P0 (b) P50

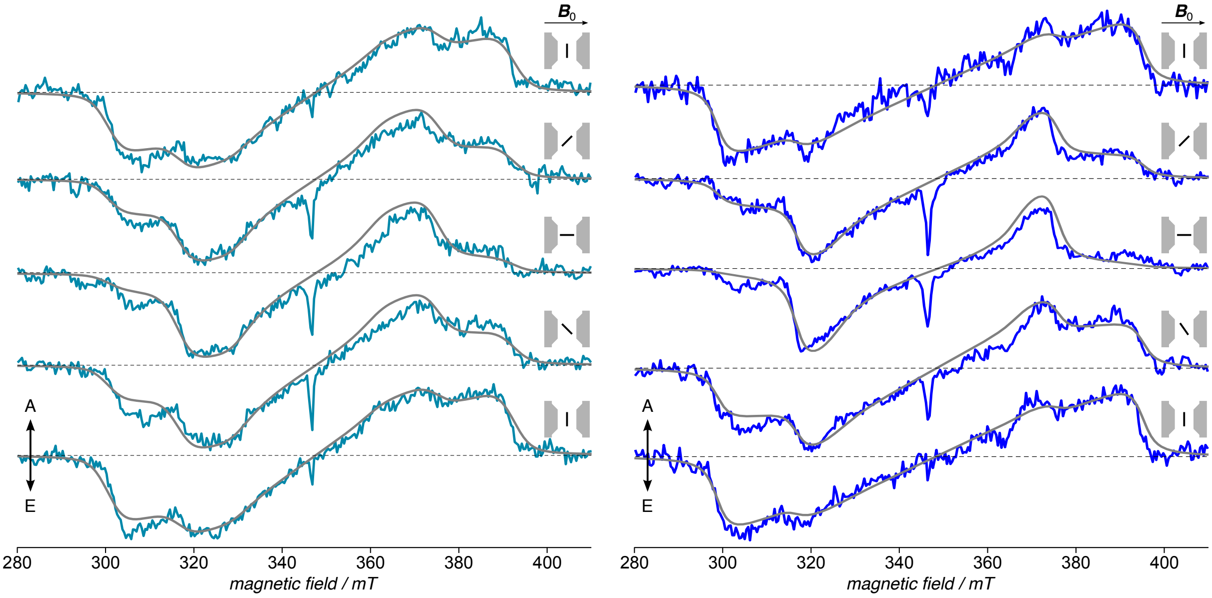

(c) P70 (d) P100

Figure S3: Angular-dependent TREPR spectra of thin films of PCDTBT with different degree of hexylation drop-cast on a quartz glass substrate, together with spectral simulations (grey lines). Spectra have been globally fitted for all five positions at once with one set of parameters. From the simulations, the orientation of the D tensor relative to the substrate plane as well as the overall degree of order can be extracted. Insets to the right show the orientation of the substrate with respect to the external magnetic field, $\boldsymbol{B}_0$. For simulation parameters see main text.

Determining the angles between TBT and Cbz moieties

As the aromatic planes of the TBT and Cbz moieties can be twisted against each other in all three directions, the tilting cannot be ascribed fully by a single dihedral angle between adjacent atoms. Hence, coordinate systems have been created in both aromatic planes and the angles between the x, y, and z axes compared to those of the planar structure.

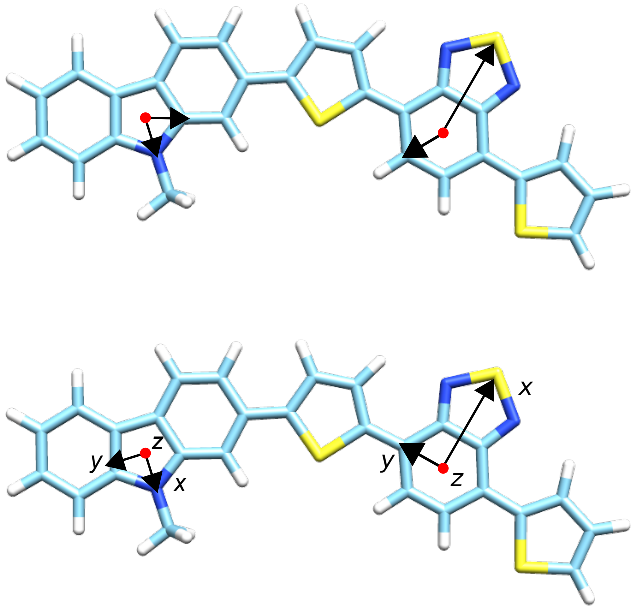

Figure S4: Illustration of constructing the vectors that have been used for determining the angles between TBT and Cbz moieties. The top panel shows the two vectors spanning the aromatic planes, whereas the complete coordinate systems in Cbz and TBT are shown in the bottom panel.

In a first step, the center of both, benzene and pyrroline rings have been calculated (red dot in Fig. S4) and the vectors from there to the S and N atom, respectively, created that form the x axis of the coordinate system. A second vector has been created pointing from the centre of the aromatic plane to one of the atoms in the aromatic plane to span this plane (Fig. S4, top). The cross product of these two vectors led to the z axis of the coordinate system. In the following, the cross product of the vectors for the x and z axis could be used to create the y axis and hence complete the coordinate system (Fig. S4, bottom).

As the cross product always generates one of two possible vectors being orthogonal to the two vectors multiplied, displaying all vectors was necessary to check that the correct vector has been found. If not, the two vectors for the cross product have to be swapped.

Quantitative analysis of spin density distributions

Whereas spin density plots on the optimised geometries of the molecules are very valuable to give an overall impression, they are less useful for a quantitative comparison.

ORCA [5] normalises the calculated spin densities internally such that the sum of all spin densities equals to the number of spins involved. In case of a triplet state with two unpaired electron spins, this sum equals to two.

To calculate the relative amount of spin density on the TBT moiety, $r^{\mathrm{abs}}_{\mathrm{TBT}}(\mathrm{M})$, for all compounds, M, investigated, the spin density on the TBT moiety, $\rho_{\mathrm{TBT}}(\mathrm{M})$, has been divided by the spin density on the entire molecule, $\rho_{\mathrm{M}}(\mathrm{M})$ as follows:

$$r^{\mathrm{abs}}_{\mathrm{TBT}}(\mathrm{M}) = \frac{\sum |\rho_{\mathrm{TBT}}(\mathrm{M})|}{\sum |\rho_{\mathrm{M}}(\mathrm{M})|} \leq 1\,.$$

As spin densities can have positive and negative sign, the absolute values have been taken in this case, hence the notation r^{abs}.

To get further insight, spin densities have been compared for the TBT unit in each of the compounds in form of a histogram.Therefore, spin densities of the TBT unit have to be normalised to the amount of spin density on the TBT moiety in the TBT compound, $\rho_{\mathrm{TBT}}(\mathrm{TBT})$, relative to the amount of spin density on the TBT moiety in the actual compound, $\rho_{\mathrm{TBT}}(\mathrm{M})$, and this time, the sign of the spin densities has to be taken into account:

$$r_{\mathrm{TBT}}(\mathrm{M}) = \frac{\sum \rho_{\mathrm{TBT}}(\mathrm{M})}{\sum \rho_{\mathrm{TBT}}(\mathrm{TBT})} \leq 1\,.$$

Note that, in our case, $\sum \rho_{\mathrm{TBT}}(\mathrm{TBT})$ does not amount to two, as one would naively expect, as the two protons present in TBT that are substituted successively in the larger compounds are not taken into account for calculating the ratio of the spin densities, but do possess some non-vanishing, although rather small, spin density. Hence this rather complicated way of calculating this ratio.

Having the two ratios of spin density on the TBT moiety as compared to the entire molecule at hand, we can proceed to calculate the correction factor $r_{\mathrm{corr}}(\mathrm{M})$ for the spin density values for the TBT moiety of a given compound:

$$r_{\mathrm{corr}}(\mathrm{M}) = \frac{r^{\mathrm{abs}}_{\mathrm{TBT}}(\mathrm{M})}{r_{\mathrm{TBT}}(\mathrm{M})}$$

and with this, the corrected spin density for the TBT moiety of a given compound amounts to:

$$\rho^{\mathrm{corr}}_{\mathrm{TBT}}(\mathrm{M}) = r_{\mathrm{corr}}(\mathrm{M}) \cdot \rho_{\mathrm{TBT}}(\mathrm{M})\,.$$

The values for $\rho^{\mathrm{corr}}_{\mathrm{TBT}}(\mathrm{M})$ for each of the atoms have been displayed in the respective histogram.

Trend of exciton localisation

For those readers more familiar with wavenumbers rather than wavelengths, we have plotted the same figure as Figure 7 in the main text, but this time with wave numbers instead of wavelengths for the singlet excitons (Fig. S5). We note that there is no difference, neither qualitatively nor in terms of the interpretation of the data. Note that for easier direct comparison to the figure

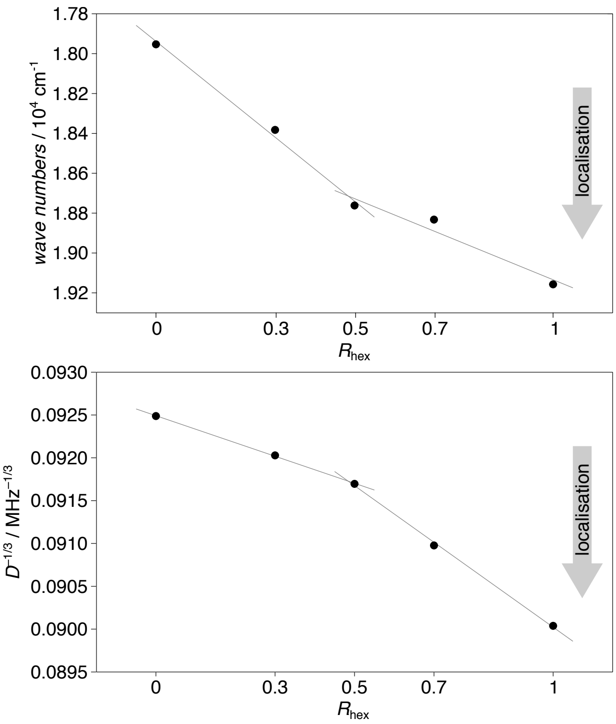

Figure S5: Trend of enhanced localisation of both, singlet and triplet exciton for increasing hexylation. The overall trend for both exciton types is identical, namely an increased exciton localisation with increased hexylation. The effect shows two linear regimes for both exciton types, with a change in slope at a hexylation ratio of 0.5, meaning statistically alternating hexylated and non-hexylated building blocks. The strength of the effect of increasing hexylation appears opposite for singlet and triplet excitons. Whereas for the singlet excitons, the effect is strongest at the beginning, for triplet excitons, the effect is more pronounced beyond a hexylation ratio of 0.5. This may be explained by the different delocalisation length of both exciton types. Note that the error bars would be within the bullets representing the data points.

in the main text as well as for having the trend of localisation pointing in the same direction for both, singlet and triplet excitons, the wave number axis is plotted in reverse order.

Rhombicity in solution and film

In the main text, only the trend of increasing delocalisation upon casting the polymer as film on a substrate has been shown graphically. Here, the effect of increased rhombicity of the cast films as compared to frozen solution is shown graphically as well (Fig. S6). Overall, no clear trend can be observed, with the fully hexylated polymer being a notable exception. Here, the overall rhombicity clearly drops compared to all other polymers. Additionally, triplet excitons in films are systematically more rhombic as compared to the identical polymer investigated in solution.

Arguments for probing the whole film morphology

Indeed, it is a very interesting question why an amorphous polymer should show overall rather strong order and orientation perpendicular to the substrate plane when cast as a film on a

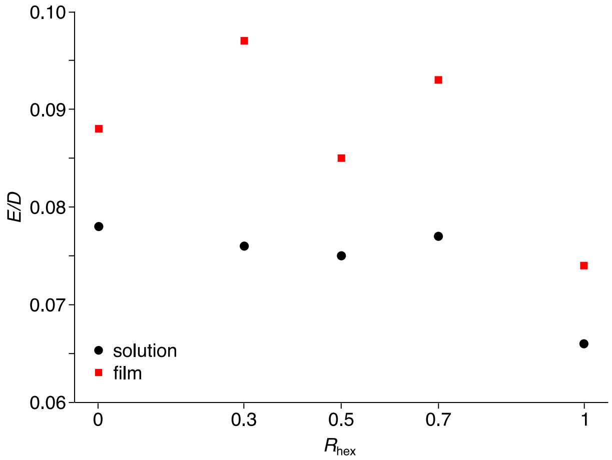

Figure S6: Film morphology enhances the rhombicity of the triplet exciton as compared to the situation in solution. Overall, no clear trend can be observed, with the fully hexylated polymer being a notable exception. Here, the overall rhombicity clearly drops compared to all other polymers. Additionally, triplet excitons in films are systematically more rhombic as compared to the identical polymer investigated in solution.

substrate. We cannot answer this question on a detailed mechanistic level at present. However, there is a number of arguments why TREPR spectrosopy probes the whole film morphology rather than very minor triplet contributions at the interface.

For TREPR spectroscopy to probe only the interface, two conditions would need to be fulfilled: (i) triplet excitons would need to exclusively diffuse towards the interface between film and substrate, where they get stuck, and (ii) TREPR spectroscopy would need to only probe the contribution of these triplet configurations. This seems highly unlikely to us for the following reasons.

First of all, the films investigated in our study have been obtained by drop-casting and are therefore rather thick, of the order of several hundreds of nanometers, if not even a few micrometers. Triplet exciton diffusion, however, is strictly limited. On the one hand, triplet excitons usually have a much longer lifetime as compared to their singlet counterparts. On the other hand, triplet excitons usually exhibit a much smaller diffusion velocity due to being much stronger bound (and hence more localised, as demonstrated, e.g., by comparing optical and TREPR measurements of polymers and their bulding blocks, [6]). Taken together, to the best of our knowledge, there is no evidence for triplet excitons in overall amorphous polymers like PCDTBT to be able to diffuse over several hundreds of nanometers. Therefore, we cannot imagine how only those triplet states actually reaching the interface between film and substrate should contribute to our signal. Note that EPR spectroscopy will always record all paramagnetic species present within the active volume of the probehead (EPR resonator).

Furthermore, diffusion is generally assumed to be an undirected process. Therefore, it is hard to imagine why triplet excitons should exclusively diffuse towards the interface between film and substrate. For logical reasons, diffusing parallel to the film–substrate interface should be equally probable. The only reason for this to be different would be a highly ordered array of polymer backbones possibly resulting in a rather directed migration of the triplet excitons. Additionally, the interfaces between film and substrate on the one hand and film and air on the other hand should generally be different. Hence, one would rather assume to see different orientations if only probing triplet states residing on the respective interfaces. From other experiments we know that conjugated polymers can exhibit two distinct triplet states at the same time (unpublished data), making simulation of the resulting spectra quite involved and requiring to take into account at least two clearly separate triplet species. Given our simulations based on a single triplet species each to fully account for the experimental data, we can safely exclude this scenario. Furthermore, it is not obvious to us why the surface between substrate and polymer film (or between film and air) should be a trap for triplet excitons.

Additionally, we have done some experiments both with films cast from less concentrated solutions, resulting in thinner films, as well as with spin-coating, resulting in much thinner films, the latter for a different polymer. In both cases, the overall signal intensity of the TREPR spectra dramatically decreased, in case of the spin-coated samples close to the detection limit of our current setup. This clearly shows that we probe not only triplet states located at the interface, but as well within the film. In both cases, however, the overall signal shape did not change, additionally showing that the signal detected originates from triplet excitons spread throughout the whole film. In addition, signals are identical for both possible orientations of the substrate plane perpendicular to the incident light, the substrate and the film-to-air surface facing the laser beam, respectively. This rules out light penetration length to have any detectable effect.

Last but not least, recent experiments on drop-cast and spin-coated films of doped conjugated polymers (unpublished data) revealed strong orientational effects in both cases using conventional cw-EPR spectroscopy of the stable paramagnetic species obtained by doping. In this case, the entire film is doped, not only the interface, and cw-EPR clearly probes all paramagnetic species present within the active volume of the probehead (resonator). Therefore, this is an additional independent proof that comparably thick drop-cast films of polymers can exhibit ordering effects that are induced by an interface towards a surface, but span the entire film.

Taken together, these arguments make us quite confident to be able to probe the entire film using TREPR spectroscopy. As this method is not restricted to highly ordered polymer films, as are other methods usually applied to obtain information on film morphology, such as X-ray scattering, it clearly corroborates and complements those other measurements.

As we stated in the beginning, having an amorphous polymer showing no orientational or ordering effects in solution exhibiting a rather strong degree of order with respect to the surface plane when cast as thin film on a substrate remains stunning. However, from our discussion above, the only conclusion reasonable to us is that the surface induces a strong degree of order in the polymer film that is not restricted to the immediate interface, but proceeds through the entire film. Note, however, that this orientation only affects the dimension perpendicular to the surface, not within the surface plane, as apparent from the simulation strategy weighting only one angle of the powder averaging. Clearly, this is ordering and orientation is an effect of preparation, and further studies on different (model) polymers varying the preparation conditions will help to further elucidate the origins of this effect. This is, however, clearly beyond the scope of the present manuscript. Note that we have used a solvent with rather high boiling point, resulting in ample time of the polymer chains to ‘react’ to the effect induced by the surface.

References

[1] Till Biskup. Structure–function relationship of organic semiconductors: Detailed insights from time-resolved EPR spectroscopy. *Front. Chem.*, 7:10, 2019.

[2] Stefan Stoll and Arthur Schweiger. EasySpin, a comprehensive software package for spectral simulation and analysis in EPR. *J. Magn. Reson.*, 178:42–55, 2006.

[3] Eric Jones, Travis Oliphant, Pearu Peterson, et al. SciPy: Open source scientific tools for Python, 2001–. [Online; accessed 2019/07/09].

[4] M. D. Mckay, R. J. Beckman, and W. J. Conover. A comparison of three methods for selecting values of input variables in the analysis of output from a computer code. *Technometrics*, 21:239–245, 1979.

[5] Frank Neese. The ORCA program package. *Wiley Interdiscip. Rev.-Comput. Mol. Sci.*, 2:73–78, 2012.

[6] Deborah L. Meyer, Rukiya Matsidik, Michael Sommer, and Till Biskup. Electronic structure trumps planarity: Unexpected narrow exciton delocalisation in PNDIT2 revealed by time-resolved EPR spectroscopy. *Adv. Electron. Mater.*, 4:1700384, 2018.

5.4. Different routes towards triplet states in organic semiconductors: direct $S_0 \rightarrow T$ excitation probed by time-resolved EPR spectroscopy

The latest version of the manuscript of the publication is added in the online version of this work. The version of record can be found in the printed version.

Clemens Matt, Deborah L. Meyer, Florian Lombeck, Michael Sommer and Till Biskup

Different routes towards triplet states in organic semiconductors: direct $S_0 \rightarrow T$ excitation probed by time-resolved EPR spectroscopy.

Molecular Physics, 117 (2019), pp. 2645–2653 (DOI: 10.1080/00268976.2018.1523479)

Contributions of all authors:

Clemens Matt: conception and study design, data aquisition (TREPR and UV-VIS), data analysis, contributions to manuscript and manuscript review

Deborah L. Meyer: data aquisition (TREPR), data analysis and manuscript review

Florian Lombeck: sample synthesis and manuscript review

Michael Sommer: conception and study design and manuscript review

Till Biskup: conception and design of study, data acquisition (TREPR and UV-VIS), data analysis, main contribution to the manuscript and manuscript review

ARTICLE

Different routes towards triplet states in organic semiconductors: Direct $S_0 \to T$ excitation probed by time-resolved EPR spectroscopy

Clemens Matt[a], Deborah Meyer[a], Florian Lombeck[b], Michael Sommer[b,c] and Till Biskup[a,*]

[a]Institut für Physikalische Chemie, Albert-Ludwigs-Universität Freiburg, Albertstraße 21, 79104 Freiburg, Germany;
[b]Institut für Makromolekulare Chemie, Albert-Ludwigs-Universität Freiburg, Stefan-Meier-Straße 31, 79104 Freiburg, Germany;
[c]Lehrstuhl Polymerchemie, Technische Universität Chemnitz, Straße der Nationen 62, 09111 Chemnitz, Germany

ARTICLE HISTORY
Compiled December 14, 2020

ABSTRACT
Understanding the electronic structure of semiconducting polymers and their respective building blocks is an essential prerequisite to develop efficient materials for organic electronics. Due to its molecular resolution and capability to directly probe and assign triplet states, (time-resolved) electron paramagnetic resonance spectroscopy is particularly suited. We present here evidence for a direct $S_0 \to T$ optical excitation of distinct triplet states in the small molecule TBT, often used as building block for semiconducting polymers. These states are subtly different in their electronic structure from those populated via intersystem crossing from excited singlet states. With these results, we extend our previous investigations of CbzTBT, the repeat unit of the polymer PCDTBT comprising the TBT and an additional carbazole moiety. Hence, the strong acceptor unit TBT seems responsible for this additional triplet route. Due to the widespread use of TBT as acceptor unit in many different co-polymers, this has potentially high impact on the efficiency of organic electronic devices.

KEYWORDS
organic semiconductors, electronic structure, triplet pathways, TBT

1. Introduction

Organic semiconductors have come a long road and are nowadays far more widespread than commonly anticipated. For example, they can be routinely found since decades in copying machines and laser printers [1]. In photovoltaics it remains to be seen whether organics can compete with the ever better and cheaper silicon-based devices with their long lifetime and robustness. But here as well, the last two decades have seen progress in an amazing pace, from the first benchmark materials with a few percent efficiency to nowadays stable and confirmed efficiencies of clearly above ten percent [2]. In the last years, a different field of organic electronics has entered our daily life, and organic light-emitting diodes [3, 4] are now routinely used in displays of commercially

---

*Email: till.biskup@physchem.uni-freiburg.de

quite successful mobile devices. This outstanding success is clearly based on a series of remarkable properties of organic semiconductors, besides others being cheap, flexible, lightweight and capable of near infinite modification and fine-tuning for the respective needs and applications, thanks to the well-developed protocols of organic synthetic chemistry.

Besides this clear success, there is still quite a number of open questions regarding the fundamental understanding of structure-function relationship in organic semiconductors in general, and besides others in particular the role of triplet states in these molecules [1, 5, 6]. Common views range from highly important to unavoidable but unimportant to detrimental for the overall efficiency. In any case, having a method at hand to directly probe both triplet states and the pathways leading to their formation is of great value for a deepened understanding and insight.

Here, we present results using time-resolved electron paramagnetic resonance (TREPR) spectroscopy [7, 8] exclusively sensitive to paramagnetic states and capable of unequivocally assigning and distinguishing triplet states from other paramagnetic states frequently occurring in organic semiconducting material, be it charge-transfer complexes [9, 10] or stable radicals [11, 12] due to defects or traces of heavy-metal catalysts left-over from synthesis.

As we have shown previously [13–17], TREPR spectroscopy of triplet excitons in organic semiconducting materials can be used to probe both, morphology and electronic structure of these molecules, including, but not restricted to the orientation of a polymer with respect to a surface as well as the overall degree of ordering [13], morphology in solution as a function of the solvent used [14], delocalisation length [15] and building block dominating the electronic structure [16]. Furthermore, we could demonstrate TREPR to help unravel triplet formation pathways and to reveal a long-forgotten route towards triplet states, namely direct $S_0 \rightarrow T$ optical excitation, to be of relevance in the repeat unit of an organic semiconductor [17]. In the present study, we extend on the latter and investigate the small molecule dithiophene-benzothiadiazole (TBT, Fig. 1) commonly found as a building block in a whole series of semiconducting polymers.

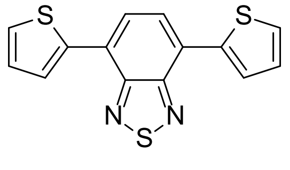

Figure 1. Chemical structure of TBT. Note that the molecule in itself is a push-pull system comprising the central benzothiadiazole unit as acceptor, flanked by two thiophenes as donors.

Previously, we investigated the repeat unit CbzTBT of the polymer PCDTBT [18, 19] well-known for its comparably high efficiency in organic photovoltaic (OPV) devices blended with fullerene [20] and its remarkable long-term stability [21–24]. Two results from our previous work [17] are of particular relevance for the study presented here. First, CbzTBT readily forms distinct triplet states if excited approximately 100 nm red-shifted from its lowest-energy optical absorption band. Second, the relative triplet yield of these states is higher as when excited within the optical absorption band. These unexpected results have been explained in terms of a direct $S_0 \rightarrow T$ optical excitation, raising a number of questions that still need to be addressed. Here, we concentrate on the TBT moiety alone and show that this unit in itself already qualitatively shows the behaviour previously observed for the extended molecule CbzTBT, consisting of the

TBT unit and a carbazole attached as an additional donor moiety on one end.

Given the widespread use of TBT as building block in other conjugated push–pull polymers consisting of alternating donor and acceptor units, our results may well have some impact far beyond the polymer systems investigated so far. Besides that, restricting ourselves to the TBT unit, in itself already a quite complicated molecule and essentially a push–pull system with the two thiophenes acting as donors for the accepting central benzothiadiazole unit, will help unravel the origin of its unexpected behaviour and guide further investigations that are beyond the scope of the present study.

2. Materials and Methods

2.1. Synthesis

Dithiophene-benzothiadiazole (TBT) was synthesised according to previously published procedures [25].

2.2. Optical spectroscopy

All samples were dissolved in *o*-dichlorobenzene (*o*-DCB) in concentration of 1 mM. Absorption spectra were recorded using a commercial UV/vis spectrometer (Shimadzu UV-1601PC) in combination with the corresponding software (UV Probe version 3.42). Temperature series were recorded using a cryostat (Optistat DN2) in combination with a temperature controller (MercuryITC, both Oxford Instruments) and using liquid nitrogen as a coolant. All measurements were performed using 1 mm path length cuvettes (Hellma QS).

2.3. EPR Instrumentation

Samples were dissolved in *o*-DCB in concentration of 1 mM, filled into synthetic quartz tubes (QSIL Ilmasil) with 3 mm inner diameter and shock-frozen in liquid nitrogen. All TREPR experiments were performed at 80 K using a setup described previously [13, 17]. Optical excitation at the respective wavelengths was carried out using an optical parametric oscillator (OPO) pumped by an Nd:YAG laser. The repetition rate of the laser was set to 10 Hz, the final pulse energy (after the OPO) to 1 mJ. Further experimental parameters (except where explicity given) are as follows: Microwave frequency, 9.689 GHz, microwave power: 2 mW (20 dB attenuation, source power 200 mW), frequency-mixer detection, video amplifier set to 42 dB amplification and 25 MHz bandwidth, 1000 averages per field point.

2.4. Spectral simulations

All simulations of triplet spectra were performed using the `pepper` routine from the EasySpin software package [26] available for MATLAB® in conjunction with a user interface for convenient data handling ensuring reproducibility and traceability [27]. Details of both, the simulations and the fitting procedure, have been detailed previously [17].

3. Results

3.1. Optical absorption spectroscopy

To get a first impression of the electronic structure of the molecule and for determining excitation wavelengths for the TREPR experiments, a steady-state absorption spectrum at room temperature was recorded for TBT (cf. Figure 2) using the same sample concentration as used for TREPR. Two distinct absorption bands are readily visible, separated by about 130 nm. The high-energy band in the near-UV region below 350 nm can be attributed predominantly to a π–π* transition. The low-energy band centred at about 455 nm and usually termed charge transfer (CT) band is mostly due to the weak intramolecular CT character of the push–pull system comprising benzothiadiazole and the two flanking thiophenes. A more detailed discussion of the optical spectra and the contributions to the different absorption bands can be found in [28].

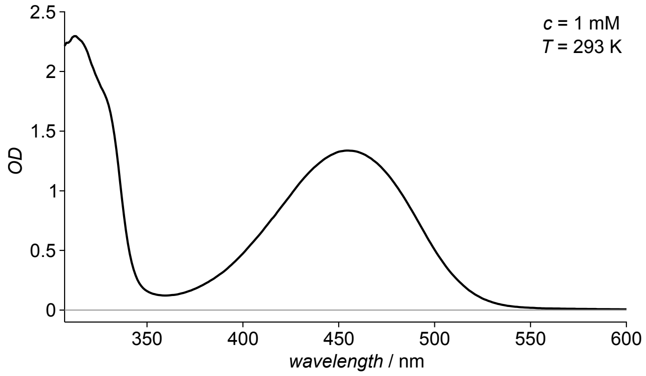

Figure 2. Absorption spectrum of TBT in *o*-DCB. The spectrum consists of two bands separated by about 130 nm, a π–π* band in the near-UV region showing some vibrational structure and a prominent band in the visible region, assigned to the partial charge-transfer character of the molecule and hence termed CT band. Due to strong absorption of the solvent in the UV region starting at about 300 nm, the spectrum has been cut to the left.

TBT clearly dominates the electronic structure even of the polymer, as has very recently been shown investigating a whole series of building blocks of PCDTBT, including TBT, using a combination of optical absorption and TREPR spectroscopy in conjunction with quantum-chemical calculations of the electron spin density distribution [16]. The CT band shows a progression toward longer wavelengths with increasingly extended conjugated system.

The absorption spectrum shows no sign of aggregation of the molecules in solution. Nevertheless, to rule out any aggregation due to cooling (as necessary for EPR-spectroscopic investigations, see below), we did perform temperature-dependent absorption measurements (Fig. 3), revealing no sign of aggregation in the solvent used, but only a small increase in overall intensity of the absorption bands upon cooling. Note that due to *o*-DCB not forming a transparent glass upon freezing, optical absorption spectra can only be recorded down to the freezing point of the solution. Furthermore, identical concentrations (1 mM) have been investigated both with optical and EPR spectroscopy. Whereas *o*-DCB is clearly not an ideal solvent from a spectroscopist's point of view, the choice is rather dictated by processing concerns for the polymers. Furthermore, solvents are known to have potentially strong impact on the morphology in solution [14]. Hence, to get insight eventually relevant for applications, using the same solvents as for manufacturing devices is crucially important. As the TREPR

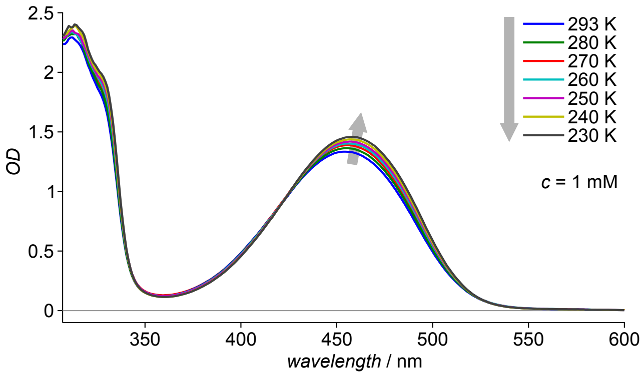

Figure 3. Temperature-dependent absorption spectra of TBT in *o*-DCB. The solvent crystallises below 230 K, resulting in scattering and hampering further optical investigation at lower temperatures. However, from the absorption spectra it is obvious that no aggregation takes place until the solution freezes.

samples have been flash-frozen in liquid nitrogen, we are quite confident to conserve the situation found in liquid solution, and rule out any formation of microcrystalline domains.

3.2. TREPR spectroscopy at different excitation wavelengths

If optically excited either in the CT band or in the π–π* transition, TBT readily forms short-lived triplet states that manifest themselves as characteristic spectra in TREPR spectroscopy (Figure 4). These spectra are entirely dominated by the zero-field splitting (ZFS) interaction resulting from the dipolar coupling of the two unpaired electron spins of the triplet state. Accordingly, the absolute values for the two characteristic parameters D and E of the corresponding interaction tensor can be directly extracted from the signal (for details, see the Supporting Information). Here, $|D|$ can be generally related to the average distance between the two spins, and thus to the delocalisation of the spin density on the molecule, and $|E|$ to the deviation of the spin density distribution from an axial symmetry, hence the degree of rhombicity. Therefore, TREPR spectra of triplet states allow for directly accessing the electronic structure of the triplet state of the underlying molecule. As the light-induced triplet states are initially created with their three sublevels populated far from thermal equilibrium, this gives rise to a huge signal enhancement of the corresponding TREPR spectra that show signals in enhanced absorption (A) and emission (E), respectively. This signal enhancement allows to omit the lock-in detection scheme used in conventional *cw*-EPR spectroscopy and therefore to increase time resolution up to about 10 ns.

TREPR spectra of TBT have been recorded under solid-state conditions at low temperature (80 K) in frozen solution for different excitation wavelengths, and the resulting spectra fitted assuming a single triplet species for each spectrum. All spectra each can be fully described assuming a single triplet species as demonstrated by the good agreement between spectral simulations and experimental data. For simulation parameters cf. Table 1 and for actual simulations, see the Supporting Information.

The narrow features in the centre of the TREPR spectra are not due to the triplet state. Such features are regularly seen for other conjugated polymers as well (*e.g.*, P3HT) [11], and possible origins are either stable radicals (due to “defects”) [12] or light-induced charge-separated states [9]. However, they are notoriously difficult to properly assign and do not contribute to nor hamper the overall interpretation of our

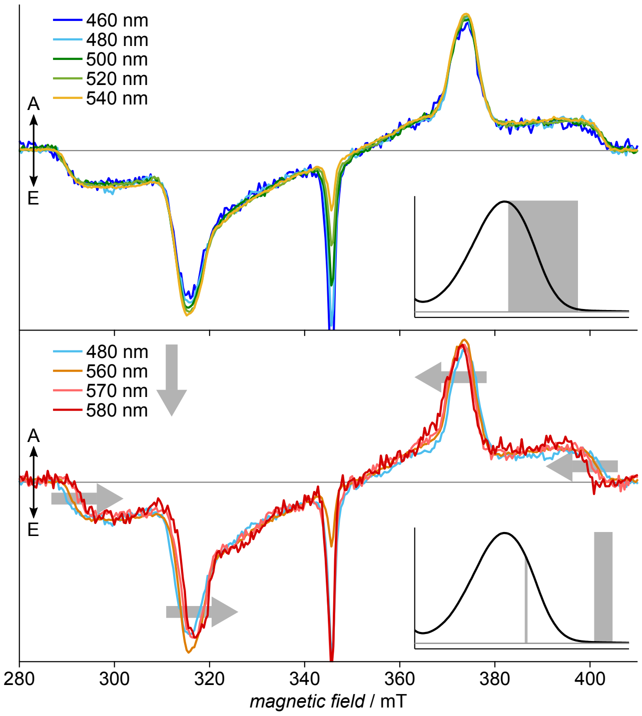

Figure 4. TREPR spectra of TBT excited at different wavelengths. All spectra are averages over 200 ns centred about 500 ns after optical excitation. Excitation red-shifted from the CT band of TBT leads to spectrally distinct states with increasing delocalisation length and correspondingly narrower spectra, as indicated by grey arrows. Spectra have been normalised to the same area. Insets show the absorption spectrum of TBT with the range of excitation wavelengths highlighted with grey areas.

data. Hence, they are not discussed any further hereafter.

The overall picture emerging from the wavelength-dependent TREPR spectra of TBT reported here is similar to what has been demonstrated previously for CbzTBT [17]. Firstly, triplet spectra are observed for excitation wavelengths clearly red-shifted from the optical absorption band. Secondly, these signals are apparently even stronger than those obtained for excitation within the CT band (see next section). And finally, the triplet spectra appear to narrow upon excitation red-shifted from the optical absorption band, as evident both from direct comparison of the spectra (Fig. 4, bottom) as well as from the simulation parameters, namely $|D|$ (cf. Tab. 1). Interestingly, except for the consistent variations in the D parameter of the zero-field splitting for excitation wavelengths $\lambda_{\text{ex}} > 540$ nm, no trends in the simulation parameters can be observed. We note that for excitation wavelengths $\lambda_{\text{ex}} > 580$ nm basically no triplet signal is visible any more (data not shown).

3.3. *Quantitative analysis of the TREPR spectra*

Whereas quantitative measurements are possible in general using conventional *cw*-EPR spectroscopy, normally this is not possible for TREPR spectra. Firstly, the signal intensity strongly depends on a series of experimental and device parameters. Secondly and even more fundamentally, these spectra consist of overlapping contributions of differently polarized (emissive or absorptive) lines that partially compensate each other, making the resulting signals particularly sensitive to even slight changes in the electronic structure of the investigated system. This imposes a series of criteria that need to be fulfilled in order to perform even a relative quantitative comparison of signal intensities of TREPR spectra. Namely, the setup used needs to be strictly identical as well as the experimental parameters. Furthermore, the overall spectral shape should change only slightly and the spectrum consist of only a small number of clearly separated contributions.

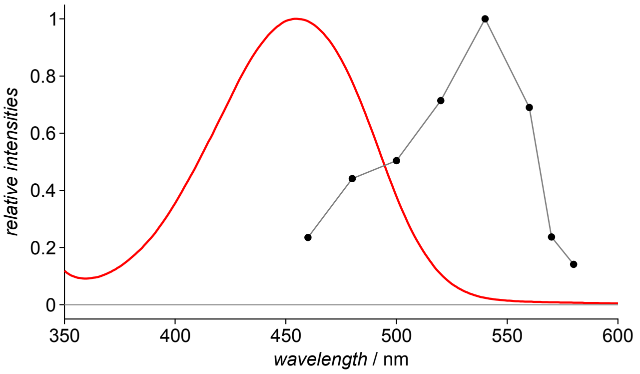

Figure 5. Comparison of the absorption spectrum of TBT (solid red line) and the relative triplet yield (black filled circles) as determined by TREPR signal intensity. Not only can triplet states be observed for excitation beyond the absorption band of TBT, but their signal intensity is even stronger, with a maximum at about 540 nm, some 80 nm red-shifted from the optical absorption maximum of the CT band.

Here, we have taken special precautions and measured the identical sample under entirely identical conditions with only the excitation wavelength changing. All other parameters have been kept identical, and the sample has not been touched between measurements. Furthermore, as evident from the simulation parameters (Tab. 1) and the experimental data (Fig. 4), the polarisation pattern only changes very slightly. Thus, for the series of TREPR measurements whose signal intensity has been plotted versus the optical absorption spectrum (Fig. 5), a direct comparison is possible. However, no quantification of the triplet yield in terms of quantum efficiencies can be drawn from the TREPR data. Furthermore, the relative triplet yield shown in Fig. 5 is only a trend, due to possible effects of sample degradation that seem much more severe in TBT as compared to CbzTBT, consistent with the strong central emissive peak in the spectra.

Table 1. Simulation parameters for the spectral simulations of selected TREPR spectra shown in Fig. 4. λ_{ex} is the excitation wavelength, D and E are the parameters of the zero-field splitting tensor of the dipolar interaction, Γ_{L} is the Lorentzian (homogeneous) line width, and $p_{1,2,3}$ are the populations of the three triplet sublevels, respectively. Note that the sign of D and E cannot be unambiguously determined and the values for p have been given assuming $D, E > 0$. Due to no change in spectral shape between 460 and 540 nm (cf. Fig. 4), only the simulation parameters for the spectrum recorded with $\lambda_{\text{ex}} = 480$ nm are included here. For full details see the Supporting Information.

λ_{ex}/nm	$\lvert D\rvert$/MHz	$\lvert E\rvert$/MHz	$\lvert E\rvert/\lvert D\rvert$	Γ_{L}/mT	$p_{1,2,3}$
480	1563±3	67±2	0.043	2.7±0.2	0, 0.159, 0.841
560	1536±2	64±1	0.042	2.3±0.1	0, 0.144, 0.856
570	1521±3	63±2	0.041	2.5±0.2	0, 0.169, 0.831
580	1493±4	65±2	0.044	2.3±0.2	0, 0.208, 0.792

4. Discussion

4.1. Direct optical excitation of the triplet state

Generally, direct optical excitation of the triplet state from the singlet ground state has been discussed early on, mostly for small molecules [29–32], but even for biological systems [33], and has recently been shown by the authors for a similar system to the one discussed here, namely CbzTBT [17]. Given our previous work on direct optical $S_0 \rightarrow T$ excitation in CbzTBT [17], it seems sensible to discuss our new data in context of those previous results. Whereas CbzTBT, *i.e.* the TBT block extended by a carbazole moiety, forms the repeat unit of the widely used polymer PCDTBT known for its remarkable stability, TBT is a building block often encountered in organic semiconductors. In this section, the commonalities between CbzTBT and TBT will be discussed, whereas the following section focusses particularly on the differences between both molecules.

In general, our results on TBT are quite similar to those previously obtained for CbzTBT, namely (i) formation of triplet states when exciting clearly red-shifted from the optical absorption band, (ii) higher triplet yield if excited outside the CT band, and (iii) distinct triplet states with smaller values for $|D|$ upon excitation beyond the absorption band are observed. Hence, the same arguments and the same interpretation brought forward for CbzTBT applies as well for TBT.

Ruling out aggregation and hence a potential red-shift in optical absorption, we are quite confident to observe a direct $S_0 \rightarrow T$ absorption in TBT, as has been described for CbzTBT already. Multiphoton processes would be an alternative explanation that we rule out based on our experimental setup not allowing to excite with the appropriate photon density to allow for such processes. Given that excitation within the CT band always leads to the same triplet signal, whereas wavelengths red-shifted from the CT band result in distinct, progressively more delocalised triplet states hints toward two different triplet formation pathways: intersystem crossing from the excited singlet state, predominantly active when exciting in the CT band, and direct $S_0 \rightarrow T$ for red-shifted excitation, with the latter having a higher relative quantum yield (cf. Fig. 5). Note, however, that the increase in relative quantum yield is not tremendously high, and that we cannot quantify the phenomenon in an absolute fashion. Generally, spin-forbidden processes have rather low probabilities in organic molecules not containing heavy atoms. Additionally, due to TREPR spectroscopy directly probing the triplet state, this method is much more sensitive compared to the indirect way of detecting phosphorescence that always competes with radiationless relaxation that entirely dominates for small band gaps.

The striking overall similarity of the triplet states presumably formed via different routes could be explained by the high similarity of the involved singlet states S_1 and S_0, respectively. This is supported by absorption and emission spectra of TBT being close to mirror-images of each other [28]. Note, however, that due to the lack of a clear vibrational fine structure of the absorption bands, only a limited amount of information is available from these optical spectra.

A somewhat similar observation of increasingly narrower TREPR signals of triplet states upon excitation towards the red flank of the absorption spectrum has been observed recently for porphyrin dimers and assigned to different conformations of the molecule an in turn differences in delocalisation over the dimer [34]. This seems not applicable to the situation presented for TBT in the present study for a number of reasons. The effects in the porphyrins have been demonstrated for excitation clearly within the absorption spectrum, not red-shifted, as in our case. Furthermore, TBT is considered to be a fairly planar molecule, with spin density delocalised over the entire molecule [16]. Additionally, the effect in the porphyrins was very subtle, even with a dihedral angle of 90 between the two porphyrin monomers. Finally, no relative quantification of the triplet yield is provided, making comparison to our data impossible in this respect. Taken together, on this ground we would like to rule out conformational aspects of the TBT molecule as potential origin of the distinct triplet states observed.

As with the distinct triplet states formed in CbzTBT upon excitation red-shifted from the optical absorption and hence with less energy than required for reaching the first excited singlet state, the very nature of these states as well as the reason for them not being accessible from those energetically higher-lying triplet state(s) populated via intersystem crossing from the excited singlet state remains largely unknown. This definitely demands further investigation by other means that are clearly out of scope of the present study. A few details will be given below.

4.2. Comparison to results on CbzTBT

Given the previous observations [17] on the somewhat larger molecule CbzTBT, the "true" repeat unit of the polymer PCDTBT, the results for TBT presented here shed some light on the factors involved in direct $S_0 \rightarrow T$ excitation and its molecular basis.

Compared with CbzTBT, TBT exhibits a smaller red shift (80 nm vs. 150 nm) between the maxima of the CT band and the triplet excitation spectrum recorded using TREPR spectroscopy. Furthermore, the differences in the TREPR spectra when exciting red-shifted from the CT band are less pronounced in TBT as compared to CbzTBT, but nevertheless follow a similar trend, particularly the narrowing of the triplet spectra, hence increased delocalisation, with increasingly red-shifted excitation. Additionally, there are more signs of photodegradation in TBT as compared to CbzTBT, the most prominent being the central "spike" in the spectra, rendering the consecutive recording and analysis of multiple TREPR spectra on the identical sample rather tricky.

Taken together, Cbz does clearly play a role in the electronic structure of the whole molecule and particularly that of the triplet exciton. This can be seen as well from the larger delocalisation of both, singlet and triplet exciton, the former via its CT band in the optical absorption spectrum, the latter via its $|D|$ value of the zero-field splitting tensor as well as the spin density distribution calculated using density-functional theory (DFT) [16]. Our recent study [16] extends the investigation of building blocks of PCDTBT to a symmetric molecule with Cbz flanking both ends of a TBT unit and clearly shows TBT to entirely dominate the electronic structure not only of the building blocks but as well the whole polymer. Hence it is tempting to speculate that the direct $S_0 \rightarrow T$ excitation of triplet states demonstrated for both, TBT and CbzTBT, prevails in the polymer as well. We note, however, that due to the rather large conformational variability of a polymer and hence a number of energetically low-lying states ("tail states") convincing arguments for a direct triplet excitation are much harder to bring forward than for small molecules. Nevertheless, the trend observed here, namely the narrowing of TREPR triplet spectra with red-shifted excitation at the edge or beyond the optical absorption, seems more widespread, as preliminary data on building blocks of both, PNDIT2 and DPP-based co-polymers, suggest (data not shown).

4.3. Limits of the current approach and possible alternative strategies

Due to its exclusive sensitivity to paramagnetic states and the unequivocal assignment of the resulting spectra, TREPR spectroscopy allows in general to record excitation spectra of TBT (and CbzTBT) triplet states. Note that the data give only relative triplet yields and that quantifying TREPR signals is only possible under special circumstances, as discussed above. Similar information could in principle be obtained by optical spectroscopy as well recording the phosphorescence intensity as a function of the excitation wavelength. However, due to *o*-DCB not forming a glass upon freezing, this will be far from easy if at all possible under experimental conditions comparable to our TREPR spectra.

Recording optical spectra of both, phosphorescence and the direct triplet excitation would generally require low temperature, ultra-pure solvents and in the latter case clearly solvents forming glass upon freezing. As has been known for long time [35–37] and very recently demonstrated using TREPR spectroscopy as well, the solvent may well have a dramatic impact on the solution morphology, namely aggregation behaviour, of both, conjugated polymers and their building blocks [14]. Again, we would like to mention that the choice of solvents, particular in the organic electronics field, is often dictated by the needs of synthetic chemistry rather than by their spectoscopic characteristics. Given the potential strong impact of the solvent on the molecular characteristics, insights relevant for the application should therefore be obtained under conditions as similar as possible compared to processing of devices.

Whereas TREPR spectra not only allow for a relative quantification of the triplet yield, but give as well some insight into the delocalisation of the spin density of the corresponding states, the spectral resolution on a wavelength axis is rather limited, as can be readily seen from Fig. 5. Acquiring additional TREPR spectra is not necessarily easy due to a slow but visible sample degradation for prolonged measurement times. Note that recording of each spectrum shown here took about 11–12 hours with our current setup, amounting in total to more than four days of continuous measurement time with 10 Hz shot repetition rate of the laser. Hence we cannot rule out the distinct triplet states observed to form more of a continuum, given the obtainable spectral resolution to be limited eventually by the line width. Nevertheless, the fact that excitation red-shifted from the optical absorption band results in distinct and different TREPR spectra is a clear hint for different electronic triplet states being involved.

4.4. Routes towards triplet states: a more complete picture

In light of the long-standing debate about the role of triplet states in organic semiconductors, the additional route towards triplet excitons, namely direct $S_0 \rightarrow T$ excitation demonstrated here for TBT and previously even more convincingly for the somewhat extended molecule CbzTBT, may well be highly relevant in terms of efficiency of organic semiconductors. A summary of all the different pathways towards triplet states relevant or at least occuring in organic electronic devices is given in Fig. 6. Whereas intersystem crossing from an excited singlet state into an excited triplet state predominates mainly in pristine polymers, back electron transfer from a charge-transfer state to a lower-lying triplet state of one of the component involved mostly occurs in blends of donor and acceptor materials [38] and is generally seen as detrimental in OPV devices. Singlet fission, *i.e.* creating two excited (triplet) states from one excitation [39], opens the door towards quantum efficiencies above one, but normally needs a special arrangement of the energy levels of singlet and tripet states involved, namely the triplet level having about half the energy of the singlet level. Direct optical excitation of triplet states would open up the possibility in OPV devices to harvest low-energy radiation and hence increase the overall efficiency.

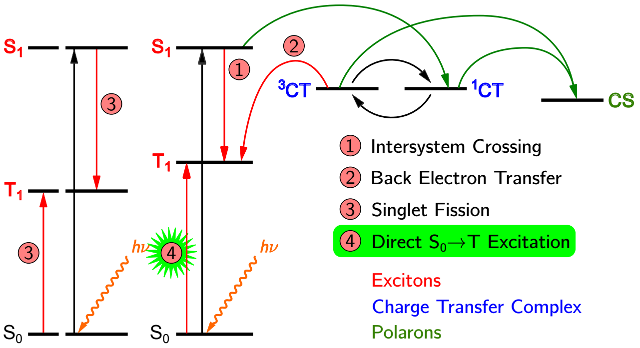

Figure 6. Overview of the different pathways towards triplet states relevant in organic electronic devices. Whereas intersystem crossing, back electron transfer from the charge transfer complex, and singlet fission are regularly discussed, the direct excitation of the triplet state from the singlet ground state is normally neglected.

In any case, TREPR spectroscopy has proven to be useful not only in unequivocally assigning the spin multiplicity and character of excited states, but as well in unravelling the origin of triplet states, as the spectral signature is highly sensitive to the (initial) population of the three triplet sublevels. Hence, back electron transfer from a charge-transfer state can clearly be distinguished from intersystem crossing, as shown already long ago for photosynthetic reaction centres [40] and lately as well for blends between semiconducting polymers and fullerenes [41].

5. Conclusions

In summary, we could demonstrate direct optical excitation of triplet states from the singlet ground state to be more widespread in organic semiconductors than previously anticipated. Furthermore, EPR spectroscopy in general and TREPR spectroscopy in particular are highly suited to directly probe and unequivocally assign triplet states. Additionally, TREPR spectroscopy gives direct access to the triplet state in solvents not easily accessible for optical spectroscopy at lower temperatures (not forming glasses), but often used in the process of building organic electronic devices. These results extend our previous investigations of the “true” repeat unit of the polymer PCDTBT, comprising the TBT and an additional carbazole moiety. Hence, the strong acceptor unit TBT seems responsible in general for this additional triplet route, in light with its dominant role in the overall electronic structure [16]. Due to the widespread use of TBT as acceptor unit in many different co-polymers, this has potentially high impact on the efficiency of organic electronic devices.

Funding

The authors thank the German Research Foundation (DFG, Grant BI-1249/3-1 to T.B., SPP1355 to M.S., IRTG Soft Matter Science 1645, Project SO-1213/8-1 to M.S.) and Albert-Ludwigs-Universität Freiburg (Innovationsfonds Forschung, to T.B., and M.S.) for financial support.

Supporting Information

Details of the EPR instrumentation, TREPR spectra of triplet states including full 2D datasets, and details for the spectral simulations of TREPR spectra are given in the Supporting Information.

References

[1] A. Köhler and H. Bässler, Mater. Sci. Eng. R-Rep. **66**, 71–109 (2009).

[2] M.A. Green, Y. Hishikawa, E.D. Dunlop, D.H. Levi, J. HohlEbinger and A.W. HoBaillie, Prog. Photovoltaics **26**, 3–12 (2018).

[3] R.H. Friend, R.W. Gymer, A.B. Holmes, J.H. Burroughes, R.N. Marks, C. Taliani, D.D.C. Bradley, D.A. Dos Santos, M.L. J. L. Brédas and W.R. Salaneck, Nature **397**, 121–128 (1999).

[4] B. Minaev, G. Baryshnikov and H. Agren, Phys. Chem. Chem. Phys. **16**, 1719–1758 (2014).

[5] A. Rao, P.C.Y. Chow, S. Gélinas, C.W. Schlenker, C.Z. Li, H.L. Yip, A.K.Y. Jen, D.S. Ginger and R.H. Friend, Nature **500**, 435–439 (2013).

[6] F. Kraffert, D. Bahro, C. Meier, M. Denne, A. Colsmann and J. Behrends, J. Magn. Reson. **282**, 10–17 (2017).

[7] M.D. Forbes, L.E. Jarocha, S. Sim and V.F. Tarasov, Adv. Phys. Organ. Chem. **47**, 1–83 (2014).

[8] T. Biskup, Mol. Phys. **111**, 3698–3703 (2013).

[9] J. Behrends, A. Sperlich, A. Schnegg, T. Biskup, C. Teutloff, K. Lips, V. Dyakonov and R. Bittl, Phys. Rev. B **85**, 125206 (2012).

[10] F. Kraffert and J. Behrends, Mol. Phys. **115**, 2373–2386 (2017).

[11] A. Sperlich, H. Kraus, C. Deibel, H. Blok, J. Schmidt and V. Dyakonov, J. Phys. Chem. B **115**, 13513–13518 (2011).

[12] R. Bauld, L.M. Fleury, M. Van Walsh and G. Fanchini, Appl. Phys. Lett. **101**, 103306 (2012).

[13] T. Biskup, M. Sommer, S. Rein, D.L. Meyer, M. Kohlstädt, U. Würfel and S. Weber, Angew. Chem. Int. Ed. **54**, 7707–7710 (2015).

[14] D.L. Meyer, R. Matsidik, S. Huettner, M. Sommer and T. Biskup, Phys. Chem. Chem. Phys. **20**, 2716–2723 (2018).

[15] D.L. Meyer, R. Matsidik, M. Sommer and T. Biskup, Adv. Electron. Mater. **4**, 1700384 (2018).

[16] C. Matt, D.L. Meyer, F. Lombeck, M. Sommer and T. Biskup, Macromolecules **51**, 4341–4349 (2018).

[17] D.L. Meyer, F. Lombeck, S. Huettner, M. Sommer and T. Biskup, J. Phys. Chem. Letters **8**, 1677–1682 (2017).

[18] N. Blouin, A. Michaud and M. Leclerc, Adv. Mater. **19**, 2295–2300 (2007).

[19] N. Blouin, A. Michaud, D. Gendron, S. Wakim, E. Blair, R. Neagu-Plesu, M. Belletête, G. Durocher, Y. Tao and M. Leclerc, J. Am. Chem. Soc. **130**, 732–742 (2008).

[20] S.H. Park, A. Roy, S. Beaupré, S. Cho, N. Coates, J.S. Moon, D. Moses, M. Leclerc, K. Lee and A.J. Heeger, Nat. Photonics **3**, 297–303 (2009).

[21] S. Cho, J.H. Seo, S.H. Park, S. Beaupré, M. Leclerc and A.J. Heeger, Adv. Mater. **22**, 1253–1257 (2010).

[22] Y. Sun, C.J. Takacs, S.R. Cowan, J.H. Seo, X. Gong, A. Roy and A.J. Heeger, Adv. Mater. **23**, 2226–2230 (2011).

[23] C.H. Peters, I.T. Sachs-Quintana, J.P. Kastrop, S. Beaupré, M. Leclerc and M.D. McGehee, Adv. Energy Mater. **1**, 491–494 (2011).

[24] J. Kong, S. Song, M. Yoo, G.Y. Lee, O. Kwon, J.K. Park, H. Back, G. Kim, S.H. Lee, H.

Suh and K. Lee, Nat. Commun. **5**, 5688 (2014).

[25] F. Lombeck, F. Marx, K. Strassel, S. Kunz, C. Lienert, H. Komber, R. Friend and M. Sommer, Polym. Chem. **8**, 4738–4745 (2017).

[26] S. Stoll and A. Schweiger, J. Magn. Reson. **178**, 42–55 (2006).

[27] D. Meyer, Ph. D. thesis, Albert-Ludwigs-Universität Freiburg, 2017.

[28] N. Banerji, E. Gagnon, P.Y. Morgantini, S. Valouch, A.R. Mohebbi, J.H. Seo, M. Leclerc and A.J. Heeger, J. Phys. Chem. C **116**, 11456–11469 (2012).

[29] G.N. Lewis and M. Kasha, J. Am. Chem. Soc. **67**, 994–1003 (1945).

[30] M. Kasha, Discuss. Faraday Soc. **9**, 14–19 (1950).

[31] D.F. Evans, J. Chem. Soc. **1957**, 1351–1357 (1957).

[32] L. Goodman and B.J. Laurenzi, Adv. Quantum Chem. **4**, 153–169 (1968).

[33] M. Delbrück, A. Katzir and D. Presti, Proc. Natl. Acad. Sci. USA **73**, 1969–1973 (1976).

[34] C.E. Tait, P. Neuhaus, M.D. Peeks, H.L. Anderson and C.R. Timmel, Phys. Chem. Chem. Phys. **18**, 5275–5280 (2016).

[35] O. Inganäs, W.R. Salaneck, J.E. Österholm and J. Laakso, Synth. Met. **22**, 395–406 (1988).

[36] C. Scharsich, R.H. Lohwasser, M. Sommer, U. Asawapirom, U. Scherf, M. Thelakkat, D. Neher and A. Köhler, J. Polym. Sci. Pt. B-Polym. Phys. **50**, 442–453 (2012).

[37] R. Steyrleuthner, M. Schubert, I. Howard, B. Klaumünzer, K. Schilling, Z. Chen, P. Saalfrank, F. Laquai, A. Facchetti and D. Neher, J. Am. Chem. Soc. **134**, 18303–18317 (2012).

[38] F. Kraffert, R. Steyrleuthner, S. Albrecht, D. Neher, M.C. Scharber, R. Bittl and J. Behrends, J. Phys. Chem. C **118**, 28482–28493 (2014).

[39] M.B. Smith and J. Michl, Chem. Rev. **110**, 6891–6936 (2010).

[40] M.C. Thurnauer, J.J. Katz and J.R. Norris, Proc. Natl. Acad. Sci. USA **72**, 3270–3274 (1975).

[41] J. Niklas, S. Beaupré, M. Leclerc, T. Xu, L. Yu, A. Sperlich, V. Dyakonov and O.G. Poluektov, J. Phys. Chem. B **119**, 7407–7416 (2015).

Different routes towards triplet states in organic semiconductors: Direct $S_0 \rightarrow T$ excitation probed by time-resolved EPR spectroscopy

— Supporting Information —

Clemens Matt[a], Deborah L. Meyer[a], Florian Lombeck[b],
Michael Sommer[b,c], and Till Biskup[a*]

[a]Institut für Physikalische Chemie, Albert-Ludwigs-Universität Freiburg,
Albertstraße 21, 79104 Freiburg, Germany
[b]Institut für Makromolekulare Chemie, Albert-Ludwigs-Universität Freiburg,
Stefan-Meier-Straße 31, 79104 Freiburg, Germany
[c]Lehrstuhl Polymerchemie, Technische Universität Chemnitz,
Straße der Nationen 62, 09111 Chemnitz, Germany

Contents

---

[*]till.biskup@physchem.uni-freiburg.de

EPR Instrumentation

TREPR spectroscopy with a time resolution of up to 10 ns allows for real-time observation, *e.g.*, of short-lived radical-pair and triplet states generated by pulsed laser excitation. In contrast to conventional continuous-wave EPR spectroscopy, which usually involves magnetic-field modulation to improve the signal-to-noise ratio, TREPR is recorded in a high-bandwidth direct-detection mode, so as not to constrain the time resolution of the experiment. Consequently, positive and negative signal amplitudes in TREPR correspond to enhanced absorptive (A) and emissive (E) electron-spin polarisations of the EPR transitions, respectively.

All TREPR experiments were performed at 80 K using a commercial EPR spectrometer (Bruker ESP380E) in conjunction with a Bruker microwave bridge (ER 046 MRT) equipped with a low-noise high-bandwidth video amplifier. The sample was placed in a synthetic-quartz (Suprasil) sample tube (3 mm inner diameter) and irradiated in a dielectric-ring resonator (Bruker ER 4118X-MD5), which was immersed in a helium gas-flow cryostat (Oxford CF-935) cooled with liquid nitrogen. The temperature was regulated to ±0.1 K by a temperature controller (Oxford ITC-503). The time resolution of the experimental setup was in the 10 ns range. A microwave frequency counter (Hewlett-Packard HP 5352B) was used to monitor the microwave frequency.

Optical excitation at the respective wavelengths was carried out with an optical parametric oscillator (OPO) system (Opta BBO-355-vis/IR) pumped by an Nd:YAG laser (Spectra Physics, Quanta Ray GCR 190-10) with a pulse width of approximately 6 ns, and a pulse energy of 1 mJ. The repetition rate of the laser was set to 10 Hz. A transient recorder (LeCroy 9354A) with a digitizing rate of 2 ns/11 bit was used to acquire the time-dependent EPR signal. To eliminate the background signal induced by the laser entering the EPR cavity, TREPR signals were accumulated at off-resonance magnetic-field positions (background) and subtracted from those recorded on-resonance. This background signal is completely independent in its shape from both, laser wavelength and magnetic field, and normally long-lived compared to the detected spin-polarised EPR signal. Background subtraction was performed directly in the transient recorder and a background signal repeatedly recorded after each tenth time trace of the experimental data.

Further experimental parameters (except where explicity given) are as follows: Microwave frequency, 9.700 GHz, microwave power: 2 mW (20 dB attenuation, source power 200 mW), frequency-mixer detection, video amplifier set to 42 dB amplification and 25 MHz bandwidth, between 850 and 1400 averages per point.

TREPR spectra of triplet states

As TREPR spectra of spin-polarised triplet states of organic molecules recorded at X-band frequencies and magnetic fields are normally dominated by the zero-field splitting (ZFS) interaction, the hamilton operator used to describe the system reduces dramatically. The only contributions that need to be taken into account are the Hamilton operator for the Zeeman interaction, $\mathcal{H}_{\text{EZ}}$, and the one for the ZFS interaction, $\mathcal{H}_{\mathrm{ZFS}}$:

$$\mathcal{H} = \mathcal{H}_{\mathrm{EZ}} + \mathcal{H}_{\mathrm{ZFS}} = \mathbf{g}\mu_{\mathrm{B}}\vec{S}\vec{B} + \vec{S}\mathbf{D}\vec{S}. \tag{S1}$$

All other contributions can be considered as small perturbations that can be accounted for using (inhomogeneous) line broadening.

The **D** tensor in its principal axis system is given to

$$\mathbf{D} = \begin{pmatrix} -\frac{1}{3}D + E & 0 & 0 \\ 0 & -\frac{1}{3}D - E & 0 \\ 0 & 0 & \frac{2}{3}D \end{pmatrix} \tag{S2}$$

where D and E are the zero-field-splitting parameters that can be directly read out from the experimental spectra (cf. Fig. S1). Note that D and E are defined such in the simulation routine used that the relation $|E| \leq |D|/3$ always holds.

Spectral simulations of TREPR spectra of triplet states

All simulations of triplet spectra have been performed using the EasySpin software package [**?**] available for MATLAB® (MathWorks), and here the routine `pepper`. Parameters included were the **g** and **D** tensor and the triplet sublevel populations (in zero field). Line broadening (Γ) was included using a combination of Lorentzian (Γ_{L}) and Gaussian (Γ_{G}) lines. For all simulations, the **g** tensor was assumed to be isotropic, with $g_{\mathrm{iso}} = 2.002$, and the population p_1 was set to zero. This left the parameters D and E of the zero-field splitting tensor **D**, the populations p_2 and p_3, and the two line widths Γ_{L} and Γ_{G} as the only free parameters that were adjusted. In the case of NDI the parameters E of the zero-field splitting tensor **D** was set two zero and was not adjusted by a fitting process.

Fitting of the spectral simulations to the experimental data was done with the routine `lsqcurvefit` from the MATLAB® Optimization Toolbox™ using the trust-region-reflective least squares algorithm.

The nonlinear least-square solver finds the m coefficients $\vec{a}$ that solve the problem

$$\min_{\vec{a}} \sum_i (f(x_i;\vec{a}) - y_i)^2 \tag{S3}$$

with y_i being the measured data and $f(x_i;\vec{a})$ the fitting function $f : \mathbb{R}^m \rightarrow \mathbb{R}^n$ with the same size n as the measured data y_i

Error estimation of the fitting parameters was carried out by using the Jacobian matrix **J**. J_{ij} is the partial derivative of the fitting function $f(x_i;\vec{a})$ with respect to a_j at the solution a_0.

$$J_{ij}(\vec{a}_0) := \left(\frac{\partial f(x_i;\vec{a})}{\partial a_j}(\vec{a}_0) \right)_{i=1\ldots n, j=1\ldots m} \tag{S4}$$

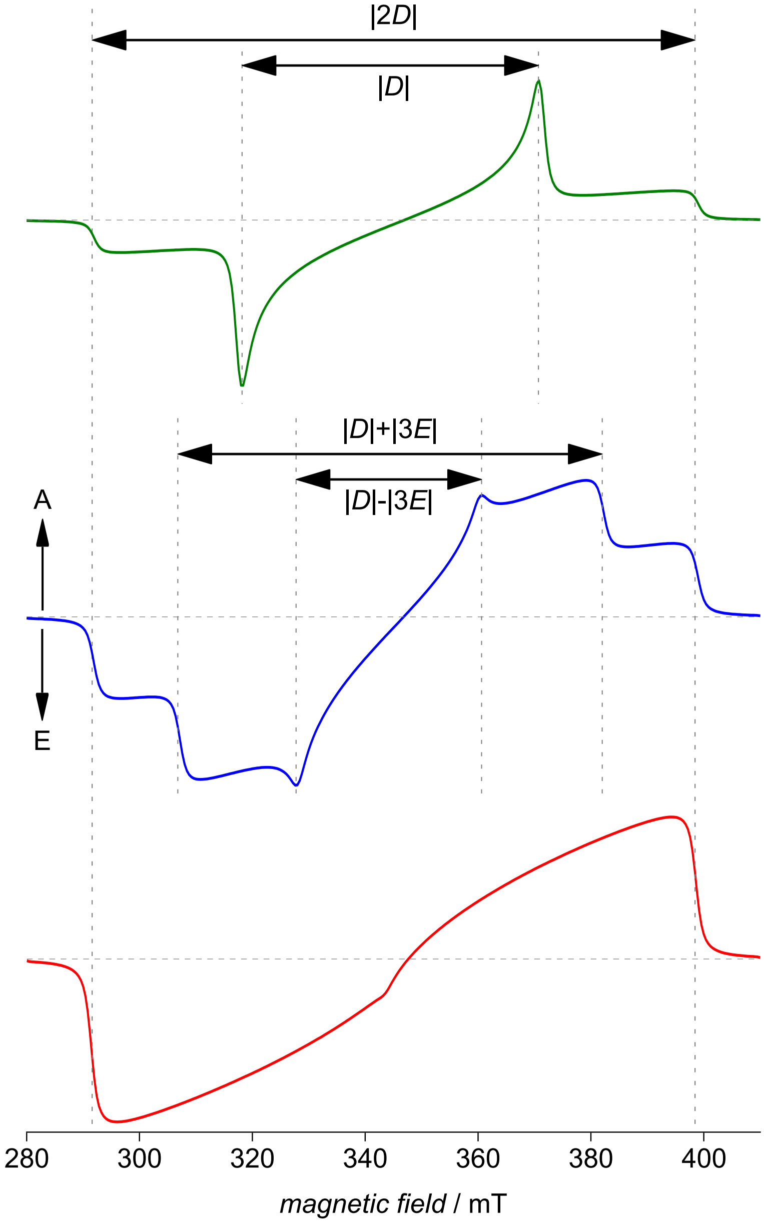

Figure S1: Characteristics of TREPR spectra of (photo-generated) triplet states. Three characteristic situations for the ratio of the two parameters D and E of the ZFS tensor are depicted here: the fully axial case (top, green), an intermediate case (blue, centre) and a fully rhombic case (red, bottom). Spectra were calculated using EasySpin. [2] The zero-field populations $p_{1,2,3}$ of the three triplet sublevels are far from thermal equilibrium, due to optical excitation and the inherent anisotropy of the intersystem crossing processes. Therefore, signals consist of both, absorptive (A) and emissive (E) contributions.

$$\mathbf{J}(\vec{a}_0) = \begin{pmatrix} \frac{\partial f(x_1;\vec{a})}{\partial a_1}(\vec{a}_0) & \dots & \frac{\partial f(x_1;\vec{a})}{\partial a_m}(\vec{a}_0) \\ & \dots & \\ \frac{\partial f(x_n;\vec{a})}{\partial a_1}(\vec{a}_0) & \dots & \frac{\partial f(x_n;\vec{a})}{\partial a_m}(\vec{a}_0) \end{pmatrix} \tag{S5}$$

The variances of the coefficients a_j are given by the diagonal elements of the covariance matrix, $\mathbf{C}$, i.e. $\sigma_{a_j}^2 = C_{jj}$, where $\mathbf{C}$ is the inverse of the matrix $\mathbf{H}$, variously referred to as the curvature or Hessian matrix.

The Hessian matrix was approximated by a series expansion, which is terminated after the first rank:

$$H_{jk} = \frac{1}{2}\frac{\partial^2\chi^2(\vec{a})}{\partial a_j \partial a_k} \approx \sum_{i=1}^{n} \frac{1}{\sigma_i^2}\frac{\partial f(x_i;\vec{a})}{\partial a_j}\frac{\partial f(x_i;\vec{a})}{\partial a_k}$$

Hence the Jacobian matrix can be used to approximate the Hessian if σ_i^2 is chosen to be equal for all points,

$$\mathbf{H} \approx \frac{1}{\sigma_i^2}\,\mathbf{J}^T \cdot \mathbf{J}. \tag{S6}$$

To speed up calculation time for the matrix product $\mathbf{J}^T \cdot \mathbf{J}$, an economy-size QR decomposition of $\mathbf{J}$ was carried out, reducing the dimension of $\mathbf{R}$ to the size of $\vec{a}$:

$$\mathbf{J} = \mathbf{Q} \cdot \mathbf{R}. \tag{S7}$$

In the following matrix multiplication, $\mathbf{Q}$ vanishes by multiplication with $\mathbf{Q}^T$:

$$(\mathbf{J}^T \cdot \mathbf{J})^{-1} = (\mathbf{R}^T \cdot \mathbf{R})^{-1} = \mathbf{R}^{-1} \cdot (\mathbf{R}^T)^{-1} = \mathbf{R}^{-1} \cdot (\mathbf{R}^{-1})^T \tag{S8}$$

In MATLAB®, this implementation leads to high computational speed and only minor numerical errors. The corresponding code would be as follows:

```
[~,R] = qr(jacobian,0);
```

The diagonal elements of the approximated $\mathbf{H}^{-1}$ can easily be calculated by element-wise squaring followed by summation over the rows of $\mathbf{R}$. Since σ_i^2 is chosen to be equal for all points, the errors for the fit parameters are given by:

```
stdDev = sqrt(variance * sum(inv(R).^2,2));
```

The fitting algorithm `lsqcurvefit` can optionally return the residuals as additional output argument, here termed `residuals`. Hence the variance of the residuals obtained as

```
variance = var(residuals);
```

was used as σ^2 for all points.

TREPR signal decay and triplet lifetime

The kinetics of TREPR signals of triplet states are rather complicated, involving spin relaxation, decay of spin polarisation, and decay of the actual triplet state, usually via intersystem crossing back into the singlet ground state. Hence, only a lower limit of the triplet lifetime can be extracted from the TREPR time profiles, based on the simple fact that regardless of all other processes, TREPR signals will only be observable as long as there exists a triplet state.

As can be seen from the full 2D datasets for all excitation wavelengths used in this study (Figs. S2 and S3), TREPR signals decay on the time scale of several microseconds. However, it is highly likely that this decay is dominated by the microwave power and other experimental parameters and that the actual triplet state lifetime extends well into tens or even hundreds of microseconds.

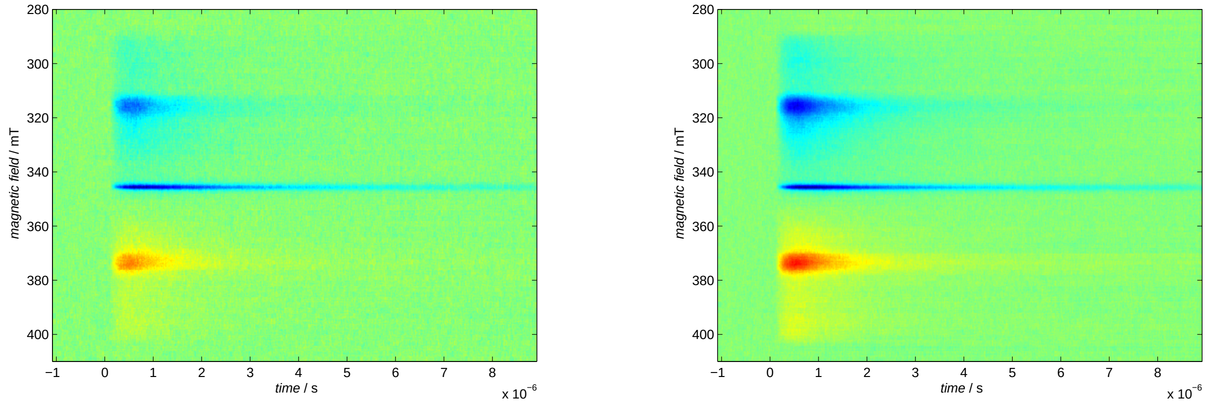

(a) 460 nm

(b) 480 nm

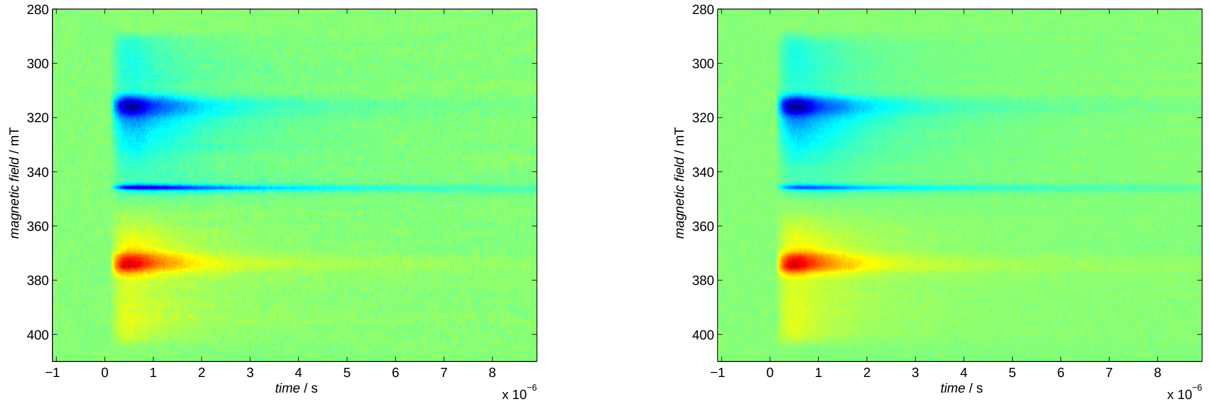

(c) 500 nm

(d) 520 nm

Figure S2: Full 2D TREPR datasets of TBT excited at different wavelengths. Blue colour denotes emissive, red colour enhanced absorptive polarisation. For experimental details see main text.

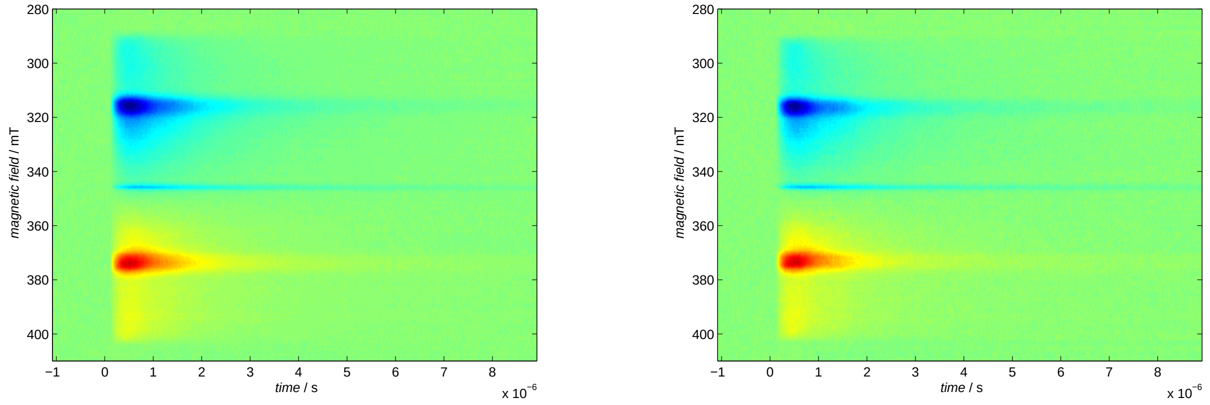

(a) 540 nm

(b) 560 nm

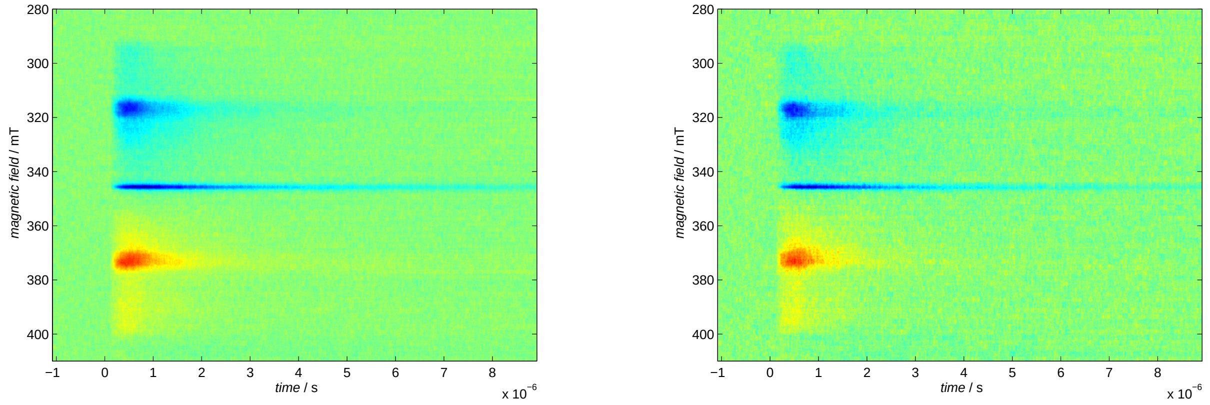

(c) 570 nm

(d) 580 nm

Figure S3: Full 2D TREPR datasets of TBT excited at different wavelengths. Blue colour denotes emissive, red colour enhanced absorptive polarisation. For experimental details see main text.

Spectral simulations of TREPR spectra of TBT

TREPR spectra of TBT have been recorded under solid-state conditions at low temperature (80 K) in frozen solution for different excitation wavelengths, and the resulting spectra fitted assuming a single triplet species for each spectrum. Figures S4 and S5 give an overview of both, the spectra obtained and their respective simulations. All spectra each can be fully described assuming a single triplet species as demonstrated by the good agreement between spectral simulations and experimental data. For simulation parameters cf. Table S1.

Table S1: Simulation parameters for the spectral simulations of the TREPR spectra shown in Figs. S4 and S5. λ_{ex} is the excitation wavelength, D and E are the parameters of the zero-field splitting tensor of the dipolar interaction, Γ_{L} is the Lorentzian (homogeneous) line width, and $p_{1,2,3}$ are the populations of the three triplet sublevels, respectively. Note that the sign of D and E cannot be unambiguously determined and the values for p have been given assuming $D, E > 0$.

λ_{ex}/nm	$\lvert D\rvert$/MHz	$\lvert E\rvert$/MHz	$\lvert E\rvert/\lvert D\rvert$	Γ_{L}/mT	$p_{1,2,3}$
460	1563±4	67±2	0.043	3.0±0.2	0, 0.172, 0.828
480	1563±3	67±2	0.043	2.7±0.2	0, 0.159, 0.841
500	1560±3	69±1	0.044	2.7±0.1	0, 0.158, 0.842
520	1558±2	70±2	0.045	2.4±0.1	0, 0.161, 0.839
540	1556±2	69±1	0.045	2.4±0.1	0, 0.153, 0.847
560	1536±2	64±1	0.042	2.3±0.1	0, 0.144, 0.856
570	1521±3	63±2	0.041	2.5±0.2	0, 0.169, 0.831
580	1493±4	65±2	0.044	2.3±0.2	0, 0.208, 0.792

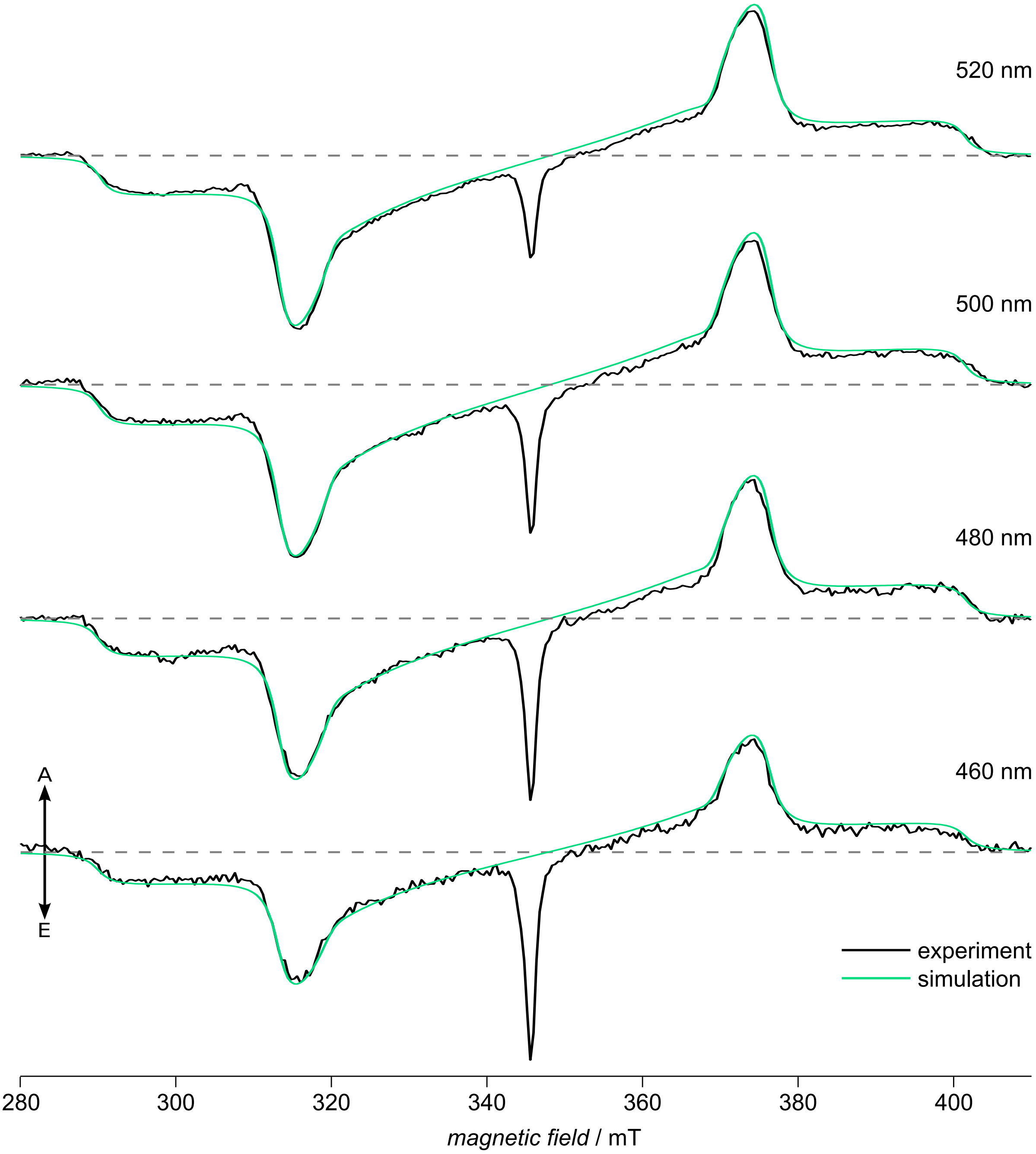

Figure S4: TREPR spectra of TBT excited at different wavelengths together with spectral simulations. Each spectrum could be reproduced by spectral simulations taking a single triplet species into account, shown as gray lines. For simulation parameters cf. Tab. S1. The narrow features in the centre of the spectra at about 345 mT are not due to the triplet state and will not be accounted for here.

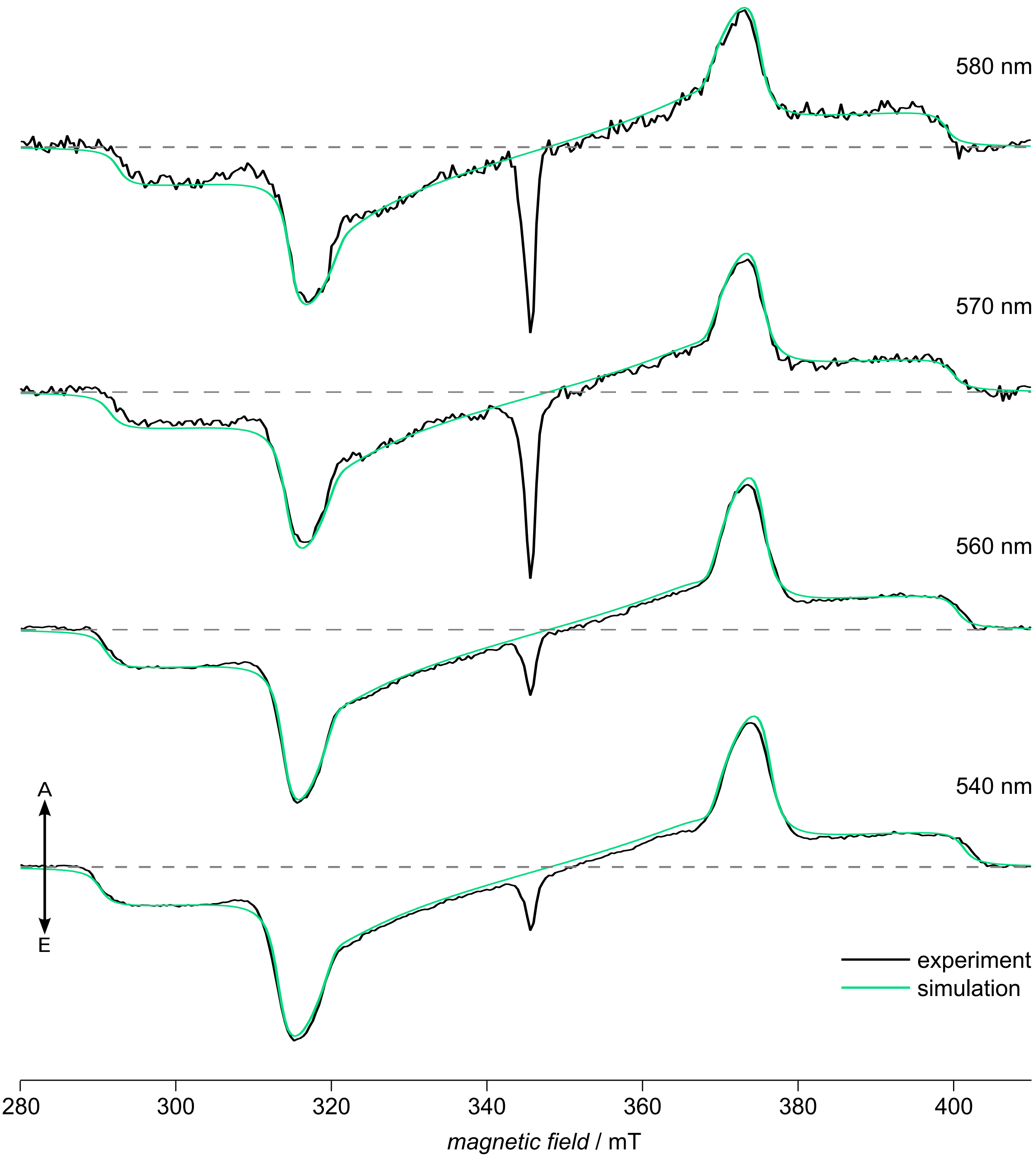

Figure S5: TREPR spectra of TBT excited at different wavelengths together with spectral simulations. Each spectrum could be reproduced by spectral simulations taking a single triplet species into account, shown as gray lines. For simulation parameters cf. Tab. S1. The narrow features in the centre of the spectra at about 345 mT are not due to the triplet state and will not be accounted for here.

5.5. Two Competing Acceptors: Electronic Structure of PNDITBT Probed by Time-Resolved Electron Paramagnetic Resonance Spectroscopy

Clemens Matt, Katja Stry, Rukiya Matsidik, Michael Sommer and Till Biskup: Two competing acceptors: Electronic structure of PNDITBT probed by time-resolved electron paramagnetic resonance spectroscopy. *J. Chem. Phys.*, 151 (2019), pp. 234901 (DOI: 10.1063/1.5128469)

Contributions of all authors:

Clemens Matt: data aquisition (DFT), data analysis, contributions to manuscript and manuscript review

Katja Stry: data aquisition (TREPR and UV-VIS) and data analysis

Rukiya Matsidik: sample synthesis and manuscript review

Michael Sommer: conception and study design and manuscript review

Till Biskup: conception and design of study, data acquisition (TREPR and UV-VIS), data analysis, main contribution to the manuscript and manuscript review

The Journal of Chemical Physics ARTICLE scitation.org/journal/jcp

Two competing acceptors: Electronic structure of PNDITBT probed by time-resolved electron paramagnetic resonance spectroscopy

Cite as: J. Chem. Phys. 151, 234901 (2019); doi: 10.1063/1.5128469
Submitted: 19 September 2019 • Accepted: 22 November 2019 •
Published Online: 17 December 2019

Clemens Matt,[1,a)] Katja Stry,[1] Rukiya Matsidik,[2,b)] Michael Sommer,[3] and Till Biskup[1,c)]

AFFILIATIONS

[1] Institut für Physikalische Chemie, Albert-Ludwigs-Universität Freiburg, Albertstraße 21, 79104 Freiburg, Germany
[2] Institut für Makromolekulare Chemie, Albert-Ludwigs-Universität Freiburg, Stefan-Meier-Straße 31, 79104 Freiburg, Germany
[3] Polymerchemie, Institut für Chemie, Technische Universität Chemnitz, Straße der Nationen 62, 09111 Chemnitz, Germany

Note: This paper is part of the JCP Special Topic on Spin Chemistry.
[a)] **Current address:** Physikalische Chemie und Didaktik der Chemie, Universität des Saarlandes, Campus B2 2, 66123 Saarbrücken, Germany.
[b)] **Current address:** Department of Material Science and Engineering, University of Washington, Seattle, WA 98195, USA.
[c)] **Electronic mail:** till.biskup@uni-saarland.de. **Current address:** Physikalische Chemie und Didaktik der Chemie, Universität des Saarlandes, Campus B2 2, 66123 Saarbrücken, Germany.

ABSTRACT

Balanced charge transport is particularly important for transistors. Hence, ambipolar organic semiconductors with comparable transport capabilities for both positive and negative charges are highly sought-after. Here, we report detailed insights into the electronic structure of PNDITBT, which is an alternating copolymer of naphthalene diimide (NDI), thiophene, benzothiodiazole (B), and thiophene (T) units, as gained by time-resolved electron paramagnetic resonance (TREPR) spectroscopy combined with quantum-chemical calculations. The results are compared to those obtained for PNDIT2 and PCDTBT, which are derivatives without B and NDI acceptor units, respectively. These two polymers show dominant n- and p-channel behavior in organic field-effect transistors. The TBT moiety clearly dominates the electronic structure of PNDITBT, although less so than in PCDTBT. Furthermore, the triplet exciton most probably delocalizes along the backbone, exhibits a highly homogeneous environment, and planarizes the polymer backbone. Obtaining the zero-field splitting tensors of these triplet states by means of quantum-chemical calculations reveals the triplet energy sublevel associated with the molecular axis parallel to the backbone to be preferentially populated, while the one perpendicular to the aromatic plane is not populated at all, consistent with the spin-density distribution. PNDITBT consisting of two acceptors (NDI and B) has a complex electronic structure, as evident from the two charge-transfer bands in its absorption spectrum. TREPR spectroscopy provides a detailed insight on a molecular level not available by and complementing other methods.

I. INTRODUCTION

Electronic devices have shaped human life over the last decades in an unprecedented manner, due to the huge success of silicon-based semiconductors.[1] Nevertheless, there are growing efforts to replace these conventional inorganic semiconductors by their organic counterparts, mostly polymers.[2–5] This comes with a number of advantages, such as mechanical flexibility,[6–9] simple and cheap processing from solutions,[10] and variability due to well-developed protocols of synthetic chemistry.[11,12]

Applications of organic semiconductors range from photovoltaics[15,16] to light-emitting diodes[17] to transistors.[18] The latter are the prerequisites of printable and therefore cheap integrated circuits[19–22] that will revolutionize how electronic devices will further shape our lives.[23,24] Ambipolar transport behavior in field effect transistors allows for simpler designs without the need for advanced

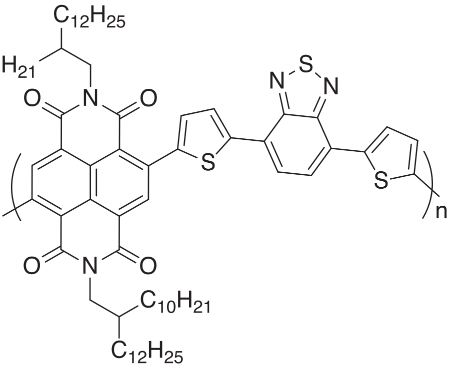

FIG. 1. Chemical structure of PNDITBT. The molecule consists of a naphthalenediimide (NDI) and a dithiophene-benzothiadiazole unit (TBT), respectively. Both building blocks have been investigated in detail before.[13,14]

patterning techniques and makes the devices independent of the polarities of the input and output voltages, besides improving our understanding of the physics of these devices.[25] Diketopyrrolopyrrole (DPP) copolymers are prime examples that often show ambipolar transport characteristics.[26,27] The properties of DPP copolymers can be further fine-tuned by the design of terpolymers with an alternating structure,[28] demonstrating that more complex conjugated backbones can have advantages over their simpler analogs. Naphthalene diimide (NDI) copolymers are better known for exhibiting good electron transport behavior and acceptor properties in solar cells,[29] but when combined with certain comonomers, ambipolar transport can be measured. One example is PNDITBT[30,31] which is built up from alternating NDI and TBT units (Fig. 1). This system carries two acceptor units separated by thiophene donors, and is, from an electronic point of view, interesting on its known. While PNDIT2[32,33] is a popular electron transport material, TBT is an often-used building block for polymers such as PCDTBT,[34,35] which is a donor material for organic solar cells. TBT itself has a donor-acceptor-donor structure with the central benzothiadiazole being the true acceptor. PCDTBT is renowned for its air-stability under solar-cell operating conditions.[36–40]

Little is known about the effect of the coupling of two alternating acceptor units on the electronic structure in a conjugated polymer. Here, we use time-resolved electron paramagnetic resonance (TREPR) spectroscopy[41,42] in conjunction with density-functional theory (DFT) calculations to gain further insights into the electronic structure of the PNDITBT polymer, showing the TBT moiety to balance the effect of NDI. Furthermore, due to its molecular resolution, this approach yields unique results complementing other methods.

II. EXPERIMENTAL AND THEORETICAL METHODS

A. Synthesis

PNDITBT with an absolute number average molecular weight obtained from NMR spectroscopy, $M_{n,\mathrm{NMR}} = 36$ kg/mol, was synthesized by direct arylation polycondensation according to previously published procedures.[43] For details, the reader is referred to the supplementary material.

B. Optical spectroscopy

PNDITBT was dissolved in 1-chloronaphthalene at 0.2 mg/ml. Absorption spectra were recorded using a commercial UV/vis spectrometer (UV-1601PC) in combination with the corresponding software (UV Probe version 3.42). Measurements were performed using 1 mm path length cuvettes.

C. EPR instrumentation

PNDITBT was dissolved in 1-chloronaphthalene in the concentration of 5 mg/ml. All TREPR experiments were performed at 80 K using a setup described previously.[14] Optical excitation at the respective wavelengths was carried out using an optical parametric oscillator (OPO) pumped by an Nd:YAG laser. The repetition rate of the laser was set to 10 Hz, the final pulse energy (after the OPO) to 1 mJ. The laser light was depolarized using a quartz-wedge achromatic depolarizer (Thorlabs DPU-25-A). For full details, the reader is referred to the supplementary material.

D. Spectral simulations

Processing and analysis of TREPR data were carried out using software written in MATLAB®. Preprocessing was carried out using the `trepr` toolbox.[44] All simulations of triplet spectra were performed using the `pepper` routine from the EasySpin software package.[45] Fitting was carried out using the `TSim` program developed by Meyer.[46] Details of both, the simulations and the fitting procedure, are given in the supplementary material.

E. DFT calculations

All calculations were performed using ORCA 3.0.3[47] using the UB3LYP[48,49] functional and the 6-31G**[50,51] basis set. For ***D*** tensor calculations, the EPR-II basis set[52] was used. For geometry optimizations, the atom-pairwise dispersion correction of Grimme was employed.[53,54] Initial geometries of the molecules were created using Avogadro 1.1.1.[55] Spin density plots were created using UCSF Chimera 1.11.2.[56] Dihedral angles between moieties were determined using Avogadro. calculations was performed (i.e., we used MATLAB routines to extract the tensor geometries from the calculations) using MATLAB routines written specifically for this purpose.

III. RESULTS

A. Optical spectroscopy

To get a first overview of the electronic structure of a polymer, optical absorption spectroscopy is very useful. Therefore, we recorded the absorption spectrum of PNDITBT in 1-chloronaphthalene at room-temperature (cf. Fig. 2). In contrast to many other donor-acceptor polymers, two absorption bands in the visible range of the spectrum can be detected that are both attributed to charge-transfer (CT), respectively. The one centered about 476 nm resembles the CT band of the TBT moiety,[14,57] while that centered about 630 nm resembles the CT band of PNDIT2.[58] By comparison to absorption spectra of PNDIT2 and its building blocks,[13] the band in the near-UV region is attributed to a π–π^*

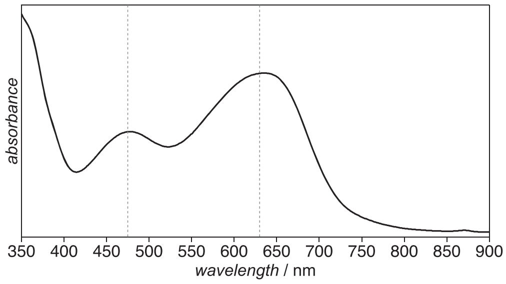

FIG. 2. Absorption spectrum of PNDITBT in 1-chloronaphthalene. Clearly visible are two absorption bands in the visible range of the spectrum centered about 476 nm and 630 nm that are both attributed to charge-transfer, respectively. The band in the near-UV region is attributed to a π–π^* transition. Due to the strong absorbance of the solvent used for wavelengths <350 nm, the spectrum is cut there. The vertical dotted lines represent the excitation wavelengths used for TREPR spectroscopy (476 nm and 630 nm, cf. Fig. 3).

transition, mainly from the NDI moiety. Due to the strong absorbance of the solvent 1-chloronaphthalene for wavelengths <350 nm, the spectrum is cut there. The appearance of two CT bands already hints at an interesting electronic structure with the two moieties NDI and TBT, both acceptors in other contexts, mutually competing. A recent study[59] showed the acceptor strength to be directly related to the bandgap and to be favorable for operation in organic solar cells.

The optical spectra recorded in 1-chloronaphthalene solution differ from those in the literature recorded for the chlorobenzene solution:[30] In particular, the low-energy band is shifted by about 90 nm to the blue in 1-chloronaphthalene compared to chlorobenzene. Given that the solution spectra in chlorobenzene and thin film spectra in chlorobenzene are almost identical,[30] the polymer is most probably aggregated in chlorobenzene, whereas it is molecularly much better dissolved in 1-chloronaphthalene. We have recorded spectra in toluene known to induce aggregation in PNDIT2[58,60] that is similar to those in chlorobenzene. Therefore, PNDITBT is most likely solvated under the conditions used in this study and not aggregated.

Besides providing first insight into the overall electronic structure, optical absorption spectra are a necessary prerequisite to determine the excitation wavelengths used for TREPR spectroscopy.

B. TREPR spectroscopy

To gain a more detailed insight into the electronic structure of conjugated polymers, TREPR spectroscopy has proven useful.[13,14,42,46,61,62] Here, we apply this technique to the polymer PNDITBT consisting of two acceptor moieties. Due to the two CT bands appearing in the optical absorption spectra, we recorded TREPR spectra for excitation in the maximum of either CT band (cf. Fig. 3). Each spectrum could be reproduced by spectral simulations taking a single triplet species into account (red lines in Fig. 3). For simulation parameters, cf. Table I, and for details of both, the simulation strategy of triplet states including the meaning of the *D* tensor of the zero-field splitting as well as the fitting procedure, see the supplementary material. The small features in the center of the spectra at about 345 mT are not due to the triplet state and will not be accounted for here. The interested reader is referred to the literature for a more thorough discussion of their potential origin.[63]

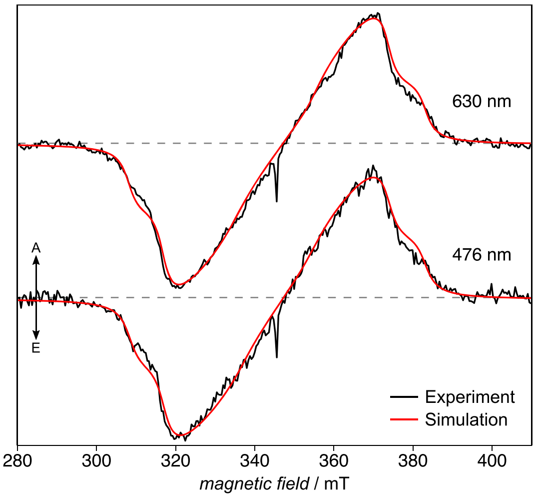

FIG. 3. TREPR spectra of light-induced triplet states of PNDITBT excited at two different wavelengths together with spectral simulations (red lines). Each spectrum could be reproduced by spectral simulations taking a single triplet species into account and shown as red lines. For simulation parameters, cf. Table I, and for details of the fitting procedure, see the supplementary material. The small features in the center of the spectra at about 345 millitesla are not due to the triplet state and will not be accounted for here. As TREPR spectroscopy uses a direct detection scheme, the spectrum shows emissive (E) and enhanced absorptive (A) signals directly.

Generally, the excitation wavelength has only a very minor impact on the overall shape of the spectra and the delocalization of the triplet exciton, as demonstrated by the simulation parameters (Table I). TREPR signals are stronger for excitation at 630 nm as compared to 476 nm, judged by the better signal-to-noise ratio of the TREPR spectra for the former excitation wavelength, given otherwise identical experimental conditions. However, we do not quantify the triplet yield as such, as it is of no relevance for the other results presented here. We note that for both excitation wavelengths, the Gaussian (inhomogeneous) linewidth, although a fitting parameter, vanishes. This points toward a very homogeneous environment of the triplet exciton, similar to the situation described for PCDTBT.[14]

TABLE I. Simulation parameters for the spectral simulations of the TREPR spectra shown in Fig. 3. λ_{ex} in nanometer is the excitation wavelength used, *D* and *E* in megahertz are the parameters of the zero-field splitting tensor of the dipolar interaction, Γ_G and Γ_L in millitesla are the Gaussian and Lorentzian linewidths, and $p_{1,2,3}$ are the populations of the three triplet sublevels, respectively, ordered in ascending energy. For details of the fitting procedure, see the supplementary material.

λ_{ex}	$\lvert D\rvert$	$\lvert E\rvert$	$\lvert E\rvert/\lvert D\rvert$	Γ_G	Γ_L	$p_{1,2,3}$
476	1047 ± 6	183 ± 3	0.17	0.00	4.5 ± 0.4	0.000, 0.332, 0.668
630	1054 ± 4	182 ± 2	0.17	0.00	4.1 ± 0.2	0.000, 0.314, 0.686

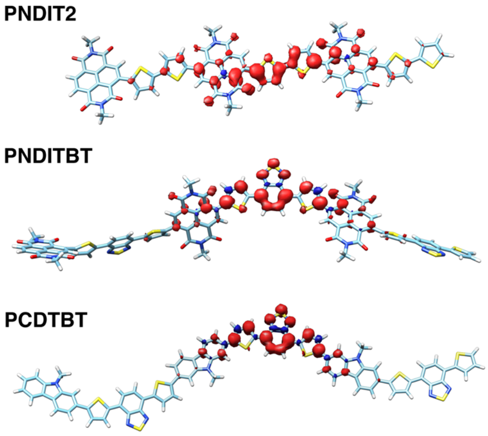

FIG. 4. Spin-density distribution for the fragments with $n = 3$ of PNDIT2, PNDITBT, and PCDTBT, respectively. Geometries have been optimized for the triplet state and spin densities calculated on the theory level B3LYP/6-31G**. The latter have been displayed for a threshold level of ±0.002. Red denotes positive and blue negative spin density. For a more quantitative approach, cf. Fig. 5.

Additionally, one of the three triplet sublevel populations is zero for both excitation wavelengths.

C. Quantum-chemical calculations

To corroborate our spectroscopic investigations, a series of quantum-chemical calculations has been performed on polymer fragments with $n = 3$. Molecular geometries have been optimized for triplet states, and the spin-density distribution and the D tensors have been calculated for PNDITBT, and for comparison, additionally, for PNDIT2 and PCDTBT. For a first overview, the geometry as well as the spin density of the triplet states of the three respective polymers is shown in Fig. 4. The maximum of the spin density is in all three cases located on a single moiety, T2 in the case of PNDIT2, and TBT in the case of PCDTBT and PNDITBT, respectively.

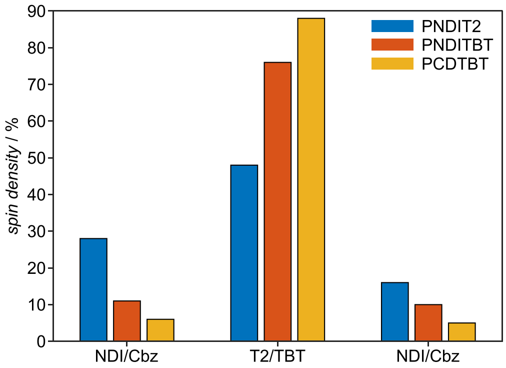

FIG. 5. Quantitative analysis of the spin-density distribution for the triplet states of PNDIT2, PNDITBT, and PCDTBT. Depicted are the relative amounts of spin density on the NDI/Carbazole (Cbz) and T2/TBT moieties, respectively. The sequence of the three moieties is the same as that in Fig. 4. For actual values, cf. Table II.

TABLE II. Quantitative analysis of the spin-density distribution for the triplet states of PNDIT2, PNDITBT, and PCDTBT as shown in Fig. 4. The values are given in percent and are graphically represented in Fig. 5. The sum of the values does not amount to 100%, as a very minor contribution comes from moieties further apart.

Polymer	NDI/Cbz	T2/TBT	NDI/Cbz
PNDIT2	28	48	16
PNDITBT	11	76	10
PCDTBT	6	88	5

Whereas those plots give a good overall idea of where the spin density is located, they do not easily allow for more quantitative analyses. Therefore, we display the relative spin density of the fragment carrying the most spin density and its neighbors in Fig. 5. From this, it is immediately obvious that the TBT moiety dominates the electronic structure on both, PNDITBT and PCDTBT, whereas the T2 moiety in PNDIT2 carries much less spin density compared to TBT in the other two polymers. For actual values of the spin densities, cf. Table II.

D tensors have been calculated in a similar fashion as previously for PCDTBT.[64] While DFT notoriously underestimates the values of D, it overestimates the corresponding E values.[64–66] Hence, the rhombicity, E/D, as obtained by the calculations is far from the experimental values. Orientations of the D tensors with respect to the molecular geometry are shown in Fig. 6. As the majority of the spin density is located on T2 and TBT, respectively, only this fragment is shown, together with a reference coordinate system. The angles between this reference and the actual D tensors are given in Table III, together with a comparison of calculated and experimental values for D and E. In all three cases, two axes are located more or less within the aromatic plane, while the third axis is perpendicular to it.

Interestingly, while DFT reveals a positive sign of D for both, PNDITBT and PCDTBT, for PNDIT2, a negative sign of D is calculated, resulting in a change in the assignment of axes as compared to the other two polymers. While in both, PCDTBT and PNDITBT, the z axis of the D tensor is perpendicular to the aromatic plane,

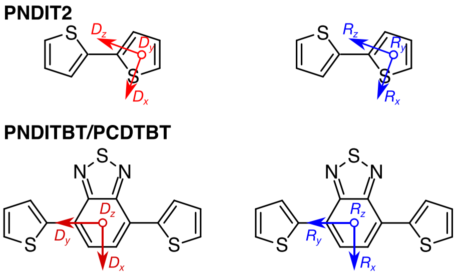

FIG. 6. Orientation of the calculated D tensors for PNDIT2, PNDITBT, and PCDTBT within the T2/TBT moieties and molecular reference frames. Assuming a right-handed coordinate system, the y component in the case of PNDIT2 is pointing toward the reader, while the z component in the case of PNDITBT and PCDTBT is pointing toward the paper plane. The deviation from the respective reference frame is given as three dihedral angles, α, β, and γ, for each of the three axes, x, y, and z, respectively. For actual values of these angles, see Table III.

TABLE III. Comparison of calculated and experimental D tensors, as well as their orientation within the molecular reference frame. D tensors for each of the compounds have been calculated using the B3LYP/EPR-II level of theory. Values for $|D|$ and $|E|$ are given in megahertz. For the orientation of the D tensor with respect to the molecular reference frame R_i with $i = x, y, z$, cf. Fig. 6. The angles α, β, and γ (in degrees) refer to the deviation of the corresponding D tensor axes from the molecular reference frame. Values for PNDIT2 have been taken from Ref. 58, for PCDTBT from Refs. 14 and 64.

	D	E	E/D	$\|D\|$	$\|E\|$	$\|E\|/\|D\|$			
Polymer	Calculated			Experimental			α	β	γ
PNDIT2	−507	−138	0.27	1095	226	0.21	11.0	2.6	10.6
PNDITBT	+521	+164	0.31	1054	182	0.17	0.7	0.3	0.7
PCDTBT	+664	+174	0.26	1254	101	0.06	0.2	0.2	0.1

TABLE IV. Dihedral angles between the aromatic planes of the NDI/Cbz and T2/TBT moieties, respectively, obtained from geometry optimization in the triplet state. The NDI/Cbz and T2/TBT moieties are planar. Angles are given in degrees and for the configuration as shown in Fig. 4. Boldface values denote the angles directly adjacent to the T2/TBT moiety carrying the maximum spin density.

Polymer	Dihedral angles				
PNDIT2	38.5	36.4	**31.0**	**33.2**	36.7
PNDITBT	40.3	38.6	**34.7**	**34.8**	37.8
PCDTBT	24.9	24.9	**12.0**	**14.6**	23.8

for PNDIT2, it would be the y axis. This is in contrast to magnetophotoselection experiments performed for NDI and NDI-T2[62] revealing the D_z axis to be perpendicular to the optical transition dipole moment and to the aromatic plane. While we cannot resolve this discrepancy between DFT calculations and experiments here, we note that it does not affect the interpretation of our data. A sign change of D would result in a change of the assignment of axes of the D tensor and the order of the energy sublevels of the respective triplet state. However, the assignment of triplet sublevel populations to molecular axes would stay the same.

Another interesting aspect revealed by the DFT calculations is the overall geometry of the three polymers. While the NDI, carbazole (Cbz), T2, and TBT moieties are basically planar by themselves, there are substantial dihedral angles between the aromatic planes of the adjacent moieties, cf. Table IV. As already shown for PCDTBT,[64] the triplet state seems to reduce the dihedral angles directly adjacent to the T2/TBT moiety carrying the maximum spin density. Furthermore, while the dihedral angles are comparable for PNDIT2 and PNDITBT, they are much smaller for PCDTBT. Note that the angles given here have been calculated for triplet state geometries and are therefore not easily comparable to the singlet state geometries reported in most other literature.

IV. DISCUSSION

Besides discussing the results obtained on PNDITBT as described above, they will be compared to the results obtained in previous studies on both, PNDIT2[13,58] and PCDTBT[14,64] (Fig. 7 and Table V). This approach allows us to reveal details of the impact on the electronic structure of the resulting polymer by coupling the two acceptors NDI and TBT in one molecule.

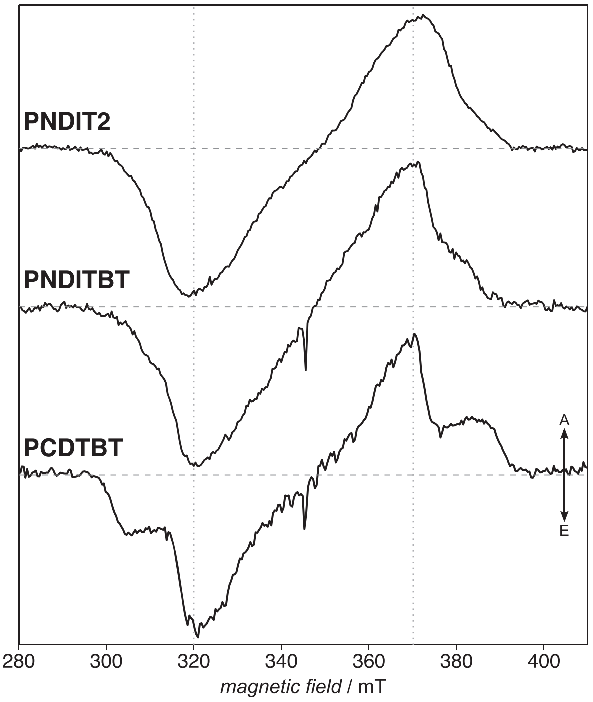

FIG. 7. Comparison of the TREPR spectra of light-induced triplet states of PNDIT2, PNDITBT, and PCDTBT. The spectrum for PNDIT2 has been taken from Ref. 58, for PCDTBT from Ref. 14. The vertical dotted lines are a guide for the eye. For PNDITBT, the spectrum for excitation at 630 nm is shown. Simulation parameters of each of the spectra are given in Table V.

A. TBT dominates the electronic structure

Similar to the situation in PCDTBT,[14] the TBT moiety dominates the electronic structure of PNDITBT. This is evident from the location of spin density (Fig. 5 and Table II), but as well from a comparison of the TREPR spectra (Fig. 7) and the respective simulation parameters (Table V). TBT dominates stronger in PCDTBT than in PNDITBT (Fig. 5). This is probably due to the weaker competition from the carbazole donor moiety in PCDTBT as compared to the NDI acceptor moiety in PNDITBT. While TREPR spectroscopy allows only for probing the triplet state, our previous investigations on building blocks of PCDTBT, comparing optical and TREPR data, reveal a close correlation between the optically probed singlet states and the triplet states.[14,64] While previously,[30] based on calculating HOMO and LUMO orbitals, it has been deduced that TBT is converted into a donor moiety in PNDITBT, the results from TREPR spectroscopy reveal a rather dominant role of TBT. Hence, we speculate that the competition between the two mutual acceptors, NDI and TBT, is key to the balanced charge transport in PNDITBT. This competition and balance is most probably as well the origin of the two distinct CT bands in the absorption spectrum (Fig. 2).

TABLE V. Simulation parameters for the spectral simulations of the TREPR spectra of PNDIT2, PNDITBT, and PCDTBT shown in Fig. 7. λ_{ex} in nanometer is the excitation wavelength used, D and E in megahertz are the parameters of the zero-field splitting tensor of the dipolar interaction, Γ_{G} and Γ_{L} in millitesla are the Gaussian and Lorentzian linewidths, and $p_{x,y,z}$ are the populations of the three triplet sublevels, respectively. As the three zero-field populations $p_{1,2,3}$ from the simulations are ordered in the ascending energy level, they can be assigned to $p_{z,x,y}$, respectively,[64] assuming $D > 0$ as obtained from the DFT calculations for PNDITBT and PCDTBT, and $p_{y,x,z}$ assuming $D < 0$ as obtained from the DFT calculations for PNDIT2. Experimental values for PNDIT2 have been taken from Ref. 58, for PCDTBT from Ref. 14.

Polymer	λ_{ex}	$\|D\|$	$\|E\|$	$\|E\|/\|D\|$	Γ_{G}	Γ_{L}	p_x	p_y	p_z
PNDIT2	622	1095 ± 4	226 ± 2	0.21	7.0 ± 0.8	2.1 ± 0.4	0.240	0.000	0.760
PNDITBT	630	1054 ± 4	182 ± 2	0.17	0.0	4.1 ± 0.2	0.314	0.686	0.000
PCDTBT	550	1254 ± 3	101 ± 1	0.08	0.0	2.4 ± 0.1	0.351	0.649	0.000

B. PNDITBT provides a homogeneous environment for the triplet exciton

PNDITBT provides a much more homogeneous environment for the triplet exciton than PNDIT2, as evident from the vanishing Gaussian linewidth in PNDITBT. This coincides with the reported much more planar backbone.[30] Generally speaking, spectral broadening can be described by a combination of both, Lorentzian and Gaussian broadening that can clearly be distinguished by their respective line shapes. While Lorentzian (homogeneous) broadening is a result of the lifetime of the excited state, Gaussian (inhomogeneous) broadening can have different physical origins, and in our case, unresolved hyperfine splittings as well as different conformations and dihedral angles along the polymer backbone. Thus, a vanishing Gaussian (inhomogeneous) contribution to the linewidth of the spectral lines is a clear hint of a homogeneous environment for the triplet state, i.e., a rather regular arrangement of the polymer backbone in terms of dihedral angles and alike. Previously, we have shown aggregation to reduce the inhomogeneous linewidth,[58] but PCDTBT that is known not to form aggregates to have a vanishing inhomogeneous linewidth.[14] Furthermore, we note that the differences in inhomogeneous broadening are by no means small, but quite substantial. However, comparing the previously reported optical spectra recorded in chlorobenzene with those presented here and recorded in 1-chloronaphthalene hints at aggregation taking place in the former solvent, but not in the latter. Therefore, an alternative explanation for the highly homogeneous environment of the triplet exciton may be that the spin density is mostly located on the planar and rigid TBT moiety. As mentioned already, we have recorded absorption spectra in toluene known to result in highly ordered aggregates in PNDIT2[58] that resemble much more those spectra recorded in chlorobenzene and reported previously.[30] Therefore, we tentatively assign the highly homogeneous environment as evident from the vanishing Gaussian linewidth (cf. Table V) to a stiff backbone, as in the case of PCDTBT.[14] This highly homogeneous environment is most probably responsible for the high charge carrier mobilities for both positive and negative charges.

C. The triplet exciton is more delocalized in PNDITBT than in PNDIT2 and PCDTBT

Comparing the TREPR spectra (Fig. 7) of the triplet states of the three polymers PNDITBT, PNDIT2, and PCDTBT, and particularly their respective simulation parameters (Table V) clearly reveals the triplet exciton to be more delocalized in PNDITBT than in the two other polymers. Possible reasons for this are that PNDITBT is (locally) more planar than PNDIT2, and that the TBT moiety is less dominant in PNDITBT as compared to the situation in PCDTBT. This can easily be rationalized by NDI competing as an acceptor with TBT, while Cbz acts as a donor in PCDTBT.

At first sight, the TBT dominating the spin density distribution in PNDITBT (Fig. 5) should result in a more localized triplet exciton as compared to PNDIT2. However, TBT is larger than T2 and thus compensates for the effect that the spin density is spread further beyond the two adjacent NDI moieties in PNDIT2 as compared to the situation in PNDITBT.

D. The rhombicity of PNDITBT lies between that of PNDIT2 and PCDTBT

The rhombicity of the triplet state, as given by the ratio $|E|/|D|$, is a measure of the overall geometry of the excited state. Comparing the rhombicity of PNDITBT with those of PNDIT2 and PCDTBT (Table V) reveals that the value for PNDITBT lies in between the other two. This is most probably due to the spin density distribution and "curvature" of the backbone. The spin density in PNDITBT is further spread than in PCDTBT, as revealed by the smaller D value (Table V). Furthermore, the TBT moiety in PNDITBT enhances the backbone curvature as compared to PNDIT2 (Fig. 4). In addition, the backbone of PNDITBT harboring the maximum of spin density (i.e., mostly the TBT moiety) is flatter than that of PNDIT2 (Table IV). Hence, the triplet state in PNDITBT is less rhombic than that of PNDIT2, but more rhombic as that of PCDTBT renowned for its entirely flat overall backbone geometry.[14] Thus, the results of the geometry optimization and the dihedral angles obtained from these geometries are consistent with the results from TREPR spectroscopy.

E. Triplet excitons planarize the backbone

Triplet excitons have previously been shown to planarize the backbone in their immediate surroundings.[64] Here, we have extended our previous investigations of PCDTBT and its hexylated modification to both PNDITBT and PNDIT2 (cf. Table IV). The obvious result, a more planar backbone at the location of the triplet exciton, renders this effect to be more general than previously anticipated. However, it seems less pronounced with NDI substituents in PNDIT2 and PNDITBT than with Cbz moieties in PCDTBT.

F. The triplet sublevel oriented along the backbone is preferentially populated

Eventually, accessing the orientation of the D tensor axes within the molecular coordinate system by means of DFT calculations allows us to assign the populations of the three triplet sublevel populations $p_{1,2,3}$ obtained from the spectral simulations and ordered in ascending energy to the tensor axes, hence relating $p_{1,2,3}$ and $p_{x,y,z}$. As already mentioned above, the negative sign of D for PNDIT2 obtained from DFT calculations is in contrast to magnetophotoselection experiments.[62] However, a sign change would not affect our assignment of the triplet sublevel populations to the molecular axes. Still the triplet energy sublevel associated with the tensor axis perpendicular to the aromatic plane would have no initial population, while that associated with the tensor axis oriented along the backbone shows the highest population. This is consistent with the overall picture of the spin density distribution (Fig. 4), as well as with the exciton delocalization along the backbone shown for PCDTBT[14] and solvated PNDIT2.[13,58]

V. CONCLUSION

TREPR spectroscopy in combination with quantum-chemical calculations provides detailed insights into the electronic structure and morphology of conjugated polymers on a molecular level not accessible by and complementing other methods. The results from quantum-chemical calculations are in the present case mostly consistent with the experimental data obtained by TREPR spectroscopy. For PNDITBT, we show the TBT moiety to dominate the electronic structure, the triplet exciton to locally planarize the backbone, and the local environment of the triplet exciton to be highly homogeneous. We assume the exciton delocalization to take place along the backbone. The comparable acceptor strength of NDI and TBT is most probably responsible for the previously reported balanced charge transport of PNDITBT, making it highly suitable for organic field-effect transistors. Furthermore, terpolymers with alternating structures and therefore more complex conjugated backbones show a rich electronic structure that demands detailed investigations. To this end, spectroscopic tools with molecular resolution such as TREPR spectroscopy are of high demand and provide the insight necessary for the rational design of new materials.

SUPPLEMENTARY MATERIAL

See the supplementary material for details of the synthesis of PNDITBT, the EPR instrumentation, the general shape of triplet states in TREPR, the spectral simulations of TREPR spectra, and a comparison of the optical absorption profiles of PNDIT2, PNDITBT, and PCDTBT.

ACKNOWLEDGMENTS

The authors thank Dr. H. Komber, IPF Dresden, for high temperature NMR measurements of PNDITBT and the German Research Foundation (DFG, Grant No. GRK 1642 to C.M., R.M., and M.S., Grant No. SO 1213/8-1 to R.M. and M.S., and Grant No. BI 1249/3-1 to T.B.) for financial support, Th. Koslowski for providing computing time, and S. Weber for providing the EPR equipment. C.M. and T.B. are grateful to C.W.M. Kay (Universität des Saarlandes) for financial and personal support.

REFERENCES

[1] G. E. Moore, "Cramming more components onto integrated circuits," Electronics **38**, 114–117 (1965).

[2] S. R. Forrest, "The path to ubiquitious and low-cost organic electronic appliances on plastic," Nature **428**, 911–918 (2004).

[3] I. McCulloch, "Rolling out organic electronics," Nat. Mater. **4**, 583–584 (2005).

[4] A. Coskun, J. M. Spruell, G. Barin, W. R. Dichtel, A. H. Flood, Y. Y. Botros, and J. F. Stoddart, "High hopes: Can molecular electronics realise its potential?," Chem. Soc. Rev. **41**, 4827–4859 (2012).

[5] A. C. Arias, J. D. MacKenzie, I. McCulloch, J. Rivnay, and A. Salleo, "Materials and applications for large area electronics: Solution-based approaches," Chem. Rev. **110**, 3–24 (2010).

[6] J. Lewis, "Material challenge for flexible organic devices," Mater. Today **9**, 38–45 (2006).

[7] S. Logothetidis, "Flexible organic electronic devices: Materials, process and applications," Mater. Sci. Eng.: B **152**, 96–104 (2008).

[8] J. A. Rogers, T. Someya, and Y. Huang, "Materials and mechanics for stretchable electronics," Science **327**, 1603–1607 (2010).

[9] H. Ling, S. Liu, Z. Zheng, and F. Yan, "Organic flexible electronics," Small Methods **2**, 1800070 (2018).

[10] M. Berggren, D. Nilsson, and N. D. Robinson, "Organic materials for printed electronics," Nat. Mater. **6**, 3–5 (2007).

[11] Z. B. Henson, K. Müllen, and G. C. Bazan, "Design strategies for organic semiconductors beyond the molecular formula," Nat. Chem. **4**, 699–704 (2012).

[12] P.-O. Morin, T. Bura, and M. Leclerc, "Realizing the full potential of conjugated polymers: Innovation in polymer synthesis," Mater. Horiz. **3**, 11–20 (2016).

[13] D. L. Meyer, R. Matsidik, M. Sommer, and T. Biskup, "Electronic structure trumps planarity: Unexpected narrow exciton delocalisation in PNDIT2 revealed by time-resolved EPR spectroscopy," Adv. Electron. Mater. **4**, 1700385 (2018).

[14] C. Matt, D. L. Meyer, F. Lombeck, M. Sommer, and T. Biskup, "TBT entirely dominates the electronic structure of the conjugated copolymer PCDTBT: Insights from time-resolved electron paramagnetic resonance spectroscopy," Macromolecules **51**, 4341–4349 (2018).

[15] L. Lu, T. Zheng, Q. Wu, A. M. Schneider, D. Zhao, and L. Yu, "Recent advances in bulk heterojunction polymer solar cells," Chem. Rev. **115**, 12666–12731 (2015).

[16] N. Yeh and P. Yeh, "Organic solar cells: Their developments and potentials," J. Renewable Sustainable Energy **21**, 421–431 (2013).

[17] C. Sekine, Y. Tsubata, T. Yamada, M. Kitano, and S. Doi, "Recent progress of high performance polymer OLED and OPV materials for organic printed electronics," Sci. Technol. Adv. Mater. **15**, 034203 (2014).

[18] A. Facchetti, "Seminconductors for organic transistors," Mater. Today **10**, 28–37 (2007).

[19] J. A. Rogers and Z. Bao, "Printed plastic electronics and paperlike displays," J. Polym. Sci., Part A: Polym. Chem. **40**, 3327–3334 (2002).

[20] H. Klauk, "Organic thin-film transistors," Chem. Soc. Rev. **39**, 2643–2666 (2010).

[21] B. Crone, A. Dodabalapur, Y.-Y. Lin, R. W. Filas, Z. Bao, A. LaDuca, R. Sarpeshkar, H. E. Katz, and W. Li, "Large-scale complementary integrated circuits based on organic transistors," Nature **403**, 521–523 (2000).

[22] H. Klauk, U. Zschieschang, J. Pflaum, and M. Halik, "Ultralow-power organic complementary circuits," Nature **445**, 745–748 (2007).

[23] T. Sekitani and T. Someya, "Human-friendly organic integrated circuits," Mater. Today **14**, 398–407 (2011).

[24] M. Stoppa and A. Chiolerio, "Wearable electronics and smart textiles: A critical review," Sensors **14**, 11957–11992 (2014).

[25]J. Zaumseil and H. Sirringhaus, "Electron and ambipolar transport in organic field-effect transistors," Chem. Rev. **107**, 1296–1323 (2007).

[26]C. B. Nielsen, M. Turbiez, and I. McCulloch, "Recent advances in the development of semiconducting DPP-containing polymers for transistor applications," Adv. Mater. **25**, 1859–1880 (2013).

[27]A. J. Kronemeijer, E. Gili, M. Shahid, J. Rivnay, A. Salleo, M. Heeney, and H. Sirringhaus, "A selenophene-based low-bandgap donor–acceptor polymer leading to fast ambipolar logic," Adv. Mater. **24**, 1558–1565 (2012).

[28]K. H. Hendriks, G. H. L. Heitges, V. S. Gevaerts, M. M. Wienk, and R. A. J. Janssen, Angew. Chem., Int. Ed. **52**, 8341–8344 (2013).

[29]M. Sommer, "Conjugated polymers based on naphthalene diimide for organic electronics," J. Mater. Chem. C **2**, 3088–3098 (2014).

[30]C. Gu, W. Hu, J. Yao, and H. Fu, "Naphthalenediimide-benzothiadiazole copolymer semiconductors: Rational molecular design for air-stable ambipolar charge transport," Chem. Mater. **25**, 2178–2183 (2013).

[31]F. Liu, H. Li, C. Gu, and H. Fu, "Naphthalene diimide and benzothiadiazole copolymer acceptor for all-polymer solar cells with improved open-circuit voltage and morphology," RSC Adv. **5**, 92151–92158 (2015).

[32]H. Yan, Z. Chen, Y. Zheng, C. Newman, J. R. Quinn, F. Dötz, M. Kastler, and A. Facchetti, "A high-mobility electron-transporting polymer for printed transistors," Nature **457**, 679–686 (2009).

[33]R. Matsidik, H. Komber, A. Luzio, M. Caironi, and M. Sommer, "Defect-free naphthalene diimide bithiophene copolymers with controlled molar mass and high performance via direct arylation polycondensation," J. Am. Chem. Soc. **137**, 6705–6711 (2015).

[34]N. Blouin, A. Michaud, and M. Leclerc, "A low-bandgap poly(2,7-carbazole) derivative for use in high-performance solar cells," Adv. Mater. **19**, 2295–2300 (2007).

[35]N. Blouin, A. Michaud, D. Gendron, S. Wakim, E. Blair, R. Neagu-Plesu, M. Belletête, G. Durocher, Y. Tao, and M. Leclerc, "Toward a rational design of poly(2,7-carbazole) derivatives for solar cells," J. Am. Chem. Soc. **130**, 732–742 (2008).

[36]S. Cho, J. H. Seo, S. H. Park, S. Beaupré, M. Leclerc, and A. J. Heeger, "A thermally stable semiconducting polymer," Adv. Mater. **22**, 1253–1257 (2010).

[37]Y. Sun, C. J. Takacs, S. R. Cowan, J. H. Seo, X. Gong, A. Roy, and A. J. Heeger, "Efficient, air-stable bulk heterojunction polymer solar cells using MoO_x as the anode interfacial layer," Adv. Mater. **23**, 2226–2230 (2011).

[38]C. H. Peters, I. T. Sachs-Quintana, J. P. Kastrop, S. Beaupré, M. Leclerc, and M. D. McGehee, "High efficiency polymer solar cells with long operating lifetimes," Adv. Energy Mater. **1**, 491–494 (2011).

[39]J. Kong, S. Song, M. Yoo, G. Y. Lee, O. Kwon, J. K. Park, H. Back, G. Kim, S. H. Lee, H. Suh, and K. Lee, "Long-term stable polymer solar cells with significantly reduced burn-in loss," Nat. Commun. **5**, 5688 (2014).

[40]S. Beaupré and M. Leclerc, "PCDTBT: En route for low cost plastic solar cells," J. Mater. Chem. A **1**, 11097–11105 (2013).

[41]M. D. Forbes, L. E. Jarocha, S. Sim, and V. F. Tarasov, "Time-resolved electron paramagnetic resonance spectroscopy: History, technique, and application to supramolecular and macromolecular chemistry," Adv. Phys. Org. Chem. **47**, 1–83 (2014).

[42]T. Biskup, "Structure–function relationship of organic semiconductors: Detailed insights from time-resolved EPR spectroscopy," Front. Chem. **7**, 10 (2019).

[43]R. Matsidik, H. Komber, and M. Sommer, "Rational use of aromatic solvents for direct arylation polycondensation: C–H reactivity versus solvent quality," ACS Macro Lett. **4**, 1346–1350 (2015).

[44]T. Biskup, "Time-resolved EPR of radical pair intermediates in cryptochromes," Mol. Phys. **111**, 3698–3703 (2013).

[45]S. Stoll and A. Schweiger, "EasySpin, a comprehensive software package for spectral simulation and analysis in EPR," J. Magn. Reson. **178**, 42–55 (2006).

[46]D. L. Meyer, F. Lombeck, S. Huettner, M. Sommer, and T. Biskup, "Direct $S_0 \rightarrow T$ excitation of a conjugated polymer repeat unit: Unusual spin-forbidden transitions probed by time-resolved electron paramagnetic resonance spectroscopy," J. Phys. Chem. Lett. **8**, 1677–1682 (2017).

[47]F. Neese, "The ORCA program package," Wiley Interdiscip. Rev.: Comput. Mol. Sci. **2**, 73–78 (2012).

[48]A. D. Becke, "Density-functional thermochemistry. III. The role of exact exchange," J. Chem. Phys. **98**, 5648–5652 (1993).

[49]C. Lee, W. Yang, and R. G. Parr, "Development of the Colle-Salvetti correlation-energy formula into a functional of the electron density," Phys. Rev. B **37**, 785–789 (1988).

[50]G. A. Petersson, A. Bennett, T. G. Tensfeldt, M. A. Al-Laham, W. A. Shirley, and J. Mantzaris, "A complete basis set model chemistry. I. The total energies of closed-shell atoms and hydrides of the first-row elements," J. Chem. Phys. **89**, 2193–2218 (1988).

[51]G. A. Petersson and M. A. Al-Laham, "A complete basis set model chemistry. II. Open-shell systems and the total energies of the first-row atoms," J. Chem. Phys. **94**, 6081–6090 (1991).

[52]V. Barone, "Structure, magnetic properties and reactivities of open-shell species from density functional and self-consistent hybrid methods," in *Recent Advances in Density Functional Methods (Part I)*, Recent Advances in Computational Chemistry Vol. 1, edited by D. P. Chong (World Scientific, Singapore, 1995), Chap. 8, pp. 287–334.

[53]S. Grimme, J. Antony, S. Ehrlich, and H. Krieg, "A consistent and accurate *ab initio* parametrization of density functional dispersion correction (DFT-D) for the 94 elements H-Pu," J. Chem. Phys. **132**, 154104 (2010).

[54]S. Grimme, S. Ehrlich, and L. Goerigk, "Effect of the damping function in dispersion corrected density functional theory," J. Comput. Chem. **32**, 1456–1465 (2011).

[55]M. D. Hanwell, D. E. Curtis, D. C. Lonie, T. Vandermeersch, E. Zurek, and G. R. Hutchison, "Avogadro: An advanced semantic chemical editor, visualization, and analysis platform," J. Cheminf. **4**, 17 (2012).

[56]E. F. Pettersen, T. D. Goddard, C. C. Huang, G. S. Couch, D. M. Greenblatt, E. C. Meng, and T. E. Ferrin, "UCSF Chimera—A visualization system for exploratory research and analysis," J. Comput. Chem. **25**, 1605–1612 (2004).

[57]N. Banerji, E. Gagnon, P.-Y. Morgantini, S. Valouch, A. R. Mohebbi, J.-H. Seo, M. Leclerc, and A. J. Heeger, "Breaking down the problem: Optical transitions, electronic structure, and photoconductivity in conjugated polymer PCDTBT and in its separate building blocks," J. Phys. Chem. C **116**, 11456–11469 (2012).

[58]D. L. Meyer, R. Matsidik, S. Huettner, M. Sommer, and T. Biskup, "Solvent-mediated aggregate formation of PNDIT2: Decreasing the available conformational subspace by introducing locally highly ordered domains," Phys. Chem. Chem. Phys. **20**, 2716–2723 (2018).

[59]O. O. Adegoke, I. H. Jung, M. Orr, L. Yu, and T. Goodson III, "Effect of acceptor strength on optical and electronic properties in conjugated polymers for solar applications," J. Am. Chem. Soc. **137**, 5759–5769 (2015).

[60]R. Steyrleuthner, M. Schubert, I. Howard, B. Klaumünzer, K. Schilling, Z. Chen, P. Saalfrank, F. Laquai, A. Facchetti, and D. Neher, "Aggregation in a high-mobility n-type low-bandgap copolymer with implications on semicrystalline morphology," J. Am. Chem. Soc. **134**, 18303–18317 (2012).

[61]M. Bennati, K. Németh, P. R. Surján, and M. Mehring, "Zero-field-splitting and π-electron spin densities in the lowest excited triplet state of oligothiophenes," J. Chem. Phys. **105**, 4441–4447 (1996).

[62]D. L. Meyer, R. Matsidik, D. Fazzi, M. Sommer, and T. Biskup, "Probing exciton delocalization in organic semiconductors: Insight from time-resolved electron paramagnetic resonance and magnetophotoselection experiments," J. Phys. Chem. Lett. **9**, 7026–7031 (2018).

[63]D. L. Meyer, N. Schmidt-Meinzer, C. Matt, S. Rein, F. Lombeck, M. Sommer, and T. Biskup, "Side-chain engineering of conjugated polymers: Distinguishing its impact on film morphology and electronic structure," J. Phys. Chem. C **123**, 20071–20083 (2019).

[64]C. Matt, F. Lombeck, M. Sommer, and T. Biskup, "Impact of side chains of conjugated polymers on electronic structure: A case study," Polymers **11**, 870 (2019).

[65]S. Sinnecker and F. Neese, "Spin–spin contributions to the zero-field splitting tensor in organic triplets, carbenes and biradicalssa density functional and *ab initio* study," J. Phys. Chem. A **110**, 12267–12275 (2006).

[66]A. Akimov, A. Masitov, D. Korchagin, S. Chapyshev, E. Misochko, and A. Savitsky, "W-band EPR studies of high-spin nitrenes with large spin-orbit contribution to zero-field splitting," J. Chem. Phys. **143**, 084313 (2015).

Supplementary Material
Two Competing Acceptors: Electronic Structure of PNDITBT Probed by Time-Resolved Electron Paramagnetic Resonance Spectroscopy

Clemens Matt,[1] Katja Stry,[1] Rukiya Matsidik,[2, a)] Michael Sommer,[3] and Till Biskup[1, b)]
[1)]*Institut für Physikalische Chemie, Albert-Ludwigs-Universität Freiburg,*
Albertstraße 21, 79104 Freiburg, Germany
[2)]*Institut für Makromolekulare Chemie, Albert-Ludwigs-Universität Freiburg,*
Stefan-Meier-Straße 31, 79104 Freiburg, Germany
[3)]*Polymerchemie, Institut für Chemie, Technische Universität Chemnitz,*
Straße der Nationen 62, 09111 Chemnitz, Germany

I. SYNTHESIS OF PNDITBT

A. Materials

All chemicals were obtained from Sigma Aldrich and used without further treatment unless otherwise stated. Pd_2dba_3 was obtained from Sigma Aldrich in 97 % purity and was used as received. Monomer $NDIBr_2$ with 2-decyltetradecyl side chains[1] and TBT[2] were made according to previously reported methods.

B. Synthesis

The polymer PNDITBT was synthesized according to a previously reported method[3]. To a dry vial containing a stirr bar, $NDIBr_2$ (164.60 mg, 0.15 mmol), TBT (45.06 mg, 0.15 mmol), K_2CO_3 (62.19 mg, 0.45 mmol), and pivalic acid (15.32 mg, 0.15 mmol) were carefully weighed, followed by adding 1.5 mL degassed mesitylene under a N_2 atmosphere and the whole was stirred for about two minutes at RT in order to fully dissolve the monomers. Then Pd_2dba_3 (1.37 mg, 0.0015 mmol) was added under nitrogen. The vial was sealed and placed into a preheated oil bath and stirred for 20 h at 120 °C. After cooling to RT, the gelated material was dissolved in chlorobenzene (CB) and precipitated into 400 ml methanol, filtered and purified via Soxhlet extraction with acetone, ethyl acetate, hexanes (in all above solvents the extracted solution is colorless), and chloroform (until colorlessness of the extracted solution). The polymer was finally collected with CB and filtered through a silica gel plug. The solvent was removed under vacuum using rotary evaporation and dried under high-vcuum overnight to give 172 mg PNDITBT in 93 % yield. PNDITBT is almost exclusively terminated by TBT units which allows for the reliable determination of the number average degree of polymerization $DP_{n,\mathrm{NMR}} = 29$ (see Fig. 1). This leads to an absolute number average molecular weight $M_{n,\mathrm{NMR}}$ = 36 kg/mol.

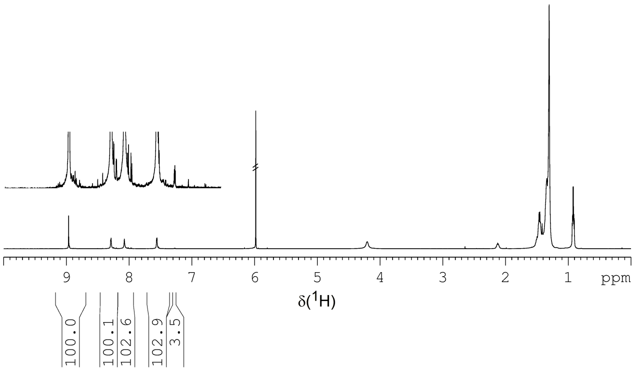

FIG. 1. ^{1}H-NMR spectra of the polymer PNDITBT at 393 K in $C_2D_2Cl_4$.

II. EPR INSTRUMENTATION

TREPR spectroscopy[4] with a time resolution of up to 10 ns allows for real-time observation, *e.g.*, of short-lived radical-pair and triplet states generated by pulsed laser excitation. In contrast to conventional continuous-wave EPR spectroscopy, which usually involves magnetic-field modulation to improve the signal-to-noise ratio, TREPR is recorded in a high-bandwidth direct-detection mode, so as not to constrain the time resolution of the experiment. Consequently, positive and negative signal amplitudes in TREPR correspond to enhanced absorptive (A) and emissive (E) electron-spin polarisations of the EPR transitions, respectively.

All TREPR experiments were performed at 80 K using a commercial EPR spectrometer (Bruker ESP380E) in conjunction with a Bruker microwave bridge (ER 046 MRT) equipped with a low-noise high-bandwidth video amplifier. The sample was placed in a synthetic-quartz (Suprasil) sample tube (3 mm inner diameter) and irradiated in a dielectric-ring resonator (Bruker ER 4118X-MD5), which was immersed in a helium gas-flow cryostat (Oxford CF-935) cooled with liquid nitrogen. The temperature was regulated to ±0.1 K by a temperature controller (Oxford ITC-503). The time resolution of the experimental setup was in the 10 ns range. A microwave

---

[a)] Current address: Emergent Molecular Function Research Team, RIKEN Center for Emergent Matter Science, 2-1 Hirosawa, Wako 351-0198, Saitama, Japan

[b)] Electronic mail: till.biskup@uni-saarland.de; Current address: Physikalische Chemie und Didaktik der Chemie, Universität des Saarlandes, Campus B2 2, 66123 Saarbrücken, Germany.

frequency counter (Hewlett-Packard HP 5352B) was used to monitor the microwave frequency.

Optical excitation at the respective wavelengths was carried out with an optical parametric oscillator (OPO) system (Opta BBO-355-vis/IR) pumped by an Nd:YAG laser (Spectra Physics, Quanta Ray GCR 190-10) with a pulse width of approximately 6 ns, and a pulse energy of 1 mJ. The repetition rate of the laser was set to 10 Hz. A transient recorder (LeCroy 9354A) with a digitizing rate of 2 ns/11 bit was used to acquire the time-dependent EPR signal. To eliminate the background signal induced by the laser entering the EPR cavity, TREPR signals were accumulated at off-resonance magnetic-field positions (background) and subtracted from those recorded on-resonance. This background signal is completely independent in its shape from both, laser wavelength and magnetic field, and normally long-lived compared to the detected spin-polarised EPR signal. Background subtraction was performed directly in the transient recorder and a background signal repeatedly recorded after each tenth time trace of the experimental data.

Further experimental parameters (except where explicity given) are as follows: Microwave frequency, 9.700 GHz, microwave power: 2 mW (20 dB attenuation, source power 200 mW), frequency-mixer detection, video amplifier set to 42 dB amplification and 25 MHz bandwidth, 1000 averages per point.

III. TREPR SPECTRA OF TRIPLET STATES

As TREPR spectra of spin-polarised triplet states of organic molecules recorded at X-band frequencies and magnetic fields are normally dominated by the zero-field splitting (ZFS) interaction, the Hamilton operator used to describe the system reduces dramatically. The only contributions that need to be taken into account are the Hamilton operator for the Zeeman interaction, $\mathscr{H}_{\mathrm{EZ}}$, and the one for the ZFS interaction, $\mathscr{H}_{\mathrm{ZFS}}$:

$$\mathscr{H} = \mathscr{H}_{\mathrm{EZ}} + \mathscr{H}_{\mathrm{ZFS}} = \boldsymbol{g}\mu_{\mathrm{B}}\boldsymbol{SB} + \boldsymbol{SDS}. \tag{1}$$

All other contributions can be considered as small perturbations that can be accounted for using (inhomogeneous) line broadening.

The $\boldsymbol{D}$ tensor in its principal axis system is given to

$$\boldsymbol{D} = \begin{pmatrix} -\frac{1}{3}D+E & 0 & 0 \\ 0 & -\frac{1}{3}D-E & 0 \\ 0 & 0 & \frac{2}{3}D \end{pmatrix} \tag{2}$$

where D and E are the zero-field-splitting parameters that can be directly read out from the experimental spectra (cf. Fig. 2). Note that D and E are defined such in the simulation routine used that the relation $|E| \leq |D|/3$ always holds.

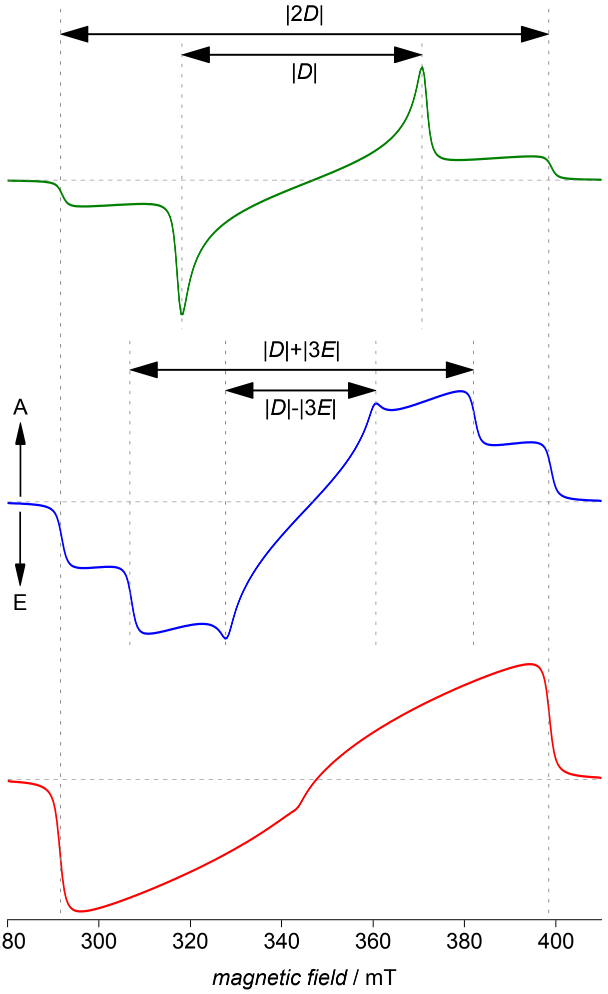

FIG. 2. Characteristics of TREPR spectra of (photo-generated) triplet states. Three characteristic situations for the ratio of the two parameters D and E of the ZFS tensor are depicted here: the fully axial case (top, green), an intermediate case (blue, centre) and a fully rhombic case (red, bottom). Spectra were calculated using EasySpin[5]. The zero-field populations $p_{1,2,3}$ of the three triplet sublevels are far from thermal equilibrium, due to optical excitation and the inherent anisotropy of the intersystem crossing processes. Therefore, signals consist of both, absorptive (A) and emissive (E) contributions.

IV. SPECTRAL SIMULATIONS OF TREPR SPECTRA OF TRIPLET STATES

All simulations of triplet spectra have been performed using the EasySpin software package[5] available for MATLAB® (MathWorks), and here the routine `pepper`. Parameters included were the $\boldsymbol{g}$ and $\boldsymbol{D}$ tensor and the triplet sublevel populations (in zero field). Line broadening (Γ) was included using a combination of Lorentzian (Γ_{L}) and Gaussian (Γ_{G}) lines. For all simulations, the $\boldsymbol{g}$ tensor was assumed to be isotropic, with $g_{\mathrm{iso}} = 2.002$. This left the parameters D and E of the zero-field splitting tensor $\boldsymbol{D}$, the populations p_1, p_2, and p_3, and the two line widths Γ_{L} and Γ_{G} as the only free parameters that were adjusted.

Fitting the spectral simulations to the experimental data was done using the `TSim` program developed by D. Meyer.[6] that internally relies on the routine `lsqcurvefit` from the MATLAB® Optimization Toolbox™ using the trust-region-reflective least squares algorithm.

The nonlinear least-square solver finds the m coefficients $\boldsymbol{a}$ that solve the problem

$$\min_{\boldsymbol{a}} \sum_i (f(x_i;\boldsymbol{a}) - y_i)^2 \tag{3}$$

with y_i being the measured data and $f(x_i;\boldsymbol{a})$ the fitting function $f : \mathbb{R}^m \rightarrow \mathbb{R}^n$ with the same size n as the measured data y_i

Error estimation of the fitting parameters was carried out by using the Jacobian matrix $\boldsymbol{J}$. J_{ij} is the partial derivative of the fitting function $f(x_i;\boldsymbol{a})$ with respect to a_j at the solution a_0.

$$J_{ij}(\boldsymbol{a}_0) := \left(\frac{\partial f(x_i;\boldsymbol{a})}{\partial a_j}(\boldsymbol{a}_0) \right)_{i=1\ldots n, j=1\ldots m} \tag{4}$$

$$\boldsymbol{J}(\boldsymbol{a}_0) = \begin{pmatrix} \frac{\partial f(x_1;\boldsymbol{a})}{\partial a_1}(\boldsymbol{a}_0) & \ldots & \frac{\partial f(x_1;\boldsymbol{a})}{\partial a_m}(\boldsymbol{a}_0) \\ \ldots & & \\ \frac{\partial f(x_n;\boldsymbol{a})}{\partial a_1}(\boldsymbol{a}_0) & \ldots & \frac{\partial f(x_n;\boldsymbol{a})}{\partial a_m}(\boldsymbol{a}_0) \end{pmatrix} \tag{5}$$

The variances of the coefficients a_j are given by the diagonal elements of the covariance matrix, $\boldsymbol{C}$, i.e. $\sigma^2_{a_j} = C_{jj}$, where $\boldsymbol{C}$ is the inverse of the matrix $\boldsymbol{H}$, variously referred to as the curvature or Hessian matrix.

The Hessian matrix was approximated by a series expansion, which is terminated after the first rank:

$$H_{jk} = \frac{1}{2} \frac{\partial^2 \chi^2(\boldsymbol{a})}{\partial a_j \partial a_k} \approx \sum_{i=1}^{n} \frac{1}{\sigma_i^2} \frac{\partial f(x_i;\boldsymbol{a})}{\partial a_j} \frac{\partial f(x_i;\boldsymbol{a})}{\partial a_k}$$

Hence the Jacobian matrix can be used to approximate the Hessian if σ_i^2 is chosen to be equal for all points,

$$\boldsymbol{H} \approx \frac{1}{\sigma_i^2} \boldsymbol{J}^{\mathrm{T}} \cdot \boldsymbol{J}. \tag{6}$$

To speed up calculation time for the matrix product $\boldsymbol{J}^{\mathrm{T}} \cdot \boldsymbol{J}$, an economy-size QR decomposition of $\boldsymbol{J}$ was carried out, reducing the dimension of $\boldsymbol{R}$ to the size of $\boldsymbol{a}$:

$$\boldsymbol{J} = \boldsymbol{Q} \cdot \boldsymbol{R}. \tag{7}$$

In the following matrix multiplication, $\boldsymbol{Q}$ vanishes by multiplication with $\boldsymbol{Q}^{\mathrm{T}}$:

$$(\boldsymbol{J}^{\mathrm{T}} \cdot \boldsymbol{J})^{-1} = (\boldsymbol{R}^{\mathrm{T}} \cdot \boldsymbol{R})^{-1} = \boldsymbol{R}^{-1} \cdot (\boldsymbol{R}^{\mathrm{T}})^{-1} = \boldsymbol{R}^{-1} \cdot (\boldsymbol{R}^{-1})^{\mathrm{T}} \tag{8}$$

In MATLAB®, this implementation leads to high computational speed and only minor numerical errors. The corresponding code would be as follows:

```
[~,R] = qr(jacobian,0);
```

The diagonal elements of the approximated $\boldsymbol{H}^{-1}$ can easily be calculated by element-wise squaring followed by summation over the rows of $\boldsymbol{R}$. Since σ_i^2 is chosen to be equal for all points, the errors for the fit parameters are given by:

```
stdDev = sqrt(variance * sum(inv(R)
    .^2,2));
```

The fitting algorithm `lsqcurvefit` can optionally return the residuals as additional output argument, here termed `residuals`. Hence the variance of the residuals obtained as

```
variance = var(residuals);
```

was used as σ^2 for all points.

[1] V. Senkovskyy, R. Tkachov, H. Komber, M. Sommer, M. Heuken, B. Voit, W. T. S. Huck, V. Kataev, A. Petr, and A. Kiriy, "Chain-growth polymerization of unusual anion-radical monomers based on naphthalene diimide: A new route to well-defined n-type conjugated copolymers," J. Am. Chem. Soc. **133**, 19966–19979 (2011).

[2] R. Matsidik, J. Martin, S. Schmidt, J. Obermayer, F. Lombeck, F. Nübling, H. Komber, D. Fazzi, and M. Sommer, "C–H arylation of unsubstituted furan and thiophene with acceptor bromides: Access to donor–acceptor–donor-type building blocks for organic electronics," J. Org. Chem. **50**, 980–987 (2015).

[3] R. Matsidik, H. Komber, and M. Sommer, "Rational use of aromatic solvents for direct arylation polycondensation: C–H reactivity versus solvent quality," ACS Macro Lett. **4**, 1346–1350 (2015).

[4] T. Biskup, "Structure–function relationship of organic semiconductors: Detailed insights from time-resolved EPR spectroscopy," Front. Chem. **7**, 10 (2019).

[5] S. Stoll and A. Schweiger, "EasySpin, a comprehensive software package for spectral simulation and analysis in EPR," J. Magn. Reson. **178**, 42–55 (2006).

[6] D. L. Meyer, F. Lombeck, S. Huettner, M. Sommer, and T. Biskup, "Direct $S_0 \rightarrow T$ excitation of a conjugated polymer repeat unit: unusual spin-forbidden transitions probed by time-resolved electron paramagnetic resonance spectroscopy," J. Phys. Chem. Letters **8**, 1677–1682 (2017).

6. Complete list of publications and contributions to conferences

Publications

1) Clemens Matt, Deborah L. Meyer, Florian Lombeck, Michael Sommer and Till Biskup.

   TBT Entirely Dominates the Electronic Structure of the Conjugated Copolymer PCDTBT: Insights from Time-Resolved Electron Paramagnetic Resonance Spectroscopy.

   Macromolecules, 51 (2018), pp. 4341–4349 (DOI: 10.1021/acs.macromol.8b00791)

2) Clemens Matt, Florian Lombeck, Michael Sommer and Till Biskup.

   Impact of Side Chains of Conjugated Polymers on Electronic Structure: A Case Study.

   Polymers, 11 (2019), pp. 870 (DOI: 10.3390/polym11050870)

3) Clemens Matt, Deborah L. Meyer, Florian Lombeck, Michael Sommer and Till Biskup.

   Different routes towards triplet states in organic semiconductors: direct $S_0 \rightarrow T$ excitation probed by time-resolved EPR spectroscopy.

   Molecular Physics, 117 (2019), pp. 2645–2653 (DOI: 10.1080/00268976.2018.1523479)

4) Kerstin Serrer, Clemens Matt, Monja Sokolov, Sylwia Kacprzak, Erik Schleicher and Stefan Weber.

   Application of commercially available fluorophores as triplet spin probes in EPR spectroscopy. *Molecular Physics*, 117 (2019), pp. 2688–2699 (DOI: 10.1080/00268976.2019.1608379)

5) Deborah L. Meyer, Noah Schmidt-Meinzer, Clemens Matt, Stephan Rein, Florian Lombeck, Michael Sommer and Till Biskup.

   Side-Chain Engineering of Conjugated Polymers: Distinguishing Its Impact on Film Morphology and Electronic Structure.

   J. Phys. Chem. C, 123 (2019), pp. 20071–20083 (DOI: 10.1021/acs.jpcc.9b02835)

6) Clemens Matt, Katja Stry, Rukiya Matsidik, Michael Sommer and Till Biskup.

   Two competing acceptors: Electronic structure of PNDITBT probed by time-resolved electron paramagnetic resonance spectroscopy.

   J. Chem. Phys., 151 (2019), pp. 234901 (DOI: 10.1063/1.5128469)

7) Dongyi Liu, Ahmed M. El-Zohry, Maria Taddei, Clemens Matt, Laura Bussotti, Zhijia Wang, Jianzhang Zhao, Omar F. Mohammed, Mariangela Di Donato, and Stefan Weber.

   Long-Lived Charge-Transfer State Induced by Spin-Orbit Charge Transfer Intersystem Crossing (SOCT-ISC) in a Compact Spiro Electron Donor/Acceptor Dyad.

   Angew. Chem. Int. Ed, 59 (2020), pp. 11591–11599 (DOI: 10.1002/anie.202003560)

8) Muhammad Imran, Ahmed M. El-Zohry, Clemens Matt, Maria Taddei, Sandra Doria, Laura Bussotti, Paolo Foggi, Jianzhang Zhao, Mariangela Di Donato, Omar F. Mohammed and Stefan Weber.

   Intersystem crossingviacharge recombination in a perylene–naphthalimide compact electrondonor/acceptor dyad.

   J. Mater. Chem. C, 8 (2020), pp. 8305–8313 (DOI: 10.1039/d0tc00017e)

9) Clemens Matt, Rukiya Matsidik, Mirjam Schröder Michael Sommer and Till Biskup.

   Identifying the "true" repeat unit of a copolymer using time-resolved electron paramagnetic resonance spectroscopy: a case study involving PNDIT2, NDI-T2 and T-NDI-T.

   J. Phys. Chem. Lett., submitted

10) Mirjam Schröder, Daniel Rauber, Clemens Matt, Christopher W. M. Kay.

    Pentacene in 1,3,5-tri(1-naphtyl)benzene: A novel standard for transient EPR spectroscopy at room temperature.

    Appl. Magn. Reson., submitted

Conferences

1) **Participation:** A discussion meeting Soft matter science in the upper Rhine valley: Research for the future, Schluchsee Germany, 2019

2) **Poster:** Clemens Matt, Deborah L. Meyer, Florian Lombeck, Michael Sommer and Till Biskup, Electronic structure of conjugated polymers: from building blocks to polymers, Doctoral students' day, Saarbrücken Germany, 2019

3) **Talk:** Clemens Matt, Exploring the triplet state of organic semiconductors via time-resolved EPR (trEPR) spectroscopy and DFT calculations, XIIth Workshop on Modern Methods in Quantum Chemistry, Mariapfarr Austria, 2020

7. Appendix

7.1. Identifying the “true” repeat unit of a copolymer using time-resolved electron paramagnetic resonance spectroscopy: a case study involving PNDIT2, NDI-T2 and T-NDI-T

Clemens Matt, Rukiya Matsidik, Mirjam Schröder, Michael Sommer and Till Biskup:

Contributions of all authors:

Clemens Matt: data aquisition (DFT and TREPR), data analysis, main contributions to manuscript and manuscript review

Rukiya Matsidik: sample synthesis and manuscript review

Mirjam Schröder: manuscript review

Michael Sommer: conception and study design and manuscript review

Till Biskup: conception and design of study, data acquisition (TREPR and UV-VIS), data analysis, contribution to the manuscript and manuscript review

The following is the latest version of the not yet accepted manuscript.

Identifying the "true" repeat unit of a copolymer using time-resolved electron paramagnetic resonance spectroscopy: a case study involving PNDIT2, NDI-T2 and T-NDI-T

Clemens Matt,[†,‖] Rukiya Matsidik,[‡,¶] Deborah L. Meyer,[†] Mirjam Schröder,[§] Michael Sommer,[¶] and Till Biskup[*,†,‖]

†*Institut für Physikalische Chemie, Albert-Ludwigs-Universität Freiburg, Albertstraße 21, 79104 Freiburg, Germany*

‡*Institut für Makromolekulare Chemie, Albert-Ludwigs-Universität Freiburg, Stefan-Meier-Straße 31, 79104 Freiburg, Germany*

¶*Lehrstuhl Polymerchemie, Technische Universität Chemnitz, Straße der Nationen 62, 09111 Chemnitz, Germany*

§*Physikalische Chemie, Universität des Saarlandes, Campus B2 2, 66123 Saarbrücken, Germany*

‖*Current Address: Physikalische Chemie, Universität des Saarlandes, Campus B2 2, 66123 Saarbrücken, Germany*

E-mail: till.biskup@uni-saarland.de

Phone: +49 (0)681 3022741. Fax: +49 (0)681 3024759

Abstract

Semiconducting polymers promise to revolutionise the way electronic devices can be built and deployed for a vast array of applications ranging from light-energy conversion to sensors to thermoelectric generators. Conjugated push-pull copolymers consisting of alternating donor and acceptor moieties are at the heart of these applications, due to the large tunability of their electronic structure. Hence, knowing the repeat unit of these materials is essential for a detailed understanding of the structure–function relationship of conjugated polymers used in organic electronics applications. Therefore, spectroscopic tools providing the necessary molecular resolution that allows to discriminate between different building blocks and to decide which one actually resembles the electronic structure of the polymer are of utmost importance. Time-resolved electron paramagnetic resonance (TREPR) spectroscopy is both, perfectly suited for this task and clearly superior to optical spectroscopy, particularly when supported by quantum-chemical calculations. This is due to its molecular resolution and unique capability of using light-induced triplet states to probe the electronic structure as well as the impact of the local environment. Here, we demonstrate the power of this approach for the polymer PNDIT2 (poly[*N*,*N'*-bis(2-octyldodecyl)-naphthalene-1,4,5,8-bis(dicarboximide)-2,6-diyl]-*alt*-5,5'-(2,2'-bithiophene)) revealing NDI-T2 unambiguously as the "true" repeat unit of the polymer, while the alternative building block T-NDI-T has a markedly different electronic structure. These results are of high importance for the rational design of conjugated polymers for organic electronics applications.

Graphical TOC Entry

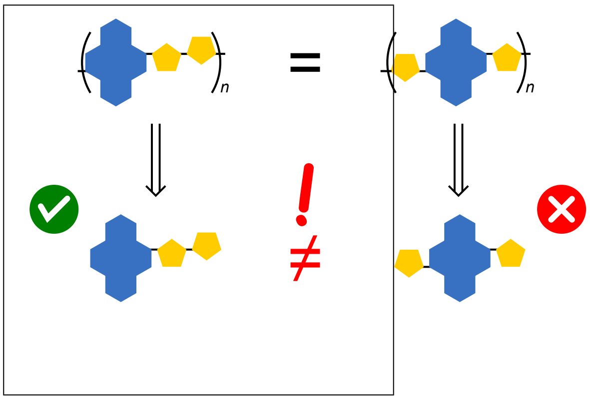

Keywords

conjugated push-pull copolymers, repeat unit, building block, electronic structure, triplet states, electron paramagnetic resonance

Introduction

Ever since the discovery of conducting polymers[1,2] that consecutively led to awarding the Nobel prize in chemistry to Alan J. Heeger, Alan G. MacDiarmid and Hideki Shirakawa in 2000 have these materials inspired the imagination of physicists, chemists, and engineers alike. (Semi-)conducting polymers not only allow to address fundamental questions of physics and chemistry of soft matter, but open the doors to an entirely new class of devices,[3] combining the power of tremendously miniaturised electronic circuits with the flexibility and ease of processing of polymeric materials. While in the first decades, mostly homopolymers have been investigated, more recently, push-pull copolymers consisting of alternating donor and acceptor moieties are increasingly important. They offer much better tunability of their electronic structure, i.e. their HOMO or LUMO level, ultimately leading to better efficiency compared to homopolymers for many applications.[4–6] However, this comes at the prize of a much more complicated electronic structure, and it is not necessarily obvious from the chemical structure which is the "true" repeat unit of such a polymer. Knowing the repeat unit is essential for characterising and understanding the electronic structure and hence the parameters determining efficiency of these materials. Identifying the repeat unit requires a combined approach of spectroscopic methods with sufficient resolution to discriminate between different possible candidates, synthetic chemistry providing the different structures, and comparison with the polymer. Here we demonstrate the power of this approach for the polymer poly[*N*,*N'*-bis(2-octyldodecyl)-naphthalene-1,4,5,8-bis(dicarboximide)-2,6-diyl]-*alt*-5,5'-(2,2'-bithiophene) (PNDIT2) and two possible repeat units, namely T-NDI-T and NDI-T2 (cf. Fig. 1), using time-resolved EPR spectroscopy and quantum-chemical calculations. The clearly superior molecular resolution of TREPR spectroscopy compared to optical methods proves crucial and allows for unequivocally identifying the actual repeat unit.

PNDIT2 is a prominent example of naphthalenediimide (NDI) based polymers[7] predominantly used as acceptor materials[8,9] or n-type semiconductors[10] in organic electronics. It is renowned for its excellent electron mobility[11–17] and consists of alternating units of NDI and thiophenes (T) which themselves act as electron acceptors (A) and donors (D), respectively. The interaction of these units determines the electronic structure of the polymer, hence a detailed characterisation and understanding is of utmost importance for guiding the targeted design of new materials. In organic solids, the electronic structure is dominated by the single molecule, in this case the polymer chain, and not by their ensemble like in their inorganic counterparts[18]. Further, if excited states such as Frenkel excitons[19] are considered, the region to focus on is reduced to the chromophore[18,20]. The size of the chromophore unit can vary for co-polymers with alternating donor and acceptor moieties, and often, it spans over about a single repeat unit, as shown for PCDTBT[21,22] and PNDIT2[12]. Identifying the chromophore unit of a semiconducting polymer is a necessary prerequisite for detailed spectroscopic and theoretical investigations. Computational methods are intrinsically restricted to small fragments of a polymer chain due to limited resources. Furthermore, focussing on fragments of increasing length has been proven useful for a detailed understanding of the complex electronic structure of a push–pull copolymer.[12,21–23] This separates contributions of donor–acceptor interactions from other effects originating in the polymer morphology that greatly complicate the spectral analysis.

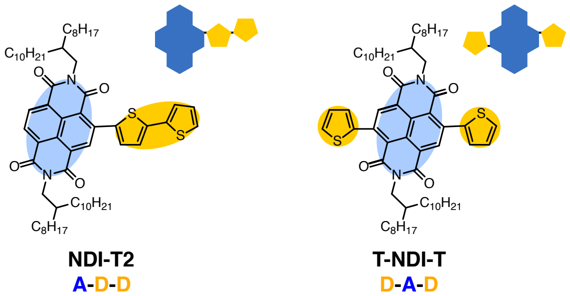

Figure 1: Chemical structures of NDI-T2 and T-NDI-T. The molecules each consist of one naphthalenediimide (NDI) and two thiophene units (T), respectively. Whereas the NDI moiety acts as an electron acceptor (A), the T units act as donors (D). The pictograms shown in the top right corner of each of the structures are used hereafter for simplicity.

In case of the polymer PNDIT2, two potential repeat units are possible: T-NDI-T and NDI-T2 as presented in Fig. 1. While upon polymerisation both units result in the same polymer, the molecules as such are two distinct chromophores with tremendously different electronic structure. This immediately raises the question which one reflects the electronic structure of the polymer PNDIT2. Steady-state optical spectroscopy is of no help here, as it lacks the resolution necessary to reveal the details of the electronic structure. Therefore, time-resolved electron paramagnetic resonance (TREPR) spectroscopy[24–26] complemented by quantum-chemical calculations was employed on both small molecules and compared with the results previously obtained for the polymer[12] to address this question. Due to its molecular resolution, EPR spectroscopy is superior here to optical spectroscopy suffering from broad, overlapping and often unstructured lines. Light-induced triplet states probed by TREPR spectroscopy have been shown to be particularly sensitive to the local molecular environment, both in terms of morphology[11,27,28] and electronic structure[12,22,23,29]. Therefore, TREPR spectroscopy in conjunction with quantum-chemical calculations is the method of choice for analysing the electronic structure of both potential repeat units of PNDIT2 with molecular resolution, and for answering the question which of them is the actual repeat unit of the polymer.

Results

For a first overview, steady-state absorption spectra in the UV/visible region were recorded for both potential repeat units of PNDIT2 (cf. Fig. 2). Both show an absorption band in the visible region which can be ascribed to a charge-transfer (CT) band[12]. The CT band of NDI-T2 is red-shifted and broader compared to that of T-NDI-T, hinting at a larger delocalisation of the singlet exciton in the former molecule. The absorption bands in the near-UV with the two characteristic features at 357 and 377 nm are associated to a π–π* transition of the NDI moiety[30] and more pronounced in case of T-NDI-T. As in other studies of push–pull copolymers[12,21,22], the intensity of the π–π* transition is larger than that of the CT band. This effect is more prominent for NDI-T2. Absorption spectra of the polymer are qualitatively identical, with a broad CT band in the visible wavelength range, red-shifted as expected compared to both potential building blocks, and a sharp π–π* transition in the near UV region[12]. Simply comparing the spectra shown in Fig. 2 with the one of the polymer does not allow to conclude which molecule is the true repeat unit of PNDIT2 in terms of the electronic structure of its chromophore, and the differences in delocalisation provide no hint in this regard, as T-NDI-T and NDI-T2 are identical in length. Therefore, we used TREPR spectroscopy known for its high molecular resolution to investigate the light-induced triplet states of both molecules and compared the result with those obtained previously for the polymer[11,12].

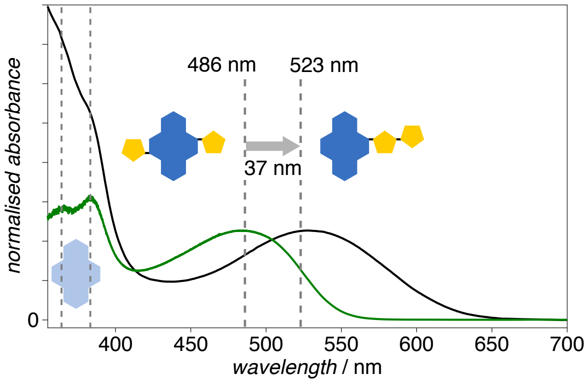

Figure 2: Absorption spectra of T-NDI-T and NDI-T2 in 1-CN. The prominent absorption band in the visible range of the spectrum centred at about 486 and 523 nm, respectively, is attributed to a charge-transfer (CT) between donor and acceptor moieties. The band in the near-UV region is attributed to a π–π* transition of the NDI moiety. For comparison, both spectra are normalised on the same CT band maximum. The vertical dotted lines in the visible range represent the excitation wavelengths used for TREPR spectroscopy (486 and 523 nm, cf. Fig. 3). Those at 357 and 377 nm mark the transitions attributed to the NDI moiety.

TREPR spectra of the light-induced triplet states of T-NDI-T and NDI-T2 are shown in Fig. 3, together with the spectrum obtained previously for the polymer[11,12]. Both exhibit the typical characteristics of light-induced triplet states[24] and can be unequivocally assigned to a single triplet species each. The spectral shape is entirely dominated by the zero-field splitting (ZFS) interaction arising from the dipolar coupling between the spins of both unpaired electrons[31]. The most important parameter in the Hamiltonian describing this interaction is the traceless ZFS tensor $\boldsymbol{D}$ characterised by the two parameters D and E. The former is proportional to r^{-3} with r being the distance between both unpaired electrons[31] and can therefore be related to the delocalisation length of the triplet exciton. The parameter E describes the rhombicity of the ZFS tensor. A vanishing E value leads to a axial system with D_x equal to D_y, whereas large E value give rise to a rhombic system. The ratio $\frac{E}{D}$ is hence a measure for the rhombicity and can not surpass the value of $\frac{1}{3}$ by definition. The rhombicity has proven to be a sensitive probe for the molecular environment of the triplet exciton, including backbone planarity and aggregation effects[11,22–24,32]. Both parameters can be extracted from the experimental data by fitting spectral simulations. Comparing the spectra recorded for both potential repeat units with those previously reported for the polymer[11,12] reveal the similarity between the spectra of NDI-T2 and PNDIT2, hinting at a similar electronic structure, while the spectrum for T-NDI-T is clearly different from the spectra of both, NDI-T2 and polymer (cf. Fig. 3).

Table 1: Comparison of the simulation parameters of the triplet spectra of PNDIT2 and some of its fragments. The simulation parameters for the polymer PNDIT2 ($n = 13$) as well as the fragments NDI and T2-NDI-T2 are reproduced from Ref.[12]. The same trend already obvious from Fig. 3 can be seen in the simulation parameters: While the spectral shape and hence simulation parameters for NDI-T2 clearly resemble those of the polymer PNDIT2, the alternative building block T-NDI-T has a distinct electronic structure clearly different from the polymer. λ_{ex} (in nm) is the excitation wavelength used, corresponding to the maximum of the CT-band, D and E are the ZFS parameters (in MHz), Γ_{L} and Γ_{G} are the Lorentzian and Gaussian line widths (in mT) and $p_{1,2,3}$ are the populations of the triplet sublevels ordered from lowest to highest energy.

	λ_{ex}	$\lvert D\rvert$	$\lvert E\rvert$	$\lvert E\rvert/\lvert D\rvert$	Γ_{G}	Γ_{L}	$p_{1,2,3}$
T-NDI-T	486	1500 ± 0.8	500 ± 0.3	0.333	8.0 ± 0.3	3.0 ± 0.2	$0.00, 1.00, 0.00$
NDI-T2	523	1143 ± 2.0	308 ± 2.0	0.270	10.9 ± 0.6	6.5 ± 0.5	$0.00, 0.00, 1.00$
PNDIT2	622	1095 ± 4.3	226 ± 2.4	0.206	7.0 ± 0.8	2.1 ± 0.4	$0.00, 0.24, 0.76$
NDI	355	2073 ± 2.1	0	0.000	5.7 ± 0.3	2.8 ± 0.3	$0.00, 0.50, 0.50$
T2-NDI-T2	554	1010 ± 87.0	328 ± 84.9	0.325	11.4 ± 0.6	3.0 ± 0.6	$0.00, 0.59, 0.41$

For the spectra of both potential repeat units, simulations have been fitted to the experimental data. The simulation parameters are listed in Tab. 1, together with those for the

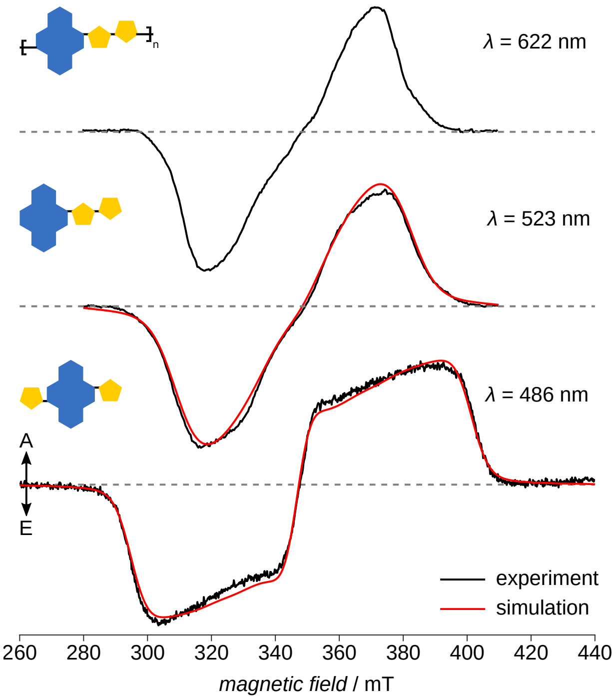

Figure 3: TREPR spectra of light-induced triplet states of T-NDI-T and NDI-T2 together with simulations (red lines) and the polymer PNDIT2. As TREPR spectroscopy uses a direct detection scheme, the spectra show emissive (E) and enhanced absorptive (A) signals directly. All samples were dissolved in 1-CN, flash-frozen and measured at 80 K with excitation at the maximum of their respective CT band. For simulation parameters, cf. Table 1 and for details of the fitting and simulations procedures, see the SI. Data for PNDIT2 were taken from Ref.[12].

polymer and other relevant building blocks. A larger D value is found for T-NDI-T, indicating a more localised triplet exciton compared to NDI-T2, in line with the results from optical spectroscopy (Fig. 2). Also a smaller rhombicity is found for the latter closer to that of the polymer, whereas T-NDI-T shows a fully rhombic spectrum. Large Gaussian line widths have been obtained for all simulations indicating the absence of aggregation in either of the compounds dissolved in 1-CN. Only one triplet sublevel of both potential repeat units is populated via inter-system crossing (ISC), p_2 for T-NDI-T and p_3 for NDI-T2, respectively, pointing towards different orbitals being involved in the ISC process. Comparing this to the situation in the polymer and the molecule T2-NDI-T2, respectively, provides further insight: While the triplet state populations of NDI-T2 and PNDIT2 are similar, with p_3 dominating, those of T-NDI-T resemble the situation in T2-NDI-T2, having the largest fraction on p_2. Taken together, both the rhombicity and the zero-field triplet sublevel populations of NDI-T2 are closer to the values obtained for the polymer than those of T-NDI-T.

To get further insight, density-functional theory (DFT) calculations of the singlet and triplet states and time-dependent DFT (TDDFT) calculations of the singlet ground state have been carried out for T-NDI-T, NDI-T2, as well as a polymer fragment. Different rotational conformers of the potential repeat units and the polymer fragment were geometry-optimised in their singlet ground state. For the polymer, a fragment of three monomers was used to represent the full molecule. Geometries and energy differences obtained for the singlet ground states are shown in Figs. S2 and S3. All geometries including the polymer fragment consist of flat NDI and thiophene moieties with substantial dihedral angles between adjacent units. Since further calculation of properties led to similar results for each conformer, only one conformer of each molecule was considered. The conformations chosen were those with the sulphur of the thiophenes pointing towards the oxygen of the NDIs, depicted in Fig. 4, consistent with the literature[12,17,33].

Single-point TDDFT[34] calculations allow to distinguish the orbitals involved in the electronic transition. The natural transition orbitals[35] (NTOs) of the holes and the particles for the first excited states are shown in Fig. 4, the corresponding excitation wavelengths are 524, 619 and 736 nm for T-NDI-T, NDI-T2 and the polymer fragment respectively. Compared with the experimentally obtained maxima of the CT band, all calculated excitations are red-shifted by several tens of nanometres, but still in the range of the CT band. While this overestimation of the B3LYP functional is known[36], range-separated hybrid functionals like CAM-B3LYP[37] or ωB97X[38] did not yield better results. The holes, describing the NTO of the remaining non-excited electron, are mainly located on the donors. The particles, describing the NTO of the excited electron, are localised on the acceptors as expected for a CT transition[21,36,39]. Upon closer inspection of the holes, small delocalisations over the NDI units can be seen, most prominent for T-NDI-T. Also the thiophene to the left side of

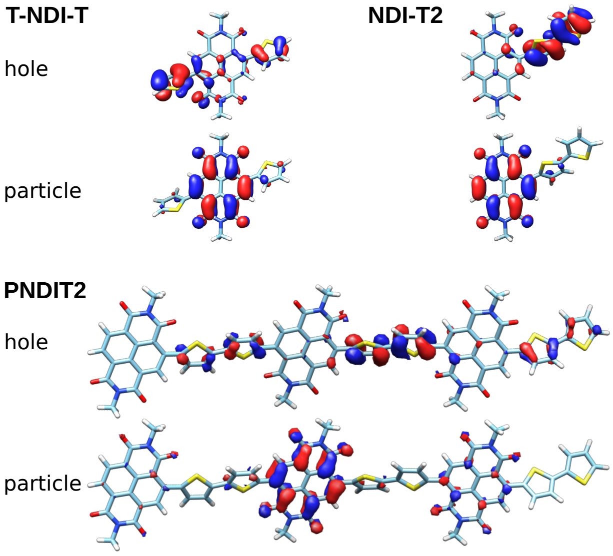

Figure 4: Natural transition orbitals (NTOs) of the hole-particle pairs of T-NDI-T, NDI-T2, and the polymer in their first excited singlet states. The B3LYP functional with the 6-31G** basis set was used. The corresponding eigenvalues λ denote the amount the two NTOs contribute to the transition. They are 0.9803 for T-NDI-T, 0.9892 for NDI-T2, and 0.9448 for the polymer. The NTOs are displayed for a threshold level of ±0.03, red denotes a positive and blue a negative sign.

T-NDI-T is contributing more than the one on the right. For NDI-T2 and the polymer, the two linked thiophenes seem to act as one donor moiety, with a large contribution to the hole and only a very small contribution to the particle.

To investigate the triplet states of the molecules, the same conformers as for the singlet state were considered. These conformers were geometry-optimised in the triplet state accordingly and spin-density distributions calculated afterwards. For both potential repeat units and the polymer fragment, the Mulliken spin density of the triplet states of each atom, except the hydrogens, and the percentage of spin density on each unit is shown as a histogram in Fig. 5. T-NDI-T exhibits a fairly symmetrical distribution with respect to the axis connecting both nitrogen atoms of the NDI moiety. The triplet exciton is mostly localised on the NDI moiety with 72% and the amount of spin density on each single atom reflects the previously mentioned symmetrical distribution. NDI-T2 on the other hand exhibits a balanced distribution of spin density over both acceptor 48% and donor 52%, with a localisation

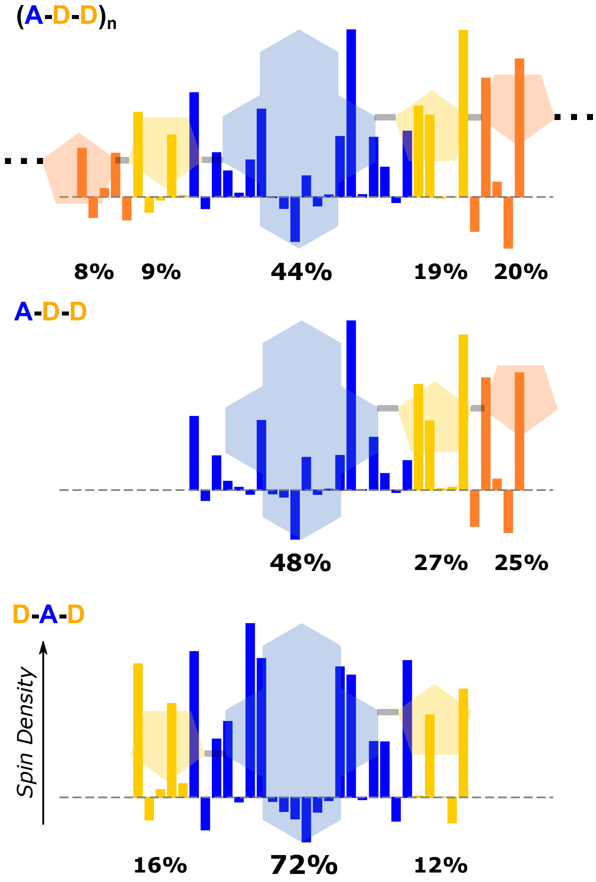

Figure 5: Mulliken spin density of both potential repeat units and the polymer. The atoms of the molecules have been labelled from left to right (for a detailed scheme, see Fig. S5). Geometries were optimised with the B3LYP functional and 6-31G** basis set. The numbers below the different units are the sum of the absolute values of the spin density localised on each of the moieties.

around the NDI-thiophene bond. Similar to other investigated polymers[22,23], delocalisation of the triplet in the polymer is mostly restricted to one acceptor and the neighbouring donors, but otherwise pretty similar to that of NDI-T2. The main difference between the polymer and NDI-T2 is the additional spin density on the second T2 unit adjacent to the NDI moiety, but with one T2 unit clearly favoured. For both, NDI-T2 and polymer, the spin density remaining on the NDI stays nearly the same (only 4% difference), while the symmetrical spin-density distribution observed for T-NDI-T (and T2-NDI-T2[12]) vanishes entirely. Taken together, quantum-chemical calculations are consistent with the TREPR-spectroscopic investigations pointing towards a great similarity between NDI-T2 and PNDIT2 revealing a clearly asymmetric electronic structure, contrastring with T-NDI-T and T2-NDI-T2 being symmetrical.

Discussion

Optical spectroscopy reveals differences in the delocalisation of the exciton of T-NDI-T and NDI-T2 that are consistent with the triplet exciton delocalisation probed by TREPR spectroscopy, but it is inconclusive with respect to revealing details of the electronic structure and its similarity to that of the polymer. TREPR spectroscopy, in contrast, provides the necessary molecular resolution and unequivocally reveals NDI-T2 to be the actual repeat unit of PNDIT2 in terms of its electronic structure, as obvious from comparing the TREPR spectra of T-NDI-T, NDI-T2, and the polymer PNDIT2 (Fig. 3). The simulation parameters reported in Tab. 1 confirm this result. The rhombicity and also the zero-field triplet sublevel populations of NDI-T2 are closer to those of the polymer than those of T-NDI-T. DFT calculations of the spin density lead to the same conclusion. The only 48 MHz smaller D value (approx. 5%) for the polymer, compared to NDI-T2, indicates that the triplet exciton is only slightly more delocalised. The same is reflected in the spin density distribution of the polymer, where 83% remain on the NDI-T2 fragment and 17% on the other neighbouring T2.

T-NDI-T shows a larger D value than NDI-T2 indicating a more localised triplet exciton, consistent with the strong localisation of 72% the spin density on the NDI moiety predicted by DFT calculations. Both results hint at NDI and T-NDI-T having a similar electronic structure. Comparing their TREPR spectra[12] reveals, however, clear differences: While NDI shows a larger D value than T-NDI-T, to be expected due to the smaller size, its spectrum is fully axial in stark contrast to the fully rhombic one of T-NDI-T. Also the zero-field triplet sublevel populations are different with p_2 and p_3 being populated equally for NDI, whereas only p_2 is populated for T-NDI-T (Tab. 1), pointing towards different orbitals involved in the ISC transition. NDI and T-NDI-T hence clearly show a markedly different electronic structure. A second molecule T-NDI-T should be compared to is the larger D-A-D system T2-NDI-T2[12]. The TREPR spectrum of the latter resembles that of T-NDI-T, particularly when comparing the rhombicity and triplet sublevel populations, leading to the same conclusion: the two building blocks considered here, T-NDI-T and NDI-T2, strongly differ from each other with respect to their electronic structures. This provides interesting hints for understanding the markedly different electronic structure of T2-NDI-T2 compared to PNDIT2 and all other fragments investigated previously:[12] The electronic structure of PNDIT2 is dominated by an intrinsically asymmetric chromophore, NDI-T2, with a single T2 unit predominantly acting as donor for one NDI acceptor unit.

Furthermore, the results of quantum-chemical calculations provide confirmation for the differences in exciton delocalisation between NDI-T2 and T-NDI-T. Delocalisation seems to be connected to the strength of the donor–acceptor interaction and hence CT character: the larger the CT character, the larger the delocalisation, as revealed by comparing the NTOs (Fig. 4). Additionally, the more localised singlet exciton on the acceptor moiety for T-NDI-T could explain the better resolved vibrational structure of the NDI unit in this molecule. Similarly, the localised spin density of the triplet exciton of T-NDI-T represents a weak donor–acceptor interaction and the broad homogeneous distribution of NDI-T2 a strong one. This is in line with previous investigations of PCDTBT, another push–pull copolymer, with a strong localisation of the spin density on the dominant acceptor and donor units of the molecule[22]. Taken together, these results show a strong donor–acceptor interaction to be characterised by a homogeneous spin density distribution on donor and acceptor moieties. Furthermore, the consistency between optical and TREPR results proves the validity and relevance of the results obtained by investigating the triplet states for the overall electronic structure of the molecule and demonstrates TREPR spectroscopy to be superior to optical spectroscopy in this respect.

Conclusions

Knowing the repeat unit of a conjugated push-pull copolymer is essential for a detailed understanding of the structure–function relationship of, but not resticted to, conjugated polymers used in organic electronics applications. Hence, spectroscopic tools providing the necessary molecular resolution that allows to discriminate between different building blocks and to decide which one actually resembles the electronic structure of the polymer are of utmost importance. Here, we demonstrate TREPR spectroscopy to be perfectly suited for this task, due to its molecular resolution and unique capability of using light-induced triplet states to probe the electronic structure as well as the impact of the local environment, and to be clearly superior to steady-state optical spectroscopy. Once the actual repeat unit in terms of its electronic structure has been identified, it can serve as a model for the entire copolymer with alternating donor and acceptor moieties.[12,22,23] Our results for the polymer PNDIT2 and the two possible repeat units T-NDI-T and NDI-T2 reveal NDI-T2 unambiguously as the "true" repeat unit of the polymer in terms of its electronic structure. This is essential for getting insight into the structure–function relationship of the polymer. Furthermore, TREPR spectroscopy and accompanying quantum-chemical calculations reveal the asymmetry of the NDI-T2 moiety to dominate the electronic structure of the polymer, providing guidelines for the rational design of new and improved materials.

Materials and Methods

Synthesis

NDI-T2 and T-NDI-T were synthesised according to published procedures[40,41].

UV-VIS spectroscopy

NDI-T2 and T-NDI-T were dissolved in 1-chloronaphthalene (1-CN) with a concentration $c = 1.3$ mg/mL (NDI-T2) and $c = 1.0$ mg/mL (T-NDI-T), respectively. UV-VIS experiments were performed with commercially available spectrometers at room temperature. For details of the experimental setup see the SI.

TREPR spectroscopy

Samples were prepared identically to those of the optical experiments in terms of concentrations and filled into synthetic-quartz-glass tubes. TREPR experiments were carried out on frozen solutions at cryogenic temperatures (80 K). For better comparison with the previous experiments[12], samples were flash-frozen in liquid nitrogen to preserve the morphology in solution. Each sample was excited at the maximum of its charge transfer (CT) band with a pulse energy of 1 mJ, using an optical parametric oscillator (OPO) pumped by a Nd:YAG laser. The laser light was depolarised in order to prevent polarisation effects as PNDIT2 and its building blocks have been shown to be sensitive to remaining polarisation of the laser light used for excitation[42]. Spectral simulations have been fitted to the experimental data using the Tsim program[43] which builds upon the `pepper` routine of the EasySpin toolbox[44]. Further details of the experimental setup and parameters are given in the SI.

DFT calculations

All initial molecular geometries were created with Avogadro 1.2.0[45]. DFT calculations were carried out using the ORCA program package[46]. In a first step, the geometries of the singlet ground state and the triplet state were optimised using the B3LYP functional[47,48], 6-31G** basis set[49,50] and D3 dispersion correction[51]. Afterwards, linear response TDDFT calculations were performed on the optimised singlet geometries using the Tamm-Dancoff approximation[52] in conjunction with B3LYP/6-31G** as functional and basis set, respectively. The

Coulomb term was handled with the resolution of identity chain of spheres approximation (RIJCOSX)[53] to increase calculation speed. Geometries and spin density delocalisations of the triplet states of all considered rotamers are shown in Figs. S2–4. All figures showing molecular geometries and spin densities were created using UCSF Chimera 1.11.2.[54]

Acknowledgement

The authors thank the German Research Foundation (DFG, Grants GRK 1642 to C.M., R.M., and M.So., SO 1213/8-1 to R.M. and M.So., and BI 1249/3-1 to T.B.) for financial support, and S. Weber and C. Kay for providing EPR equipment.

Supporting Information Available

Details of experiments, simulations and the fitting procedure; different conformers in singlet ground state; spin-density distribution for the triplet states; atom labelling scheme for Fig. 5.

Author information

Corresponding author: Till Biskup, till.biskup@uni-saarland.de

The authors declare no competing financial interest.

References

(1) Chiang, C. K.; Fincher, C. R., Jr.; Park, Y. W.; Heeger, A. J.; Shirakawa, H.; Louis, E. J.; Gau, S. C.; MacDiarmid, A. G. Electrical conductivity in doped polyacetylene. *Phys. Rev. Lett.* **1977**, *39*, 1098–1101.

(2) Shirakawa, H.; Louis, E. J.; MacDiarmid, A. G.; Chiang, C. K.; Heeger, A. J. Syn-

thesis of electrically conducting organic polymers: halogen derivatives of polyacetylene, $(CH)_x$. *J. Chem. Soc. Chem. Commun.* **1977**, *1977*, 678–580.

(3) Heeger, A. J. Semiconducting and metallic polymers: the fourth generation of polymeric materials (Nobel lecture). *Angew. Chem. Int. Ed.* **2001**, *40*, 2591–2611.

(4) Cheng, Y.-J.; Yang, S.-H.; Hsu, C.-S. Synthesis of conjugated polymers for organic solar cell applications. *Chem. Rev.* **2009**, *109*, 5868–5923.

(5) Facchetti, A. Polymer donor–polymer acceptor (all-polymer) solar cells. *Mater. Today* **2013**, *16*, 123–132.

(6) Armin, A.; Li, W.; Sandberg, O. J.; Xiao, Z.; Ding, L.; Nelson, J.; Neher, D.; Vandewal, K.; Shoaee, S.; Wang, T. et al. A history and perspective of non-fullerene electron acceptors for organic solar cells. *Adv. Energy Mater.* **2021**, *11*, 20003570.

(7) Zhou, N.; Facchetti, A. Naphthalenediimide (NDI) polymers for all-polymer photovoltaics. *Mater. Today* **2018**, *21*, 377–390.

(8) Earmme, T.; Hwang, Y.-J.; Murari, N. M.; Subramaniyan, S.; Jenekhe, S. A. All-polymer solar cells with 3.3% efficiency based on naphthalene diimide-selenophene copolymer acceptor. *J. Am. Chem. Soc.* **2013**, *135*, 14960–14963.

(9) Sharma, S.; Kolhe, N. B.; Gupta, V.; Bharti, V.; Sharma, A.; Datt, R.; Chand, S.; Asha, S. K. Improved all-polymer solar cell performance of n-type naphthalene diimide–bithiophene P(NDI2OD-T2) copolymer by incorporation of perylene diimide as coacceptor. *Macromolecules* **2016**, *49*, 8113–8125.

(10) Schmidt, S. B.; Hönig, M.; Shin, Y.; Cassinelli, M.; Perinot, A.; Caironi, M.; Jiao, X.; McNeill, C. R.; Fazzi, D.; Biskup, T. et al. Radical anion yield, stability, and electrical conductivity of naphthalene diimide copolymers n-doped with tertiary amines. *ACS Appl. Polym. Mater.* **2020**, *2*, 1954–1963.

(11) Meyer, D. L.; Matsidik, R.; Huettner, S.; Sommer, M.; Biskup, T. Solvent-mediated aggregate formation of PNDIT2: Decreasing the available conformational subspace by introducing locally highly ordered domains. *Phys. Chem. Chem. Phys.* **2018**, *20*, 2716–2723.

(12) Meyer, D. L.; Matsidik, R.; Sommer, M.; Biskup, T. Electronic structure trumps planarity: Unexpected narrow exciton delocalisation in PNDIT2 revealed by time-resolved EPR spectroscopy. *Adv. Electron. Mater.* **2018**, *4*, 1700384.

(13) Steyrleuthner, R.; Schubert, M.; Howard, I.; Klaumünzer, B.; Schilling, K.; Chen, Z.; Saalfrank, P.; Laquai, F.; Facchetti, A.; Neher, D. Aggregation in a high-mobility n-type low-bandgap copolymer with implications on semicrystalline morphology. *J. Am. Chem. Soc.* **2012**, *134*, 18303–18317.

(14) Brinkmann, M.; Gonthier, E.; Bogen, S.; Tremel, K.; Ludwigs, S.; Hufnagel, M.; Sommer, M. Segregated *versus* mixed interchain stacking in highly oriented films of naphthalene diimide bithiophene copolymers. *ACS Nano* **2012**, *6*, 10319–10326.

(15) Tremel, K.; Fischer, F. S. U.; Kayunkid, N.; Di Pietro, R.; Tkachov, R.; Kiriy, A.; Neher, D.; Ludwigs, S.; Brinkmann, M. Charge transport anisotropy in highly oriented thin films of the acceptor polymer P(NDI2OD-T2). *Adv. Energy Mater.* **2014**, *4*, 1301659.

(16) Giussani, E.; Brambilla, L.; Fazzi, D.; Sommer, M.; Kayunkid, N.; Brinkmann, M.; Castiglioni, C. Structural characterization of highly oriented naphthalene-diimide-bithiophene copolymer films via vibrational spectroscopy. *J. Phys. Chem. B* **2015**, *119*, 2062–2073.

(17) Caironi, M.; Bird, M.; Fazzi, D.; Chen, Z.; Di Pietro, R.; Newman, C.; Facchetti, A.; Sirringhaus, H. Very low degree of energetic disorder as the origin of high mobility in an *n*-channel polymer semiconductor. *Adv. Funct. Mater.* **2011**, *21*, 3371–3381.

(18) Schwoerer, M.; Wolf, H. C. *Organische Molekulare Festkörper*; WILEY-VCH: Weinheim, Germany, 2005.

(19) Frenkel, Y. On the transformation of light into heat in solids. I. *Phys. Rev.* **1931**, *37*, 17–44.

(20) Köhler, A.; Bässler, H. *Electronic Processes in Organic Semiconductors*; WILEY-VCH: Weinheim, Germany, 2015.

(21) Banerji, N.; Gagnon, E.; Morgantini, P.-Y.; Valouch, S.; Mohebbi, A. R.; Seo, J.-H.; Leclerc, M.; Heeger, A. J. Breaking down the problem: optical transitions, electronic structure, and photoconductivity in conjugated polymer PCDTBT and in its separate building blocks. *J. Phys. Chem. C* **2012**, *116*, 11456–11469.

(22) Matt, C.; Meyer, D. L.; Lombeck, F.; Sommer, M.; Biskup, T. TBT entirely dominates the electronic structure of the conjugated copolymer PCDTBT: Insights from time-resolved electron paramagnetic resonance spectroscopy. *Macromolecules* **2018**, *51*, 4341–4349.

(23) Matt, C.; Lombeck, F.; Sommer, M.; Biskup, T. Impact of side chains of conjugated polymers on electronic structure: A case study. *Polymers* **2019**, *11*, 870.

(24) Biskup, T. Structure–function relationship of organic semiconductors: Detailed insights from time-resolved EPR spectroscopy. *Front. Chem.* **2019**, *7*, 10.

(25) Weber, S. Transient EPR. *eMagRes* **2017**, *6*, 255–270.

(26) Forbes, M. D.; Jarocha, L. E.; Sim, S.; Tarasov, V. F. Time-resolved electron paramagnetic resonance spectroscopy: history, technique, and application to supramolecular and macromolecular chemistry. *Adv. Phys. Org. Chem.* **2014**, *47*, 1–83.

(27) Biskup, T.; Sommer, M.; Rein, S.; Meyer, D. L.; Kohlstädt, M.; Würfel, U.; Weber, S.

Ordering of PCDTBT revealed by time-resolved electron paramagnetic resonance spectroscopy of its triplet excitons. *Angew. Chem. Int. Ed.* **2015**, *54*, 7707–7710.

(28) Meyer, D. L.; Schmidt-Meinzer, N.; Matt, C.; Rein, S.; Lombeck, F.; Sommer, M.; Biskup, T. Side-chain engineering of conjugated polymers: Distinguishing its impact on film morphology and electronic structure. *J. Phys. Chem. C* **2019**, *123*, 20071–20083.

(29) Meyer, D. L.; Matsidik, R.; Fazzi, D.; Sommer, M.; Biskup, T. Probing exciton delocalization in organic semiconductors: Insight from time-resolved electron paramagnetic resonance and magnetophotoselection experiments. *J. Phys. Chem. Letters* **2018**, *9*, 7026–7031.

(30) Alp, S.; Şule Erten,; Karapire, C.; Köz, B.; Doroshenko, A. O.; Içli, S. Photoinduced energy–electron transfer studies with naphthalene diimides. *J. Photochem. Photobiol. A Chem.* **2000**, *135*, 103–110.

(31) Atherton, N. M. *Principles of Electron Spin Resonance*; Ellis Horwood Ltd.: Chichester, England, 1993.

(32) Matt, C.; Stry, K.; Matsidik, R.; Sommer, M.; Biskup, T. Two competing acceptors: Electronic structure of PNDITBT probed by time-resolved electron paramagnetic resonance spectroscopy. *J. Chem. Phys.* **2019**, *151*, 234901.

(33) Fazzi, D.; Caironi, M. Multi-length-scale relationships between the polymer molecular structure. *Phys. Chem. Chem. Phys.* **2015**, *17*, 8573–8590.

(34) Runge, E.; Gross, E. K. U. Density-functional theory for time-dependent systems. *Phys. Rev. Lett.* **1984**, *52*, 997–1000.

(35) Martin, R. L. Natural transition orbitals. *J. Chem. Phys.* **2003**, *118*, 4775.

(36) Pan, Y. Y.; Huanga, J.; Wanga, Z. M.; Zhangb, S. T.; Yua, D. W.; Yang, B.; Mac, Y. G. Accurate description of hybridized local and charge-transfer excited-state in donor–acceptor molecules using density functional theory. *RSC Adv.* **2016**, *6*, 108404–108410.

(37) Yanai, T.; Tew, D. P.; Handy, N. C. A new hybrid exchange–correlation functional using the Coulomb-attenuating method (CAM-B3LYP). *Chem. Phys. Lett.* **2004**, *393*, 51–57.

(38) Chai, J.-D.; Head-Gordon, M. Systematic optimization of long-range corrected hybrid density functionals. *J. Chem. Phys.* **2008**, *128*, 084106.

(39) Zhou, C.; Xiao, S.; Wang, M.; Jiang, W.; Liu, H.; Zhang, S.; Yang, B. Modulation of excited state property based on benzo[a, c]phenazine acceptor: three typical excited states and electroluminescence performance. *Front. Chem.* **2019**, *7*, 141.

(40) Matsidik, R.; Komber, H.; Luzio, A.; Caironi, M.; Sommer, M. Defect-free naphthalene diimide bithiophene copolymers with controlled molar mass and high performance via direct arylation polycondensation. *J. Am. Chem. Soc.* **2015**, *137*, 6705–6711.

(41) Matsidik, R.; Martin, J.; Schmidt, S.; Obermayer, J.; Lombeck, F.; Nübling, F.; Komber, H.; Fazzi, D.; Sommer, M. C–H arylation of unsubstituted furan and thiophene with acceptor bromides: Access to donor–acceptor–donor-type building blocks for organic electronics. *J. Org. Chem.* **2015**, *50*, 980–987.

(42) Meyer, D. ESR-spektroskopische Untersuchungen lichtinduzierter Zustände in Materialien mit Relevanz für die organische Elektronik. Morphologie, Delokalisation, Entstehungswege von Triplett-Zuständen. Ph.D. thesis, Albert-Ludwigs-Universität Freiburg, 2017.

(43) Meyer, D. L.; Lombeck, F.; Huettner, S.; Sommer, M.; Biskup, T. Direct $S_0 \to T$ excitation of a conjugated polymer repeat unit: unusual spin-forbidden transitions probed

by time-resolved electron paramagnetic resonance spectroscopy. *J. Phys. Chem. Letters* **2017**, *8*, 1677–1682.

(44) Stoll, S.; Schweiger, A. EasySpin, a comprehensive software package for spectral simulation and analysis in EPR. *J. Magn. Reson.* **2006**, *178*, 42–55.

(45) Hanwell, M. D.; Curtis, D. E.; Lonie, D. C.; Vandermeersch, T.; Zurek, E.; Hutchison, G. R. Avogadro: an advanced semantic chemical editor, visualization, and analysis platform. *J. Cheminformatics* **2012**, *4*, 17.

(46) Neese, F. The ORCA program package. *Wiley Interdiscip. Rev.-Comput. Mol. Sci.* **2012**, *2*, 73–78.

(47) Becke, A. D. Density-functional thermochemistry. III. The role of exact exchange. *J. Chem. Phys.* **1993**, *98*, 5648–5652.

(48) Lee, C.; Yang, W.; Parr, R. G. Development of the Colle-Salvetti correlation-energy formula into a functional of the electron density. *Phys. Rev. B* **1988**, *37*, 785–789.

(49) Petersson, G. A.; Bennett, A.; Tensfeldt, T. G.; Al-Laham, M. A.; Shirley, W. A.; Mantzaris, J. A complete basis set model chemistry. I. The total energies of closed-shell atoms and hydrides of the first-row elements. *J. Chem. Phys.* **1988**, *89*, 2193–2218.

(50) Petersson, G. A.; Al-Laham, M. A. A complete basis set model chemistry. II. Open-shell systems and the total energies of the first-row atoms. *J. Chem. Phys.* **1991**, *94*, 6081–6090.

(51) Grimme, S.; Antony, J.; Ehrlich, S.; Krieg, H. A consistent and accurate ab initioparametrization of density functionaldispersion correction (DFT-D) for the 94 elements H–Pu. *J. Chem. Phys.* **2010**, *132*, 154104.

(52) Grimme, S. A simplified Tamm-Dancoff density functional approach for the electronic excitation spectra of very large molecules. *J. Chem. Phys.* **2013**, *138*, 244104.

(53) Neese, F.; Wennmohs, F.; Hansen, A.; Becker, U. Efficient, approximate and parallel Hartree–Fock and hybrid DFT calculations. A 'chain-of-spheres' algorithm for the Hartree–Fock exchange. *Chem. Phys.* **2009**, *356*, 98–109.

(54) Pettersen, E. F.; Goddard, T. D.; Huang, C. C.; Couch, G. S.; Greenblatt, D. M.; Meng, E. C.; Ferrin, T. E. UCSF Chimera—A visualization system for exploratory research and analysis. *J. Comput. Chem.* **2004**, *25*, 1605–1612.

Identifying the “true” repeat unit of a copolymer using time-resolved electron paramagnetic resonance spectroscopy: a case study involving PNDIT2, NDI-T2 and T-NDI-T

— Supporting Information —

Clemens Matt,[a,b] Rukiya Matsidik,[c,d] Deborah L. Meyer,[a] Mirjam Schröder,[e]
Michael Sommer,[d] Till Biskup[a,b,*]

[a]Institut für Physikalische Chemie, Albert-Ludwigs-Universität Freiburg,
Albertstraße 21, 79104 Freiburg, Germany
[b]Current Address: Physikalische Chemie, Universität des Saarlandes,
Campus B2 2, 66123 Saarbrücken, Germany
[c]Institut für Makromolekulare Chemie, Albert-Ludwigs-Universität Freiburg,
Stefan-Meier-Straße 31, 79104 Freiburg, Germany
[d]Institut für Chemie, Polymerchemie, Technische Universität Chemnitz,
Straße der Nationen 62, 09111 Chemnitz, Germany
[e]Physikalische Chemie, Universität des Saarlandes,
Campus B2 2, 66123 Saarbrücken, Germany

Contents

---

[*] till.biskup@uni-saarland.de

Optical spectroscopy

Absorption spectra were recorded using commercial UV/vis spectrometers (Shimadzu UV2450 and Analytik Jena SPECORD 210 PLUS) in combination with the corresponding software (UV-Probe version 2.43 and WinASPECT PLUS version 4.2.0.0). Cuvettes with a path length of 1 mm for T-NDI-T and 10 mm for NDI-T2 were used.

EPR instrumentation

TREPR spectroscopy with a time resolution of up to 10 ns allows for real-time observation, *e.g.*, of short-lived radical-pair and triplet states generated by pulsed laser excitation.[1–3] In contrast to conventional continuous-wave EPR spectroscopy, which usually involves magnetic-field modulation to improve the signal-to-noise ratio, TREPR is recorded in a high-bandwidth direct-detection mode, so as not to constrain the time resolution of the experiment. Consequently, positive and negative signal amplitudes in TREPR correspond to enhanced absorptive (A) and emissive (E) electron-spin polarisations of the EPR transitions, respectively.

TREPR experiments were performed at 80 K using similar experimental setups described below.

Setup 1 (NDI-T2)

The TREPR spectrum of NDI-T2 was recorded using a commercial EPR spectrometer (Bruker ESP380E) in conjunction with a Bruker microwave bridge (ER 046 MRT) equipped with a low-noise high-bandwidth video amplifier. The sample was placed in a synthetic-quartz (QSIL Ilmasil) sample tube (3 mm inner diameter) and irradiated in a dielectric-ring resonator (Bruker ER 4118X-MD5), which was immersed in a helium gas-flow cryostat (Oxford CF-935) cooled with liquid nitrogen. The temperature was regulated to ±0.1 K by a temperature controller (Oxford ITC-503). The time resolution of the experimental setup was in the 10 ns range. A microwave frequency counter (Hewlett-Packard HP 5352B) was used to monitor the microwave frequency.

Optical excitation at the respective wavelengths was carried out with an optical parametric oscillator (OPO) system (Opta BBO-355-vis/IR) pumped by an Nd:YAG laser (Spectra Physics, Quanta Ray GCR 190-10) with a pulse width of approximately 6 ns, and a pulse energy of 1 mJ. The repetition rate of the laser was set to 10 Hz. The residual polarisation of the laser beam is rather substantial, a quartz-wedge achromatic depolariser (Thorlabs DPU-25-A) was used.

A transient recorder (LeCroy 9354A) with a digitizing rate of 2 ns/11 bit was used to acquire the time-dependent EPR signal. To eliminate the background signal induced by the laser entering the EPR cavity, TREPR signals were accumulated at off-resonance magnetic-field positions (background) and subtracted from those recorded on-resonance. This background signal is completely independent in its shape from both, laser wavelength and magnetic field, and normally long-lived compared to the detected spin-polarised EPR signal. Background subtraction was performed directly in the transient recorder and a background signal repeatedly recorded after each tenth time trace of the experimental data.

Further experimental parameters are as follows: Microwave frequency, 9.700 GHz, microwave power: 2 mW (20 dB attenuation, source power 200 mW), frequency-mixer detection, video amplifier set to 42 dB amplification and 25 MHz bandwidth, 800 averages per point.

Setup 2 (T-NDI-T)

The TREPR spectrum of T-NDI-T was recorded using a commercial EPR spectrometer (Bruker EMX) in conjunction with a Bruker microwave bridge (Bruker EMX premiumX). The sample was placed in a synthetic-quartz (QSIL Ilmasil) sample tube (3 mm inner diameter) and irradiated in a dielectric-ring resonator (Bruker ER 4118X-MD5), which was immersed in a closed-cycle cryostat (Cryogenic CF VTC) cooled with helium. The temperature was regulated to ±0.1 K by a temperature controller (Lake Shore 350). The time resolution of the experimental setup was in the 300 ns range. The built-in microwave frequency counter was used to monitor the microwave frequency.

Optical excitation at the respective wavelengths was carried out with OPO system (GWU primoScan/BB/120-INDI) pumped by an Nd:YAG laser (Spectra-Physics Quanta-Ray INDI PS 51/52) with a pulse width of approximately 6 ns, and a pulse energy of 1 mJ. The repetition rate of the laser was set to 20 Hz. A transient recorder (Teledyne LeCroy HDO9204) with a digitizing rate of 2 ns/9 bit was used to acquire the time-dependent EPR signal. To eliminate the background signal induced by the laser entering the EPR cavity, TREPR signals were accumulated at off-resonance magnetic-field positions (background) and subtracted from those recorded on-resonance. This background signal is completely independent in its shape from both, laser wavelength and magnetic field, and normally long-lived compared to the detected spin-polarised EPR signal.

TREPR spectra of triplet states

As TREPR spectra of spin-polarised triplet states of organic molecules recorded at X-band frequencies and magnetic fields are normally dominated by the zero-field splitting (ZFS) interaction, the hamilton operator used to describe the system reduces dramatically. The only contributions that need to be taken into account are the Hamilton operator for the Zeeman interaction, $\mathcal{H}_{\mathrm{EZ}}$, and the one for the ZFS interaction, $\mathcal{H}_{\mathrm{ZFS}}$:

$$\mathcal{H} = \mathcal{H}_{\mathrm{EZ}} + \mathcal{H}_{\mathrm{ZFS}} = \mathbf{g}\mu_{\mathrm{B}}\vec{S}\vec{B} + \vec{S}\mathbf{D}\vec{S}. \tag{S1}$$

All other contributions can be considered as small perturbations that can be accounted for using (inhomogeneous) line broadening.

The **D** tensor in its principal axis system is given to

$$\mathbf{D} = \begin{pmatrix} -\frac{1}{3}D + E & 0 & 0 \\ 0 & -\frac{1}{3}D - E & 0 \\ 0 & 0 & \frac{2}{3}D \end{pmatrix} \tag{S2}$$

where D and E are the zero-field-splitting parameters that can be directly read out from the experimental spectra (cf. Fig. S1). Note that D and E are defined such in the simulation routine used that the relation $|E| \leq |D|/3$ always holds. D can be described by:

$$D = \frac{3D_z}{2} = \frac{3}{4}\left(\frac{\mu_0}{4\pi}\right)(g_e\beta_e)^2 \left\langle \frac{r^2 - 3z^2}{r^5} \right\rangle , \tag{S3}$$

with the distance between both unpaired electrons r. It can be correlated with the delolcalization length of the triplet exciton. A large value would mean a strong dipole-dipole interaction with a small distance between the electrons. The opposite is true for a small value of D.

Spectral simulations of TREPR spectra of triplet states

Processing and analysis of TREPR data was carried out using software written in MATLAB®. Preprocessing was carried out using the `trepr` toolbox.[2] All simulations of triplet spectra were performed using the `pepper` routine from the EasySpin software package [4]. Fitting was carried out using the `TSim` program developed by D. Meyer.[5] Parameters included were the **g** and **D** tensor and the triplet sublevel populations (in zero field). Line broadening (Γ) was included using a combination of Lorentzian (Γ_L) and Gaussian (Γ_G) lines. For all simulations, the **g** tensor was assumed to be isotropic, with $g_\mathrm{iso} = 2.002$, and the population p_1 was set to zero. This left the parameters D and E of the zero-field splitting tensor **D**, the populations p_2 and p_3, and the two line widths Γ_L and Γ_G as the only free parameters that were adjusted. In the case of NDI the parameters E of the zero-field splitting tensor **D** was set two zero and was not adjusted by a fitting process.

Fitting of the spectral simulations to the experimental data was performed by using the routine `lsqcurvefit` from the MATLAB® Optimization Toolbox™ and here using the trust-region-reflective least squares algorithm.

The nonlinear least-square solver finds the m coefficients $\vec{a}$ that solve the problem

$$\min_{\vec{a}} \sum_i (f(x_i;\vec{a}) - y_i)^2 \tag{S4}$$

with y_i being the measured data and $f(x_i;\vec{a})$ the fitting function $f : \mathbb{R}^m \rightarrow \mathbb{R}^n$ with the same size n as the measured data y_i

Error estimation of the fitting parameters was carried out by using the Jacobian matrix $\mathbf{J}$. J_{ij}

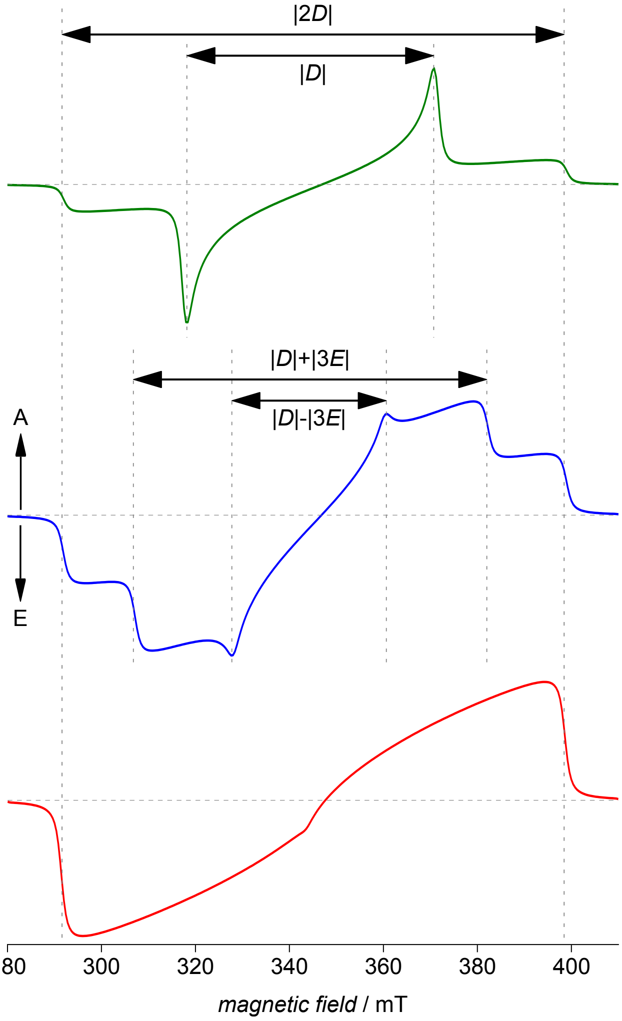

Figure S1: Characteristics of TREPR spectra of (photo-generated) triplet states. Three characteristic situations for the ratio of the two parameters D and E of the ZFS tensor are depicted here: the fully axial case (top, green), an intermediate case (blue, centre) and a fully rhombic case (red, bottom). Spectra were calculated using EasySpin. [2] The zero-field populations $p_{1,2,3}$ of the three triplet sublevels are far from thermal equilibrium, due to optical excitation and the inherent anisotropy of the intersystem crossing processes. Therefore, signals consist of both, absorptive (A) and emissive (E) contributions.

is the partial derivative of the fitting function $f(x_i;\vec{a})$ with respect to a_j at the solution a_0.

$$J_{ij}(\vec{a}_0) := \left(\frac{\partial f(x_i;\vec{a})}{\partial a_j}(\vec{a}_0)\right)_{i=1\ldots n, j=1\ldots m} \tag{S5}$$

$$\mathbf{J}(\vec{a}_0) = \begin{pmatrix} \frac{\partial f(x_1;\vec{a})}{\partial a_1}(\vec{a}_0) & \ldots & \frac{\partial f(x_1;\vec{a})}{\partial a_m}(\vec{a}_0) \\ \ldots & & \\ \frac{\partial f(x_n;\vec{a})}{\partial a_1}(\vec{a}_0) & \ldots & \frac{\partial f(x_n;\vec{a})}{\partial a_m}(\vec{a}_0) \end{pmatrix} \tag{S6}$$

The variances of the coefficients a_j are given by the diagonal elements of the covariance matrix, $\mathbf{C}$, i.e. $\sigma^2_{a_j} = C_{jj}$, where $\mathbf{C}$ is the inverse of the matrix $\mathbf{H}$, variously referred to as the curvature or Hessian matrix.

The Hessian matrix was approximated by a series expansion, which is terminated after the first rank:

$$H_{jk} = \frac{1}{2}\frac{\partial^2\chi^2(\vec{a})}{\partial a_j \partial a_k} \approx \sum_{i=1}^{n} \frac{1}{\sigma_i^2}\frac{\partial f(x_i;\vec{a})}{\partial a_j}\,\frac{\partial f(x_i;\vec{a})}{\partial a_k}$$

Hence the Jacobian matrix can be used to approximate the Hessian if σ_i^2 is chosen to be equal for all points,

$$\mathbf{H} \approx \frac{1}{\sigma_i^2}\,\mathbf{J}^T \cdot \mathbf{J}. \tag{S7}$$

To speed up calculation time for the matrix product $\mathbf{J}^T \cdot \mathbf{J}$, an economy-size QR decomposition of $\mathbf{J}$ was carried out, reducing the dimension of $\mathbf{R}$ to the size of $\vec{a}$:

$$\mathbf{J} = \mathbf{Q} \cdot \mathbf{R}. \tag{S8}$$

In the following matrix multiplication, $\mathbf{Q}$ vanishes by multiplication with $\mathbf{Q}^T$:

$$(\mathbf{J}^T \cdot \mathbf{J})^{-1} = (\mathbf{R}^T \cdot \mathbf{R})^{-1} = \mathbf{R}^{-1} \cdot (\mathbf{R}^T)^{-1} = \mathbf{R}^{-1} \cdot (\mathbf{R}^{-1})^T \tag{S9}$$

In MATLAB®, this implementation leads to high computational speed and only minor numerical errors. The corresponding code would be as follows:

```
[~,R] = qr(jacobian,0);
```

The diagonal elements of the approximated $\mathbf{H}^{-1}$ can easily be calculated by element-wise squaring followed by summation over the rows of $\mathbf{R}$. Since σ_i^2 is chosen to be equal for all points, the errors for the fit parameters are given by:

```
stdDev = sqrt(variance * sum(inv(R).^2,2));
```

The fitting algorithm `lsqcurvefit` can optionally return the residuals as additional output argument, here termed `residuals`. Hence the variance of the residuals obtained as

```
variance = var(residuals);
```

was used as σ^2 for all points.

DFT calculations

For T-NDI-T, NDI-T2, and the PNDIT2 fragment, different conformers have been considered that differ from each other in the orientation of the thiophene sulfur atom towards the O atom of the NDI unit. The results of the geometry optimisation of the singlet states, together with the energy differences, are depicted in Figs. S2 and S3. In each case, the conformer labelled “C1” with the lowest energy has been used for further calculations. For detailed numbers, see Tab. S1.

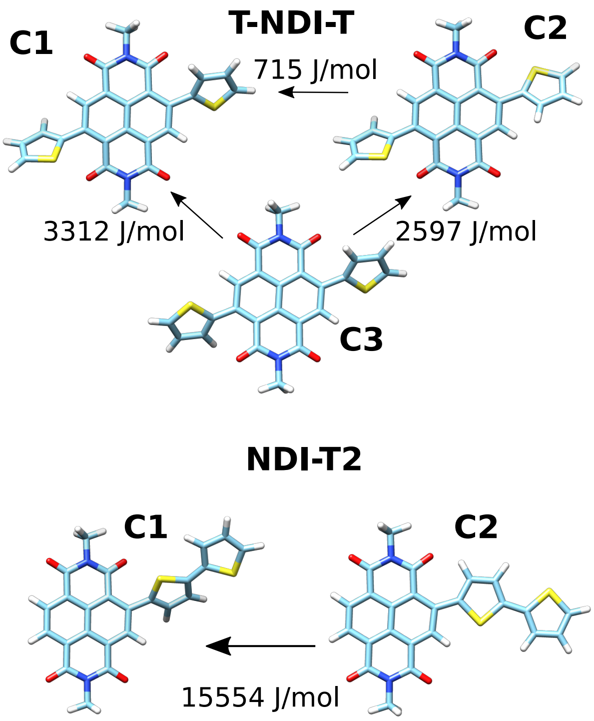

Figure S2: Different geometry-optimised conformers of the singlet ground state of NDI-T2 and T-NDI-T with their energy differences. The arrows point towards the conformation with lower energy. All geometries are optimised with the B3LYP functional and a 6-31G** basis set, together with a D3 dispersion correction.

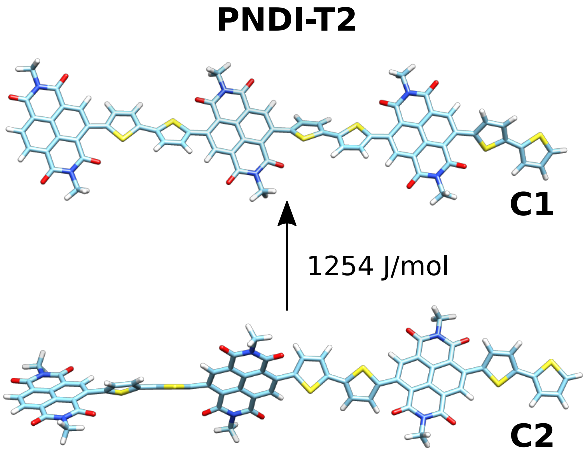

Figure S3: Different geometry-optimised conformers of the singlet ground state PNDI-T2 with their energy difference. The arrow points towards the conformation with lower energy. All geometries are optimised with the B3LYP functional and a 6-31G** basis set, together with a D3 dispersion correction.

Table S1: Energies of the singlet ground states of the different conformers. The energy differences ΔE were compared with the energy at room temperature $R \cdot T \sim 3300$ J/mol

Molecule	Conformer	Energy (Hartee)	ΔConformers	ΔE (J/mol)
T-NDI-T	C1	−2129.065658519785	C2-C1	715
T-NDI-T	C2	−2129.064669405509	C3-C1	3312
T-NDI-T	C3	−2129.064396998741	C3-C2	2596
NDI-T2	C1	−2129.078349874169	C2-C1	15554
NDI-T2	C2	−2129.072425356022		
PNDI-T2	C1	−6384.857367446895	C2-C1	1254
PNDI-T2	C2	−6384.856889756274		

Similarly, spin densities for the triplet states of the different conformers have been calculated and are depicted in Fig. S4. Again, in the main text only the conformers with the lowest energy, labelled “C1”, are considered.

The labelling of the atoms used to plot the histogram of the Mulliken spin density in the main text is shown in Fig. S5.

References

[1] Malcolm D.E. Forbes, Lauren E. Jarocha, SooYeon Sim, and Valery F. Tarasov. Time-resolved electron paramagnetic resonance spectroscopy: history, technique, and application to supramolecular and macromolecular chemistry. *Adv. Phys. Org. Chem.*, 47:1–83, 2014.

[2] Till Biskup. Time-resolved EPR of radical pair intermediates in cryptochromes. *Mol. Phys.*, 111:3698–3703, 2013.

[3] Till Biskup. Structure–function relationship of organic semiconductors: Detailed insights from time-resolved EPR spectroscopy. *Front. Chem.*, 7:10, 2019.

[4] Stefan Stoll and Arthur Schweiger. EasySpin, a comprehensive software package for spectral simulation and analysis in EPR. *J. Magn. Reson.*, 178:42–55, 2006.

[5] Deborah L. Meyer, Florian Lombeck, Sven Huettner, Michael Sommer, and Till Biskup. Direct $S_0 \rightarrow T$ excitation of a conjugated polymer repeat unit: unusual spin-forbidden transitions probed by time-resolved electron paramagnetic resonance spectroscopy. *J. Phys. Chem. Letters*, 8:1677–1682, 2017.

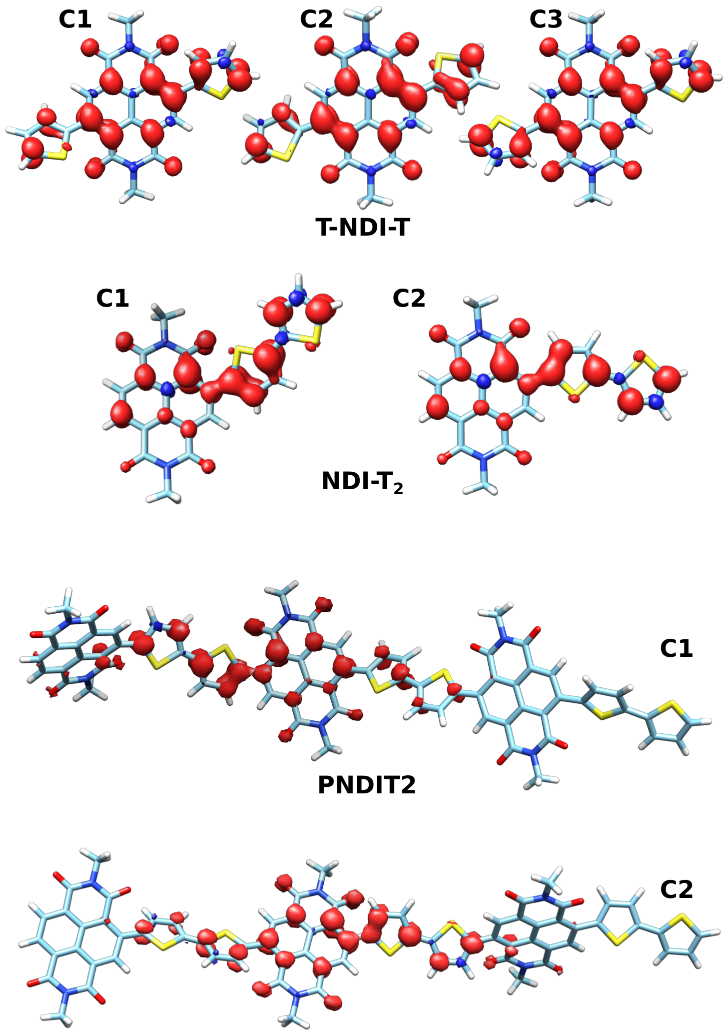

Figure S4: Calculated spin-density distribution for the two potential repeat units and the polymer fragment and their conformers. Geometries have been optimised for the triplet state with the B3LYP functional and 6-31G** basis set. Spin densities have been displayed for a threshold level of ±0.003, red denotes positive and blue negative spin density.

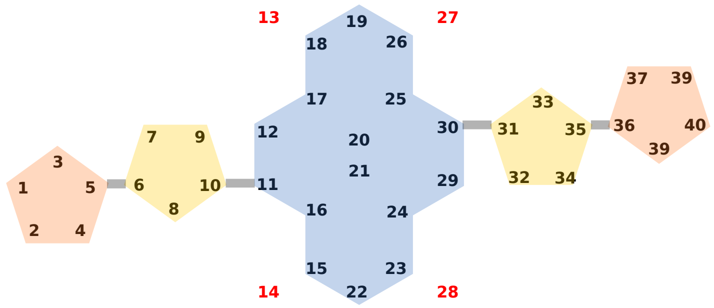

Figure S5: Atom labelling scheme for Fig 5 of the main text. The atoms were labelled from left to right, with T-NDI-T ranging from position 6 to 35 and NDI-T2 from 11 to 40.

Bibliography

[1] Hideo Akamatu, Hiroo Inokuchi and Yoshio Matsunaga. Electrical conductivity of the perylene–bromine complex. *Nature* 173 (1954), pp. 168–169.

[2] David Keams and Melvin Calvin. Photovoltaic Effect and Photoconductivity in Laminated Organic Systems. *Journal of Chemical Physics* 29 (1958), pp. 950–951.

[3] Martin Pope, Hartmut Paul Kallmann and Peter Magnante. Electroluminescence in Organic Crystals. *Journal of Chemical Physics* 38 (1963), pp. 2042–2043.

[4] Xuezhou Peng, Gilles Horowitz, Denis Fichou and Francis Garnier. All-organic thin-film transistors made of alpha-sexithienyl semiconducting and various polymeric insulating layers. *Applied Physics Letters* 57 (1990), pp. 2013–2015.

[5] Masahiro Hiramoto and Yusuke Shinmura. "Organic Solar Cells". In: *Springer Handbook of Electronic and Photonic Materials*. Basel, Switzerland: Springer International Publishing, 2017, pp. 1329–1338.

[6] Richard H. Friend et al. Electroluminescence in conjugated polymers. *Nature* 397 (1999), pp. 121–128.

[7] Jiri Janata and Mira Josowicz. Conducting polymers in electronic chemical sensors. *Nature Materials* 2 (2002), pp. 19–24.

[8] Howard E. Katz and Jia Huang. Thin-film organic electronic devices. *Annual Review of Materials Research* 39 (2009), pp. 71–92.

[9] Abraham Nitzan and Mark A. Ratner. Electron Transport in Molecular Wire Junctions. *Science* 300 (2003), pp. 1384–1389.

[10] Alan J. Heeger. Semiconducting and metallic polymers: the fourth generation of polymeric materials (Nobel lecture). *Angewandte Chemie International Edition English* 40 (2001), pp. 2591–2611.

[11] Alan G. MacDiarmid. "Synthetic metals": a novel role for organic polymers (Nobel lecture). *Angewandte Chemie International Edition English* 40 (2001), pp. 2581–2590.

[12] Hideki Shirakawa. The discovery of polyacetylene film: the dawning of an era of conducting polymers (Nobel lecture). *Angewandte Chemie International Edition English* 40 (2001), pp. 2574–2580.

[13] *Nobel Prize in Chemistry 2000*. 27.11.2020. URL: `https://www.nobelprize.org/prizes/chemistry/2000/summary/`.

[14] Nicolas Blouin, Alexandre Michaud and Mario Leclerc. A low-bandgap poly(2,7-carbazole) derivative for use in high-performance solar cells. *Advanced Materials* 19 (2007), pp. 2295–2300.

[15] Nicolas Blouin, Alexandre Michaud, David Gendron, Salem Wakim, Emily Blair, Rodica Neagu-Plesu, Michel Belletête, Gilles Durocher, Ye Tao and Mario Leclerc. Toward a rational design of poly(2,7-carbazole) derivatives for solar cells. *Journal of the American Chemical Society* 130 (2008), pp. 732–742.

[16] He Yan, Zhihua Chen, Yan Zheng, Christopher Newman, Jordan R. Quinn, Florian Dötz, Marcel Kastler and Antonio Facchetti. A high-mobility electron-transporting polymer for printed transistors. *Nature* 457 (2009), pp. 679–686.

[17] Beatriz M. Illescas and Nazario Martín. [60]Fullerene-based electron acceptors. *Comptes Rendus Chimie* 9 (2006), pp. 1038–1050.

[18] Tao Liu and Alessandro Troisi. What makes fullerene acceptors special as electron acceptors in organic solar cells and how to replace them. *Advanced Materials* 25 (2013), pp. 1038–1041.

[19] Antonio Facchetti. Polymer donor–polymer acceptor (all-polymer) solar cells. *Materials Today* 16 (2013), pp. 123–132.

[20] Baobing Fan, Lei Ying, Zhenfeng Wang, Baitian He, Xiao-Fang Jiang, Fei Huang and Yong Cao. Optimisation of processing solvent and molecular weight for the production of green-solvent-processed all-polymer solar cells with a power conversion efficiency over 9%. *Energy & Environmental Science* 10 (2017), pp. 1243–1251.

[21] Sung Heum Park, Anshuman Roy, Serge Beaupré, Shinuk Cho, Nelson Coates, Ji Sun Moon, Daniel Moses, Mario Leclerc, Kwanghee Lee and Alan J. Heeger. Bulk heterojunction solar cells with internal quantum efficiency approaching 100%. *Nature Photonics* 3 (2009), pp. 297–302.

[22] Florian Lombeck, Dawei Di, Le Yang, Lorenzo Meraldi, Stavros Athanasopoulos, Dan Credgington, Michael Sommer and Richard H. Friend. PCDTBT: From polymer photovoltaics to light-emitting diodes by side-chain-controlled luminescence. *Macromolecules* 49 (2016), pp. 9382–9387.

[23] Jay Lewis. Material challenge for flexible organic devices. *Materials Today* 9 (2006), pp. 38–45.

[24] Stergios Logothetidis. Flexible organic electronic devices: Materials, process and applications. *Materials Science and Engineering B—Solid State Materials for Advanced Technology* 152 (2008), pp. 96–104.

[25] John A. Rogers, Takao Someya and Yonggang Huang. Materials and mechanics for stretchable electronics. *Science* 327 (2010), pp. 1603–1607.

[26] Hakan Usta and Antonio Facchetti. “Organic Semiconductors for Transparent Electronics”. In: *Flexible Carbon-based Electronics*. Wiley-VCH, 2018. Chap. 2, pp. 13–49.

[27] Stephen R. Forrest. The path to ubiquitious and low-cost organic electronic appliances on plastic. *Nature* 428 (2004), pp. 911–918.

[28] Magnus Berggren, Daniel Nilsson and Nathaniel D. Robinson. Organic materials for printed electronics. *Nature Materials* 6 (2007), pp. 3–5.

[29] Mihai Irimia-Vladu. “Green” electronics: biodegradable and biocompatible materials and devices for sustainable future. *Chemical Society Reviews* 43 (2014), pp. 588–610.

[30] Anna Köhler and Heinz Bässler. *Electronic Process in Organic Semiconductors.* First edition. Wiley-VCH, 2015.

[31] Stephen R. Forrest. Excitons and the lifetime of organic semiconductor devices. *Philosophical Transactions of the Royal Society A — Mathematical, Physical and Engineering Sciences* 373 (2015), p. 20140320.

[32] Oleksandr V. Mikhneno, Paul W. M. Blom and Thuc-Quyen Nguyen. Exciton diffusion in organic semiconductors. *Energy & Environmental Science* 8 (2015), pp. 1867–1888.

[33] Heinz Bässler and Anna Köhler. Charge transport in organic semiconductors. *Topics in Current Chemistry* 312 (2012), pp. 1–66.

[34] Stavros Athanasopoulos, Emmanuelle Hennebicq, David Beljonne and Alison B. Walker. Trap Limited Exciton Transport in Conjugated Polymers. *Journal of Physical Chemistry C* 112 (2008), pp. 11532–11538.

[35] Till Biskup. Structure–Function Relationship of Organic Semiconductors: Detailed Insights From Time-Resolved EPR Spectroscopy. *Frontiers in Chemistry* 7 (2019), p. 10.

[36] Deborah L. Meyer, Rukiya Matsidik, Sven Huettner, Michael Sommer and Till Biskup. Solvent-mediated aggregate formation of PNDIT2: Decreasing the available conformational subspace by introducing locally highly ordered domains. *Physical Chemistry Chemical Physics* 20 (2018), pp. 2716–2723.

[37] Deborah L. Meyer, Florian Lombeck, Sven Huettner, Michael Sommer and Till Biskup. Direct $S_0 \rightarrow T$ excitation of a conjugated polymer repeat unit: unusual spin-forbidden transitions probed by time-resolved electron paramagnetic resonance spectroscopy. *Journal of Physical Chemistry Letters* 8 (2017), pp. 1677–1682.

[38] Deborah L. Meyer, Rukiya Matsidik, Michael Sommer and Till Biskup. Electronic structure trumps planarity: Unexpected narrow exciton delocalisation in PNDIT2 revealed by time-resolved EPR spectroscopy. *Advanced Electronic Materials* 4 (2018), p. 1700384.

[39] Till Biskup, Michael Sommer, Stephan Rein, Deborah L. Meyer, Markus Kohlstädt, Uli Würfel and Stefan Weber. Ordering of PCDTBT revealed by time-resolved electron paramagnetic resonance spectroscopy of its triplet excitons. *Angewandte Chemie International Edition English* 54 (2015), pp. 7707–7710.

[40] Natalie Banerji, Eric Gagnon, Pierre-Yves Morgantini, Sebastian Valouch, Ali Reza Mohebbi, Jung-Hwa Seo, Mario Leclerc and Alan J. Heeger. Breaking down the problem: optical transitions, electronic structure, and photoconductivity in conjugated polymer PCDTBT and in its separate building blocks. *Journal of Physical Chemistry C* 116 (2012), pp. 11456–11469.

[41] Deborah L. Meyer. “ESR-Spektroskopische Untersuchungen lichtinduzierter Zustände in Materialien mit Relevanz für die organische Elektronik”. Dissertation. Albert-Ludwigs-Universität Freiburg, 2017.

[42] Wolfgang Lubitz, Eduard Reijerse and Maurice van Gastel. [NiFe] and [FeFe] Hydrogenases Studied by Advanced Magnetic Resonance Techniques. *Chemical Reviews* 107 (2007), pp. 4331–4365.

[43] Asako Okafuji, Alexander Schnegg, Erik Schleicher, Klaus Möbius and Stefan Weber. G-Tensors of the Flavin Adenine Dinucleotide Radicals in Glucose Oxidase: A ComparativeMultifrequency Electron Paramagnetic Resonance and Electron-Nuclear Double Resonance Study. *Journal of Physical Chemistry B* 112 (2008), pp. 3568–3574.

[44] Gavin W. Morley, Petra Lueders, M. Hamed Mohammady, Setrak J. Balian, Gabriel Aeppli1, Christopher W. M. Kay, Wayne M. Witzel, Gunnar Jeschke and Tania S. Monteiro. Quantum control of hybrid nuclear–electronic qubits. *Nature Materials* 12 (2013), pp. 103–107.

[45] David Kieferand Alexander Giovannitti et al. Enhanced n-Doping Efficiency of a Naphthalenediimide-Based Copolymer through Polar Side Chains for Organic Thermoelectrics. *ACS Energy Letters* 3 (2018), pp. 278–285.

[46] Hannes Kraus, Victor A. Soltamov, Daniel Riedel, Stefan Väth, Fanziska Fuchs, Andreas Sperlich, Pavel G. Baranov, Vladimir Dyakonov and Georgy V. Astakhov. Room-temperature quantum microwave emittersbased on spin defects in silicon carbide. *Nature Physics* 10 (2014), pp. 157–162.

[47] Thomas D. Smith and John R. Pilbrow. The determination of structural properties of dimeric transition metal ion complexes from epr spectra. *Coordination Chemistry Reviews* 13 (1974), pp. 173–278.

[48] Jurek Krzystek, Andrew Ozarowski and Joshua Telser. Multi-frequency, high-field EPR as a powerful tool to accurately determine zero-field splitting in high-spin transition metal coordination complexes. *Coordination Chemistry Reviews* 250 (2006), pp. 2308–2324.

[49] Monalisa Goswami, Andrei Chirila, Christophe Rebreyend and Bas de Bruin. EPR Spectroscopy as a Tool in Homogeneous Catalysis Research. *Topics in Catalysis* 58 (2015), pp. 719–750.

[50] Reinhard Stösser, Ulrich Marx, Werner Herrmann, Jabor K. Jabor and Angelika Brückner. In Situ EPR Study of Chemical Reactions in Q-Band at Higher Temperatures: A Challenge for Elucidating Structure-Reactivity Relationships in Catalysis. *Journal of the American Chemical Society* 132 (2010), pp. 9873–9880.

[51] Gary P. Laroff, Richard W. Fessenden and Robert H. Schuler. Electron spin resonance spectra of radical intermediates in the oxidation of ascorbic acid and related substances. *Journal of the American Chemical Society* 94 (1972), pp. 9062–9073.

[52] Clyde A. Hutchison Jr. and Billy W. Mangum. Paramagnetic resonance absorption in naphthalene in its phosphorescent state. *Journal of Chemical Physics* 34 (1961), pp. 908–922.

[53] Till Biskup, Erik Schleicher, Asako Okafuji, Gerhard Link, Kenichi Hitomi, Elizabeth D. Getzoff and Stefan Weber. Direct Observation of a Photoinduced Radical-Pair Intermediate in a Cryptochrome DASH Blue-Light Photoreceptor. *Angewandte Chemie International Edition English* 48 (2009), pp. 404–407.

[54] Gareth R. Eaton, Sandra S. Eaton, David P. Barr and Ralph T.Weber. *Quantitative EPR*. First edition. SpringerWienNewYork, 2010.

[55] D. T. Burns and B. D. Flockhart. Application of quantitative EPR. *Philosophical Transactions of the Royal Society A — Mathematical, Physical and Engineering Sciences* 333 (1990), pp. 37–48.

[56] Andrei V. Astashkin and Arthur Schweiger. Electron-spin transient nutation: a new approach to simplify the interpretation of ESR spectra. *Chemical Physics Letters* 174 (1990), pp. 595–602.

[57] Arthur Schweiger and Gunnar Jeschke. *Principles of Pulse Electron Paramagnetic Resonance*. First edition. Oxford University Press, 2001.

[58] M. Uchida and M. Ono. Improvement for Oxidative Flavor Stability of Beer—Role of OH-Radical in Beer Oxidation. *Journal of the American Society of Brewing Chemists* 54 (1996), pp. 198–204.

[59] Marianne K. Thomsen, Dorthe Kristensen and Leif H. Skibsted. Electron spin resonance spectroscopy for determination of the oxidative stability of food lipids. *Journal of the American Oil Chemists' Society* 77 (2000), pp. 725–730.

[60] Ashutosh Shukla. *Electron Spin Resonance in Food Science*. First edition. Academic Press, 2016.

[61] Tor Arne Vestad, Eirik Malinen, Anders Lund, Eli Olaug Hole and Einar Sagstuen. EPR dosimetric properties of formates. *Applied Radiation and Isotopes* 59 (2003), pp. 181–188.

[62] Evgenii Konstantinovich Zavoisky. Paramagnetic relaxation of liquid solutions for perpen-dicular fields. *Journal of Experimental and Theoretical Physics* 15 (1945), pp. 344–350.

[63] Paul Dirac, Maurice Adrien and Ralph Howard Fowler. The quantum theory of the electron. *Proceedings of the Royal Society A — Mathematical Physical and Engineering Sciences* 117 (1928), pp. 610–624.

[64] Pieter Zeeman. Ueber einen Einfluss der Magnetisirung auf die Natur des von einer Substanz emittirten Lichtes. *Verhandlungen der Physikalischen Gesellschaft zu Berlin* 15 (1896), pp. 128–130.

[65] John E. Harriman. *Theoretical Foundations of Electron Spin Resonance*. First edition. Academic Press, 1978.

[66] Charles P. Poole Jr. and Horacio A. Farach. *Theory of Magnetic Resonance*. Second edition. John Wiley & Sons, Ltd, 1987.

[67] N. M. Atherton. *Principles of Electron Spin Resonance.* Chichester, England: Ellis Horwood Ltd., 1993.

[68] Wolfgang Pauli. Zur Quantenmechanik des magnetischen Elektrons. *Zeitschrift für Physik* 43 (1927), pp. 601–623.

[69] John A. Weil and James R. Bolton. *Electron Paramagnetic Resonance: Elementary Theory and Practical Applications.* Second edition. Hoboken, USA: John Wiley & Sons, Inc., 2007.

[70] Erwin Schrödinger. Quantisierung als Eigenwertproblem. *Annalen der Physik* 384 (1926), pp. 361–376.

[71] John William Strutt Baron Rayleigh. *The Theory of Sound.* First edition. London, England: Macmillan and Co, 1877.

[72] Frank Jensen. *Indroduction to Computational Chemistry.* Third edition. Chichester, England: John Wiley & Sons, Ltd., 2017.

[73] Christopher J. Cramer. *Essentials of Computational Chemistry Theories and Models.* Chichester, England: John Wiley & Sons, Ltd., 2004.

[74] Roman Boča. Zero-field splitting in metal complexes. *Coordination Chemistry Reviews* 248 (2004), pp. 757–815.

[75] Gunnar Jeschke. *Kurze Einführung in die elektronenparamagnetische Resonanzspektroskopie.* Universität Konstanz, 2008.

[76] Mitchel Weissbluth. "Hydrogen Atom". In: *Atoms and Molecules.* New York, USA: Academic Press, 1978. Chap. 16, pp. 322–345.

[77] *Documentation of Easyspin 5.2.29.* Retrieved 09.01.2021. URL: `https://easyspin.org/easyspin/documentation/`.

[78] Sabine Richert, Claudia E. Tait and Christiane R. Timmel. Delocalisation of photoexcited triplet states probed by transient EPR and hyperfine spectroscopy. *Journal of Magnetic Resonance* 280 (2017), pp. 103–116.

[79] Kerstin Serrer, Clemens Matt, Monja Sokolow, Sylwia Kacprzak, Erik Schleicher and Stefan Weber. Application of commercially available fluorophores as triplet spin probes in EPR spectroscopy. *Molecular Physics* 117 (2019), pp. 2688–2699.

[80] *Tom Davis, Arrow3, MATLAB Central File Exchange.* Retrieved May 12, 2021. URL: `https://www.mathworks.com/matlabcentral/fileexchange/14056-arrow3`.

[81] Malcolm D.E. Forbes, Lauren E. Jarocha, SooYeon Sim and Valery F. Tarasov. Time-resolved electron paramagnetic resonance spectroscopy: history, technique, and application to supramolecular and macromolecular chemistry. *Advances in Physical Organic Chemistry* 47 (2014), pp. 1–83.

[82] Stefan Weber. Transient EPR. *eMagRes* 6 (2017), pp. 255–270.

[83] Antoine B. Zahlan, ed. *The Triplet State.* First edition. Cambridge University Press, 1967.

[84] Noboru Hirota and Seigo Yamauchi. Short-lived excited triplet states studied by time-resolved EPR spectroscopy. *Journal of Photochemistry and Photobiology C: Photochemistry Reviews* 4 (2003), pp. 109–124.

[85] Rashid R. Valiev, Victor N. Cherepanov, Glib V. Baryshnikov and Dage Sundholm. First-principles method for calculating the rate constants of internal-conversion and intersystem-crossing transitions. *Physical Chemistry Chemical Physics* 20 (2018), pp. 6121–6133.

[86] Nicholas J. Turro, V. Ramamurthy and J. C. Scaiano. *Principles of Molecular Photochemistry: An Introduction.* First edition. University Science Books, 2008.

[87] Zachary E. X. Dance, Sarah M. Mickley, Thea M. Wilson, Annie Butler Ricks, Amy M. Scott, Mark A. Ratner and Michael R. Wasielewski. Intersystem crossing mediated by photoinduced intramolecular charge transfer: julolidine–antrhacene molecules with perpendicular π systems. *Journal of Physical Chemistry A* 112 (2008), pp. 4194–4201.

[88] Marion Charlotte Thurnauer, Joseph J. Katz and James Ritchie Norris. The triplet state in bacterial photosynthesis: Possible mechanisms of the primary photo-act. *Proceedings of the National Academy of Sciences* 72 (1975), pp. 3270–3274.

[89] Kobi Hasharoni, Haim Levanon, Scott R. Greenfield, David J. Gosztola, Walter A. Svec and Michael Roman Wasielewski. Mimicry of the Radical Pair and Triplet States in Photosynthetic Reaction Centers with a Synthetic Model. *Journal of the American Chemical Society* 117 (1995), pp. 8055–8056.

[90] Gilbert N. Lewis and M. Kasha. Phosphorescence in fluid media and the reverse process of singlet–triplet absorption. *Journal of the American Chemical Society* 67 (1945), pp. 994–1003.

[91] Michael Kasha. Characterization of electronic transitions in complex molecules. *Discussions of the Faraday Society* 9 (1950), pp. 14–19.

[92] Deborah L. Meyer, Florian Lombeck, Sven Huettner, Michael Sommer and Till Biskup. Direct $S_0 \rightarrow T$ excitation of a conjugated polymer repeat unit: unusual spin-forbidden transitions probed by time-resolved electron paramagnetic resonance spectroscopy. *Journal of Physical Chemistry Letters* 8 (2017), pp. 1677–1682.

[93] Gunnar Jeschke. *Kruze Einführung in die elektroparamagnetische Resonanzspektroskopie.* Universität Konstanz, 2008.

[94] Johan van Tol, Louis Claude Brunel and Alexander Angerhofer. Transient EPR at 240 GHz of the Excited Triplet Stateof Free-Base Tetra-Phenyl Porphyrin. *Applied Magnetic Resonance* 21 (2001), pp. 335–340.

[95] Claudia E. Tait, Patrik Neuhaus, Harry L. Anderson and Christiane R. Timmel. Triplet state delocalization in a conjugated porphyrin dimer probed by transient electron paramagnetic resonance techniques. *Journal of the American Chemical Society* 137 (2015), pp. 6670–6679.

[96] Charles P. Poole Jr. *Electron Spin Resonance.* Second edition. John Wiley & Sons, Ltd, 1983.

[97] Attila Szabo and Neils Ostlund. *Modern Quantum Chemistry.* First edition. Mineola, New York: Dover Publications Inc, 1996.

[98] Matrin Kaupp, Michael Bühl and Vladimir G. Malkin. *Calculation of NMR and EPR Parameters.* First edition. Wiley-VCH, 2004.

[99] Erwin Schrödinger. An undulatory theory of the mechanics of atoms and molecules. *Physical Review* 28 (1926), pp. 1049–1070.

[100] Max Born and Robert Oppenheimer. Zur Quantentheorie der Molekeln. *Annalen der Physik* 389 (1927), pp. 457–484.

[101] Michael Springborg. *Quantenchemie.* First edition. Berlin, Germany: De Gruyter, 2017.

[102] John C. Slater. The theory of complex spectra. *Physical Review* 34 (1929), pp. 1293–1322.

[103] Wolfgang Pauli. Über Zusammenhang des Abschlusses der Elektronengruppen im Atom mit der Komplexstruktur der Spektren. *Zeitschrift für Physik* 31 (1925), pp. 765–783.

[104] Vladimir Fock. Näherungsmethode zur Lösung des quantenmechanischen Mehrkörperproblems. *Zeitschrift für Physik* 61 (1930), pp. 126–148.

[105] Walter Ritz. Über eine neue Methode zur Lösung gewisser Variationsprobleme der mathematischen Physik. *Journal für die reine und angewandte Mathematik* 135 (1909), pp. 1–65.

[106] Douglas R. Hartree. The Wave Mechanics of an Atom with a Non-Coulomb Central Field. Part I. Theory and Methods. *Mathematical Proceedings of the Cambridge Philosophical Society* 24 (1928), pp. 89–110.

[107] Douglas R. Hartree. The Wave Mechanics of an Atom with a Non-Coulomb Central Field. Part II. Some Results and Discussion. *Mathematical Proceedings of the Cambridge Philosophical Society* 24 (1928), pp. 111–132.

[108] Clemens C. J. Roothaan. New Developments in Molecular Orbital Theory. *Reviews of Modern Physics* 23 (1951), pp. 69–89.

[109] George G. Hall. The molecular orbital theory of chemical valency VIII. A method of calculating ionization potentials. *Proceedings of the Royal Society A — Mathematical Physical and Engineering Sciences* 205 (1951), pp. 541–552.

[110] Samuel Francis Boys. Electronic wave functions - I. A general method of calculation for the stationary states of any molecular system. *Proceedings of the Royal Society A — Mathematical Physical and Engineering Sciences* 200 (1950), pp. 542–554.

[111] *Basis sets.* Retrieved 09.11.2020. URL: `https://www.basissetexchange.org/`.

[112] Xinguo Ren, Patrick Rinke, Volker Blum, Jürgen Wieferink, Alexandre Tkatchenko, Andrea Sanfilippo, Karsten Reuter and Matthias Scheffler. Resolution-of-identity approach to HartreeFock, hybrid density functionals, RPA, MP2 and GW numeric atom-centered orbital basis functions. *New Journal of Physics* 14 (2012), p. 053020.

[113] Frank Neese. An Improvement of the Resolution of the Identity Approximation for the Formation of the Coulomb Matrix. *Journal of Computational Chemistry* 24 (2003), pp. 1740–1747.

[114] Róbert Izsák, Andreas Hansen and Frank Neese. The resolution of identity and chain of spheres approximations for the LPNO-CCSD singles Fock term. *Molecular Physics* 110 (2012), pp. 2413–2417.

[115] Adel A. El-Azhary and Hans U. Suter. Comparison between Optimized Geometries and Vibrational Frequencies Calculated by the DFT Methods. *Journal of Physical Chemistry* 100 (1996), pp. 15056–15063.

[116] Pierre Hohenberg and Walter Kohn. Inhomogeneous electron gas. *Physical Review* 136 (1964), B864–B871.

[117] Walter Kohn and Lu Jeu Sham. Self-consistent equations including exchange and correlation effects. *Physical Review* 140 (1965), A1133–A1138.

[118] Paul A. M. Dirac. Note on Exchange Phenomena in the Thomas Atom. *Mathematical Proceedings of the Cambridge Philosophical Society* 26 (1930), pp. 376–385.

[119] John C. Slater. A Simplification of the Hartee-Fock Method. *Physical Review* 81 (1951), pp. 385–390.

[120] David Matthew Ceperley and Bernie Julian Alder. Ground State of the Electron Gas by a stochastic Method. *Physical Review Letters* 47 (1980), pp. 566–569.

[121] Axel D. Becke. Density-functional exchange-energy approximation with correct asymptotic behavior. *Physical Review A* 38 (1988), pp. 3098–3100.

[122] John P. Perdew. Density-functional approximation for the correlation energy of the inhomogeneous electron gas. *Physical Review B* 33 (1986), pp. 8822–8824.

[123] Chengteh Lee, Weitao Yang and Robert G. Parr. Development of the Colle-Salvetti correlation-energy formula into a functional of the electron density. *Physical Review B* 37 (1988), pp. 785–789.

[124] Axel D. Becke. Density-functional thermochemistry. III. The role of exact exchange. *Journal of Chemical Physics* 98 (1993), pp. 5648–5652.

[125] Wolfram Koch and Max C. Holthausen. *A Chemist's Guide to Density Functional Theory*. Second edition. Wiley-VCH, 2001.

[126] Stefan Grimme. Density functional theory with London dispersion corrections. *Wiley Interdisciplinary Reviews-Computational Molecular Science* 1 (2011), pp. 211–228.

[127] Robert Sanderson Mulliken. Electronic Population Analysis on LCAO-MO Molecular Wave Functions. *Journal of Chemical Physics* 23 (1955), pp. 1833–1840.

[128] Frank Neese. Prediction of molecular properties and molecular spectroscopy with density functional theory: From fundamental theory to exchange-coupling. *Coordination Chemistry Reviews* 523 (2009), pp. 526–563.

[129] Frank Neese. Spin-spin contributions to the zero-field splitting tensor in organic triplets, carbens and biradicals – A density functional ab initio study. *Journal of Physical Chemistry A* 110 (2006), pp. 12267–12275.

[130] Roy McWeeny and Yosuke Mizuno. The Density Matrix in Many-Electron Quantum Mechanics. II. Separation of Space and Spin Variables; Spin Coupling Problems. *Proceedings of the Royal Society A — Mathematical Physical and Engineering Sciences* 259 (1961), pp. 554–577.

[131] Christoph Riplinger, Joseph P. Y. Kao, Gerald M. Rosen, Velavan Kathirvelu, Gareth R. Eaton, Sandra S. Eaton, Andrei Kutateladze and Frank Neese. Prediction of molecular properties and molecular spectroscopy with density functional theory: From fundamental theory to exchange-coupling. *Journal of the American Chemical Society* 131 (2009), pp. 10092–10106.

[132] Erich Runge and E. K. U. Gross. Density-Functional Theory for Time-Dependent Systems. *Physical Review Letters* 52 (1984), pp. 997–1000.

[133] Mark E. Casida. “Time-Dependent Density Functional Response Theory for Molecules”. In: *Recent Advances in Density Functional Methods Part I*. Singapore: World Scientific, 1995. Chap. 5, pp. 155–192.

[134] Andreas Dreuw and Martin Head-Gordon. Single-Reference ab Initio Methods for the Calculation of Excited States of Large Molecules. *Chemical Reviews* 105 (2005), pp. 4009–4037.

[135] Richard L. Martin. Natural transition orbitals. *Journal of Chemical Physics* 118 (2003), pp. 4775–4777.

[136] Stefan Stoll. “Spectral Simulations in Solid-State Electron Paramagnetic Resonance”. Dissertation. Eidgenössische Technische Hochschule Zürich, 2003.

[137] Till Biskup. *trEPR-Toolbox*. Retrieved 13.01.2021. URL: `https://www.till-biskup.de/de/software/matlab/trepr/index`.

[138] Till Biskup. *TSim Module*. Retrieved 13.01.2021. URL: `https://www.till-biskup.de/de/software/matlab/tsim/index`.

[139] *Download of Easyspin 5.2.29*. Retrieved 13.01.2021. URL: `https://easyspin.org/easyspin/`.

[140] *MathWorks, MATLAB Homepage*. Retrieved 10.05.2021. URL: `https://www.mathworks.com/products/matlab.html`.

[141] Robert Steyrleuthner, Marcel Schubert, Ian Howard, Bastian Klaumünzer, Kristian Schilling, Zhihua Chen, Peter Saalfrank, Frédérik Laquai, Antonio Facchetti and Dieter Neher. Aggregation in a high-mobility n-type low-bandgap copolymer with implications on semicrystalline morphology. *Journal of the American Chemical Society* 134 (2012), pp. 18303–18317.

[142] Manfred Hesse, Herbert Meier and Bernd Zeeh. *Spektroskopie Methoden in der organischen Chemie*. Seventh edition. Stuttgart, Deutschland: Georg Thieme Verlag, 2005.

[143] Frank Neese. The ORCA program system. *Wiley Interdisciplinary Reviews-Computational Molecular Science* 2 (2012), pp. 73–78.

[144] Florian Weigend and Reinhart Ahlrichs. Balanced basis sets of split valence, triple zeta valence and quadruple zeta valence quality for H to Rn: Design and assessment of accuracy. *Physical Chemistry Chemical Physics* 7 (2005), pp. 3297–3305.

[145] G. A. Petersson, Andrew Bennett, Thomas G. Tensfeldt, Mohammad A. Al-Laham, William A. Shirley and John Mantzaris. A complete basis set model chemistry. I. The total energies of closed-shell atoms and hydrides of the first-row elements. *Journal of Chemical Physics* 89 (1988), pp. 2193–2218.

[146] G. A. Petersson and Mohammad A. Al-Laham. A complete basis set model chemistry. II. Open-shell systems and the total energies of the first-row atoms. *Journal of Chemical Physics* 94 (1991), pp. 6081–6090.

[147] Yongfang Li. Molecular design of photovoltaic materials for polymer solar cells: toward suitable electronic energy levels and broad absorption. *Accounts of Chemical Research* 45 (2012), pp. 723–733.

[148] Junwu Chen and Yong Cao. Development of novel conjugated donor polymers for high-efficiency bulk-heterojunction photovoltaic devices. *Accounts of Chemical Research* 42 (2009), pp. 1709–1718.

Danksagung

Zuerst möchte ich mich bei meiner Familie bedanken, welche mich über die ganzen Jahre meines Studiums an allen Fronten kräftig unterstützt hat und mir damit diese schöne Zeit ermöglichte. Besonderer Dank gilt meiner Mutter Anne Vögele, die mir vor allem in den schwierigen Zeiten meines Lebens zur Seite stand. Des weiteren möchte ich mich bei meiner Verlobten Annie Bueno, welche mich immer wieder anspornte mit meiner Arbeit voran zu kommen trotz schwieriger Umstände bedanken. Ich bin sehr froh, dass du mit mir durch diese fordernde Zeit der Fernbeziehung und der Lockdowns gegangen bist. Für die hervorragende Betreuung während meiner gesamten Doktorarbeit möchte ich mich ganz herzlich bei PD Dr. Till Biskup bedanken. Die viele Unterstützung und Wertschätzung meiner Arbeit hat mich stets motiviert mich insbesondere im Bereich der Dichte-Funktional-Theorie, trotz fehlender Expertise, weiterzuentwickeln. Für die gemeinsame Zeit an Spektrometer und Rechner, sowie die vielen inspirativen Gespräche möchte ich mich recht herzlich bedanken. Vielleicht schaffe ich es ja irgendwann mal einen Test für meine Software zu schreiben.

Prof. Dr. Christopher W. M. Kay möchte ich ganz herzlich dafür danken, dass ich meine Doktorarbeit in Saarbrücken fortsetzen durfte. Das Vertrauen in meine Fähigkeiten und die Übertragung von mehr Verantwortung habe meine persönliche Entwicklung deutlich vorangebracht. Die schönen außeruniversitären Aktivitäten, wie das Wandern und Radfahren werde ich sehr gut in Erinnerung behalten.

Ich bedanke mich nachdrücklich bei Prof. Dr. Stefan Weber für die schöne Zeit im 8. Stock und für seinen Einsatz während und nach meiner Freiburger Zeit.

Bedanken möchte ich mich ebenfalls bei Prof. Dr. Michael Sommer, Dr. Rukiya Matsidik und Dr. Florian Lombeck für die Probenpräparation und die ausgezeichnete Zusammenarbeit. Ohne diese fantastische Kooperation, wäre diese Arbeit nicht möglich gewesen.

Mein Dank gilt noch allen Mitarbeitern und Mitarbeiterinnen der Arbeitskreise Weber und Kay, welche ich im Rahmen dieser Arbeit kennenlernen durfte. Es war eine große Freude an beiden Standorten zu arbeiten. Mitarbeiter und Mitarbeiterinnen beider zugehörigen Werkstätten sind selbstverständlich auch gemeint.

Für die Korrekturen der Arbeit will ich mich abschließend bei PD Dr. Till Biskup, Dr. Hilke Bahmann, Hannes Matt, Mirjam Schröder, Dr. Daniel Rauber und Alex Ulyet bedanken.